STUDY OF HIGH-Q^2 DIS PROCESSES AT HERA

Mario Martínez Pérez

Facultad de Ciencias
Departamento de Física Teórica.

UAM
UNIVERSIDAD AUTONOMA
DE MADRID

A thesis submitted in partial fulfilment
of the requirements
for the Degree of Doctor of Science
March 1998

Acknowledgements

I would like to thank those persons who helped me during my PhD. studies. I thank Prof. Fernando Barreiro, Prof. Luis Labarga and Prof. Jose del Peso who gave me the opportunity to work in a wonderful High-Energy-Physics laboratory like DESY. I would like to thank Prof. Juan Terrón, who so much helped me during a big part of my PhD. studies and allowed me to learn so many things.
I would like also to thank all those persons from DESY who helped me during these last four years. In particular, I thank Dr. U. Katz and Prof. G. Wolf for their invaluable comments and suggestions on the analyses presented in this thesis. I thank all my PhD. colleagues from the Univ. Madrid Group for their continuous support and affection. I desire the best for all of them. I would like to dedicate few lines to thank all my friends; those who gave me great moments here in Hamburg and those who waited for me there in Madrid and never forgot me.

Quisiera rendir homenaje a toda mi familia. A mis padres, cuyo esfuerzo y sacrificio me ha permitido realizar cosas que ellos jamás pudieron y siempre quisieron hacer. Todo lo que soy y seré se lo debo a ellos y siempre a ellos rendiré tributo. A mis hermanos, tan cercanos en edad, con quienes comparto experiencias de juventud e incertezas futuras. A mi hermana, que por ser la menor siempre ocupó un lugar privilegiado en todos nosotros y a quien últimamente no he visto crecer, sorprendiéndome siempre con su altura casi ya mayor que la mía. A todos ellos quisiera haber dedicado todo ese tiempo que la distancia no me ha permitido.

Contents

Preface

The scattering of leptons on protons at large momentum transfers allows the study of the fundamental forces of nature at very small distances. The comparison between neutral and charged-current interactions at these very high momentum transfers, permits, for the first time, to reach the region where the electromagnetic and weak forces are of the same magnitude, as a consequence of their unification. The investigation of charged current events from positron-proton and electron-proton interactions, which involve different couplings to different quark flavours, gives information about the structure of the weak theory and the parton distributions within the proton. Furthermore, the cross-section measurements performed in the high momentum transfer region are sensitive to the appearance of physics beyond the Standard Model.

The study of the hadronic final states in those interactions permits to investigate the strong interaction aspects of the physics processes involved. The dynamics of jet production, the internal structure of the jets and the differences between gluon and quark jets constitute fundamental predictions of QCD.

In the first chapter, a brief discussion on the theoretical and phenomenological aspects relevant to the analyses is presented. It starts with the most fundamental aspects of the theory, like the QCD lagrangian and the parton model picture, and finishes with more 'concrete' issues like the design of jet-finder algorithms or the simulation of complete high-energy physics events with Monte Carlo generators.

Chapter 2 presents the characteristics of HERA as the first electron-proton collider. A detailed description of the main components of the ZEUS detector is provided, including a discussion on the luminosity measurement procedure and the design of the data acquisition system. In the last part of the chapter, several methods to reconstruct the kinematic variables are shown.

Chapter 3 shows a detailed description of the analysis performed on charged-current interactions at high-Q^2. In this study, measurements of the cross sections for $e^{\pm}p$ charged-current interactions are presented and used to determine the W boson mass. In the last part of the chapter, the cross sections for neutral and charged-current interactions are compared at very high-Q^2, showing the similarity between both interactions at these very high virtualities of the exchanged boson. In addition, some detailed studies and further results are collected in appendixes A and B.

The hadronic final states in high-Q^2 deep-inelastic-scattering processes are discussed in chapters 4 and 5, using the concept of 'jet' as the fundamental object.

Chapter 4 presents the analysis performed on 'jet shapes', which includes the study of the jet shapes in neutral and charged-current interactions. The measurements are compared with theoretical predictions and with similar results from other processes like ep-photoproduction, e^+e^- and $p\overline{p}$ interactions showing the differences between the jets coming from quarks and gluons.

Chapter 5 shows measurements of inclusive jet cross sections in neutral-current inter-

actions with $Q^2 > 125$ GeV^2. These measurements are sensitive to the appearance of interactions beyond the Standard Model. The measurements are compared to the predictions of the Standard Model. Some detailed aspects of the jet analyses are described in appendixes C and D.
Chapter 6 is devoted to summary and conclusions.

The results of this thesis have led to the following publications:

- *Study of charged current ep interactions at $Q^2 > 200$ GeV^2 with the ZEUS detector at HERA*. ZEUS Collab., M. Derrick et al., Z. Phys. C72 (1996) 47.
- *Measurement of Jet Shapes in High Q^2 DIS at HERA*. ZEUS Collab., J. Breitweg et al., N-649 Contributed paper to the International Europhysics Conference on High Energy Physics, Jerusalem, Israel, 1997 and to be submitted to Z. Phys.
- *Measurement of the Inclusive Jet Cross Section in High-Q^2*. ZEUS Collab., J. Breitweg et al., N-663 Contributed paper to the International Europhysics Conference on High Energy Physics, Jerusalem, Israel, 1997.

Chapter 1

Introduction

1.1 Deep Inelastic Processes

To lowest order in perturbation theory, we can describe the deep inelastic electron-proton scattering (DIS) ($ep \to eX$) to be mediated by the exchange of an intermediate boson (γ,Z^0 or $W^\pm$), as shown in figure 1.1. If the charge of the lepton is conserved, which means that the intermediate boson is neutral, the process is referred to as a *neutral-current process*. If the lepton is converted into a neutrino via the exchange of a charged vector, the interaction is defined as a *charged-current process*. At a given center of mass energy $\sqrt{s}$ the kinematics of inclusive DIS scattering are completely described by two Lorentz-invariant quantities (see figure 1.1)

$$Q^2 = -q^2 = -(k - k')^2 \text{ and } \nu = \frac{pq}{M},$$

where k(k') is the 4-momentum of the incoming (outgoing) lepton and M is the mass of the proton. Nevertheless, it is common to replace ν and Q^2 by the dimensionless variables

$$x = \frac{Q^2}{2pq}, \qquad y = \frac{pq}{pk}$$

which take values in the range $0 < x, y < 1$. In the naive quark-parton model, the Bjorken scaling variable x is the fraction of the momentum of the proton carried by the struck quark. The variable y is the fractional energy of the initial lepton transferred to the proton in its rest frame. Finally, Q^2 denotes the virtuality of the exchanged boson. The invariant mass of the hadronic final state (W) can be related to the kinematic variables using energy-momentum conservation at the hadronic vertex $W^2 = (p')^2 = Q^2\frac{1-x}{x}$. The cross sections for these processes can be calculated by factorising it into a leptonic tensor $L_{\mu\nu}$, which describes the leptonic vertex, and a tensor $W^{\mu\nu}$ which parametrizes the form of the current at the hadronic vertex.

$$d\sigma \sim L_{\mu\nu} W^{\mu\nu}(q, p)$$

Since the electroweak couplings at the leptonic vertex are known, the study of deep-inelastic processes allows us to extract information on the structure of the proton. In the case of single photon exchange the most general expression for the hadronic tensor $W^{\mu\nu}$, which can be constructed out of Lorentz invariant terms defined using the metric $g^{\mu\nu}$ and the independent variables p and q, is

$$W^{\mu\nu} = W_1(-g^{\mu\nu} + \frac{q^\mu q^\nu}{q^2}) + W_2\frac{1}{M^2}(p^\mu - \frac{pq}{q^2}q^\mu)(p^\nu - \frac{pq}{q^2}q^\nu)$$

which defines the structure functions of the proton $W_1(Q^2,\nu)$ and $W_2(Q^2,\nu)$. In general, deep-inelastic scattering is expected to be a complicated process, and the behaviour of the structure functions W_1 and W_2 with ν and Q^2 will reflect such complication. However, in the limit $Q^2 \to \infty$, $\nu \to \infty$ with $x = Q^2/2M\nu$ fixed, Bjorken formulated the hypothesis that the structure functions scale as

$$MW_1(Q^2,\nu) \to F_1(x)$$

$$\nu W_2(Q^2,\nu) \to F_2(x).$$

Experimental support [1] for these predictions led initially to an examination of the theoretical basis of Bjorken's arguments, and to the formulation of the simple and intuitive picture provided by the quark parton model.

1.2 The Quark-Parton Model

The interpretation of the approximated scaling behaviour of the proton structure functions is that the exchanged photon interacts with point-like constituents (called partons by Feynman) within the proton. At high Q^2 and ν it is intuitively reasonable that the virtual photon is probing very short-distance scales within the proton. In this situation, Feynman supposed that the photon interacts with small (pointlike) constituents within the proton, which carry only a certain fraction of the momentum and energy of the proton. We can imagine the proton as constantly dissociating into virtual states of free partons. In deep inelastic scattering the collision time is much shorter that the virtual state lifetime and the partons can be treated as free during the collision. Hence the partons scatter incoherently and the virtual-boson-nucleon cross section is calculated as a sum of the parton cross sections.

$$\frac{d^2\sigma}{dxdQ^2} = \sum_i e_i^2 f_i(x,Q^2)(\frac{d^2\sigma_i}{dxdQ^2})$$

where e_i is the charge of parton i and $f_i(x,Q^2)$ is the probability of finding a parton i with momentum fraction between x and $x+dx$ in the proton. The structure functions will have a simple interpretation within the parton model:

$$F_1(x) = \frac{1}{2}\sum_i e_i^2 f_i(x)$$

$$F_2(x) = \sum_i e_i^2 x f_i(x)$$

The structure function F_2 is the sum over the momentum-weighted probability distributions of all partons weighted by the squares of their charges. The relationship $F_2(x) = 2xF_1(x)$ is called the Callan-Gross relation [2]: it is a direct consequence of the assumption that the partons within the proton are 1/2-spin particles.

1.3 Quantum Chromodynamics

The quark-parton model, as formulated above, ignores completely the dynamical role of gluons as the carriers of the strong force between coloured quarks. Strong interactions are described by Quantum Chromodynamics (QCD): a local non-abelian gauge theory of quarks and gluons in which SU(3) is the gauge group and gluons are the gauge bosons. The expression for the classical Lagrangian density is

$$L = -\frac{1}{4}F^A_{\alpha\beta}F^{\alpha\beta}_A + \sum_{flavours} \overline{q}_a(\gamma^\mu D_\mu - m)_{ab}q_b$$

where $F^A_{\alpha\beta}$ is the field strength tensor derived from the gluon field A^A_α as

$$F^A_{\alpha\beta} = [\partial_\alpha A^A_\beta - \partial_\beta A^A_\alpha - gf^{ABC}A^B_\alpha A^C_\beta]$$

and the indices A, B, C run over the eight colour degrees of freedom of the gluon field. The last term in the expression for $F^A_{\alpha\beta}$ distinguishes QCD from QED and gives rise to cubic and quartic gluon seft-interactions. The latter couplings are not possible between photons in QED. The sum in the lagrangian runs over the different flavours of the quarks, g is the coupling constant which determines the strength of the interaction and f^{ABC} are the structure constants of the SU(3) colour group. The quark fields (q_a) are in the triplet representation of the colour group ($a = 1, 2, 3$) and D is the covariant derivative which takes the form

$$(D_\alpha)_{ab} = \partial_\alpha\delta_{ab} + ig(t^C A^C_\alpha)_{ab}$$

$$(D_\alpha)_{AB} = \partial_\alpha\delta_{AB} + ig(T^C A^C_\alpha)_{AB}$$

where t and T are matrices in the fundamental and adjoint representations of SU(3). A representation for the generators T^A is provided by the eight Gell-Mann matrices. By convention, the normalization of the SU(N) matrices is chosen to be

$$Tr(t^A t^B) = T_R\delta^{AB}, \qquad T_R = 1/2$$

With this choice, the colour matrices obey the following relations:

$$\sum_A t^A_{ab}t^A_{ba} = C_F\delta_{ab}, \quad C_F = \frac{N^2-1}{2N}$$

$$Tr(T^C T^D) = \sum_{A,B} f^{ABC}f^{ABD} = C_A\delta_{CD}, \qquad C_A = N$$

In this way the values for C_F and C_A for SU(3) will be 4/3 and 3 respectively.

Another intrinsic characteristic of QCD, due to the non-abelian character of the theory, is "asymptotic freedom": the running coupling constant $\alpha_s = g^2/4\pi$ decreases as the scale at which the interaction takes place increases. At high momentum transfers (short distances) the value of α_s is small enough that quarks can be considered free. As a result, perturbation theory can be used for the calculation of invariant amplitudes in QCD. However, the coupling constant becomes relatively large when the interacting quarks become further apart and the perturbative expansion breaks down.

1.3.1 Scaling Violations

The naive Quark-Parton Model has to be modified by QCD as quarks interact through gluons, and can radiate gluons. Radiated gluons in turn can split into quark-antiquark pairs (sea quarks) or gluons. This gluon radiation results in a transverse momentum component of the quarks. Consequently quarks can also couple to longitudinally polarized photons and the Callan-Gross relation is no longer satisfied exactly.

Another consequence of gluon radiation is the scaling violations of the structure functions, which now exhibit a logarithmic dependence on Q^2 at fixed x. Although the gluons cannot interact directly with the exchanged boson, they modify the expressions for the cross sections and the structure functions via QCD radiative corrections and carry a large fraction of the momentum of the proton. This is interpreted as follows: at low Q^2 the resolution of the exchanged boson is rather broad, so that only just the quark substructure of the proton is probed. As Q^2 is increased the virtual photon resolves finer structure: i.e. the splitting of gluons into quark-antiquark pairs or more gluons, and the radiation of gluons from quarks. In this way, the distribution of quarks evolves with the probing scale, Q^2. This evolution is described by the Dokshitzer-Gribov-Lipatov-Altarelli-Parisi equations [3] for the quark and gluon distributions

$$\frac{dq_i(x,Q^2)}{dlnQ^2} = \frac{\alpha_s}{2\pi}\int_x^1 \frac{dy}{y}[q_i(y,Q^2)P_{qq}(x/y) + g(y,Q^2)Pqg(x/y)]$$

$$\frac{dg(x,Q^2)}{dlnQ^2} = \frac{\alpha_s}{2\pi}\int_x^1 \frac{dy}{y}[q_i(y,Q^2)P_{gq}(x/y) + g(y,Q^2)Pgg(x/y)$$

where the quantity $\frac{\alpha_s}{2\pi}P_{qq}(x/y)$ gives the probability that a quark with momentum fraction y radiates a gluon and carries afterwards a momentum fraction $x(< y)$; similarly for the other splitting functions. P_{qg} gives the probability that a gluon splits into a $q\overline{q}$ pair, and dynamically generates the sea quarks in the proton (see figure 1.2).

Due to gluon radiation, the expression for F_2 to leading order in α_s is modified to

$$\frac{F_2(x,Q^2)}{x} = \sum_f e_f^2 \int_x^1 \frac{dy}{y}[q(y)[\delta(1-x/y)+$$

$$\frac{\alpha_s}{2\pi}P_{qq}(x/y)ln(Q^2/\mu^2)] + g(y)[\frac{\alpha_s}{2\pi}P_{qg}(x/y)ln(q^2/\mu^2)]]$$

where μ^2 is an arbitrary cut-off included in order to avoid the singularities of the calculation. The solution of the DGLAP equations provides the Q^2 evolution of the parton distributions. The structure functions depend logarithmically on Q^2 as a signal of the presence of gluons inside the proton and of their interactions among the quarks. The x dependence of the parton distributions can only be obtained from the data. A variety of parameterizations, most of them obtained using the DGLAP evolution equations and constrained by experimental data, exists for the proton structure functions. As an example two sets of different parameterizations are briefly presented:

- The MRS parameterizations [4], obtained using the next-to-leading order DGLAP evolution, uses the following functional forms for the distributions of quarks and gluons

  $$xf_i(x) = A_i x^{\delta_i}(1-x)^{\eta_i}(1+\epsilon_i\sqrt{x}+\gamma_i x),$$

  where f_i is a particular parton density and $(A_i, \delta_i, \eta_i, \epsilon_i, \gamma_i)$ are parameters to be fixed. The parameters are determined by a χ^2 minimization to experimental data.

- The CTEQ Collaboration [5] uses the same functional form as MRS for the quark densities. However, the gluon distribution is parametrized according to the expression
$$xg(x) = A_o x^{A_1}(1-x)^{A_2}(1+A_3 x^{A_4}).$$
The parameters are determined by a fit to experimental data.

1.4 Cross Sections for DIS

In leading-order electroweak theory the unpolarized differential neutral-current cross section for the scattering of a charged lepton on a proton is given by the expression [6]

$$\frac{d^2\sigma(e^{\mp})}{dxdQ^2} = \frac{4\pi\alpha^2}{xQ^4}[y^2 xF_1(x,Q^2) + (1-y)F_2(x,Q^2) \pm (y-\frac{y^2}{2})xF_3(x,Q^2)]$$

in terms of the nucleon structure functions F_1, F_2 and F_3. The F_3 term measures parity violating contributions which arise from Z^o exchange. As said above, the first two structure functions are related through the Callan-Gross relation $2xF_1 = F_2$, which holds for spin 1/2 quarks when neglecting masses, intrinsic transverse momenta and order α_s QCD effects. Since these effects are usually very small (except in the low-x region), they are usually not included. In the standard model the structure functions are given by

$$F_2(x,Q^2) = \sum_f A_f(Q^2)[xq_f(x,Q^2) + x\overline{q_f}(x,Q^2)] \text{ and}$$

$$xF_3(x,Q^2) = \sum_f B_f(Q^2)[xq_f(x,Q^2) - x\overline{q_f}(x,Q^2)],$$

where q_f ($\overline{q_f}$) describes the density of a quark (antiquark) flavour f in the proton. The flavour-dependent coefficients A_f and B_f are given by

$$A_f(Q^2) = e_f^2 - 2e_f v_e v_f P_Z + (v_e^2 + a_e^2)(v_f^2 + a_f^2)P_Z^2 \text{ and}$$

$$B_f(Q^2) = -2e_f a_e a_f P_Z + 4v_e v_f a_e a_f P_Z^2,$$

where e_f is the electric charge, v_f and a_f are the neutral-current-vector and axial-vector couplings, and P_Z denotes the ratio of γ and Z^o propagators ($Q^2/(Q^2+M_Z^2)$). The individual contributions from γ exchange, Z^o exchange and $\gamma - Z^o$ interference are easily recognizable in the expression above. The pure-γ-exchange term dominates completely at low Q^2. With increasing Q^2 first the $\gamma - Z$ interference term (linear in P_Z) and then the pure weak term (quadratic in P_Z) become important.
The differential cross sections for charged current interactions are given by the expressions

$$\frac{d^2\sigma(e^-p)}{dxdQ^2} = \frac{\pi\alpha^2}{4sin^4\theta_W(Q^2+M_W^2)^2}\sum_{i,j}|V_{u_i,d_j}|^2 u_i(x,Q^2) + (1-y)^2|V_{u_i,d_j}|^2\overline{d_i}(x,Q^2)]\text{and}$$

$$\frac{d^2\sigma(e^+p)}{dxdQ^2} = \frac{\pi\alpha^2}{4sin^4\theta_W(Q^2+M_W^2)^2}\sum_{i,j}|V_{u_i,d_j}|^2\overline{u_i}(x,Q^2) + (1-y)^2|V_{u_i,d_j}|^2 d_i(x,Q^2)],$$

where V_{u_i,d_j} are the elements of the Kobayashi-Maskawa matrix, u_i and d_j denote up-type and down-type quark flavours, respectively, and i, j are familiar indices. A good approximation is to consider only four massless quarks flavours (u, d, s, c) and use unitarity relations $\sum_j |V_{u_i,d_j}|^2 = \sum_j |V_{u_j,d_i}|^2$.

The expressions for the cross sections presented above actually include matrix elements corresponding to the contributions from $O(\alpha_s)$ processes. These processes are presented in figure 1.3. The virtual photon can interact with a gluon within the proton producing a quark-antiquark pair in the final state. The struck quark can also emit a hard gluon in the final state. These diagrams contribute to the production of multijet events in DIS. The matrix elements for those processes are divergent in the limit when the gluon energy or the opening angle between partons vanishes. These soft and collinear singularities are partly cancelled by virtual corrections and partly absorbed in the definition of the parton densities.

1.5 Low-Q^2 Processes: Photoproduction

Electron-proton collisions at low Q^2 offer a rich physics potential. The high center of mass energy available at HERA ($\sqrt{s} \sim 300GeV$) allows the study of photoproduction over a wide energy range. Photon-proton cross sections are measurable in a range from about 100 GeV to 250 GeV. Due to their large rates, low-Q^2 processes contribute in a major way as backgrounds to DIS analyses. In the Vector Dominance Model (VDM) [7] the photon can fluctuate into a low-mass vector meson (ρ, ω, ϕ) which in turn interacts with the proton. As a result, the photon-proton cross section can be related to the vector-meson proton cross section via the parton model to pion-proton and kaon-proton cross sections. The photoproduction processes via vector meson production are expected to have a soft component: diffractive elastic/inelastic scattering processes (due to pomeron exchange between the vector meson and the proton) and a hard component coming from interactions between a parton from the proton and a parton from the vector meson (see figure 1.4).

In addition, the photon can couple directly to the quarks. This coupling gives rise to additional processes which become important at high energies. Hard photoproduction processes are classified (at leading order) in two types (see figure 1.5). In the *direct process* the photon behaves as a gauge boson: $\gamma g \to q\overline{q}$ and $\gamma q \to qg$. These subprocesses are identical to the $O(\alpha_s)$ subprocesses in DIS, apart from the different virtuality of the photon which participates in the hard interaction. In the *resolved processes* the photon acts as a source of partons which interact with those in the proton.

1.6 Multipartonic Production

The description of the hadronic final state in high-energy processes requires the calculation of multiple parton emission in QCD. For these higher order QCD processes it is usually not possible to perform exact matrix element calculations and one has instead to use approximation schemes. Two different approaches will be considered here: the parton-shower approach (PS) [8], based on the QCD parton-branching processes and the Colour Dipole Model (CDM) [9] where the gluons are radiated from colour dipoles between the separated quarks and gluons originating from the initial hard processes. Both models are able to describe the measurements in e^+e^- experiments [10]. However, the situation in deep inelastic scattering is more complicated. In this case there are strong interactions between partons before the basic hard electroweak interaction. In the following sections, a short description of each model is presented.

1.6.1 The Parton Shower Approach

In DIS the quark struck by the electroweak boson can emit partons both before and after the interaction giving rise to initial and final-state parton showers, respectively. A parton close to the mass-shell in the incoming nucleon can initiate a parton cascade where in each branching one parton becomes increasingly off-shell with a space-like virtuality ($m^2 < 0$) and the other is on-shell or has a time-like virtuality ($m^2 > 0$). This initial-state space-like shower results in a space-like quark which interacts with the electroweak boson that turns it into an outgoing quark which is either on shell or has a time-like virtuality. In the latter case, a final state time-like shower will result where the off-shell mass is reduced by branching into daughter partons with decreasing off-shell masses and decreasing opening angles. This shower continues until all partons are essentially on-shell. The general behaviour of initial and final-state showers are similar since they are both based on the branching processes $q \to gq$, $g \to gg$ and $g \to q\overline{q}$ as described by the DGLAP equations in the leading-logarithm approximation of perturbative QCD.

The final-state radiation is analogous to parton radiation in $e^+e^- \to q\overline{q}$ (see figure 1.6). The evolution is based on the Sudakov form factor [11], which expresses the probability that a parton does not branch between some initial maximum virtuality and some minimum value. From this one can find the mass of the decaying parton, the energy fraction in the branching and the flavour of the daughter partons. The process is iterated with a reduced virtuality until all parton virtualities are below some cutoff m_o^2 around 1 GeV^2. Coherence in soft gluon emission is taken into account through angular ordering [12] (decreasing opening angles in subsequent branches). Initial-state radiation is handled within the backwards-evolution scheme, where the shower is constructed from the hard electroweak interaction backwards with decreasing virtualities down to the on-shell partons in the incoming nucleon. This is a more complicated process since the nucleon parton densities must be taken into account. When combining the initial and final-state radiation to construct the complete model, special precautions have to be taken in order to preserve energy-momentum conservation and keep the normal definition of the kinematic variables, in particular that of x-Bjorken.

The amount and hardness of the initial and final-state radiation depends on the degree of off-shellness of the struck quark just before and after the boson vertex. These virtualities are chosen, based on a Sudakov form factor, between m_0^2 and a maximum to be set by the energy or momentum transfer scale in the process. Whereas only one scale is present in e^+e^-, any function of Q^2 and W^2 is possible in DIS. The parton-shower approach has some shortcomings due to its approximate nature. The separation of initial and final-state parton emission implies the neglect of interference terms between the two and it is not gauge invariant. The use of leading-order approximation means that the emission of the partons that are soft or close to the direction of the emitting partons should be well described, while the emission of hard partons at large angles could be mistreated. Therefore, the rate of events with extra hard partons that give rise to separate jets will be not well described. These problems were partially solved in e^+e^- by correcting the first emission in the parton shower to agree with the result from exact first order matrix-elements. In DIS, this matching is more difficult due to the more complicated matrix elements. Starting with the matrix elements, the hard emission is generated and extra, but softer emissions are then added using the parton-shower approach. The singular region of the matrix elements is avoided by a cutoff in the invariant mass of every parton pair $m_{ij} > y_{cut}W^2$.

1.6.2 The Colour Dipole Model

The Colour Dipole Model (CDM) is based on the fact that a gluon emitted from a $q\overline{q}$ pair in an e^+e^- collision can be treated as a radiation from the colour dipole between the q and $\overline{q}$, and that to a good approximation the emission of a second softer gluon can be treated as a radiation from two independent dipoles, one between the q and g and one between the g and $\overline{q}$ (see figure 1.7). This approach can be generalized and the emission of a third gluon is given by three independent dipoles, and so on.

For DIS, the CDM does not divide the process in initial and final state, as is made in the parton-shower approach discussed above. Instead it is assumed that all the radiation can be described by the colour dipole formed between the struck quark and the proton remnant. In e^+e^- both the q and $\overline{q}$ are treated as point-like particles, but in DIS only the struck quark can be considered point-like while the proton remnant is an extended object. It is a well known fact that emission of small wave lenghts from an extended antenna is suppressed and that for an antenna with a certain transverse size, effectively only a part proportional to the transverse wavelenght $\lambda \propto 1/p_T$ is actually participating in the emission. In the model this feature is implemented so that only a fraction

$$a = (\mu/p_T)^\alpha$$

of the proton remnant takes part in the emission of a gluon with transverse momentum p_T, where μ describes the inverse size and α the dimension of the proton remnant. In this way, the radiation is only dependent on the W^2 of the hard interaction, and the maximum p_T^2 is given by

$$p_T^2 < (\frac{W}{2})^{4/3}\mu^{2/3}$$

However, there is also a small dependence on x introduced by defining $\mu = \mu_o/(1-x)$, where μ_o is the original inverse size of the proton and μ the inverse size of the remnant after a quark with momentum fraction x has been hit. The CDM model correctly takes into account the QCD coherence effects included in the parton-shower approach by imposing angular ordering in the final state emissions. The colour coherence effects due to the extension of the proton remnant included in the CDM has however no correspondence in the parton shower-approach, where the remnant is a non-radiating spectator.

The CDM describes in principle only the p_t and rapidity y of each emission defined as

$$p_T^2 = s(1-x_1)(1-x_3) \quad \text{and} \quad y = \frac{1}{2} ln\frac{1-x_1}{1-x_3},$$

where x_1 and x_3 are the center of mass energy fractions of the emitting partons after the emission $x_i = 2e_i/\sqrt{s}$. To describe completely an emission, there are two more degrees of freedom to fix. One is the azimuthal angle of the emitted gluon which is assumed to be distributed between 0 and 2π. The other describes the distribution of transverse recoil among the emitting partons. This is also different in DIS as compared to e^+e^-. Since

only a fraction of the hadron remnant takes part in the emission, only that part should be allowed to recoil. This is realized by introducing an extra "recoil" gluon taking a fraction a of the remnants energy. The recoil is then distributed between this recoil gluon and the other emitting parton.
Although gluon emission in the CDM is close to the form of the exact matrix element, the so called boson-gluon fusion (BGF) process is not included at all. Therefore, a matching procedure has been introduced for the first emission in a DIS event. In this procedure, the initial dipole between the struck quark and the hadron remnant can either emit a gluon according to the $O(\alpha_s)$ matrix element or emit the antipartner of the struck quark according to the BGF matrix element. The selection of the process is, as usual, made by the Sudakov form-factor prescription. In the case of BGF, there is then two dipoles, connecting each of the struck quarks with the hadron remnant, which continue to radiate independently. If in the first step a gluon is emitted, the antipartner of the struck quark can be emitted in a later stage by using the normal initial state $g \to q\overline{q}$ splitting functions and the input structure functions in a way similar to a conventional initial state parton shower. Again the Sudakov form-factor is used to choose between this option and emitting gluons from either of the existing dipoles, and if a $g \to q\overline{q}$ splitting is chosen a new dipole is formed between the emitted antipartner and the corresponding part of the hadron remnant.

1.7 Hadronization Models

After the parton shower has finished, the final state consists of a set of partons with virtualities of the order of the cutoff scale m_o^2. From this point, the low momentum-transfer (long-distance) regime, in which non-perturbative effects cannot be neglected, has to be considered. In this regime, the coloured partons are transformed into colourless hadrons, a process called *hadronization* or *fragmentation*. This process is still not understood from first principles.

One general approach to hadronization, based on the observation that perturbation theory seems to work well down to rather low scales, is the hypothesis of *local parton-hadron duality* [13], where it is supposed that the flow of momentum and quantum numbers at the hadron level is established at the parton level. Hence, the flavour of the quark initiating a jet should be found in a hadron near the jet axis. The extent to which the hadron flow deviates from the parton flow reflects the smearing of order Λ due to hadron formation. Several phenomenological models have been constructed. Here three different models will be described: the *independent fragmentation model*, the *string model* and the *cluster model*.

1.7.1 Independent Fragmentation Model

The simplest scheme, suggested by Field and Feynman [14], for generating distributions of hadrons from those of partons is to assume that each parton fragments independently. The fragmenting quark q creates a colour field in which a new light $q'\overline{q}'$ pair is produced. A meson $q\overline{q}'$ is formed with a fraction z of the energy of the quark q. The leftover quark q', with energy fraction $(1-z)$, is fragmented in the same way, and so on until the leftover energy falls below some cutoff (see figure 1.8). For gluon fragmentation, the gluon is first

split into a quark-antiquark pair, either assigning all the gluon's momentum to one or the other with equal probability, so that the gluon behaves as a quark of random flavour, or using the $g \to q\overline{q}$ splitting function.
Such a prescription contains an arbitrary function $f(z)$ plus other input parameters for the flavour/spin/mass options at each step. These parameters must be determined from the comparison with experimental data. Afterwards, the model has predictive power. The details of the procedure are, however, not fixed. One can identify z with the energy fraction or $E + p_L$ fraction instead. The $q\overline{q}'$ pairs formed can be identified with low-mass hadronic clusters instead of single mesons. The original Field-Feynman parameterization

$$f(z) = 1 - a + 3a(1-z)^2$$

used the variable $E+p_L$, with $a = 0.77$ determined from data. They assumed that the $u\overline{u}$, $d\overline{d}$, $s\overline{s}$ probabilities were 0.4, 0.4 and 0.2, respectively, and that an equal mix of low-mass spin 0 and spin 1 mesons are formed. The quark has a gaussian distribution in p_T with $\sigma \sim 0.35$ GeV [15].

1.7.2 The String Model

The assumption of linear confinement provides the starting point for the string model [16]. As a q and $\overline{q}$ move apart from their common vertex, the physical picture is that of a colour vortex line being stretched between both partons. The transverse dimensions of the tube are of the order of the hadronic size (~ 1 fm). If the tube is assumed to be uniform along its length, this produces a confinement picture with a linearly rising potential. In order to obtain a Lorentz covariant and causal description of the energy flow due to this linear confinement, a massless relativistic string with no transverse degree of freedom is needed. From hadron spectroscopy, the string constant, i.e. the amount of energy per unit lenght, is of the order of $k \sim 1$ GeV/fm. As q and $\overline{q}$ move apart the potential energy stored inside the string increases, and the string may break by the production of a new $q'\overline{q}'$ pair, so that the system splits into two colour-singlet systems $q\overline{q}'$ and $q'\overline{q}$. If the invariant mass of either of these string pieces is large enough, further breaks may occur (see figure 1.9). In the Lund string model [17], the string break-up process is assumed to proceed until only on-mass-shell hadrons remain, each hadron corresponding to a small piece of string. In order to generate the quark-antiquark pairs, the Lund model invokes the idea of quantum mechanical tunnelling. This leads to a flavour independent gaussian spectrum of the p_T of the pairs and a suppression of heavy-quark production. A tunnelling mechanism can also be used to explain the production of baryons. In the simplest possible approach a diquark in a colour antitriplet state is just treated like an ordinary antiquark, such that a string can break either into quark-antiquark or into antidiquark-diquark production.

If several partons are moving apart from a common origin, the string structure between partons becomes more complicated. For a $q\overline{q}g$ event, a string is stretched from the q end via the gluon (g) to the $\overline{q}$ end. The $q\overline{q}g$ string will fragment along its length. To first approximation there is one fragmenting string piece between q and g and a second one between g and $\overline{q}$. When considered in detail, the string motion and fragmentation is more complicated, with the appearance of additional string regions during the time evolution of the system. These corrections are especially important for soft and collinear gluons, since they provide a smooth transition between events where such radiation took place and events where it did not. In this way, the string fragmentation model is *infrared safe* with respect to soft or collinear gluon emission.

1.7.3 The Cluster Model

An important property of the branching process is the preconfinement of colour [18]. This suggests a class of *cluster hadronization models*, in which colour-singlet clusters of partons form after the perturbative phase of jet development and then decay into the observed hadrons. The simplest way for colour-singlet clusters to form after parton branching is through non-perturbative splitting of gluons into $q\overline{q}$ pairs [19]. Neighbouring quarks and antiquarks can then combine into singlets. The mass of the resulting clusters is typically two or three times $\sqrt{m_o}$. If a low value of m_o is used (of the order of 1 GeV^2) most clusters have masses of up to a few GeV and it is reasonable to consider them as superpositions of resonances. The hadronic energy and transverse momentum distributions for final states e^+e^- are quite well described without including additional adjustable fragmentation functions.

1.8 Jet Physics

High-energy quarks and gluons are not directly observable due to the confinement of colour charge in QCD. Instead they are revealed through the appearance of *jets*, collimated flows of hadrons, that can be reconstructed from the observed particles. To make a quantitative comparison between theory and experiment, one must go beyond a qualitative definition and use a precise algorithm for defining a jet.

1.8.1 Jet Search Algorithms

Jet algorithms are not uniquely defined and the experimental results depend on the criteria used to define a jet. However, a well designed jet algorithm must have some basic properties: it must be easy to apply to the measured hadronic final state and infrared-safe so that the cross sections can be calculated order-by-order in perturbation theory. In perturbative QCD there is a collinear divergence when any two massless partons are parallel. In the calculation of the total cross section this divergence is cancelled by the contribution from the virtual correction to the equivalent process, with the two partons replaced by their sum. However, for this cancellation to take place also in the jet calculation, it is necessary to ensure that a collinear pair of particles are treated identically to a single particle with their combined momentum. From the experimental point of view, the equivalent problem is the fact that parallel particles go into the same calorimeter cell and can never be resolved. Likewise the requirement of infrared safety, i.e insensitivity to emission of low energy particles, is necessary in perturbative calculations to avoid the soft divergence and in the experiments to avoid bias from the threshold trigger of the calorimeter cells and the background noise. One of the first attempts to define jet cross sections in perturbative theory was made by Sterman and Weinberg in e^+e^- collisions [20]. They showed how to define cross sections free of singularities by integrating over finite ranges of energy and angle. The cross section for the processes $e^+e^- \rightarrow qqg$ has the form:

$$\frac{1}{\sigma}\frac{d^2\sigma}{dx_1 dx_2} = C_F \frac{\alpha_s}{2\pi}\frac{x_1^2 + x_2^2}{(1-x_1)(1-x_2)}$$

where x_1, x_2 are the energy fractions of the final state quark and antiquark $x_1 = 2E_q/\sqrt{s}$, and $x_2 = 2E_{\overline{q}}/\sqrt{s}$. This cross section has a singularity when one or both x_i are close to 1.

This corresponds to the collinear and infared singularities in the gluon emission. For this process, Sterman and Weinberg introduced the quantity $\sigma_2(s, \theta, \epsilon, \delta)$, which is the two-jet cross section, defined for all events where a fraction (1-ϵ) or more of the total energy is emitted within two opposite cones of half-angle δ, making an angle θ with the beam axis (see figure 1.10). The total cross section for this process can be written as an incoherent sum of two and three-jets cross section: $\sigma = \sigma_2 + \sigma_3$. The fraction of two and three-jet events are

$$f_2 = \sigma_2/\sigma = 1 - 8C_F\frac{\alpha_s}{2\pi}[ln\frac{1}{\delta}[ln(\frac{1}{2\epsilon} - 1) - 3/4 + 3\epsilon] + +\frac{\pi^2}{12} - 7/16 - \epsilon + \frac{3}{2}\epsilon^2 + O(\delta^2 ln\epsilon)]$$

and

$$f_3 = \sigma_3/\sigma = 1 - f_2$$

At higher orders in perturbation theory, the final state can consists of more than three jets. It turns out that this algorithm is not well-suited to analyse these multijet events. Several algorithms are available and currently used in the measurements of jet cross sections. In the following three different jet algorithms, developed in the e^+e^- and $p\overline{p}$ experiments, are presented:

The Jade Algorithm

The jet reconstruction procedure of the JADE algorithm [21] starts by calculating the distance parameter m_{ij} for all pairs of particles according to the expression

$$m_{ij}^2 = 2E_iE_j(1 - cos\theta_{ij}),$$

where E_i and E_j are the energies of the particles i and j, and θ_{ij} is the angle between them. The parameter m_{ij} is the invariant mass of particle i and j under the approximation that both particles are massless. The pair with the smallest m_{ij} is combined into a cluster by adding their four-vectors. The procedure is repeated until all remaining pairs have an invariant mass exceeding a preselected cut-off value, $m_{ij}^2 > y_{cut}M^2$, determined by a resolution parameter y_{cut} and a reference mass M. The final clusters represent the jets of the event.

The Cone Algorithm

Another approach to jet-reconstruction is to form cones around localized flows of energy. This was originally developed for $p\overline{p}$ colliders by the UA1 collaboration [22]. The total solid angle coverage of the detector is subdivided into equal cells in pseudoradity ($\eta = -ln(tan(\theta/2))$) and azimuthal angle ($\phi$). The deposited transverse energy ($E_T = Esin(\theta)$) is summed up in each cell and all cells with E_T greater that a preselected value are taken as possible initiators of jets. Taking this initiator, the algorithm checks if the total transverse energy in a cone around the initiator exceeds a minimum $E_{T,min}$, where the cone size is given by $\Delta R = \sqrt{\Delta\eta^2 + \Delta\phi^2}$. The jet energy is given by the sum of the energies of the cells and its direction by the energy-weighted averages

$$E_T^{jet} = \sum_{N_{cell}} E_T^{cell} \qquad \eta^{jet} = \frac{1}{E_T^{jet}}\sum_{N_{cell}} E_T^{cell}\eta^{cell} \qquad \phi^{jet} = \frac{1}{E_T^{jet}}\sum_{N_{cell}} E_T^{cell}\phi^{cell}$$

In this scheme, not all the particles are necessarily assigned to jets.

The K_T Algorithm

A two-step procedure, similar to the one of the JADE algorithm, is used in the K_T algorithm for DIS processes [23], where the first step comprises preclustering of hadrons into a beam-jet and so-called final state macro jets. A second step aims at resolving jet structures within the system of macro jets. In the preclustering, a variable K_{Tij} is calculated for all pairs of particles/clusters i and j according to the scheme

$$K_{Tij}^2 = 2(1 - cos\theta_{ij})min(E_i^2, E_j^2)$$

where θ_{ij} is the angle between the momenta vectors of i and j and E_i and E_j are the corresponding energies. In addition a distance parameter K_{Tip} is calculated for all particles/clusters i according to

$$K_{Tip}^2 = 2(1 - cos\theta_{ip})E_i^2$$

where θ_{ip} is the angle between i and the proton direction. One specific feature of the K_T algorithm for DIS processes is that all quantities are calculated in the Breit frame, i.e. the reference system where the exchanged vector boson has a four-vector $q = (0, 0, 0, -Q)$. The boson and proton are here both along the z-axis, but longitudinally boosted compared to their c.m.s. system. Consequently, for small angles and for $E_i \leq E_j$, K_{Tij} can be regarded as the transverse momentum, in the Breit frame, of i with respect to the direction of j while K_{Tip} can be regarded as the transverse momentum of i with respect to the proton direction. At this stage a new variable (E_T) is introduced in the algorithm and the variables defined as

$$y_{ij} = \frac{K_{Tij}}{E_T^2} \qquad y_{ip} = \frac{K_{Tip}^2}{E_T^2}$$

are calculated. The algorithm proceeds by checking if the smallest y-value obtained is less than one. If this is the case and the y-value is of the type y_{ij} then i and j are combined into a new cluster. If on the other hand, the smallest y-value is of the type y_{ip} then i is regarded as a part of the spectator jet and is removed from further treatment. The procedure is repeated until all y-values are larger than one. One can therefore regard E_T^2 as the resolution parameter in the algorithm's first step which tries to separate the spectator-jet from the macro-jet. The algorithm then continues with a second step in which a parameter Q_o is introduced and the variable $y_{cut} = Q_o^2/E_T^2$ is calculated. All particles in the event which were not assigned to the spectator jet in the first step are used again. For every pair of particles the y_{ij}-value is calculated and the pair giving the smallest y-value is compared with the y_{cut} value. If $y_{ij} < y_{cut}$ the hadrons are combined into a cluster. When all the y-values exceeds the y_{cut}-value the procedure is stopped and the remaining clusters are the final jets. The parameter Q_o is thus a second resolution parameter which is used to resolve the macro jets.

1.8.2 The Jet Shape

A large fraction of the hadronic final states in hadron-hadron, electron-hadron and electron-positron collisions consists of high-energy jets. These jets have an extended structure in phase space which can be studied both experimentally and theoretically. One possible measurement of such structure is the jet shape, which depends on the transverse energy and rapidity of the jet and the jet algorithm. A measurement of the jet shape is very interesting mainly because in a single measurement, both the hard and the soft part of

QCD are probed. The internal structure of a jet is expected to depend mainly on the type of primary parton, quark or gluon, from which it originated and to a lesser extent on the particular hard scattering process. At sufficiently high-transverse-energy of the jet (E_T^{jet}), the jet shape is expected to be driven mainly by gluon emission off the primary parton. Close to the jet axis, the shape is dominated by collinear gluon emission. At large angles the shape reflects large-angle gluon-emission, which can be calculated perturbatively (see figure 1.11). For the jet-cone algorithm (see previous section) the E_T distribution within the cone of the jet can be analysed by studying the fractional E_T profiles. Mathematically the differential jet shape is defined by the normalized average transverse energy density $\rho(r)$

$$\rho(r) = \frac{1}{N_{jets}} \sum_{jets} \frac{E_T^{jet}(r, r+\Delta r)}{E_T^{jet}(r=R)}$$

where R is the cone radius used in the jet algorithm and $E_T^{jet}(r, r+\Delta r)$ is defined as the fraction of the transverse energy of the jet which lies in the region between the two cones of radius r and $r+\Delta r$ respectively. The integrated jet shape, $\psi(r)$, defined as the average fraction of the transverse energy of the jet which lies inside an inner cone of radius r concentric to the jet cone:

$$\psi(r) = \frac{1}{N_{jets}} \sum_{jets} \frac{E_T^{jet}(r)}{E_T^{jet}(r=R)},$$

is also used to compare with the theoretical predictions. The quantity $1-\psi(r, R, E_T^{jet}, \eta^{jet})$ describes the fraction of E_T^{jet} that lies in the annulus between r and R. It is this quantity that is most easily calculated in perturbative theory as it avoids the collinear singularities at $r = 0$ [24, 25].

1.8.3 Quark and Gluon Jets

The calculations of multiplicity distributions in QCD predict that the average multiplicity of any type of object in a gluon jet should asymptotically become $C_A/C_F = 9/4$ times greater than that in a quark jet [26]

$$< N_q >\sim \frac{C_F}{C_A} N_g(Q^2) \approx exp(\frac{1}{b}\sqrt{\frac{2C_A}{\pi\alpha_s(Q^2)}}),$$

and that the asymptotic multiplicity distribution should also become wider for a gluon jet by the factor $\sqrt{C_A/C_F}$

$$\sigma_{N_q} \sim (1 + \frac{C_F}{3C_A})N_q^2, \qquad \sigma_{N_g} \sim \frac{4}{3}N_g^2$$

These differences arise from the greater effective colour charge-squared of the gluon, which is proportional to C_A as opposed to C_F for the quark. Another characteristic difference is that gluon jets should be broader than quark jets. From the expression for the ratio of two jet events in e^+e^- interactions obtained using the jet-algorithm by Sterman-Weinberg (see section 1.8.1), the angular size of the quark jets for a given small energy fraction ϵ follows the expression

$$\delta_q \sim exp[\frac{\pi(1-f_2)}{4C_F\alpha_s(Q^2)ln\epsilon}]$$

Since $1/\alpha_s$ increases logarithmically with energy, this means that the angular jet width, for a fixed fraction f_2, decreases as a negative power of Q^2. For gluon jets, an analogous calculation gives a factor C_A in place of C_F and therefore

$$\delta_g \sim \delta_q^{C_F/C_A}.$$

Thus the power decrease of the angular width is less rapid for gluon jets.

1.9 Event Generators for ep Processes

For the extraction of physical quantities from the measurements, Monte Carlo generators are necessary. From an experimental point of view, the detectors have an incomplete coverage of the solid angle (due to the presence of the beam-pipe and other non-instrumented areas). Furthermore, in order to isolate a particular physical process in the data some selection cuts must be applied. In developing the selection criteria and computing the acceptance corrections (which must include detector effects) Monte Carlo generated events, which mimic the true data to a high degree, have to be used. From the theoretical point of view, as was already mentioned, the large distance hadronization processes cannot be calculated using perturbative QCD and have to be treated phenomenologically in a Monte Carlo fragmentation procedure.

Several Monte Carlo programs are presently used to generated the different hard processes in ep interactions. Resolved photoproduction processes are generated by the PYTHIA [27] and HERWIG [28] programs, where the Weizsäcker-Williams approximation [29] for the flow of quasi-real photons is used. The hard subprocesses are always $2 \rightarrow 2$ processes and higher QCD corrections are simulated via initial and final-state parton showers. Direct photoproduction processes are simulated by the AROMA [30] and HERWIG [1] programs using the complete matrix elements, while PYTHIA uses the Weizsäcker-Williams approximation. For DIS, the programs HERWIG and LEPTO [31] simulate $2 \rightarrow 3$ hard processes and include the matrix elements for $O(\alpha_s)$ diagrams (see figure 1.3). PYTHIA is also able to simulate DIS processes but the $O(\alpha_s)$ processes are simulated via the parton-shower approach. The colour dipole model (for the simulation of higher order QCD parton emissions) is implemented in ARIADNE [32]. Since ARIADNE produces only the parton cascade, it is interfaced to LEPTO and PYTHIA programs for the hadronization. Evolved distributions for quarks and gluons inside the proton and the photon are used for the computation of the cross sections and for the backward evolution of the parton showers. For that purpose, the Monte Carlo programs use the structure functions collected in the PDFLIB library [33].

The string hadronization model is the basic of the JETSET program [27]. This program gives a very detailed description of the final states in e^+e^- collisions up to the highest energies studied so far. All the programs mentioned above use JETSET in order to simulate the hadronization procedure except HERWIG with use a low-mass cluster hadronization.

QED radiative corrections are implemented in PYTHIA for DIS and direct photoproduction processes using a leading-logarithmic approximation. For DIS, they are implemented in the DJANGO [34] program which is an interface between HERACLES [35] and LEPTO.

[1] Only Boson-Gluon-Fusion into heavy-quarks processes are considered.

The existing generators have a large number of theoretical uncertainties related to the choice of the quark masses, the structure functions used in the generation of the events, the parameters setting for the parton showers, the choice of the scale, the description of the proton remnant, etc. The use of different Monte Carlo generator in order to unfold the measured data permits to include such uncertainties in the systematic errors of the measurements.

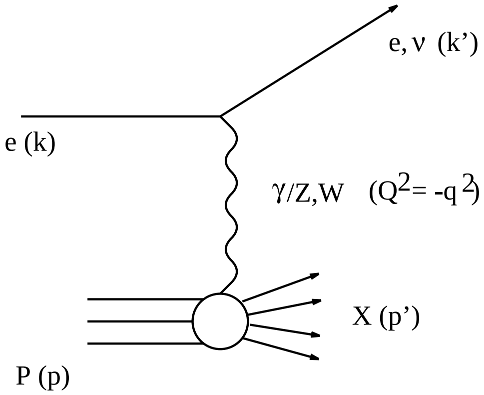

Figure 1.1: Lowest-order Feynman diagram for DIS.

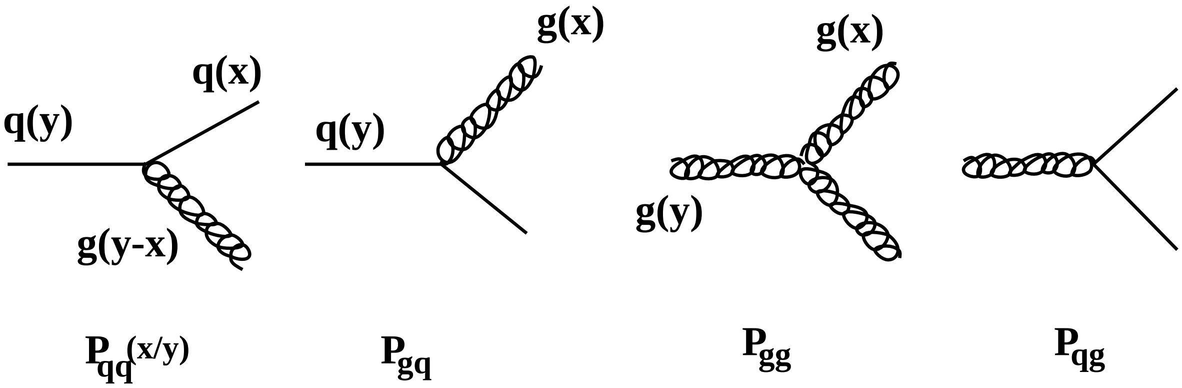

Figure 1.2: Splitting Functions $P_{ij}(x/y)$.

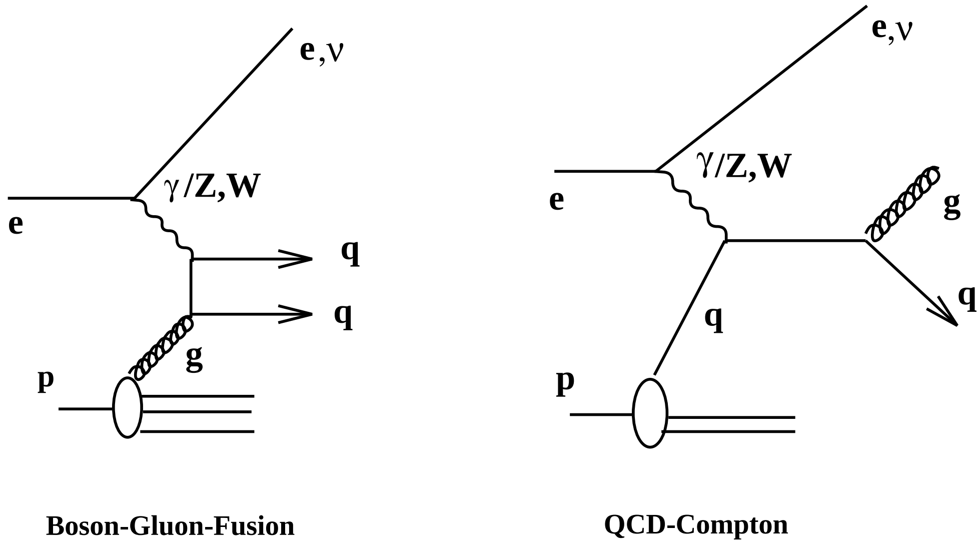

Figure 1.3: $O(\alpha_s)$ diagrams for DIS.

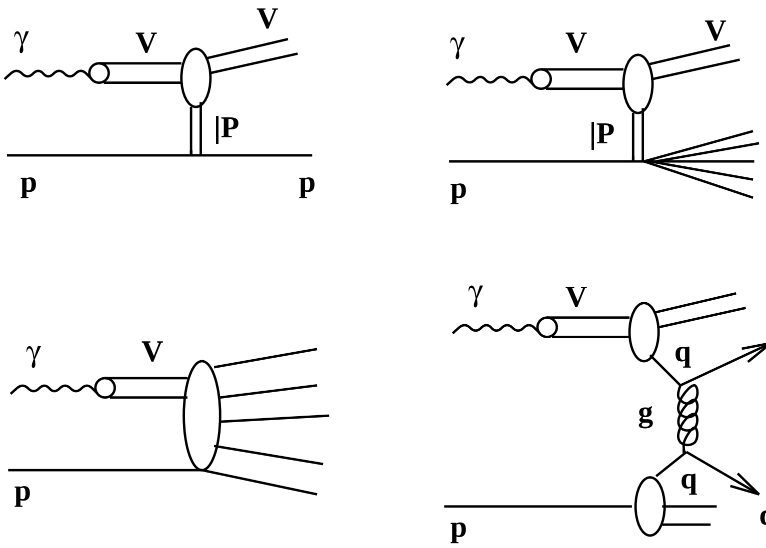

Figure 1.4: Diagrams for photoproduction processes: VDM for diffractive elastic/inelastic scattering, non-diffractive scattering and hard scattering.

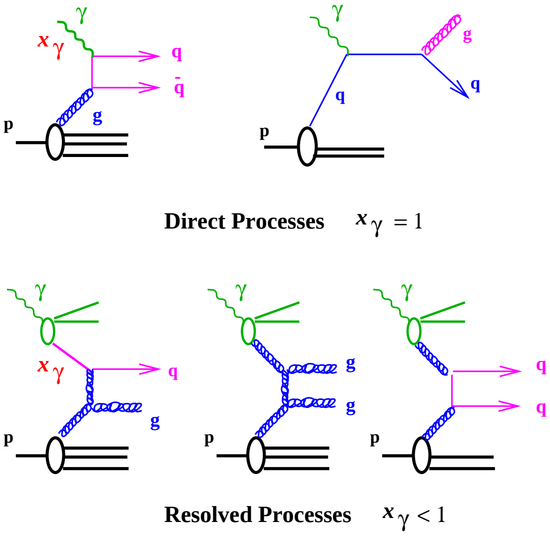

Figure 1.5: Diagrams for hard photoproduction processes: direct and resolved contributions.

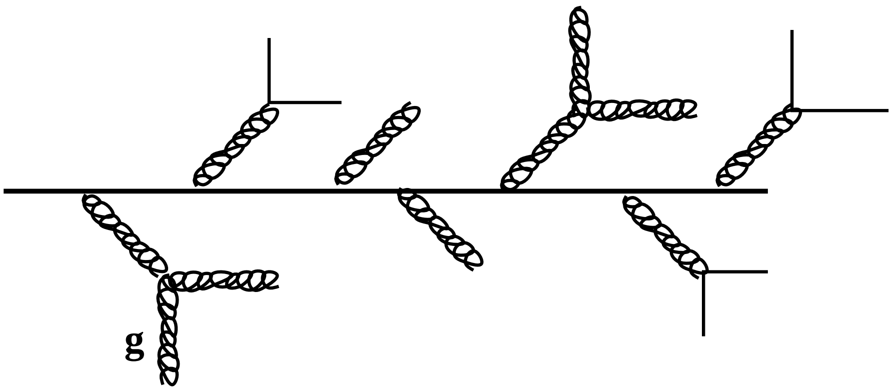

Figure 1.6: Simulation of higher order QCD processes by the Parton Shower Cascade Model.

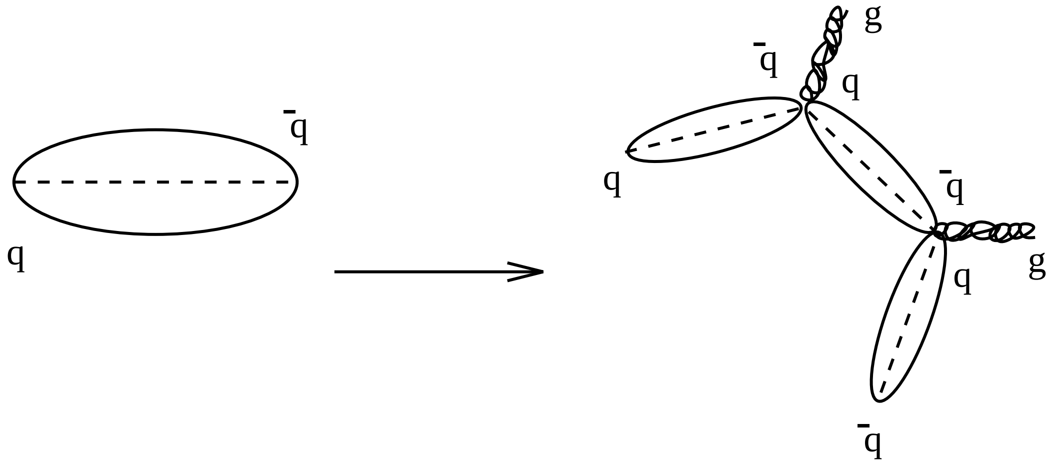

Figure 1.7: Simulation of higher order QCD processes by the Colour Dipole Model.

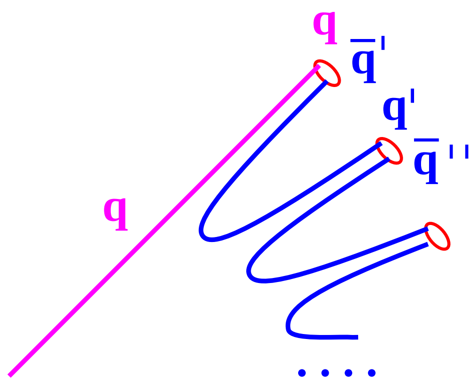

Figure 1.8: Independent fragmentation model for the hadronization process.

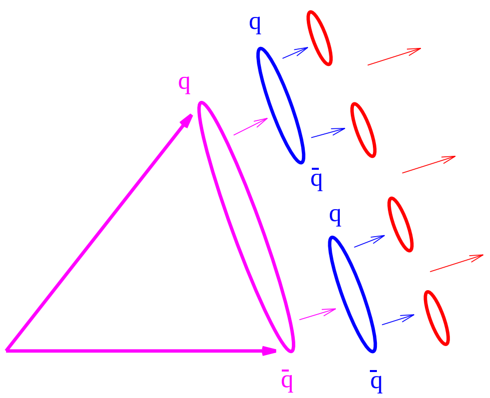

Figure 1.9: Description of the fragmentation process by the string model.

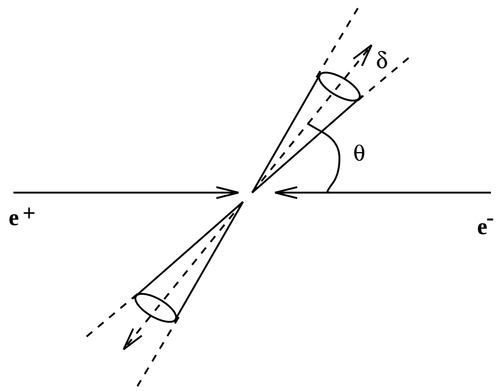

Figure 1.10: Sterman-Weinberg definition of the jet algorithm for e^+e^- interactions.

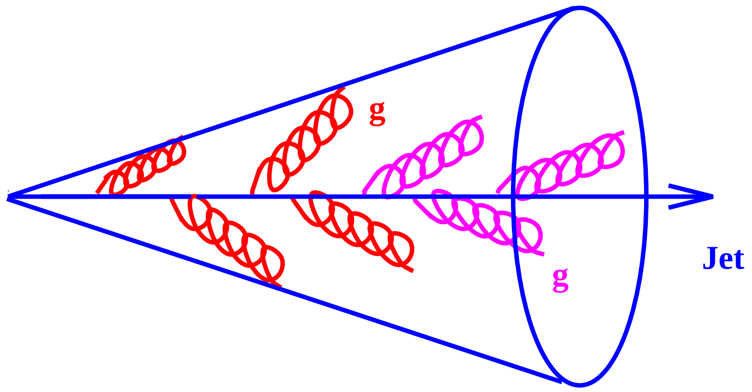

Figure 1.11: Gluon radiation within a jet.

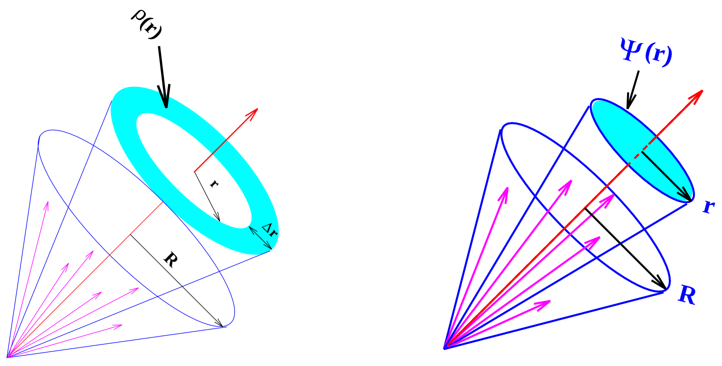

Figure 1.12: Jet shape definition for a jet-cone algorithm.

Bibliography

[1] Riordan E M et al. 1975 SLAC-PUB-1634

[2] C.G. Callan and D.J. Gross 1969 Phys. Rev. Lett. 22 156

[3] L.N.Lipatov, Sov J. Nucl. Phys 20 (1975) 95;
V.N. Gribov and L.N. Lipatov, Sov J. Nucl. Phys 15 (1972) 438;
G. Altarelli and G. Parisi, Nucl. Phys B126 (1977) 298;
Y.L. Dokshitzer Sov. Phys. JETP 46 (1977) 641.

[4] A.D.Martin, R.G.Roberts, W.J.Stirling, Phys. Rev. **D47**(1993)867.

[5] CTEQ Collaboration, J.Botts et al., Phys. Lett. **B304**(1993)159.

[6] B. Andersson, G. Gustafson, G. Ingelman and T. Sjöstrand, Z. Phys. C9 (1981) 233
M. Bengtsson and T. Sjöstrand Z Phys C37 (1988) 465

[7] J.J. Sakurai, *Proceedings of the Fourth International Symposium on Electron and Photon Interactions at High Energies* (Daresbury, England, 1969)
R.P. Feynman, *Photon-Hadron Interactions* (Benjamin, N.York, 1972)

[8] M. Bengtsson and T. Sjöstrand, Phys. Lett B185 (1987) 435; Nucl. Phys. B289 (1987) 810

[9] Y. Azimov, Y. Dokshitzer, V. Khoze and S. Troyan, Phys. Lett. B165 (1985) 147; G. Gustafson, Phys. Lett. B175 (1986) 453; G. Gustafson and U. Petersson, Nucl. Phys. B306 (1988) 746; B. Andersson, G. Gustafson and L. Lönnblad, Z. Phys. C43 (1989) 625.

[10] A. Petersen et. al., Phys Rev. D37 (1988) 1.
M.Z. Akrawy et al. OPAL Collaboration, Phys. Lett. B246 (1990) 285.

[11] V.V. Sudakov, Zh.E.F.T. 30 (1956) 87 (Sov. Phys. J.E.T.P 30 (1956) 65

[12] A.H. Mueller, Phys. Lett. 104B, 161 (1981);
B.I. Ermolaev and V.S. Fadin, JETP Lett. 33, 269 (1981);
A. Bassetto, M. Ciafaloni and G. Maschesini, Phys. Rep. 100, 201 (1983)

[13] Y.I.Azimov, Y.L.Dokshitzer, V.A. Khoze and S.I. Troyan, Z. Phys C27 (1985) 65.

[14] R.D. Field and R.P. Feynman, Phys. Rev D15 (1977) 2590,
Nucl Phys. B138 (1978) 1.

[15] TASSO Collaboration M. Althoff et. all, Z. Phys C22 (1984) 307.

[16] B. Andersson, G. Gustafson and B. Söderberg, Z. Phys C20 (1983) 317, Nucl Phys B264 (1986) 29.
B. Andersson, G. Gustafson, G Ingelman and T. Sjöstrand, Phys Rep. 97 (1983) 33.

[17] B. Andersson et al., Phys. Rep. 97 (1983) 31.

[18] D. Amati and G. Veneziano, Phys Lett B83 (1979) 87;
A. Bassetto, M. Ciafaloni and G. Marchesini, Phys Lett. B83 (1979) 207;
G. Maschesini, L. Trentadue and G. Veneziano, Nucl Phys B181 (1980) 335.

[19] R.D. Field and S. Wolfram, Nucl Phy. B213 (1983) 65.

[20] G. Sterman and S. Weinberg, Phys Rev. Lett. 39 (1977) 1436.

[21] W. Bartel et al. JADE Collaboration, Z. Phys. C33 (1986) 23;
S. Bethe et al. JADE Collaboration, Phys Lett. B213 (1988) 235.

[22] UA1 Collaboration, G.Arnison et al., Phys. Lett. **B123**(1983)115;
J.Huth et al., Proc. 1990 DPF Summer Study on High–Energy Physics, Snowmass, Colorado, ed. E.L.Berger (World Scientific, Singapore, 1990, p.134).

[23] S. Catani, Y.L. Dokshitzer, B.R. Webber, Phys Letter. B298 (1993) 469.

[24] S.D. Ellis, Z. Kunszt and D.E. Soper, Phys. Rev. Lett. 69 (1992) 3615.

[25] W.T. Giele, E.W.N. Glover and D.A. Kosower, Nucl. Phys. B403 (1993) 633.

[26] R.K. Ellis, W.J. Stirling and B.R. Webber, *QCD and Collider Physics* Cambrigde University Press 1996.

[27] T.Sjöstrand, CERN–TH 7112–93 (1994);
T.Sjöstrand, LU–TP–95–20 (1995).

[28] B.R.Webber, Proc. 1991 Workshop on Physics at HERA, ed. W.Buchmüller and G.Ingelman (DESY, Hamburg, 1992), Vol. 3, p.1363.

[29] C.F. Weizsäcker, Z. Phys. 88 (1934)612; E.J. Williams, Phys Rev. 45 (1934) 729.

[30] G.Ingelman and G.Schuler, Proc. 1991 Workshop on Physics at HERA, ed. W.Buchmüller and G.Ingelman (DESY, Hamburg, 1992), Vol. 3, p.1346.

[31] G.Ingelman, Proc. 1991 Workshop on Physics at HERA, ed. W.Buchmüller and G.Ingelman (DESY, Hamburg, 1992), Vol. 3, p.1366.

[32] L.Lönnblad, LU TP–89–10;
L.Lönnblad, Comp. Phys. Comm. **71**(1992)15.

[33] H. Plothow-Besch Comp. Phy. Comm. 75 (1993) 396-416.

[34] G.Schuler and H.Spiesberger, Proc. 1991 Workshop on Physics at HERA, ed. W.Buchmüller and G.Ingelman (DESY, Hamburg, 1992), Vol. 3, p.1419.

[35] A.Kwiatkowski, H.Spiesberger and H.J.Möhring, Proc. 1991 Workshop on Physics at HERA, ed. W.Buchmüller and G.Ingelman (DESY, Hamburg, 1992), Vol. 3, p.1294.

Chapter 2

HERA and the ZEUS Detector

2.1 The HERA Storage Ring

The Hadron Electron Ring Accelerator (HERA) located at the DESY (Deutsches Elektronen-Synchrotron) laboratory in Hamburg (Germany) is the first electron-proton collider in the world. The tunnel in which it resides was built 10 to 25 m under the surface of the earth and it has a circumference of 6.3 Km. The storage ring was constructed out of four circular arcs with a radius of 779 meters and four straight segments each 360 meters long (see figure 2.1). Four interaction points (IP) are placed in the straight segments, where the experiments H1, ZEUS, HERMES and HERA-B are located.

One of the remarkable features of the HERA collider, which distinguishes it from other colliders, is the asymmetry between the two beam energies. HERA was designed to collide electrons and protons with nominal energies of 30 GeV and 820 GeV respectively, resulting in a center-of mass energy of $\sqrt{s} = 314$ GeV.

Beam injection is performed by a procedure involving several preaccelerators (see figure 2.2). Electrons are initially accelerated up to 200 MeV in the electron linear accelerator LINAC II, and then in the DESY II synchrotron up to an energy of 7.5 GeV. Afterwards, the electrons are injected into PETRA, where their energy is increased up to 14 GeV, before they are transferred to HERA. The protons start as H^- ions in the proton LINAC and are accelerated up to 50 MeV. After acceleration in DESY III (to 7.5 GeV), the electrons are stripped off and the protons are injected in PETRA, where their energy increases up to 40 GeV, before injection into HERA.

While the high momentum of the proton beam requires superconducting magnets, the electrons are controlled with convectional magnets. The HERA proton ring consists of 422 main dipoles delivering a bending field of 4.68 T and 244 main quadrupoles. Standard cells of 47 m length combining 4 dipoles, 4 quadrupoles, 4 sextupoles and correction magnets are installed in the arcs of the proton ring and are cooled down to 4.2 K. The conventional electron ring consists of 456 main dipoles of 0.164 T and 605 main dipoles grouped in 12 m long magnet modules which contain one dipole, one quadrupole, one or two sextupoles and several correction dipoles. The energy loss due to synchrotron radiation is compensated by 500 MHz copper cavities installed in the straight sections of HERA. In addition, 16 superconducting 4-cell cavities with a field gradient of 5 MV/m are used to accelerate the electrons from 14 GeV (injection energy) to the maximum energy. The electrons and protons are stored in separated bunches with a distance of 28.8 m between two successive bunches. This distance corresponds to a bunch crossing time of 96 ns (see figure 2.3). In order to maximize the luminosity, up to 210 bunches of particles can be stored for each beam. Unpaired bunches with only protons or only electrons as well as empty bunches are used to estimated the number of background events coming from interactions with the residual beam gas in the storage ring and cosmic rays.

Close to the interaction region, protons and electrons have to run in the same orbit in order to collide at zero angle. The distance of about 81 cm between the electron and the proton rings has to be traversed. A total of 123 guiding magnets are used to deflect the protons until they run in the same vacuum pipe as the electrons. After passing the IP they are brought back to the level of the proton ring. From the '94 running period it was decided to accelerate positrons instead of electrons in order to achieve longer lepton-beam life-times. Interactions with almost stationary positively charged ions, most likely originating from the ion getter pumps of the HERA vacuum system, tend to defocus the electron beam. For a positron beam the pile-up of the ions is avoided due to the repulsive electromagnetic force of the positively charged positrons.

Figure 2.4 shows the luminosity delivered by HERA during the several running periods from 1992, when the experiment started, up to 1997. HERA has increased enormously its luminosity thanks to the improvements and better understanding of the collider.

2.2 The ZEUS Detector

ZEUS is one of the currently four experiments at the HERA collider. It is a large multipurpose detector designed to study the wide spectrum of HERA physics. The ZEUS Collaboration consists of almost 500 physicists coming from more than 50 institutes and 12 different nations. It is located 30 m underground in the Sourth Hall of the HERA tunnel outside of the DESY site. A detailed description of the ZEUS detector can be found in [1].

Cross sections through the ZEUS detector are shown in figures 2.5 and 2.6. The ZEUS geometry is described by a right-handed coordinate system with its origin at the positron-proton IP. The z-axis is pointing along the incoming proton direction and the x-axis horizontally towards the center of HERA. A polar coordinate system (r, θ, ϕ) is used, where θ is the polar angle w.r.t. the positive z-axis and ϕ the azimuthal angle w.r.t. the x-angle.

Starting from the IP (see figure 2.5) ZEUS consists of charged particle tracking detectors: central, forward and rear tracking detectors (CTD, FTD, RTD). The tracking chambers are surrounded by a high-resolution Uranium-Scintillator Calorimeter (UCAL). The UCAL is divided into three sections: the FCAL in the forward region, the RCAL in the rear region and the BCAL, a barrel section surrounding the central region. The small-angle rear tracking detector (SRTD) is situated behind the RTD and covers the face of the RCAL to a radius of $\sim$ 34 cm around the center of the beam-pipe hole. At a longitudinal depth of 3 radiation lengths in the RCAL the hadron-electron separator (HES), consisting of 3x3 cm^2 silicon diodes, is installed for the discrimination between electromagnetic and hadronic showers originating from low energetic particles ($<$ 5 GeV). Between the UCAL and the CTD there is a superconducting solenoid. The coil has an overall length of 2.46 m and an inner diameter of 1.91 m, and produces a magnetic field of 1.4 Tesla. The axial field produced by the solenoid is used to measure the momentum of the charged particles. A second low-resolution calorimeter (BAC) was constructed in order to measure the energy leakage out of the main calorimeter. The BAC is made out of 7.3 cm thick iron plates and also serves as the return yoke for the magnetic flux from the solenoid. In order to detect muons and measure their momenta, muon chambers are located between the BAC and the CAL, as well as after the iron return yoke. The muon detector, as in the UCAL case, is divided into three parts, forward (FMUI,FMUO), rear (RMUI,RMUO), and barrel (BMUI,BMUO). In the rear part of the main detector, at 7.5 m upstream of the IP, an iron-scintillator VETOWALL is used to reject beam-related background. A small lead-scintillator counter, located around the beam pipe at $z = -3.15$ m, monitors the synchrotron radiation accompanying the beams and the timing and longitudinal structure of the proton and electron bunches. At $\sim 20 - 90$ m downstream in the proton-beam direction the leading-proton spectrometer (LPS) and the forward-neutron calorimeter (FNC) detect protons and neutrons scattered through small angles, respectively. The proton remnant tagger (PRT) is a lead-scintillator counter located at $z = 5.1$ m around the beam pipe and covers the pseudorapidity [1] range $4.3 < \eta < 5.8$. In the electron-beam direction, two small lead/scintillator calorimeters are installed at -34 m and -104 m for the measurement of outgoing photons, used for the luminosity determination. They are also used to detect $Q^2 \sim 0$ scattering and radiative events. The short time interval of 96 ns between bunch crossings at HERA results in a nominal rate of 10 MHz. ZEUS uses a three-level trigger system to reduce the rate to a few Hz (see section 2.2.7). In the next sections, a brief description is given of the components relevant to the analyses presented here.

2.2.1 The Central Tracking Detector

The CTD is a cylindrical wire chamber with nine superlayers of eight sense wire layers each, as shown in figure 2.8 which covers an angular range of $15^o < \theta < 164^o$. The inner radius of the chamber is 16.2 cm, the outer radius 85 cm, and the length is 241 cm. The chamber uses a 50/50 argon/ethane mixture bubbled through ethanol. Five of the superlayers have wires parallel to the chamber axis, four layers are stereo layers which have wires with a small angle ($5^o or 7^o$) with respect to the beam, and are used to determine the z-coordinate of the hits. For trigger purposes, the three inner axial layers are additionally equipped with a z-by-timing system which determines the z-position of the hit from the difference in arrival times of a pulse at both ends of the chamber. The position resolution in the $r - \phi$ plane is 100-120 μm (depending slightly on polar angle θ). The z resolution using the stereo wires equals 1.0 to 1.4 mm, and when using z-by-timing 4 cm. The momentum resolution of the CTD is $\sigma(p)/p = 0.005p \bigoplus 0.0016$ for particles traversing all 9 superlayers. The detector measures dE/dx with an accuracy better than 6 %.
In the forward region the acceptance of the CTD is extended by the FTD, a system of three planar drift chambers. Between the 3 FTD chambers, modules of a transition radiation detector (TRD), designed to enhance hadron-electron separation in forward going jets, are positioned. FTD and TRD together form the forward detector FDET. In the rear direction, a single chamber (RTD) of identical design as those from the FTD extends the CTD acceptance to polar angles between 160 and 170^o. These components were only operative since the 1995 running period.

[1]The pseudorapidity is defined as $\eta = -ln(tan\frac{\theta}{2})$.

2.2.2 The Uranium-Scintillator Calorimeter (UCAL)

In high-energy experiments the energy of the particles and jets is measured with calorimeters which are the central components of the large experiments at present storage rings. One of the essential properties of a calorimeter is its sensitivity to both charged and neutral particles. The energy resolution of the measurement scales with increasing energies as

$$\frac{\sigma(E)}{E} \sim \frac{1}{\sqrt{E}},$$

and that the depth D required to stop incoming particles increases only logarithmically with the particle energy E

$$D \sim a + b\ lnE$$

High energy particles entering a layer of material produce a cascade of particles. In the case of an incoming electron or photon an electromagnetic shower of secondary photons, electrons and positrons is initiated. The shower development depends on the energy of the incoming particle and the absorber material, characterized by its specific density, the atomic number Z and the atomic mass A. The longitudinal and transverse shower dimensions are commonly measured in units of the *radiation length* X_o. The radiation length is the mean distance over which a high-energy electron loses all but 1/e of its energy by bremsstrahlung. An appropriate energy scale is given by the *critical energy* E_c, defined as the energy at which the energy loss of an electron due to bremsstrahlung is equivalent to the energy loss through ionization of the passed matter. Since the energy loss of an electron by bremsstrahlung is approximately proportional to its energy and the ionization loss increases only logarithmically, the longitudinal development is determined by the high-energy part of the shower and scales as the radiation length in the material. An estimation of the depth D_{98} required to contain 98 % of an electromagnetic shower produced by a 25 GeV electron leads to $D_{98} = 22X_o$ [2].

In contrast to electromagnetic showers, cascades produced by an incoming hadron are more complex, because in addition to the mentioned electromagnetic processes pure hadronic interactions such as spallation processes and fission of heavy nuclei lead to neutral hadrons, nuclear fragments and excited nuclei so that the measurable signal is reduced due to nuclear binding energy, neutrino production and fragments of nuclei leaving no visible signal in the calorimeter. The length scale appropriate for hadronic showers is the nuclear interaction length λ_{int} defined as $\lambda_{int} = A/N_A\sigma_i$, where N_A is the Avogadro number and σ_i denotes the inelastic cross section. A good approximation of λ_{int} [2] is given by

$$\lambda_{int} = 35\frac{A^{1/3}}{\rho}[cm]$$

where ρ is the density in units $[g/cm^3]$. The depth required to contain a 95 % of the hadronic shower energy is given by the parameterization [3]

$$D_{95} \sim 0.2LnE + 2.5E^{0.3} + 0.7$$

According to this, a shower of a 300 GeV hadron can be contained in calorimeter with a depth of $7.1\lambda_{int}$.

The ZEUS Calorimeter.

The high resolution ZEUS calorimeter is a sampling calorimeter with equal response to electrons and hadrons ($e/h = 1$) using absorber plates of depleted uranium and plastic scintillator layers as active plates. The depleted uranium plates are a composition of 98.1% U^{238}, 1.7% Nb and less than 0.2% U^{235}. The optical readout is performed via plastic wavelength shifters, lightguides and photomultipliers. In order to obtain equal calorimeter response to electron (photons) and hadrons 3.3 mm thick uranium plates corresponding to one radiation length alternate with 2.6 mm thick scintillator plates. For a detailed description see [4] and [5]. The main features of the high-resolution calorimeter are:

- hermeticity over a large solid angle (99.7 % of the solid angle is covered).
- energy resolution for hadrons of $\sigma(E)/E = 35\%/\sqrt{E} \bigoplus 2\%$.
- energy resolution for electrons of $\sigma(E)/E = 18\%/\sqrt{E} \bigoplus 2\%$.
- calibration of the absolute energy scale to 1%.
- precise angular resolution for particles ($\leq 10\%$ mrad).
- longitudinal segmentation for hadron-electron separation.
- short signal processing time at the nano-second level.

The solenoid and the tracking chambers are completely enclosed by the uranium calorimeter, except in the region around the beam-pipe. The UCAL is constructed in three main parts, the hollow cylindrical central part of BCAL with a polar angle acceptance of $36^o < \theta < 129.1^o$ and the two end caps FCAL and RCAL, which cover the polar range of $2.2^o < \theta < 39.9^o$ and $128^o < 176.5^o$, respectively (see figure 2.7). The total depth of the three different calorimeter sections takes into account the Lorentz boost and reflects the maximum energy deposition of scattered particles. The FCAL has a maximum depth of 7.1 interaction length (λ), while BCAL has 5.3λ and RCAL 4λ. Each section is divided into modules and further subdivided into towers which provide granularity for position reconstruction.
The three calorimeter components are structures similar and are subdivided longitudinally into an electromagnetic calorimeter (FEMC, BEMC, REMC) with a depth of $\sim 1\lambda$ which is sufficient to fully contain the electromagnetic showers, and a hadronic calorimeter (HAC). In FCAL and BCAL the HAC section is divided into two subsections HAC1 and HAC2, while the RCAL has only one HAC section.
The whole calorimeter has a modular structure, The FCAL and RCAL calorimeter consists of 24 modules which follow the same construction principles, as shown in figure 2.9 where an isometric view of a FCAL module is presented. For a detailed description of the BCAL modules see [1]. The FCAL and RCAL modules have the same width of 20 cm and have a height varying from 2.2 m to 4.6 m so that roughly a cylindrical structure with a radius of ~ 2.3 m can be built. The depth varies from 7.1λ in the central region to 5.6λ in the outer horizontal regions. The centre module of the FCAL and RCAL calorimeter

are split into a separate upper and lower module. The horizontal segmentation is determined by the width of the modules. The transverse segmentation depends on the height of the wavelength shifters which collect the scintillator light. Each longitudinal section (EMC, HAC1, HAC2) is read out in both sides by wavelength shifters. For FCAL the segmentation of the EMC section is 5x20 cm, and for RCAL 10x20 cm. These sections are called EMC towers. The hadronic towers of FCAL and RCAL have a segmentation of 20x20 cm.
Due to the optical read out combined with photomultipliers a fast readout processing can be performed which allows the determination of the arrival times of incoming particles at the nano-second level. The timing resolution for each calorimeter cell is $\sigma_t = 1.5/\sqrt{E} \oplus 0.5$ns, where E(GeV) is the energy deposited in the cell [6]. The timing information from the calorimeter is useful for removing both beam-gas and cosmic ray related backgrounds. The time $t = 0$ns is defined to be the time at which the particles originating from ep collisions at the interaction point arrive at the calorimeter. When particles from beam-gas interactions which occur behind the RCAL deposit energy in the RCAL, the time at which the energy is deposit is negative. Therefore, a cut on the RCAL time can remove beam-gas events. In addition, the "up-down" time difference (the difference between the time at which energy is deposited in cells at the top and at bottom of the BCAL) should be zero. However, for cosmic rays the up-down time difference will be greater than 10 ns. Therefore, cosmic rays events can also be removed with the calorimeter time information. The vertex position along the z-axis can also be measured using calorimeter time information. The time, t, at which energy is deposited in the FCAL near the beam-pipe from an ep interaction will depend on the z vertex position according to the equation $t = -2z/c$, where c is the speed of light. The correlation between the z vertex position measured using the tracking detectors and the FCAL timing information can also be used to remove beam-gas interactions.
The calibration of the calorimeter can be performed using several redundant tools, which are described in [5]. The main calibration source is the use of the natural uranium radioactivity, the so called uranium noise (UNO), which produce a low background current in the photomultiplier. The integrated signal of the UNO provides a stable diagnostic tool for monitoring and calibration of the high-resolution calorimeter.

2.2.3 The Backing Calorimeter

The main purpose of the BAC is to measure the energy leakage out of the main high-resolution calorimeter. In addition, it is used to detect muons from ep interactions and cosmics. The BAC totally covers the CAL using as absorber material the 7.3 cm thick plates of the yoke. The iron yoke for the return of the magnetic has the shape of an octagonal cylinder which is closed by endcaps on both sides. The yoke can be magnetized by copper coils, in order to create a magnetic field for an independent measurement of the momentum of muons in the barrel muon chambers. It consists of slabs of iron separated by 3.7 cm gaps instrumented with proportional tubes.

2.2.4 The Muon Chambers

This detector component consists of muon chambers inside and outside of the iron yoke, and measures tracks penetrating the calorimeter and cosmic rays. This detector is constructed in three main modules: the forward (FMUON), barrel (BMUON) and rear region

(RMUON); more components are placed in the forward region in order to cover the higher particle flux. By measuring the momenta of reconstructed track segments, and comparing this measurement with track segments in the CTD, prompt muons can be detected. Each barrel chamber consists of 2 double layers of limited streamer tubes, with wires oriented along the beam axis. The position resolution is better than 1 mm. The barrel muon chambers accept muon tracks at $\theta > 34^o$. In order to reach the muon chamber, muons must traverse the UCAL and BAC. As a minimum ionizing particle, the muon typically deposits ~ 2 GeV in the UCAL and this is the energy needed for the muon to be detected in the inner muon chambers. In crossing the iron yoke between the inner and outer muon chambers, the muon loses approximately 1 GeV of energy.
The forward direction is equipped with special muon chambers, which give an independent measurement of the muon momentum up to 100 GeV and down to very small angles. The detector consists of a toroidally magnetized iron region, interleaved with sections of drift chambers, limited streamer tubes and time of flight counters. The outer diameter of the toroids is 6 m and the average magnetic field inside is 1.7 T.

2.2.5 Further Components

Veto Wall
The veto wall (VETO) is an iron wall, equipped with two layers of scintillator on both sides, and placed 7 m from the IP in the electron direction. Its dimensions are 800 cm x 760 cm x 87 cm, with a square hole of 95x95 cm^2 in the center for the beam pipe and magnets. Its main purpose is to shield the detector against particles from the proton beam halo and to give a veto signal for the main detector components.

C5 Counter
The C5 Counter is a scintillator counter which is located near the collimator C5, about 3 m in the electron direction, very close to the beam (4 cm - 10 cm). It main purpose is to provide an accurate time measurement for the background in order to veto events which are not in the time window of the crossing of electron and proton bunches. From this timing information it is possible to reduce the background rate by an order of magnitude.

2.2.6 Luminosity Measurement

Any process that is to be used to monitor the luminosity seen by an experiment must fulfil the requirements that its cross section must be fairly large, so that a short measurement time is needed for a reasonably accurate estimate of the instantaneous luminosity, and that its cross section must be very well known, i.e. calculable and be short of uncertainties.

For HERA, the ep-bremsstrahlung process

$$ep \rightarrow e'p\gamma$$

is used for the luminosity measurement. For the experimental measurement of this process, the outgoing electron and photon should be measured in coincidence in the so called luminosity monitor (LUMI), with $E_{e'} + E_\gamma = E_e$, i.e. the scattered electron and photon energies must add up to the electron beam energy. The cross section for this processes is given semi-classically by the Bethe-Heitler formula [7]. It has been shown that, within the experimental conditions, this cross section agrees excellently with QED calculations [8]. The radiative corrections to this process have been calculated and amount to -0.3% within the measurable area of phase space. The ZEUS luminosity monitor consists of two separate detectors, one for the photon branch and one for the electron branch, The layout of the luminosity monitor components is shown in figure 2.10.

Photons emerging from the bremsstrahlung process at scattering angles $\theta_\gamma \leq 0.5$ mrad leave the proton beam pipe through a window located at a distance of 92.5 m from the IP, and are measured in a lead-scintillator electromagnetic calorimeter at 107 m from the IP. In front of the photon calorimeter, a 2 radiation length carbon filter absorbs the large flux of synchrotron radiation photons, which typically have low energy ($\sim$ KeV), whereas the ep-bremsstrahlung photons used for the luminosity measurement have energies well above 1 GeV. A Cerenkov counter placed between the filter and the calorimeter detects events in which the photon has been converted in the filter. The acceptance for bremsstrahlung photons is about 98%, independent of energy.

Electrons scattered at angles $\theta_{e'} \leq 6$ mrad, and with energies $0.2E_e \leq E_{e'} \leq 0.9E_e$ are deflected by the beam magnets away from the nominal electron beam orbit. They leave the electron beam line through a window at 27.3 m from the IP, and hit the electron calorimeter located at 34.7 m from the IP. The acceptance is measured to be above 70 % and flat for scattered electrons with energies in the range $0.35E_e \leq E_{e'} \leq 0.65E_e$. This is the region used in the luminosity measurement. In addition, the electron calorimeter of the LUMI can be used to tag electrons scattered at very small angles. In this case, no coincidence with the photon calorimeter is required. This electron-tagger mode covers the Q^2 range between 10^{-7} and $2 \cdot 10^{-2}$ (GeV/c^2), although the location of this calorimeter is such that only a fraction of the electrons, in this range of Q^2, are tagged.

The luminosity value is easily obtained from the observed ep-bremsstrahlung rate R_{ep} by $L = R_{ep}/\sigma_{obs}$, where σ_{obs} is the ep-bremsstrahlung cross section corrected for detector inefficiencies and acceptances. The uncertainty in σ_{obs} is small and, therefore, the error in the luminosity measurement is largely dominated by the uncertainty in R_{ep}. The luminosity measurement suffers from a number of background processes. By requiring a coincidence between a high energy electron and photon, this background is dominated by interactions of electrons with the remaining gas in the beam pipe. The contribution of this background to the total counting rate of the luminosity monitor can be estimated by using the pilot electron bunches. Let the fully measured counting rate of the luminosity detector be R_{tot}, the rate of the pilot-bunches be R_{pilot}, the total current in the electron ring be I_{tot}, and the current in the pilot bunches be I_{pilot}, then the actual ep-bremsstrahlung rate R_{ep} for the luminosity measurement can be estimated as:

$$R_{ep} = R_{tot} - R_{pilot}\frac{I_{tot}}{I_{pilot}}.$$

2.2.7 The Trigger and Data Acquisition Systems

At HERA one of the challenges for the data acquisition system is the bunch crossing time of 96 ns, clearly too short to perform a full data readout or to make a trigger decision. The purpose of the ZEUS trigger system is to distinguish interesting physics events from the background events. The total interaction rate, which is dominated by background from upstream interactions of the proton beam with residual gas in the beam pipe, is of the order 10-100 KHz while the rate of ep physics events in the detector is of the order of 3-5 Hz. In addition, other background sources like electron-gas collisions, halo muons and cosmic rays also are present. Background suppression is achieved by a sophisticated three-level trigger system [9], where each successive level has more time available to compute more complicated trigger decisions. A schematic diagram of the ZEUS trigger and data acquisition systems is presented in figure 2.11.

The *First Level Trigger* (FLT) is a hardware trigger, designed to reduce the input rate below 1 kHz. Each component of the detector ZEUS has its own FLT, which stores the data in a pipeline, and makes a trigger decision within 2 μs after the bunch crossing. The decisions from all the FLTs are collected by the Global First Level Trigger (GFLT), which decides whether to accept or reject the event, and returns this decision to the component readouts within 4.6 μs, corresponding to 46 bunch crossings. The FLT operates only on a small subset of the detector data in order to achieve such rate in the decision. At this level most of the beam-gas and beam-halo events are eliminated.
If the event is accepted, the data are transferred to the *Second Level Trigger* (SLT), which is software-based and runs on a network of transputers. It is designed to reduce the rate below 100 Hz. For the SLT almost all the event information and the full dynamic range are used. The Global Secon Level Trigger (GSLT) receives all of the second level trigger information from the individual components as well as the trigger information from the GFLT. The SLT produces a decision 3 ms after the corresponding ep-interaction. If the event is accepted by the GSLT, all the detector components send their data to the Event Builder, which collects all the information to form a complete event. The event is then passed to the *Third Level Trigger* (TLT). The TLT is software based and runs a reduced version of the off-line data analysis code. It is designed to reduce the rate to a few Hz. Events accepted by the TLT are written to tape.

2.3 Reconstruction of the Kinematic Variables

A precise reconstruction of x and Q^2 from the final state is of vital importance for the description of DIS events. The kinematic reconstruction based on quantities measurable in the ZEUS detector using several methods is described in this section. In deep inelastic scattering, the kinematics of the event must be reconstructed from the measured final state. At lowest order in pQCD, this final state consists of the scattered lepton (e or ν) and the scattered quark

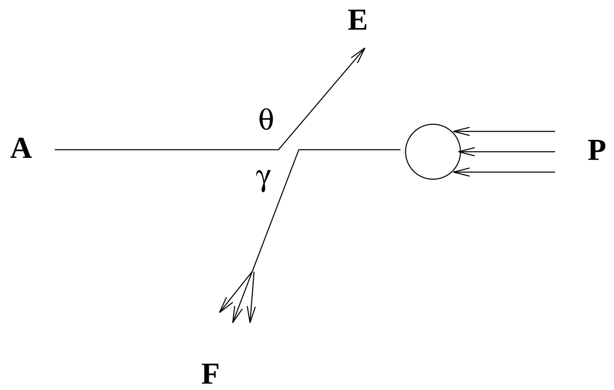

where A, E and θ are the initial energy, final energy and scattered angle of the lepton, respectively, and P, F, and γ are the beam proton energy, the final hadronic energy and the angle of the final hadronic system respectively. The kinematics of the event can be reconstructed from any combination of the variables E,F,θ and γ. In the following, four of the possible methods are presented: using either the scattered lepton, the information of the hadronic final state or a combination of the scattered lepton and hadronic system kinematic variables.

2.3.1 Reconstruction from the Scattered Electron

In neutral-current DIS there will be an electron in the final state. In fixed target experiments, x and Q^2 are reconstructed from the angle and energy of the final-state electron. Using the definition of the kinematic variables given in the previous chapter, the following expressions are obtained:

$$Q^2_{ele} = 2AE(1 + cos\theta)$$

$$y_{ele} = 1 - \frac{E}{2A}(1 - cos\theta)$$

$$x_{ele} = \frac{Q^2_{ele}}{sy_{ele}}$$

It is noted that the relation

$$Q^2_{ele} = \frac{P^2_{T,ele}}{1 - y_{ele}}$$

holds. The contours of constant energy or scattering angle in the (x, Q^2) plane, accessible at HERA, are displayed in figure 2.12. It is seen that at low values of Q^2, the electron scattering angle is large (measured respect to the proton direction), i.e. the electrons hit the UCAL in the rear part or, to a lesser extent, in the barrel part. Occasionally the scattered electron is deflected to the forward part of the detector. The scattering angle increases with Q^2, and is largely independent of x, except at high values of y.

The very low-Q^2 region, which is not covered by the nominal vertex data due to the beam hole in the ZEUS calorimeter, is indicated by the grey-shading in the right hand plot. From the expressions:

$$(\Delta Q^2/Q^2)_E = \Delta E/E$$

$$(\Delta Q^2/Q^2)_\theta = \tan(\frac{\theta}{2})\Delta\theta$$

$$(\Delta x/x)_E = \frac{1}{y}\Delta E/E$$

$$(\Delta x/x)_\theta = tan(\frac{\theta}{2})(x\frac{P}{A} - 1)\Delta\theta$$

it is seen that the resolution in Q^2 as obtained by the electron variables is very good (except for very small scattering angles). However, the resolution in x becomes very poor at low y due the limited energy resolution.

2.3.2 Reconstruction from the Hadronic Final State

It is possible to obtain a complete independent reconstruction method using the hadronic final state, since ZEUS is an almost 4π-detector. For neutral-current DIS events this method allows to extend the measurable region in the (Q^2, x) plane. For charged-current DIS events, where the neutrino leaves the detector undetected, this method provides the only way to reconstruct the kinematics.
From the scattered-quark energy F and angle with respect to the proton direction γ, the kinematics can be reconstructed using the following expressions:

$$y = \frac{F(1 - cos\gamma)}{2A}$$

$$Q^2 = \frac{F^2 sin^2\gamma}{1 - y}$$

$$x = \frac{Q^2}{sy}$$

However it is not possible to measure directly F and γ. One possibility could be to look for jets in the final state and associate one (or more) of them with the struck quark. For any given event, the ensemble of reconstructed jets may include such a current jet, but also jets originating from hard and soft QCD processes, and a jet originating from the target remnant. This greatly obscures the direct use of F and γ for kinematics reconstruction. Instead, the hadronic energy flow as measured in the cells of a segmented calorimeter can be used without explicit jet finding. Jacquet and Blondel [10] proposed such a method, based on appropriated weighting of the energy deposits in the cells. The idea is that the hadronic final state consists of a component that has taken part in the hard scattering (which therefore contains the information on F and γ) and a component that was only an spectator in the interaction (the target remnant). The kinematics can be accurately reconstructed from the hadronic energy flow if the latter component is suppressed. The spectator component is characterized by a boost in the incoming proton direction. The Jacquet-Blondel method uses the following expressions:

$$y_{jb} = \frac{\sum_i (E_{h,i} - p_{z,i})}{2A}$$

$$Q^2_{jb} = \frac{(\sum_i P_{T,i})^2}{1 - y}$$

$$x_{jb} = Q^2_{jb}/sy_{jb}$$

where the sums run over all the hadronic particles in the final state. The influence of the target remnant and any hadronic energy lost in the forward beam hole, characterized by low p_T and low $E - p_z$, is suppressed. The problem with the use of the hadronic energy flow lies in the limited hadronic energy resolution of a calorimeter. Figure 2.13 shows the contours of constant current-jet energy and angle in the (x, Q^2)-plane. In contrast to the electron method, the effect on the resolution in x from the measurement errors of the jet energy is small at high-x. However, the forward beam hole at $\gamma \sim 2.2^o$ limits the reach of this reconstruction method to $y > 10^{-3}$. At very low x and high y a similar limit is set by the rear beam hole (see grey-shaded regions in the right hand plot).

2.3.3 Reconstruction from Mixed Methods

The methods which combine information from the electron and hadronic energy flow are known as mixed methods. Taking into account the advantages of both the electron and Jacquet-Blondel methods, it is straightforward to design the following equations:

$$y_{mix} = y_{jb}$$

$$Q^2_{mix} = Q^2_{ele}$$

$$x_{mix} = \frac{Q^2_{mix}}{s y_{mix}}$$

The Double-Angle Method

In addition, it has been proved useful to use θ and γ in the event kinematics reconstruction (the "double angle" method) [11]:

$$y_{da} = \frac{sin\theta(1 - cos\gamma)}{sin\gamma + sin\theta - sin(\theta + \gamma)}$$

$$Q^2_{da} = 4A^2 \frac{sin\theta(1 + cos\gamma)}{sin\gamma + sin\theta - sin(\theta + \gamma)}$$

$$x = \frac{A}{P} \frac{sin\gamma + sin\theta + sin(\theta + \gamma)}{sin\gamma + sin\theta - sin(\theta + \gamma)}$$

Angles are easier to measure with accuracy than energies, and do not suffer (in first order) from calorimeter energy calibration uncertainties. The difficulty in the double angle method appears in the determination of γ. It has been suggested to determine γ from the Jacquet-Blondel expressions:

$$cos\gamma = \frac{Q^2_{jb}(1 - y_{jb}) - 4A^2 y^2_{jb}}{Q^2_{jb}(1 - y_{jb}) + 4A^2 y^2_{jb}}$$

which is equivalent to (in terms of the 4-momentum of the final hadrons)

$$cos\gamma = \frac{(\sum p_x)^2 + (\sum p_y)^2 - (\sum E - p_z)^2}{(\sum p_x)^2 + (\sum p_y)^2 + (\sum E - p_z)^2}.$$

When the p_T of the spectator jet and the jet masses are neglected, this expression is equivalent to the angle of the current jet,

$$cos\gamma = \frac{\sum E_i cos\gamma_i}{\sum E_i},$$

where the sum runs over all the particles in the jet.

The Σ Method

The Σ method [12] combines the measurements of energies and angles of the electron and hadron system. Making use of the relation

$$\sum_i (E_{h,i} - p_{z,i}) + E(1 - cos\theta) = 2A,$$

which holds exactly for a hermetic detector, a new expression for y can be written

$$y_\Sigma = \frac{\sum_i (E_{h,i} - p_{z,i})}{\sum_i (E_{h,i} - p_{z,i} + E(1 - cos\theta)},$$

which gives y at the hard interaction vertex even if an initial state radiation (ISR) photon has been emitted. Using the expression

$$Q^2_\Sigma = \frac{E^2 sin^2\theta}{1 - y_\Sigma},$$

it is possible to determine Q^2 independently of ISR assuming that the initial-state radiated photon is collinear to the beam line and does not carry transverse momentum. The value of x_Σ is calculated from y_Σ and Q^2_Σ using the relation $x_\Sigma = Q^2_\Sigma / s y_\Sigma$.

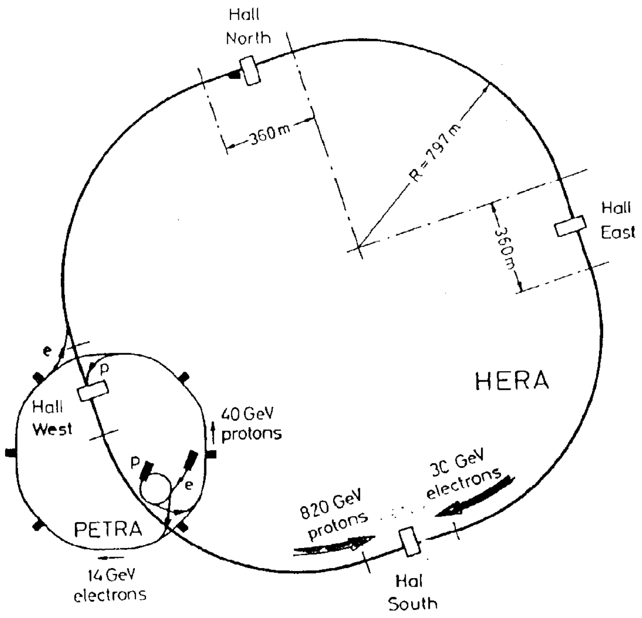

Figure 2.1: Layout of the HERA collider.

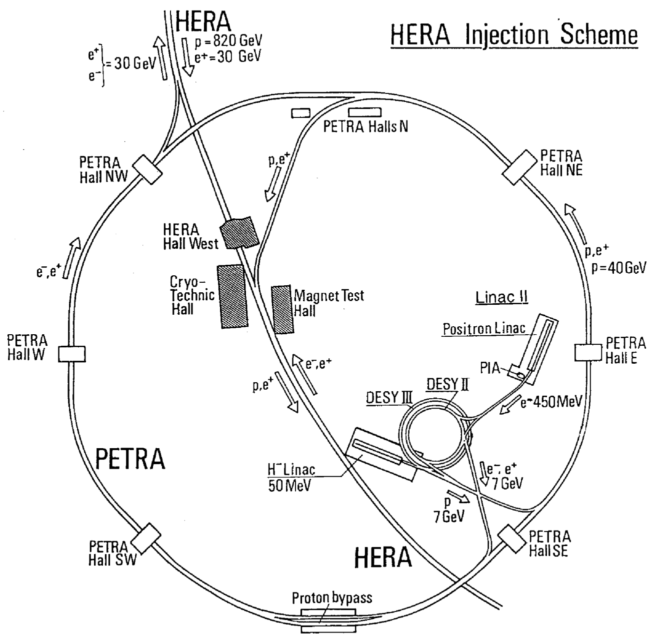

Figure 2.2: Scheme of the injection facilities at DESY.

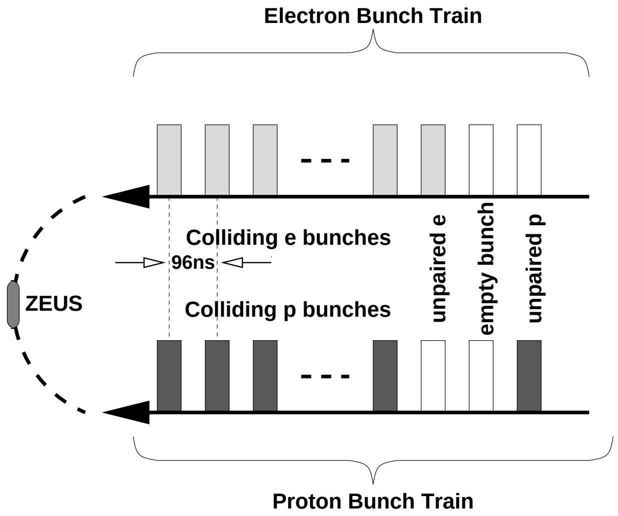

Figure 2.3: Bunch distribution for electrons and protons.

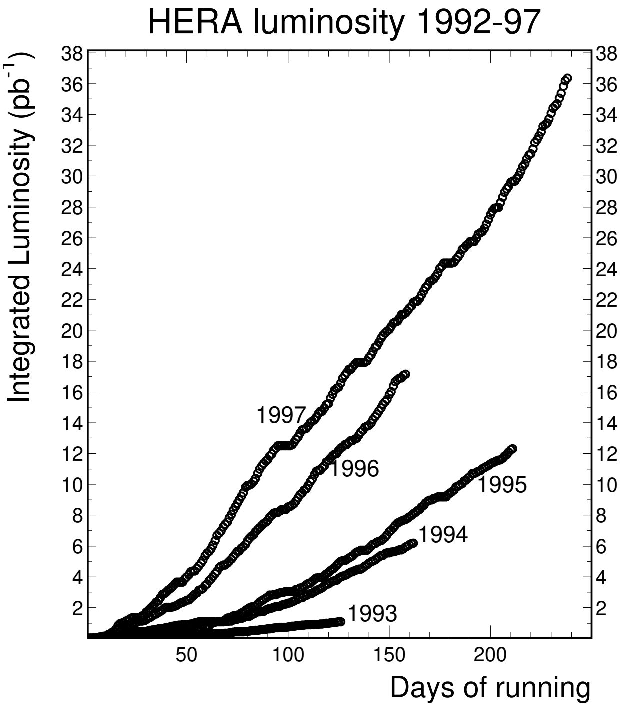

Figure 2.4: Delivered luminosity during 1992-1997 by HERA.

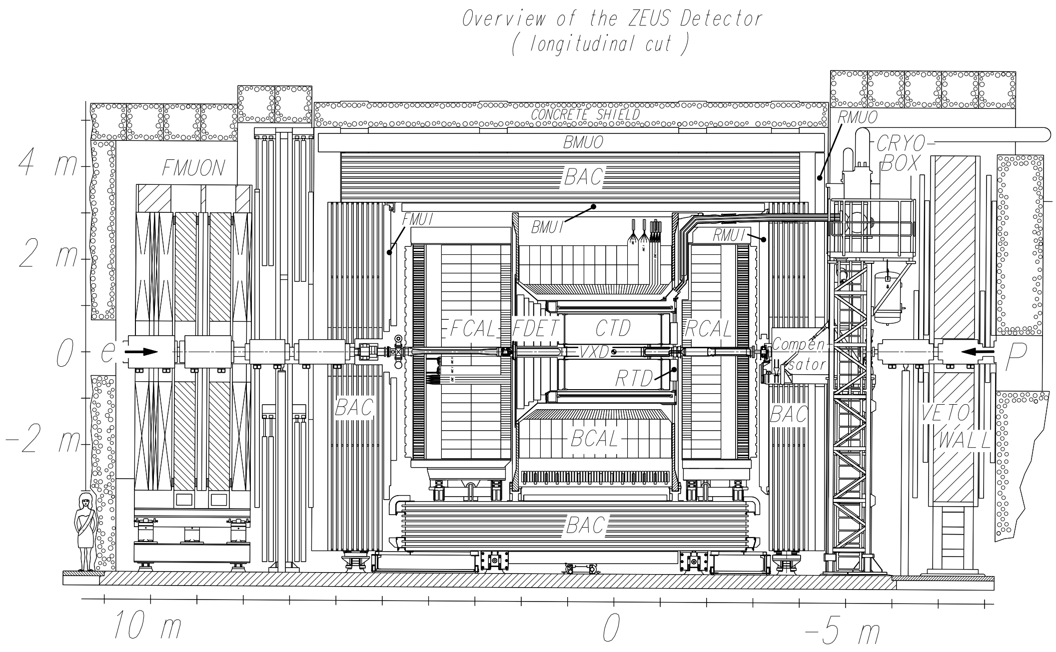

Figure 2.5: Cross section of the ZEUS detector parallel to the beam direction.

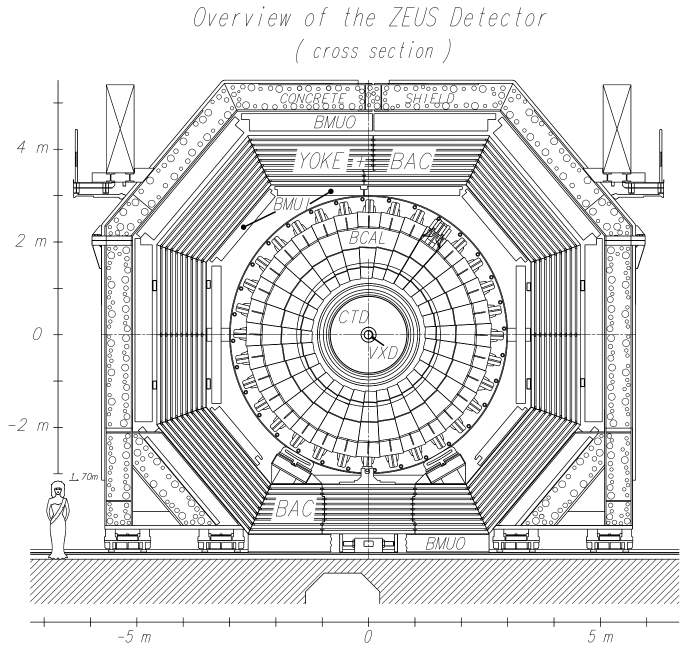

Figure 2.6: Cross section of the ZEUS detector perpendicular to the beam direction.

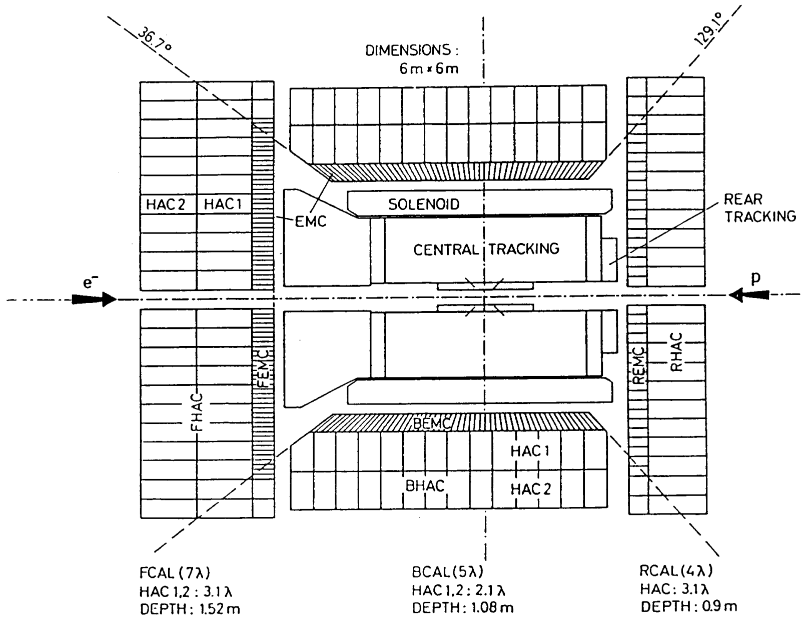

Figure 2.7: Layout of the ZEUS high-resolution uranium-scintillator calorimeter.

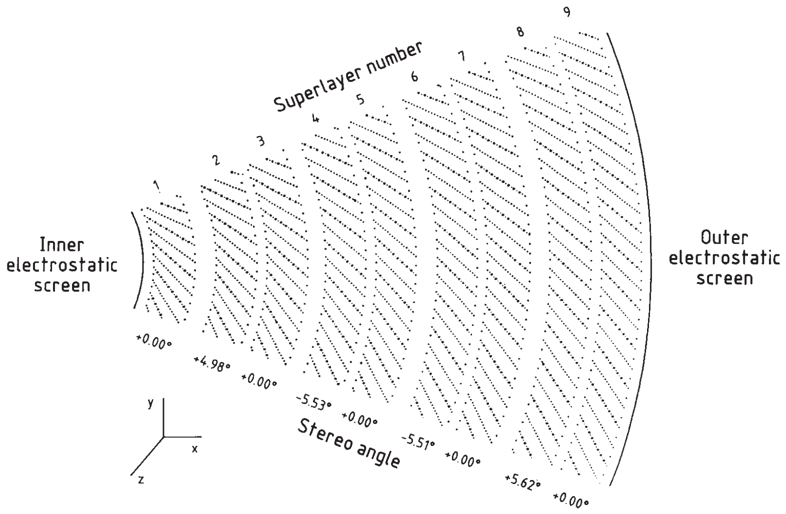

Figure 2.8: Wire layout of one octant of the Central Tracking Detector.

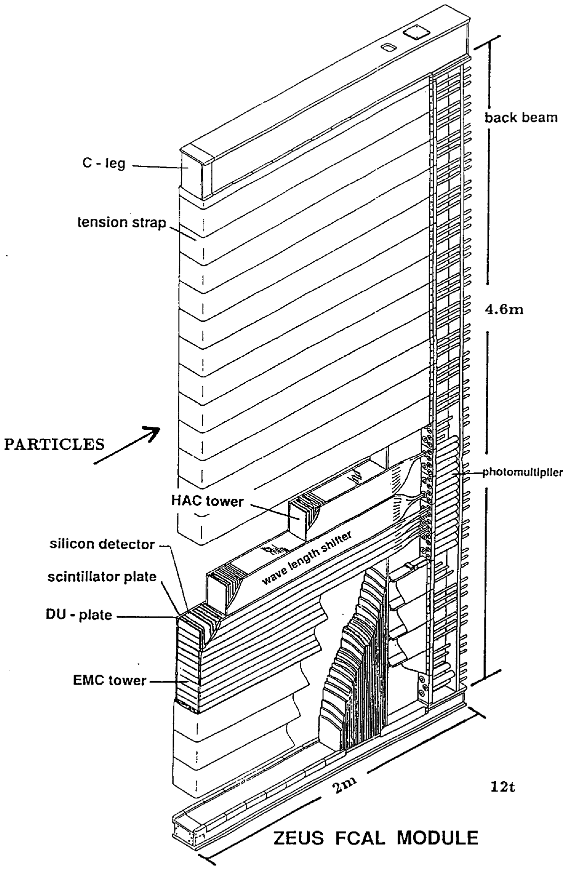

Figure 2.9: Internal structure of an FCAL module.

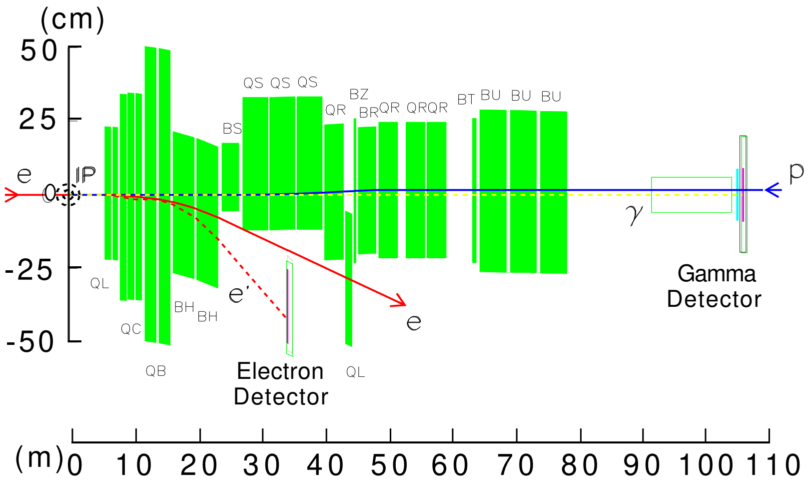

Figure 2.10: Layout of the ZEUS luminosity monitor.

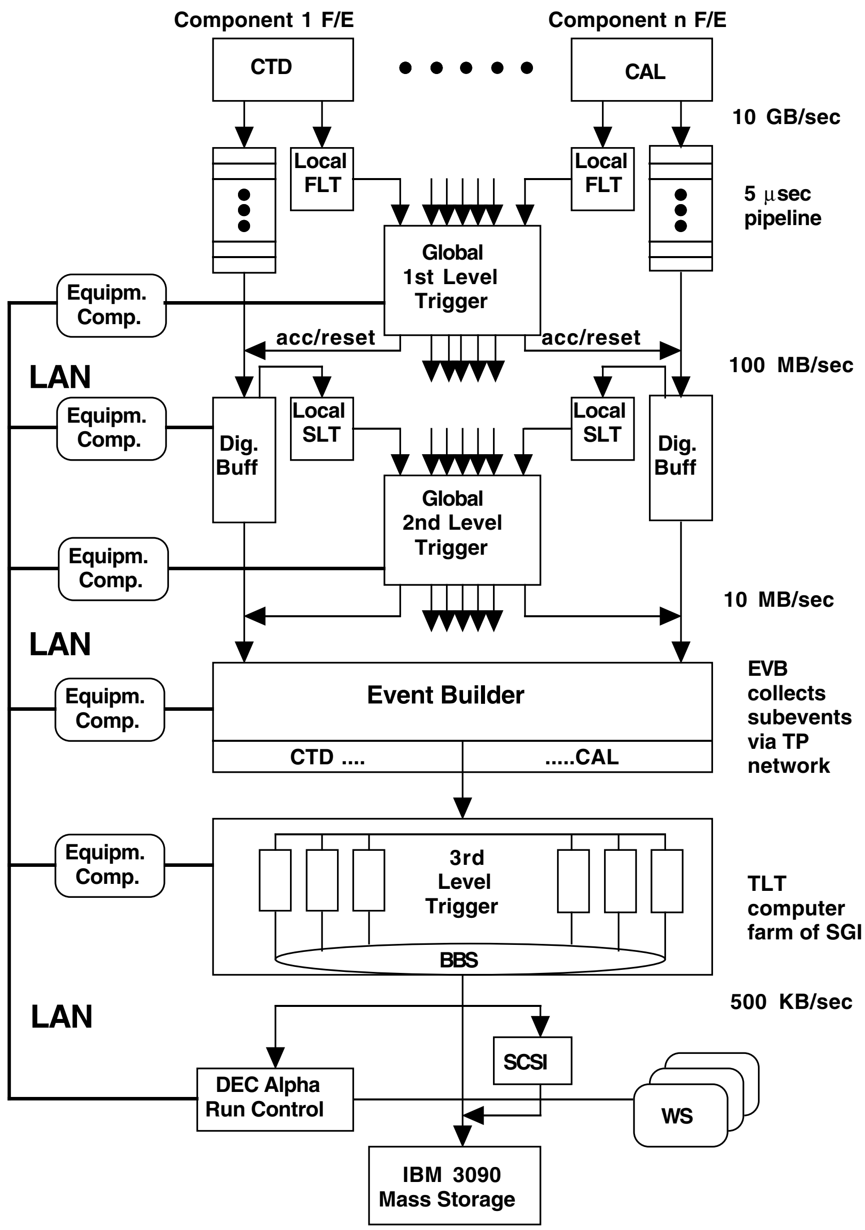

Figure 2.11: Schematic diagram of the ZEUS trigger and data acquisition systems.

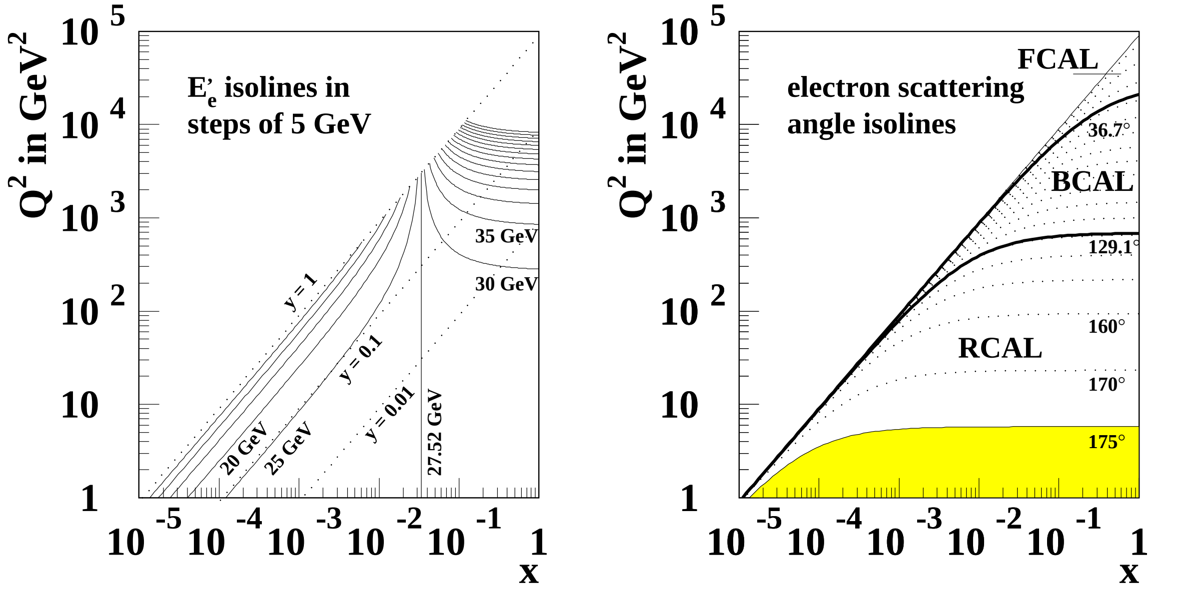

Figure 2.12: Contours of constant electron energy (left) and scattering angle (right) in the (x, Q^2) plane.

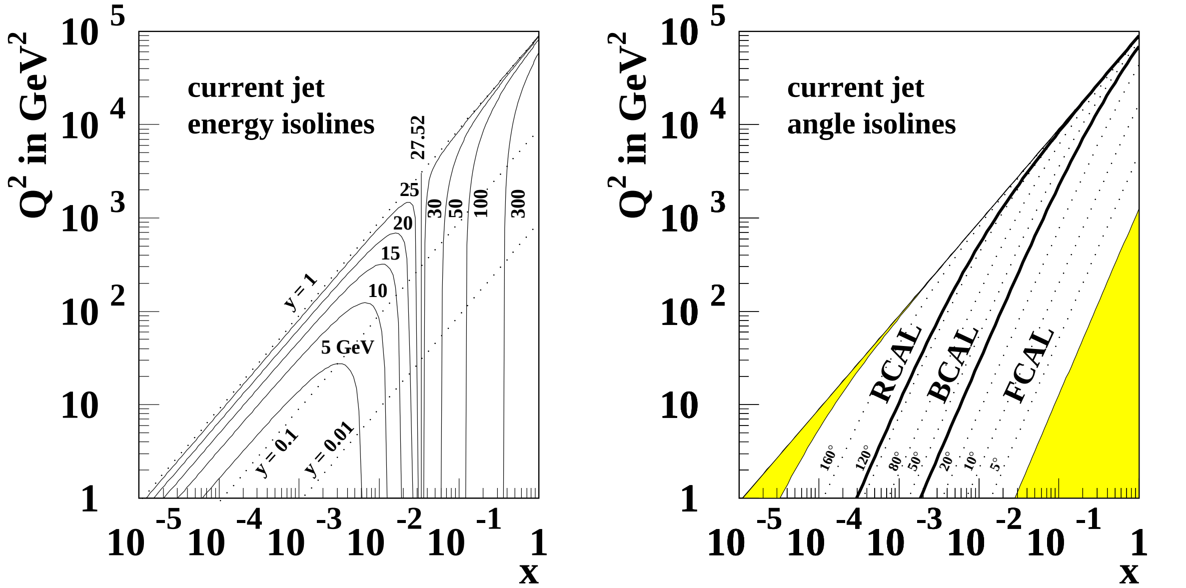

Figure 2.13: Contours of constant jet energy (left) and hadronic angle (right) in the (x, Q^2) plane.

Bibliography

[1] U. Holm et al. *The ZEUS Detector. Status Report.* 1993

[2] U. Amaldi. *Fluctuations in Calorimetry Measurements.* Physica Scripta 23, (1981) 409-424.

[3] C.W.Fabjan. *Calorimetry in High Energy Physics* CERN-EP/85-54

[4] J. Straver, *Design, Construction and Beam Test of the High Resolution Uranium Scintillator Calorimeter for ZEUS.* Doctoral Thesis (1991)

[5] J. Krüger. *The Uranium Scintillator Calorimeter for the ZEUS Detector at the Electron-Proton Collider HERA.* DESY-Report, DESY F35-92-02, (1992).

[6] M. Derrick et al. Nucl. Instr. Meth. A309 (1991) 77;
A. Andresen er al. Nucl. Instr. Meth. A309 (1991) 101;
A. Bernstein et al. Nucl. Instr. Meth. A336 (1993) 23.

[7] H. Bethe and W. Heitler, Proc. Roy. Soc. **A146**(1934) 83

[8] M. van der Horst, Thesis, University of Amsterdam, 1991.

[9] W.H. Smith et al. Nucl Instr. Meth. A335 (1995) 278-294

[10] F.Jacquet and A.Blondel, Proceedings of the study for an *ep* facility for Europe, DESY 79–48 (1979), p.391.

[11] S.Bentvelsen, J.Engelen, P.Kooijman, Proc. 1991 Workshop on Physics at HERA, ed. W.Buchmüller and G.Ingelman (DESY, Hamburg, 1992), Vol. 1, p.23.

[12] U. Bassler, G. Bernardi. Nucl. Intr. Meth. A 361 (1995) 197.

Chapter 3

Charged Current Interactions at High Q^2

3.1 Introduction

In comparison to fixed target neutrino scattering experiments [1], the HERA ep collider extends the kinematic region for studying charged–current (CC) deep inelastic scattering (DIS) by about two orders of magnitude in Q^2 and also to lower x at a given value of Q^2. Both the H1 [2] and ZEUS [3] collaborations have previously reported cross section measurements for the process $e^-p \to \nu_e X$, where X denotes the hadronic final state. These investigations, based on the data collected in 1993, established that the Q^2 dependence of the CC cross section is consistent with that of the W propagator and that the CC and neutral–current (NC) cross sections have similar magnitude for $Q^2 \gtrsim M_W^2$ (M_W denotes the W mass). The H1 collaboration has also measured the integrated cross section [4] and the differential cross section $d\sigma/dQ^2$ [5] for $e^+p \to \overline{\nu}_e X$ with missing transverse momentum ($\not{P}_t$) above 25 GeV.

This chapter reports on measurements of the integrated and differential cross sections for both e^+p and e^-p CC DIS in the kinematic region $Q^2 > 200\,\mathrm{GeV}^2$, performed using the data collected by ZEUS during the 1994 running period. In 1994 ZEUS has accumulated $2.93\,\mathrm{pb}^{-1}$ of e^+p data and $0.27\,\mathrm{pb}^{-1}$ of e^-p data in collisions of 820 GeV protons with 27.5 GeV electrons. In order to study both e^+ and e^- induced CC reactions, these data samples have been combined with the $0.55\,\mathrm{pb}^{-1}$ of e^-p data taken in 1993 with an electron beam energy of 26.7 GeV [3]. The differential cross sections were measured as functions of x, y and Q^2 and were compared with Monte Carlo predictions. The Q^2-dependence was used to determine the W mass.

As discussed in chapter 1, the unpolarized e^+p and e^-p charged–current differential cross sections (including the leading order QCD evolution in Q^2) are:[1]

$$\frac{d^2\sigma_{e^+p\to\overline{\nu}X}}{dxdQ^2} = \frac{G_F^2}{2\pi}\left(\frac{M_W^2}{M_W^2+Q^2}\right)^2 \sum_{i=1}^{2}\left[\overline{u}_i(x,Q^2) + (1-y)^2\, d_i(x,Q^2)\right] ,$$

$$\frac{d^2\sigma_{e^-p\to\nu X}}{dxdQ^2} = \frac{G_F^2}{2\pi}\left(\frac{M_W^2}{M_W^2+Q^2}\right)^2 \sum_{i=1}^{2}\left[u_i(x,Q^2) + (1-y)^2\, \overline{d}_i(x,Q^2)\right] ,$$

[1] For the current integrated luminosity, any contributions to the CC cross section from hard subprocesses involving 3$^{\mathrm{rd}}$ generation quarks (b,t) can be neglected.

where u_i and d_i are the densities of up–type and down–type quarks of the $i^{\rm th}$ generation in the proton, G_F is the Fermi coupling constant, and y is the fractional energy transfer to the proton in its rest system. The factor $(1-y)^2$, which suppresses the quark (antiquark) contribution to the e^+p (e^-p) cross section, is a direct consequence of the $V-A$ structure of the weak coupling.

As the previous equations show, the charged current couples to different quark flavors for e^+ and e^- beams and the valence and sea contributions have very different y dependences. In addition, the Q^2 dependence of the cross section allows a measurement of the W propagator effect and thus a determination of the W mass in the space–like region, complementing the measurements of direct W production at $p\overline{p}$ colliders [6].

In section 2 a short description of the Monte Carlo samples used is provided. The selection criteria used in order to isolate the CC signal is explained in section 3. In the sections 4 and 5 the procedure designed to obtain the final measurements is presented. The several cross checks, background estimations and systematic studies are explained in detail. In sections 6 and 7 the whole measurements are presented and compared with the Monte Carlo predictions and the value of the W boson is obtained. Some too detailed parts of the analysis are collected in appendix A. Finally, section 8 shows the comparison with the measured differential cross sections for neutral current interactions at high-Q^2, analysis performed by ZEUS and partially described in appendix B.

3.2 Monte Carlo Simulation

Simulated CC DIS events with electroweak radiative corrections were generated using LEPTO [7] interfaced to HERACLES [8] via DJANGO [9]. The MRSA set of NLO parton density parameterizations was used. The hadronic final state was simulated using the color–dipole model as implemented in ARIADNE [11] for the QCD cascade and JETSET [12] for the hadronization. In addition, MC samples using the MEPS option of LEPTO instead of ARIADNE were generated.

MC samples of NC DIS and photoproduction events were employed to simulate backgrounds to CC DIS. For the NC DIS simulation the same programs were used as for the CC events. Samples of both direct and resolved photoproduction events were generated using both PYTHIA [12] and HERWIG [13]. Photoproduction of $c\overline{c}$ and $b\overline{b}$ pairs was simulated using both PYTHIA and AROMA [14].

All simulated events were passed through a GEANT based [15] detector simulation and processed with the same analysis programs as the data.

3.3 Event Selection

3.3.1 Trigger Configuration

Data were collected with a three–level trigger system [16]. The first–level trigger conditions used in this analysis were based on electromagnetic energy, transverse energy, and missing transverse energy in the calorimeter. The thresholds were significantly below the corresponding cuts applied in the subsequent selection. The second level trigger rejected backgrounds (mostly p–gas interactions and cosmic rays) for which the calorimeter timing was inconsistent with an ep interaction. Events were accepted as CC candidates if the following conditions were all fulfilled:

1. The missing transverse momentum $\not{P}_t$ exceeded 9 GeV (see next section).
2. $\not{P}_t$ evaluated from all calorimeter cells except those adjacent to the forward beam pipe exceeded 8 GeV.
3. Either a track was found in the CTD or at least 10 GeV was deposited in the FCAL.

The third–level trigger applied stricter timing cuts and also pattern recognition algorithms to reject cosmic rays.

3.3.2 Event Selection

In CC ep reactions the final state neutrino remains undetected. This fact imposed special conditions both for the reconstruction of kinematic variables and for the event selection.
The Jacquet–Blondel method [17] was used to reconstruct the kinematic variables from the measured missing transverse momentum,

$$\not{P}_t = \sqrt{\left(\sum_i p_X^i\right)^2 + \left(\sum_i p_Y^i\right)^2} ,$$

and the quantity δ, given by

$$\delta = \sum_i \left(E^i - p_Z^i\right) ,$$

where the sums run over all EMC and HAC cells with energy deposits E^i above 60 MeV and 110 MeV, respectively, and the $\vec{p}^{\,i}$ are the momenta assigned to each calorimeter cell (calculated assuming zero mass and using the geometrical cell center and the measured vertex position). The Jacquet–Blondel estimators of y, Q^2 and x are given by

$$y_{JB} = \frac{\delta}{2E_e} , \qquad Q^2_{JB} = \frac{\not{P}_t^{\,2}}{1 - y_{JB}} , \qquad x_{JB} = \frac{\not{P}_t^{\,2}}{s\, y_{JB}(1 - y_{JB})} ,$$

where E_e is the electron beam energy.
The number of CC triggers was about 10^5, almost entirely due to p–gas interactions, cosmic rays, and beam halo muons. After a preselection which required a tracking vertex and stricter timing cuts than at the trigger level, about 6300 e^+p and 1500 e^-p candidates remained (cf. table 3.1). In the following, we describe the cuts which were applied to extract the CC signal. Table 3.1 gives the numbers of events remaining after each selection cut, as well as the corresponding efficiencies estimated using the ARIADNE MC samples.
The following conditions were imposed on all events passing the trigger:

- $\not{P}_t > 11$ GeV was required. The trigger simulation indicated that this cut was sufficiently far above the 9 GeV trigger threshold to ensure high trigger efficiency.
- The events had to have a fitted tracking vertex, determined from at least one track compatible with intersecting the beam line. The vertex position had to fulfill $|Z_{\rm vtx}| < 45$ cm, where $Z_{\rm vtx} = 0$ at the nominal interaction point. This cut eliminated a large fraction of non–ep background.

- $\not{P}_t^{\text{out}}/\not{P}_t > 0.6$ was required, where $\not{P}_t^{\text{out}}$ is the net transverse momentum for all calorimeter cells with a polar angle above 9° with respect to the nominal vertex position. This cut rejected p–gas and p–beampipe collisions, for which $\not{P}_t$ is concentrated at small polar angles.

- There had to be at least one reconstructed track originating from the vertex, which had a polar angle between 15° and 164° and a transverse momentum exceeding 0.2 GeV. This requirement removed cosmic ray events and p–gas interactions with spurious vertices caused by low–energy secondary interactions in the beam pipe.

- The difference $\Delta\phi$ between the azimuth of the net transverse momentum as measured by the CTD tracks with polar angle between 15° and 164°, and the azimuth measured by the calorimeter, was required to fulfill $|\Delta\phi| < 1$ rad. This requirement removed overlays of cosmic rays on ep–interactions.

- In addition, a pattern recognition algorithm based on the topology of the calorimeter energy distribution was applied to reject cosmic rays and beam halo muons.

Simulation of backgrounds due to NC DIS and photoproduction interactions showed that such events passing the above cuts were concentrated at low $\not{P}_t$. The same was found for the non–ep background. Hence the following additional cuts were applied to events with $\not{P}_t < 30$ GeV:

- $y_{JB} < 0.8$, which reduced NC DIS background.

- $\not{P}_t/E_t > 0.4$, where $E_t = \sum_i \sqrt{(p_X^i)^2 + (p_Y^i)^2}$ is the total transverse energy. This cut demanded an azimuthally collimated energy flow and rejected photoproduction and also p–gas background.

- $P_t^{\text{tracks}}/\not{P}_t > 0.1$, where $P_t^{\text{tracks}} = \sqrt{\left(\sum_j P_X^{\text{track}\,j}\right)^2 + \left(\sum_j P_Y^{\text{track}\,j}\right)^2}$ and j runs over all vertex–fitted tracks with polar angles between 15° and 164°. This cut effectively tightened the $\not{P}_t^{\text{out}}/\not{P}_t$ requirement (cf. above) and also removed events with additional non–ep related energy deposits in the calorimeter (mainly cosmic rays).

The resulting sample was visually scanned and 3 non–ep background events were identified in the e^+p sample and removed (all were overlays of muons and p–gas reactions). No non–ep background was found in the e^-p sample. An event picture, corresponding to one CC candidate is presented in figure 3.1. Figures 3.2 and 3.3 show the distribution of the kinematic variables for the e^+p and e^-p selected events respectively, compared with the Monte Carlo predictions. Good agreement is observed.

The distribution in x and Q^2 of the final samples of 56 e^+p events and 30 e^-p events is also shown in figure 3.8. All events in these samples have a corrected Q^2 (cf. section 3.5.1) above 200 GeV^2.

3.4 The Neutral–Current Control Sample

The acceptance corrections and the methods of reconstructing the kinematic variables were based on the MC simulation described above. In order to verify the accuracy of the simulation, several systematic checks were performed using a sample[2] of high–Q^2 NC events selected as follows:

- As in the CC case, the NC trigger requirements were based on the calorimeter energy deposits. The same timing cuts were applied as for the CC trigger. Photoproduction background was efficiently suppressed by the cut $\delta > 25\,\mathrm{GeV}$.
- In the offline NC selection, an electron candidate with at least 10 GeV energy had to be identified by a neural–network algorithm using the pattern of the calorimeter energy deposits [18]. The electron had to be isolated (less than 2 GeV of energy not associated with the electron in an (η, ϕ)–cone of radius $R = 0.5$ centered on the electron direction) and had to have a matching track if it was in the region $20° < \theta < 160°$. In addition, the event had to have a reconstructed tracking vertex, and satisfy $35\,\mathrm{GeV} < \delta < 65\,\mathrm{GeV}$ and $Q^2 > 200\,\mathrm{GeV}^2$, where Q^2 was reconstructed using the double angle (DA) method [19].
- For the selected NC events, the track(s) and the calorimeter deposits associated with the electron were deleted from the data, and the reconstruction of the event vertex was repeated.
- These modified NC events were then processed through the complete CC analysis chain. In order to account for the different cross sections, a weight

  $$w = \frac{d\sigma_{e^+p\to\overline{\nu}X}/dx\,dQ^2}{d\sigma_{e^+p\to e^+X}/dx\,dQ^2} \quad \text{for } e^+p \qquad \text{resp.} \qquad w = \frac{d\sigma_{e^-p\to\nu X}/dx\,dQ^2}{d\sigma_{e^-p\to e^-X}/dx\,dQ^2} \quad \text{for } e^-p$$

  was assigned to each event, where leading order differential cross sections, evaluated at x and Q^2 as reconstructed by DA method, were used.

The control sample was not corrected for the efficiency of the NC event selection, for remaining backgrounds, or for migrations due to mismeasurement of x and Q^2. The distributions of Q^2_{JB}, x_{JB}, y_{JB} and $\not{P}_t$ agreed sufficiently well with the corresponding CC MC distributions to allow for quantitative checks of the efficiency calculations and correction methods. All these studies were summarized in appendix A.

3.5 Cross Section Evaluation

The integrated and differential cross sections were calculated from the observed numbers of events and the integrated luminosity after subtracting the estimated photoproduction background and correcting for detection efficiencies and migrations.

The e^-p data from 1993 and 1994 were combined by appropriately weighting the 1993 event numbers in each individual bin under consideration. The weights, which account for slight differences in the electron beam energies and in the trigger and detector configurations, were in the range between 0.95 and 1.05.

All statistical errors have been evaluated using the observed numbers of events and asymmetric Poisson confidence intervals.

[2] Data collected in 1994 were used.

3.5.1 Reconstruction of Kinematic Variables

Due to the energy loss of the hadrons in inactive material in the central detector, the calorimeter measurement underestimated both $\not{P}_t$ and δ (see figure 3.4). The detector simulation was used to derive corrected values $\not{P}_{t\,\mathrm{cor}}$ and y_{cor}, as second–order polynomials of the respective raw values $\not{P}_t$ and y_{JB}, where the coefficients for the y correction depend on $\not{P}_t$ (see figures 3.5,3.6). The correction of $\not{P}_t$ was about 20% at low $\not{P}_t$, decreasing to $\approx 10\%$ for $\not{P}_t \gtrsim 50\,\mathrm{GeV}$; in y, the corrections were highest for $y \approx 0.1$ and low $\not{P}_t$ ($\approx 20\%$), decreasing with both increasing y and increasing $\not{P}_t$. The corrected values ${Q^2}_{\mathrm{cor}}$ and x_{cor} were calculated in terms of $\not{P}_{t\,\mathrm{cor}}$ and y_{cor}. Figure 3.7 shows the reconstruction of the kinematic variables, after the correction functions were applied, as predicted from Monte Carlo. The correction was tested using the NC control sample (cf. section 3.4) by evaluating the means and widths of the distributions of $\delta A = (A_{\mathrm{cor}} - A_{DA})/A_{DA}$ for $A = Q^2, x$ or y in all intervals of these variables (see appendix A).

3.5.2 Background Subtraction

The contamination from NC events, estimated using a LEPTO Monte Carlo sample [7], was negligible. The background from photoproduction processes was determined by applying the selection algorithm to photoproduction events, simulated with HERWIG, which had transverse energy $E_t > 20\,\mathrm{GeV}$ (E_t being determined from the momenta of all final state particles). While the simulated photoproduction events which passed the CC selection all had $E_t > 30\,\mathrm{GeV}$, they were concentrated at low $\not{P}_t$. The estimated photoproduction contamination in the lowest bins of x and Q^2 was $\sim 15\%$.

No event passing the CC selection was found in the MC samples simulating heavy quark photoproduction, yielding an upper limit on the cross section for this background of less than 0.2% of the CC cross section. The heavy quark background is therefore neglected.

No subtraction has been applied for non–ep background (cosmic and beam halo muons, p–gas reactions, and overlays of such events with ep reactions). This background is negligible after event selection and visual scanning.

3.5.3 Acceptance Correction and Unfolding

Bin–to–bin migrations and the efficiencies of trigger and selection cuts were taken into account using a bin–by–bin correction method, where the correction factors were calculated from the Monte Carlo simulation. Typical acceptance corrections range from 40% to 80%, with an average of about 60% (cf. tables 3.1 and 3.2 to 3.5). The statistical errors of the correction factors were about 10 times smaller than the statistical errors of the data and have been neglected. In addition to the acceptance corrections, ζ, defined as the ratio of the number of events reconstructed in a given bin to the number of events generated in the same bin, tables 3.2 to 3.5 also show the purities, ξ, defined as the fraction of the events reconstructed in a given bin which were also generated in the same bin.

The efficiency calculation was checked using the NC control sample. Both the overall acceptances and those of individual cuts (cf. table 3.1) typically agreed with the MC values within 5% (see appendix A).

The bin–by–bin unfolding procedure described above was cross checked by applying a single step matrix unfolding based on Bayes' theorem [20]. For this purpose the matrices

$A_{i,j} = Q^2_{i,cor}/Q^2_{j,gen}$, $B_{i,j} = x_{i,cor}/x_{j,gen}$ and $C_{i,j} = y_{i,cor}/y_{j,gen}$ are determined, where Q^2_{cor}, x_{cor} ,y_{cor} denote the the variables corrected by the fit, (as was explained above). The matrices used for the unfolding procedure, for the positron case, are presented below:

$$\begin{pmatrix} 29.4 & 6.4 & 0.3 & 0.06 & 0.2 \\ 6.7 & 42.3 & 10.2 & 0.8 & 0.3 \\ 0.0 & 7.7 & 50.8 & 13.5 & 2.7 \\ 0.0 & 0.0 & 5.3 & 57.8 & 18.5 \\ 0.0 & 0.0 & 0.0 & 3.4 & 56.0 \end{pmatrix}$$

$$A_{ij}(CC\ MC) = Q^2_{i,cor,cuts}/Q^2_{j,gen}(\%)$$

$$\begin{pmatrix} 28.5 & 6.6 & 0.3 & 0.1 & 0.0 \\ 9.9 & 55.7 & 12.1 & 2.8 & 0.07 \\ 0.0 & 7.5 & 61.0 & 12.0 & 0.4 \\ 0.0 & 0.08 & 4.1 & 56.1 & 12.9 \\ 0.0 & 0.0 & 0.1 & 2.2 & 42.3 \end{pmatrix}$$

$$B_{ij}(CC\ MC) = x_{i,cor,cuts}/x_{j,gen}(\%)$$

$$\begin{pmatrix} 44.5 & 6.0 & 6.0 & 2.0 & 0.9 \\ 6.5 & 68.7 & 9.2 & 2.3 & 1.3 \\ 0.0 & 5.1 & 60.8 & 13.3 & 2.5 \\ 0.0 & 0.0 & 4.6 & 51.1 & 17.7 \\ 0.0 & 0.0 & 0.0 & 1.8 & 12.4 \end{pmatrix}$$

$$C_{ij}(CC\ MC) = y_{i,cor,cuts}/y_{j,gen}(\%)$$

The off–diagonal elements of the unfolding matrix were usually less than 25% of the corresponding diagonal elements, indicating that migrations between bins were small. In cases where the data are poorly modeled by the MC or where migrations play a dominant rôle, the two methods are expected to yield significantly different results. The resulting differences were however found to be well below the statistical errors. They are included in the systematic uncertainties (cf. tables 3.2 and 3.3).

3.5.4 Systematic Uncertainties

In the following, we summarize the studies which were performed in order to estimate the systematic uncertainties. For the case of $d\sigma/dQ^2$, the dominant systematic uncertainties are detailed in tables 3.2 and 3.3. The remaining systematic errors were all below 5% and typically below 1%. Where appropriate, independent checks of systematic uncertainties have been calculated using the NC control sample. The systematic deviations observed in this sample agreed well with the values quoted below (see appendix A).

- In the detector simulation, the calorimeter energy scale was varied by $\pm 3\%$ ($\pm 5\%$ in the FCAL), corresponding to the level at which it is currently understood. Using the BAC it was checked that this variation also covers possible effects due to energy leakage out of the UCAL. Using the BAC energy deposits to correct jet energies in CC events increased $\not{P}_t$ by about 2% on average.

  Such an energy scale uncertainty gives rise to uncertainties in the cross section which are typically between 5% and 10%, but can be up to 30% in the highest Q^2 and y bins.

- The systematic uncertainty of the photoproduction background subtraction was estimated as the quadratic sum of its statistical error and an additional $\pm 50\%$ uncertainty which accounted for differences between E_t and $\not{P}_t/E_t$ spectra of photoproduction data and MC.

  The uncertainty of the background estimate mainly affected the lowest Q^2 and x bins. It was the dominant systematic error in the lowest x bin for e^+p reactions.

- The reconstruction of the kinematic variables was modified in the following way: in each bin[3] of $A = \not{P}_t$ or y the reconstructed values of $\not{P}_t$ and y were multiplied with $1/(1 + \langle \delta A \rangle)$ (cf. section 3.5.1), where δA was averaged over the weighted NC control sample events in this bin. This corresponded to correcting on average to the DA values as derived from the NC control sample (see appendix A). Q^2, x and y were calculated from the resulting values. This changed the measured cross sections by 10% or less, except in the lowest and highest Q^2 bins, where variations of up to 15% were seen.

- In order to check the simulation of the tracking, the combined acceptance of all cuts using tracking information was evaluated for the NC control sample, in each interval of Q^2, x and y, both for data and for simulated NC events. The data/MC ratio of these acceptances was found to be consistent with unity. In almost all bins the deviation was less than 3%, which was used as the overall systematic uncertainty.

- A one step Bayes unfolding was used instead of the bin–by–bin unfolding (cf. discussion in section 3.5.3). This variation caused uncertainties of $10 - 15\%$ in the lowest and the highest bins of Q^2, x and y (-25% in the highest y bin for e^+p).

- In the trigger simulation, the first level trigger thresholds were increased to a level where the measured trigger efficiencies were close to 100%. Except in the lowest Q^2 bins, where effects up to 4% were observed, this had a negligible effect indicating that the efficiency calculations were insensitive to the detailed shape of the trigger turn–on curves.

- In order to test the sensitivity to the details of the parton shower simulation, the MEPS model was used instead of the ARIADNE MC for calculating acceptance corrections and for unfolding. This affected the cross section results only negligibly.

  In addition, the selection cuts on $\not{P}_t$, $\Delta\phi$, the track requirements, and the cuts at low $\not{P}_t$ have been varied using the MEPS MC sample instead of the data, and the

[3] For $\not{P}_t$, the bin boundaries were 0–20–30–40–50–∞ GeV.

ARIADNE sets for acceptance corrections and unfolding. This tested whether the simulated shapes of the relevant distributions differ in the vicinities of these cuts.

Each of the cut variations changed the results by less than typically 1%, except the $\not{P}_t$ variation in the lowest x and Q^2 bins (up to 5%) and the track requirement (up to 3% in some bins).

- Different parton distribution functions (MRSD0 [21], MRSD$'_-$ [22], GRV [23] and CTEQ 2pM [24]) were used in the MC samples used for the acceptance corrections. The resulting variations were small and have been neglected.

The overall systematic uncertainty for each result (including ratios of cross sections and the W mass) was calculated by evaluating the variation of this result due to each of the modifications of the analysis procedure described above (including the luminosity uncertainties of $\pm 2.0\%$ for the e^+p sample and $\pm 3.0\%$ for the e^-p sample) and then separately summing in quadrature the positive and negative deviations.

3.6 Measurement of the Charged Current Cross Sections

The values of the cross section, σ_i, in bins of Q^2, for e^+p and e^-p data, are listed in tables 3.2 and 3.3 respectively. Also shown are the dominant systematic errors as described in section 3.5.4. The results are plotted in figure 3.9a, where the SM predictions are also shown.

The results for Q^2>200 GeV^2 in bins of x and y are given in tables 3.4 and 3.5. The differential CC cross sections are shown in figures 3.10a and 3.11a together with the corresponding SM predictions.

Figures 3.9b, 3.10b and 3.11b show the ratios $\sigma_{e^+p\to\overline{\nu}X}/\sigma_{e^-p\to\nu X}$ as functions of the respective variables. The curves again represent the SM predictions. The results are collected in table 3.6.

3.6.1 Discussion of the Results

- No significant deviations of the measured cross sections from the SM predictions are observed. This is quantified by the χ^2 values which are listed in table 3.7.

- The differential cross sections $d\sigma/dQ^2$ fall steeply with Q^2 (cf. figure 3.9), reflecting the influence of the W propagator, the decrease of the parton densities with increasing $x = Q^2/sy$, and the $(1-y)^2$ terms in the cross section. The differences between the e^+p and e^-p cross sections are due to the different x and y behavior (cf. discussion below).

- As can be seen from figure 3.10, at low x, $d\sigma/dx$ is about the same for e^+p and e^-p scattering. This reflects the fact that the cross sections become equal if valence quark distributions can be neglected and if $\overline{d}(x,Q^2) = \overline{u}(x,Q^2)$.

  The decrease of $d\sigma/dx$ with increasing x is more rapid for e^+p scattering than for e^-p scattering. This behavior is also expected: in e^+p reactions, scattering on valence quarks is reduced by the $(1-y)^2$ factor; in addition, the e^+ couples to $d(x,Q^2)$, which is suppressed at high x relative to $u(x,Q^2)$ which is relevant for e^-p scattering (cf. e.g. [25]).

The x dependence of the e^+p to the e^-p cross section ratio is illustrated by the ratios for $x<0.1$ and for $x>0.1$ (with $Q^2>200$ GeV^2):

$$\frac{\sigma_{e^+p\to\overline{\nu}X}}{\sigma_{e^-p\to\nu X}} = \begin{cases} 0.91\,^{+0.41}_{-0.27}\,[\mathrm{stat}] \pm 0.04\,[\mathrm{syst}] & \text{for} \quad 0<x<0.1 \\ \\ 0.26\,^{+0.14}_{-0.09}\,[\mathrm{stat}] \pm 0.01\,[\mathrm{syst}] & \text{for} \quad 0.1<x<1\,. \end{cases}$$

The corresponding SM predictions are 0.64 and 0.32. The measured ratios confirm the suppression of the e^+p CC cross section at high x.

The SM predictions for $d\sigma/dx$ have also been evaluated using different parton distribution functions (MRSD$'_-$, GRV, CTEQ 2pM). The largest differences have been observed between the sets MRSD$'_-$ and CTEQ 2pM for x between 0.01 and 0.1, where the cross section predicted by MRSD$'_-$ is up to 10% lower than the CTEQ 2pM values, both for e^+p and e^-p scattering. The MRSA, CTEQ 2pM and GRV predictions agree to better than 5%.

- The measured differential cross sections $d\sigma/dy$ agree with the theoretical predictions. The SM curves in figure 3.11 reveal that the expected shapes are very similar for e^+p and e^-p scattering, indicating that the relative contributions of the $(1-y)^2$ terms are about equal in both cases.

  As $y\to 1$, the cross section ratio e^+p/e^-p is given by $1/\left(\frac{u_v}{u_s+c}+1\right)$ (assuming $\overline{u}=u_s$ and $\overline{c}=c$, the indices v and s indicating valence and sea quark distributions, respectively). The fact that the prediction, corresponding to $u_v/(u_s+c)\approx 1$, is above the data for $y>0.4$, is only moderately significant in view of the large errors.

  At $y\to 0$, the cross section ratio e^+p/e^-p approaches $(d_v+S)/(u_v+S)$, where $S=d_s+u_s+s+c$ (assuming again that the quark and antiquark sea distributions are identical for each flavor).

In order to further study the influence of the $V\!-\!A$ helicity structure and the parton distributions, figure 3.12 shows $d\sigma/dy$ separately for $x<0.1$ (where sea quarks dominate the cross section) and for $x>0.1$ (where the valence contribution is larger). Here three equal size y bins are used.

For low x, the predicted y shapes are similar for e^+p and e^-p scattering, the differences being mainly due to residual valence contributions. The most significant deviation of the measured cross sections from the prediction is observed in the lowest y bin ($y<0.33$), where the measured $\sigma_{e^-p\to\nu X}$ is about two standard deviations below the SM prediction.

For $x>0.1$, both the e^+p and the e^-p cross sections decrease with increasing y. For e^-p, this can be attributed to residual sea quark contributions and to the W propagator which enters via the dependence of the average Q^2 on y. For e^+p scattering, the decrease of $d\sigma/dy$ with increasing y is even faster due to the $(1-y)^2$ term in the cross section. All measured values are compatible with the predictions, indicating that the slight deviations observed at $y\sim 0.3$ in the e^+p/e^-p ratios are due to the low–x data.

The integrated cross sections for $Q^2 > 200\,\mathrm{GeV}^2$ are obtained by summing the cross sections in the Q^2 bins of tables 3.2 and 3.3,[4] resulting in[5]

$$\begin{aligned}
\sigma_{e^+p\to\overline{\nu}X}(Q^2 > 200\,\mathrm{GeV}^2) &= 30.3\,^{+\ 5.5}_{-\ 4.2}\,[\mathrm{stat}]\,^{+1.6}_{-2.6}\,[\mathrm{syst}]\,\mathrm{pb} \\
\sigma_{e^-p\to\nu X}(Q^2 > 200\,\mathrm{GeV}^2) &= 54.7\,^{+15.9}_{-\ 9.8}\,[\mathrm{stat}]\,^{+2.8}_{-3.4}\,[\mathrm{syst}]\,\mathrm{pb}\ .
\end{aligned}$$

These measurements are compatible with the respective SM predictions of 32.3 pb and 65.8 pb. The e^+p/e^-p ratio is

$$\frac{\sigma_{e^+p\to\overline{\nu}X}}{\sigma_{e^-p\to\nu X}}(Q^2 > 200\,\mathrm{GeV}^2) = 0.55\,^{+0.16}_{-0.12}\,[\mathrm{stat}]\,^{+0.02}_{-0.03}\,[\mathrm{syst}]\ ,$$

in agreement with the SM prediction of 0.49.

3.7 Determination of the W mass

The Q^2 dependence of the CC cross section is largely determined by the propagator term $\mathcal{P}(M_W, Q^2)=[M_W^2/(M_W^2 + Q^2)]^2$. In order to determine the value of M_W, the differential cross section was factorized according to $d\sigma/dQ^2 = \mathcal{P}(M_W, Q^2)\cdot\Phi(Q^2)$. The function $\Phi(Q^2)$, containing the Q^2 dependence of the parton densities and couplings, was taken from the MC simulation, using the MRSA parton distributions. The procedure is made in such a way that first the $M_W = 1\ TeV$ MC Q^2 distribution is fitted by a polinomial function of $log_{10}(Q^2)$. Since the Q^2 values involved are negligible compared with $(M_W)^2 = (1\ TeV)^2$, $\Phi(Q^2)$ is fixed by this fit. If this procedure is adequate the SM 80.2 GeV Monte Carlo has to be fitted by the same polinomial function times the propagator term as above. The accuracy of the procedure is shown in figure 3.13. Once we are sure that the fit is able to follow the distribution for so large range in Q^2, it is justified to use the same method to compute the W mass. Thus, in the formulae above, $\phi(Q^2)$ remains unchanged and M_W is considered as a free parameter. A binned log–likelihood fit with M_W as the free parameter, applied simultaneously to the e^+p and e^-p data samples (see figure 3.14), yielded

$$M_W = 79\,^{+8}_{-7}\,[\mathrm{stat}]\,^{+4}_{-4}\,[\mathrm{syst}]\,\mathrm{GeV}\ ,$$

in agreement with the average value $M_W = 80.22 \pm 0.26\,\mathrm{GeV}$ [26] obtained from direct measurements of the W mass at $p\overline{p}$ colliders. As a matter of comparison the M_W values obtained using only e^+p or e^-p data are

$$M_W(e^+p) = \left(77\,^{+11}_{-9}\,[\mathrm{stat}]\,^{+4}_{-3}\,[\mathrm{syst}]\right)\ \mathrm{GeV}\ ,$$

$$M_W(e^-p) = \left(82\,^{+12}_{-10}\,[\mathrm{stat}]\,^{+5}_{-5}\,[\mathrm{syst}]\right)\ \mathrm{GeV}\ ,$$

The systematic uncertainty of M_W has been evaluated using the method described in section 3.5.4. The dominant contribution is the calorimeter energy scale.

[4] Summing the single cross sections implies using an average of the acceptances evaluated for the single bins, which is slightly different from the global acceptance quoted in table 3.1.

[5] The systematic uncertainties of the integrated e^+p and e^-p cross sections are correlated to about 75%.

3.8 Comparison of Neutral and Charged Current Cross Sections

In the Standard Model, electron-proton scattering processes occur via the exchange of gauge bosons ($\gamma, Z^0, W^\pm$). At long wavelengths (small momentum transfers), interactions of the massless photon dominate over the exchange of the heavy bosons. However, at the ep storage ring HERA, for the first time, scattering can be observed at sufficiently short wavelengths that the 'weak' and 'electromagnetic' scattering cross sections have comparable magnitudes. As discussed in chapter 1, the NC differential cross section $d^2\sigma/dxdQ^2$, neglecting radiative corrections, can be expressed as

$$\frac{d^2\sigma(e^\pm p)}{dxdQ^2} = \frac{2\pi\alpha^2}{xQ^4}[Y_+F_2(x,Q^2) \mp Y_-xF_3(x,Q^2) - y^2F_L(x,Q^2)],$$

$$Y_\pm = 1 \pm (1-y)^2$$

where x is the Bjorken variable, α is the fine structure constant, and $y = Q^2/sx$. The structure functions F_2 and F_3 can be expressed in leading order QCD as sums of the product of quark couplings and quark momentum distributions in the proton:

$$F_2 = \frac{1}{2}\sum_f xq_f^+[(V_f^L)^2 + (V_f^R)^2 + (A_f^L)^2 + (A_f^R)^2]$$

$$xF_3 = \sum_f xq_f^-[V_f^L A_f^L - V_f^R A_f^R]$$

where $xq_f^\pm = xq_f(x,Q^2) \pm x\overline{q}_f(x,Q^2)$ and $xq_f = xq_f(x,Q^2)(x\overline{q}_f(x,Q^2))$ are the quark (antiquark) momentum distributions. The functions V_f and A_f can be written:

$$V_f^{L,R} = e_f - (v_e \pm a_e)v_f P_Z(Q^2)$$

$$A_f^{L,R} = -(v_e \pm a_e)a_f P_Z(Q^2)$$

where the weak couplings $a_i = T_i^3$ and $v_i = T_i^3 - 2e_i sin^2\theta_W$ are functions of the weak isospin T_i^3 and the Weinberg angle θ_W, and P_Z is proportional to the ratio of Z and photon propagators:

$$P_Z = \frac{1}{4sin^2_{\theta_W}cos^2_{\theta_W}}\frac{Q^2}{Q^2+M_Z^2}$$

The relative contribution of the longitudinal structure function F_L is expected to remain below 1% in the kinematic range considered and will be neglected.

The differential cross sections for neutral and charged current interactions are shown in figure 3.15. The description of the measurement of the neutral current $d\sigma/dQ^2$ differential cross section [27] is collected in appendix B. The rapid fall of the NC cross section with increasing Q^2 is mainly due to the massless photon propagator. As it was discussed in the previous chapter, the Q^2- dependence of the CC cross section is sensitive to the mass of the weak boson, M_W, in the propagator. From the lowest bin in Q^2 to the highest, the ratio of the neutral and charged current cross sections decreases by two order of magnitude to around unity, thus demonstrating the equal strengths of the weak and electromagnetic forces at high Q^2 coming from the unification of electromagnetic and weak interactions at the (W,Z) mass scales.

cut description	e^+p		e^-p	
	data	MC(Q^2>200 GeV^2)	data	MC(Q^2>200 GeV^2)
$Q^2 > 200\,\mathrm{GeV}^2$ (MC only)	—	100 %	—	100 %
Trigger and preselection	6307	83.2%	1450	86.1%
$\not{P}_t > 11\,\mathrm{GeV}$	2981	80.0%	940	83.1%
$\lvert Z_{\mathrm{vtx}}\rvert < 45\,\mathrm{cm}$	1283	71.0%	500	74.7%
$\not{P}_t^{\mathrm{out}}/\not{P}_t > 0.6$	958	70.3%	301	73.9%
good track	741	68.2%	237	71.7%
$\lvert\Delta\phi\rvert < 1$	342	66.8%	113	70.3%
$y_{JB} < 0.8$	279	66.2%	98	69.2%
$\not{P}_t/E_t > 0.4$	208	65.0%	59	68.1%
$P_t^{\mathrm{tracks}}/\not{P}_t > 0.1$	87	63.0%	36	66.3%
Muon,timing,sparks	59	63.0%	30	66.3%
Visual scan (data only)	56	—	30	—

Table 3.1: Data reduction by the selection cuts described in section 3.3. The columns denoted "data" indicate the numbers of events remaining after applying the cuts. The "MC" columns show the cumulative selection efficiencies for the ARIADNE MC simulation.

e^+p	Q^2 [GeV^2]					
	200 – 437	437 – 955	955 – 2089	2089 – 4517	4517 – 10000	> 200
N_{evt}	8	15	12	14	7	56
$\langle Q^2 \rangle$ [GeV^2]	310	670	1450	3070	6510	1910
N_{bg}	1.2	0.2	0	0	0	1.4
ζ	0.38	0.58	0.70	0.76	0.71	0.62
ξ	0.76	0.72	0.73	0.76	0.79	1.0
σ^{exp} [pb]	6.1	8.7	5.8	6.3	3.4	30.3
$\Delta\sigma^{\mathrm{exp}}$ [stat] [pb]	$^{+3.0}_{-2.2}$	$^{+2.9}_{-2.3}$	$^{+2.2}_{-1.7}$	$^{+2.2}_{-1.7}$	$^{+1.8}_{-1.3}$	$^{+5.5}_{-4.2}$
$\Delta\sigma^{\mathrm{exp}}$ [syst] [pb]	$^{+1.3}_{-2.7}$	$^{+0.6}_{-0.6}$	$^{+0.3}_{-0.3}$	$^{+0.6}_{-0.3}$	$^{+0.7}_{-0.4}$	$^{+1.6}_{-2.6}$
σ^{th} [pb]	6.2	8.3	8.3	6.4	2.5	32.3
Systematic checks						
Check	$\Delta\sigma^{\mathrm{exp}}$ [%]					
E scale +3% (+5% in FCAL)	12.6	6.3	2.1	− 3.3	−10.8	2.1
E scale −3% (−5% in FCAL)	−18.7	− 3.0	− 3.3	3.8	13.6	− 2.0
Unfolding	− 0.9	1.1	1.7	− 1.5	13.8	− 1.0
Q^2, x, y reconstruction	−15.7	− 2.1	2.0	7.6	5.8	− 0.3
$N_{\mathrm{bg}} + \Delta N_{\mathrm{bg}}$	−36.2	− 3.4	0.0	0.0	0.0	− 7.3
$N_{\mathrm{bg}} - \Delta N_{\mathrm{bg}}$	16.1	1.5	0.0	0.0	0.0	3.3

Table 3.2: Cross sections for CC e^+p scattering in intervals of Q^2, and for $Q^2 > 200\,\mathrm{GeV}^2$. The rows denoted N_{evt}, $\langle Q^2 \rangle$, N_{bg}, ζ, ξ, σ^{exp}, and σ^{th} show the raw event numbers, the mean Q^2 according to the SM prediction, the estimated number of background events from photoproduction, the bin–by–bin acceptance corrections, the purities, the experimental cross sections, and the theoretical cross sections, respectively. For σ^{exp} the statistical errors $\Delta\sigma^{\mathrm{exp}}$ [stat] and systematic uncertainties $\Delta\sigma^{\mathrm{exp}}$ [syst] are quoted. The latter are calculated from the deviations resulting from the systematic studies described in the text (including the luminosity uncertainty of 3% and the overall uncertainty of 3% assigned to the efficiency of those selection cuts involving track quantities). The dominant contributions are detailed in the lower part of the table.

e^-p	Q^2 [GeV^2]						
	200 – 437	437 – 955	955 – 2089	2089 – 4517	4517 – 10000	10000 – 21877	> 200
N_{evt}	3	3	7	6	9	2	30
$\langle Q^2 \rangle$ [GeV^2]	310	670	1470	3140	6700	13900	3340
N_{bg}	0.3	0.1	0	0	0	0	0.4
ζ	0.39	0.56	0.74	0.78	0.74	0.59	0.66
ξ	0.74	0.73	0.70	0.74	0.80	0.83	1.0
σ^{exp} [pb]	8.4	6.3	11.6	9.4	14.9	4.1	54.7
$\Delta\sigma^{\mathrm{exp}}$ [stat] [pb]	$^{+8.2}_{-4.6}$	$^{+6.2}_{-3.4}$	$^{+6.3}_{-4.3}$	$^{+5.6}_{-3.7}$	$^{+6.8}_{-4.9}$	$^{+5.4}_{-2.7}$	$^{+15.9}_{-9.8}$
$\Delta\sigma^{\mathrm{exp}}$ [syst] [pb]	$^{+1.6}_{-2.7}$	$^{+0.6}_{-0.7}$	$^{+0.7}_{-0.7}$	$^{+0.8}_{-0.6}$	$^{+1.9}_{-1.6}$	$^{+1.5}_{-1.2}$	$^{+2.8}_{-2.9}$
σ^{th} [pb]	7.9	12.2	15.1	15.7	10.6	3.7	65.8
Systematic checks							
Check	$\Delta\sigma^{\mathrm{exp}}$ [%]						
E scale +3% (+5% in FCAL)	14.2	7.1	2.8	0.9	− 3.9	−24.9	2.0
E scale −3% (−5% in FCAL)	−10.9	− 7.8	− 2.6	1.2	9.5	26.9	1.1
Unfolding	− 0.5	0.0	− 3.3	− 4.2	− 9.3	24.3	− 2.1
Q^2, x, y reconstruction	−15.2	− 5.9	2.2	6.8	7.8	−14.5	− 1.0
$N_{\mathrm{bg}} + \Delta N_{\mathrm{bg}}$	−25.9	− 5.0	0.0	0.0	0.0	0.0	− 4.0
$N_{\mathrm{bg}} - \Delta N_{\mathrm{bg}}$	11.1	2.7	0.0	0.0	0.0	0.0	1.7

Table 3.3: Cross sections for CC e^-p scattering in intervals of Q^2, and for $Q^2 > 200\,\mathrm{GeV}^2$. The rows denoted N_{evt}, $\langle Q^2 \rangle$, N_{bg}, ζ, ξ, σ^{exp}, and σ^{th} show the raw event numbers, the mean Q^2 according to the SM prediction, the estimated number of background events from photoproduction, the bin–by–bin acceptance corrections, the purities, the experimental cross sections, and the theoretical cross sections, respectively. For σ^{exp} the statistical errors $\Delta\sigma^{\mathrm{exp}}$ [stat] and systematic uncertainties $\Delta\sigma^{\mathrm{exp}}$ [syst] are quoted. The latter are calculated from the deviations resulting from the systematic studies described in the text (including the luminosity uncertainty of 2% and the overall uncertainty of 3% assigned to the efficiency of those selection cuts involving track quantities). The dominant contributions are detailed in the lower part of the table.

e^+p	x					
	0.006 – 0.014	0.014 – 0.033	0.033 – 0.076	0.076 – 0.17	0.17 – 0.40	0.40 – 1.0
N_{evt}	3	20	11	13	9	0
$\langle x \rangle$	0.010	0.023	0.052	0.115	0.249	0.480
N_{bg}	1.4	0	0	0	0	0
ζ	0.41	0.78	0.79	0.68	0.48	0.18
ξ	0.68	0.72	0.77	0.82	0.88	0.84
σ^{exp} [pb]	1.3	8.7	4.7	6.5	6.4	0.0
$\Delta\sigma^{\text{exp}}$ [stat] [pb]	$^{+1.3}_{-0.7}$	$^{+2.4}_{-1.9}$	$^{+1.9}_{-1.4}$	$^{+2.3}_{-1.8}$	$^{+2.9}_{-2.1}$	$^{+3.5}_{-0.0}$
$\Delta\sigma^{\text{exp}}$ [syst] [pb]	$^{+1.0}_{-1.3}$	$^{+0.5}_{-0.7}$	$^{+0.4}_{-0.2}$	$^{+0.5}_{-0.7}$	$^{+0.8}_{-0.6}$	$^{+0.0}_{-0.0}$
σ^{th} [pb]	3.4	6.3	8.4	8.3	4.2	0.5

e^-p	x					
	0.006 – 0.014	0.014 – 0.033	0.033 – 0.076	0.076 – 0.17	0.17 – 0.40	0.40 – 1.0
N_{evt}	3	5	5	9	8	0
$\langle x \rangle$	0.010	0.024	0.053	0.119	0.256	0.489
N_{bg}	0.4	0	0	0	0	0
ζ	0.41	0.77	0.84	0.72	0.55	0.17
ξ	0.61	0.73	0.73	0.85	0.87	0.83
σ^{exp} [pb]	7.8	7.9	7.3	15.3	17.6	0.0
$\Delta\sigma^{\text{exp}}$ [stat] [pb]	$^{+7.6}_{-4.2}$	$^{+5.3}_{-3.4}$	$^{+4.9}_{-3.2}$	$^{+7.0}_{-5.1}$	$^{+8.7}_{-6.3}$	$^{+13.2}_{-0.0}$
$\Delta\sigma^{\text{exp}}$ [syst] [pb]	$^{+1.5}_{-2.5}$	$^{+0.7}_{-0.7}$	$^{+0.4}_{-0.5}$	$^{+1.1}_{-2.0}$	$^{+3.0}_{-1.6}$	$^{+0.0}_{-0.0}$
σ^{th} [pb]	4.2	8.4	14.9	19.2	14.8	2.7

Table 3.4: Cross sections for CC e^+p (top) and e^-p (bottom) scattering for $Q^2 > 200\,\text{GeV}^2$ in intervals of x. The rows denoted N_{evt}, $\langle x \rangle$, N_{bg}, ζ, ξ, σ^{exp}, and σ^{th} show the raw event numbers, the mean x according to the SM prediction, the estimated number of background events from photoproduction, the bin–by–bin acceptance corrections, the purities, the experimental cross sections, and the theoretical cross sections, respectively. For σ^{exp} the statistical errors $\Delta\sigma^{\text{exp}}$ [stat] and systematic uncertainties $\Delta\sigma^{\text{exp}}$ [syst] are quoted.

e^+p	y				
	0.0 – 0.2	0.2 – 0.4	0.4 – 0.6	0.6 – 0.8	0.8 – 1.0
N_{evt}	14	27	11	3	1
$\langle y \rangle$	0.101	0.293	0.496	0.695	0.895
N_{bg}	0	0.2	1.2	0	0
ζ	0.49	0.86	0.79	0.73	0.15
ξ	0.90	0.79	0.77	0.70	0.80
σ^{exp} [pb]	9.6	10.7	4.2	1.4	2.3
$\Delta\sigma^{\mathrm{exp}}$ [stat] [pb]	$^{+3.3}_{-2.5}$	$^{+2.5}_{-2.1}$	$^{+1.7}_{-1.3}$	$^{+1.4}_{-0.8}$	$^{+5.4}_{-1.9}$
$\Delta\sigma^{\mathrm{exp}}$ [syst] [pb]	$^{+0.5}_{-0.7}$	$^{+0.6}_{-0.5}$	$^{+0.6}_{-1.0}$	$^{+0.2}_{-0.1}$	$^{+0.6}_{-1.1}$
σ^{th} [pb]	11.8	8.3	5.4	3.7	3.0

e^-p	y				
	0.0 – 0.2	0.2 – 0.4	0.4 – 0.6	0.6 – 0.8	0.8 – 1.0
N_{evt}	6	5	11	5	3
$\langle y \rangle$	0.101	0.293	0.496	0.696	0.895
N_{bg}	0	0.1	0.3	0	0
ζ	0.51	0.91	0.81	0.77	0.20
ξ	0.92	0.79	0.81	0.74	0.90
σ^{exp} [pb]	14.4	6.6	16.2	7.9	19.0
$\Delta\sigma^{\mathrm{exp}}$ [stat] [pb]	$^{+8.6}_{-5.7}$	$^{+4.4}_{-2.9}$	$^{+6.4}_{-4.9}$	$^{+5.2}_{-3.4}$	$^{+18.5}_{-10.3}$
$\Delta\sigma^{\mathrm{exp}}$ [syst] [pb]	$^{+1.2}_{-1.6}$	$^{+0.3}_{-0.4}$	$^{+1.3}_{-1.4}$	$^{+0.8}_{-0.5}$	$^{+4.4}_{-7.6}$
σ^{th} [pb]	23.7	15.6	11.0	8.7	6.9

Table 3.5: Cross sections for CC e^+p (top) and e^-p (bottom) scattering for $Q^2 > 200\,\mathrm{GeV}^2$ in intervals of y. The rows denoted N_{evt}, $\langle y \rangle$, N_{bg}, ζ, ξ, σ^{exp}, and σ^{th} show the raw event numbers, the mean y according to the SM prediction, the estimated number of background events from photoproduction, the bin–by–bin acceptance corrections, the purities, the experimental cross sections, and the theoretical cross sections, respectively. For σ^{exp} the statistical errors $\Delta\sigma^{\mathrm{exp}}$ [stat] and systematic uncertainties $\Delta\sigma^{\mathrm{exp}}$ [syst] are quoted.

	Q^2		x		y	
Interval	$\frac{\sigma_{e^+p}}{\sigma_{e^-p}}$	$\frac{\sigma_{e^+p}}{\sigma_{e^-p}}\Big\|_{\mathrm{MC}}$	$\frac{\sigma_{e^+p}}{\sigma_{e^-p}}$	$\frac{\sigma_{e^+p}}{\sigma_{e^-p}}\Big\|_{\mathrm{MC}}$	$\frac{\sigma_{e^+p}}{\sigma_{e^-p}}$	$\frac{\sigma_{e^+p}}{\sigma_{e^-p}}\Big\|_{\mathrm{MC}}$
1	$0.7\,^{+1.2}_{-0.4}$	0.78	$0.2\,^{+0.5}_{-0.1}$	0.81	$0.7\,^{+0.6}_{-0.3}$	0.50
2	$1.4\,^{+2.0}_{-0.7}$	0.68	$1.1\,^{+1.0}_{-0.5}$	0.75	$1.6\,^{+1.3}_{-0.7}$	0.53
3	$0.5\,^{+0.4}_{-0.2}$	0.55	$0.6\,^{+0.6}_{-0.3}$	0.56	$0.3\,^{+0.2}_{-0.1}$	0.49
4	$0.7\,^{+0.6}_{-0.3}$	0.41	$0.4\,^{+0.3}_{-0.2}$	0.43	$0.2\,^{+0.3}_{-0.1}$	0.43
5	$0.2\,^{+0.2}_{-0.1}$	0.24	$0.4\,^{+0.3}_{-0.2}$	0.28	$0.1\,^{+0.5}_{-0.1}$	0.43

Table 3.6: Cross section ratios e^+p/e^-p in bins of Q^2, x and y. The bins are the same as in tables 2 to 5. For the measured cross section ratios the statistical errors are quoted. The SM predictions for the cross section ratios are also included.

Distribution	χ^2	N_{DOF}	$p(\chi^2, N_{\mathrm{DOF}})$
$d\sigma/dQ^2$ (e^+p)	1.9	5	0.86
$d\sigma/dQ^2$ (e^-p)	3.2	6	0.78
$d\sigma/dx$ (e^+p)	9.9	5	0.08
$d\sigma/dx$ (e^-p)	3.7	5	0.59
$d\sigma/dy$ (e^+p)	5.0	5	0.42
$d\sigma/dy$ (e^-p)	7.8	5	0.17

Table 3.7: Quality of agreement between experimental results and SM predictions: for the various differential cross sections χ^2, N_{DOF}, and $p(\chi^2, N_{\mathrm{DOF}})$ denote the χ^2 value calculated using statistical errors only, the number of degrees of freedom, and the corresponding χ^2–probability.

Δy	$\sigma_{e^+}(y)(x<0.1)$	SM (e^+)	$\sigma_{e^-}(y)(x<0.1)$	SM (e^-)
$0.0-0.33$	$12.0^{+3.0+0.8}_{-2.4-1.0}$	9.8	$3.6^{+4.7+0.2}_{-2.3-0.3}$	13.7
$0.33-0.66$	$6.5^{+2.1+0.8}_{-1.7-1.2}$	7.5	$13.2^{+6.5+1.3}_{-4.7-1.4}$	11.9
$0.66-1.0$	$2.4^{+2.3+0.3}_{-1.3-0.4}$	4.9	$8.8^{+8.6+0.5}_{-4.8-1.0}$	9.2

Table 3.8: Cross sections for e^+p and e^-p, in intervals of y for x less than 0.1, compared with the SM predictions.

Δy	$\sigma_{e^+}(y)(x>0.1)$	SM (e^+)	$\sigma_{e^-}(y)(x>0.1)$	SM (e^-)
$0.0-0.33$	$8.0^{+3.0+0.5}_{-2.3-0.4}$	8.0	$16.7^{+9.0+1.0}_{-6.2-0.8}$	21.0
$0.33-0.66$	$0.8^{+1.0+0.2}_{-0.5-0.1}$	1.5	$9.4^{+5.1+1.6}_{-3.5-0.8}$	6.8
$0.66-1.0$	$0.0^{+3.9}_{-0.0}$	0.4	$4.5^{+4.4+1.5}_{-2.5-1.3}$	3.3

Table 3.9: Cross sections for e^+p and e^-p, in intervals of y for x greater than 0.1, compared with the SM predictions.

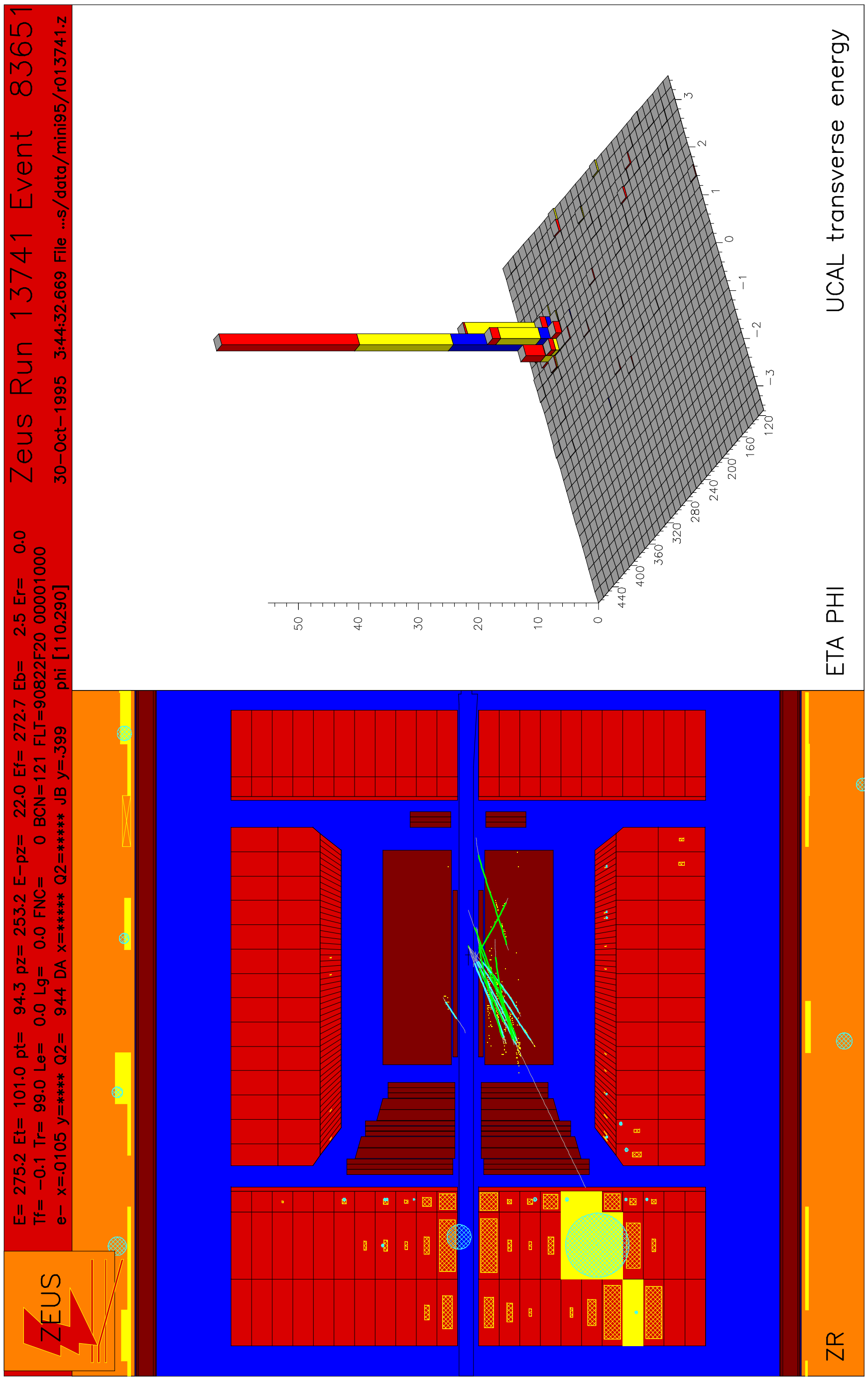

Figure 3.1: Event picture for one selected CC candidate. The outgoing neutrino leaves the calorimeter undetected.

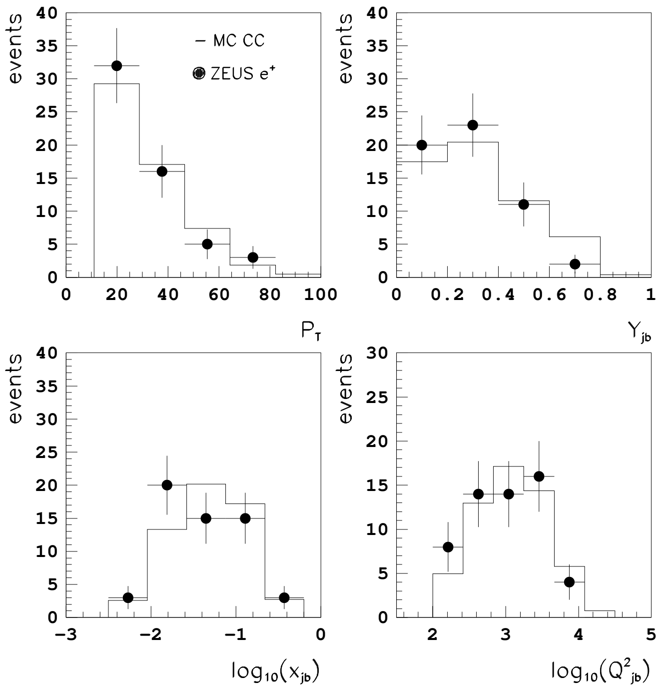

Figure 3.2: Distributions of the measured kinematic variables for the selected e^+p charged current candidates compared with Monte Carlo predictions normalized to the number of events observed in the data.

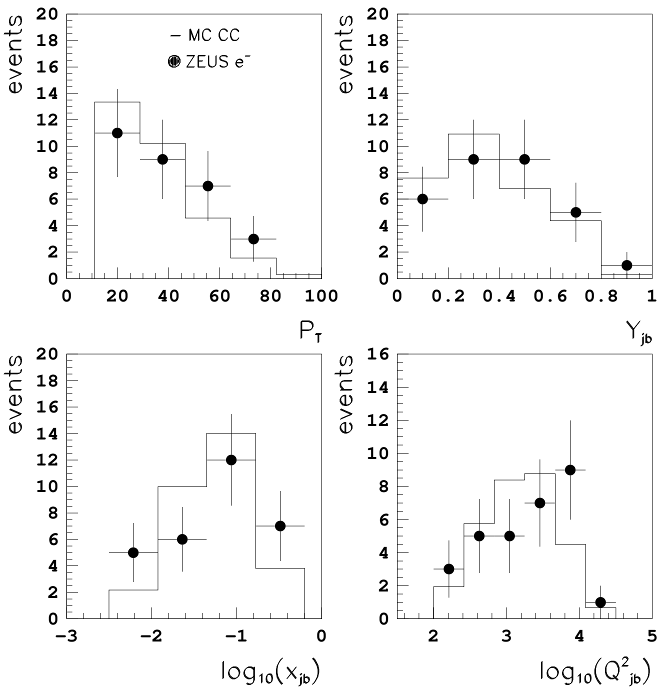

Figure 3.3: Distributions of the measured kinematic variables for the selected e^-p charged current candidates compared with Monte Carlo predictions normalized to the number of events observed in the data.

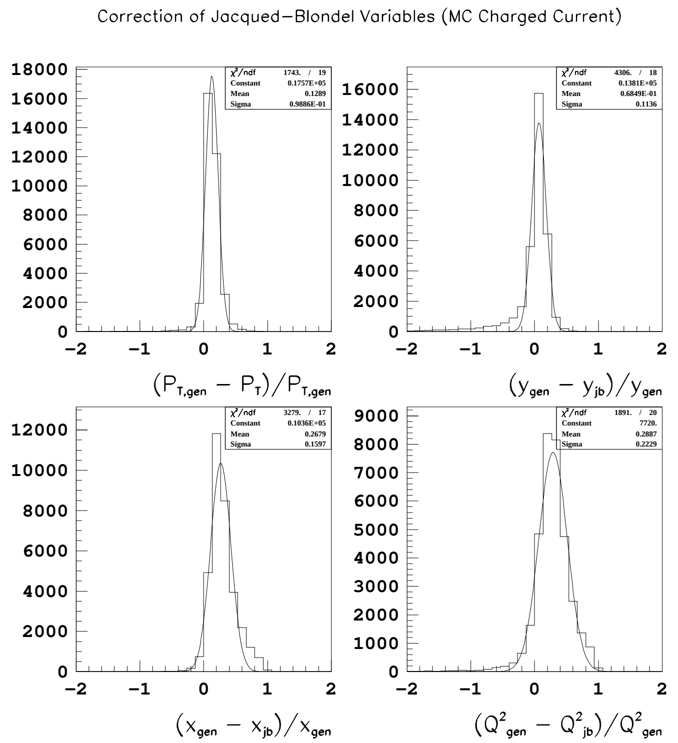

Figure 3.4: Reconstruction of the kinematic variables as computed using the Jacquet-Blondel method compared with the true generated variables.

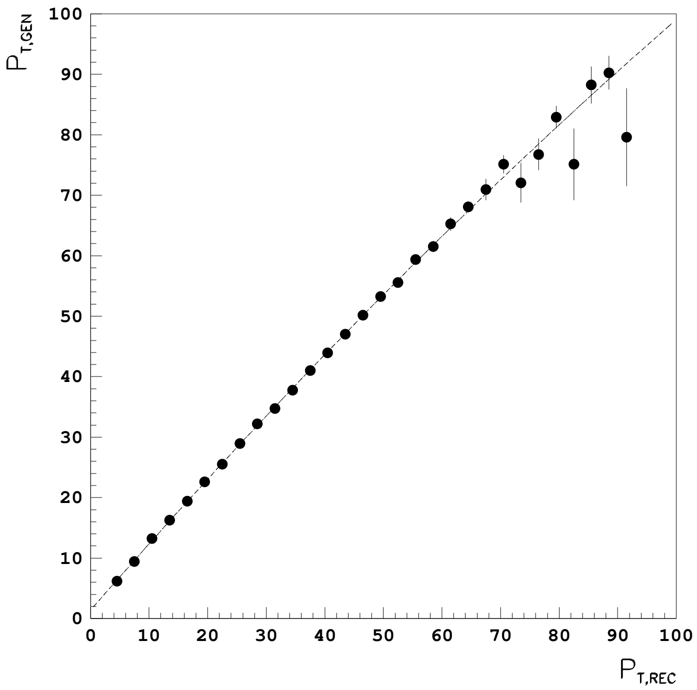

Figure 3.5: Correlation between the missing transverse momentum measured in the calorimeter and the true transverse momentum as computed from the true Q^2 and y values.

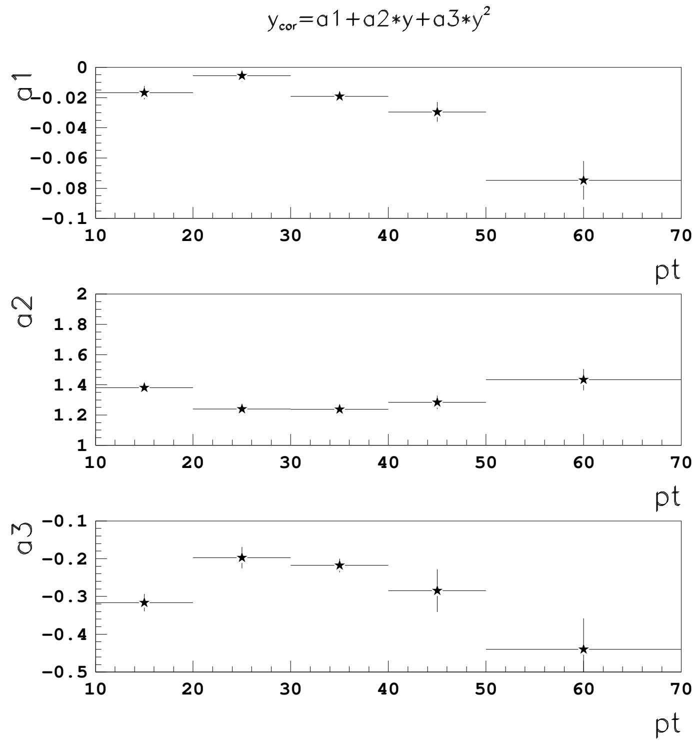

Figure 3.6: Correction of the y_{jb}-variable in different bins of the measured missing transverse momentum. The correction was designed as a polinomial function where the dependence on the missing transverse momentum was included in the coefficients.

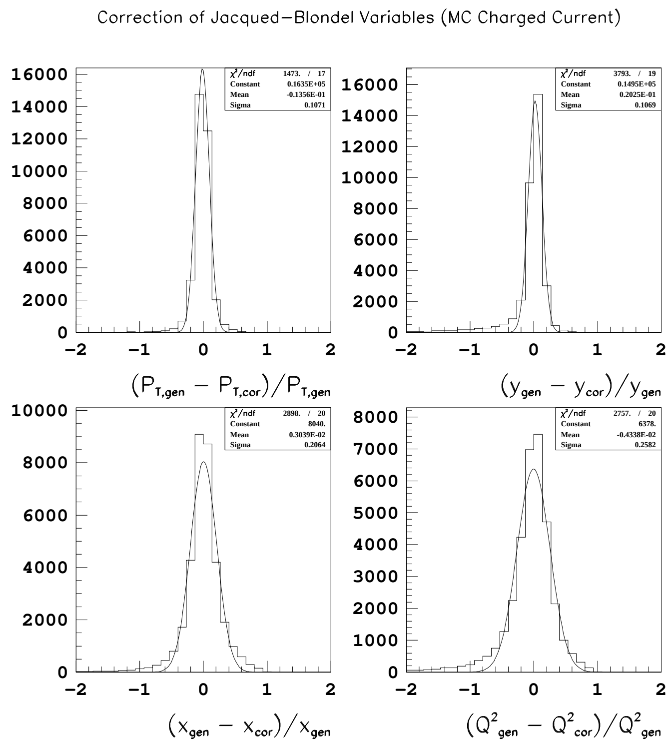

Figure 3.7: Reconstruction of the kinematic variables after applying the correction procedure. The Q^2 and x corrected values were computed from the corrected P_t and y.

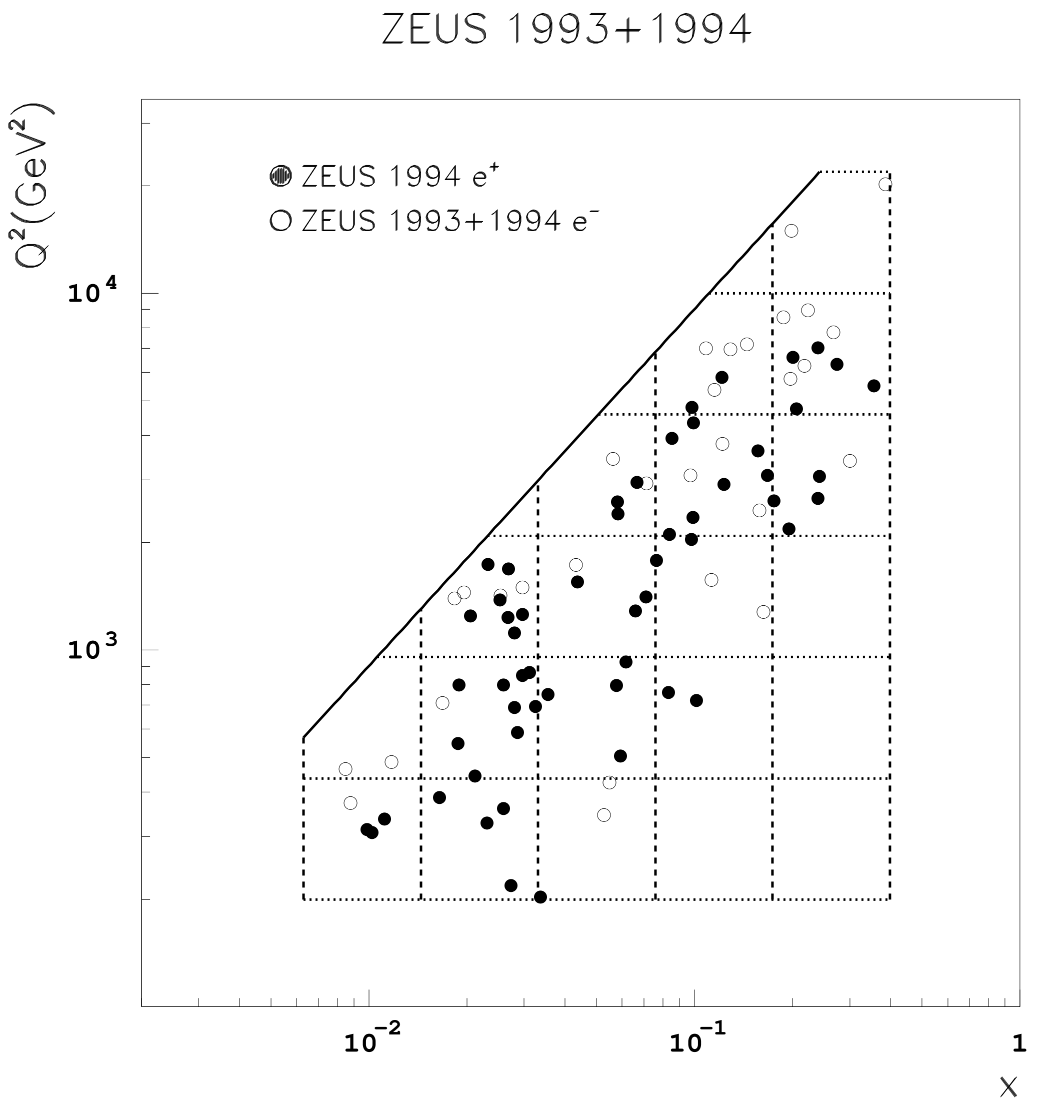

Figure 3.8: Distribution of events in the (x, Q^2) plane. The filled (open) circles indicate the selected e^+p (e^-p) CC events in a sample with integrated luminosity of $2.93\,\mathrm{pb}^{-1}$ ($0.82\,\mathrm{pb}^{-1}$). The horizontal lines of the grid show the Q^2, the vertical lines the x bins used for the analysis. The solid diagonal line indicates the kinematic limit $y = 1$.

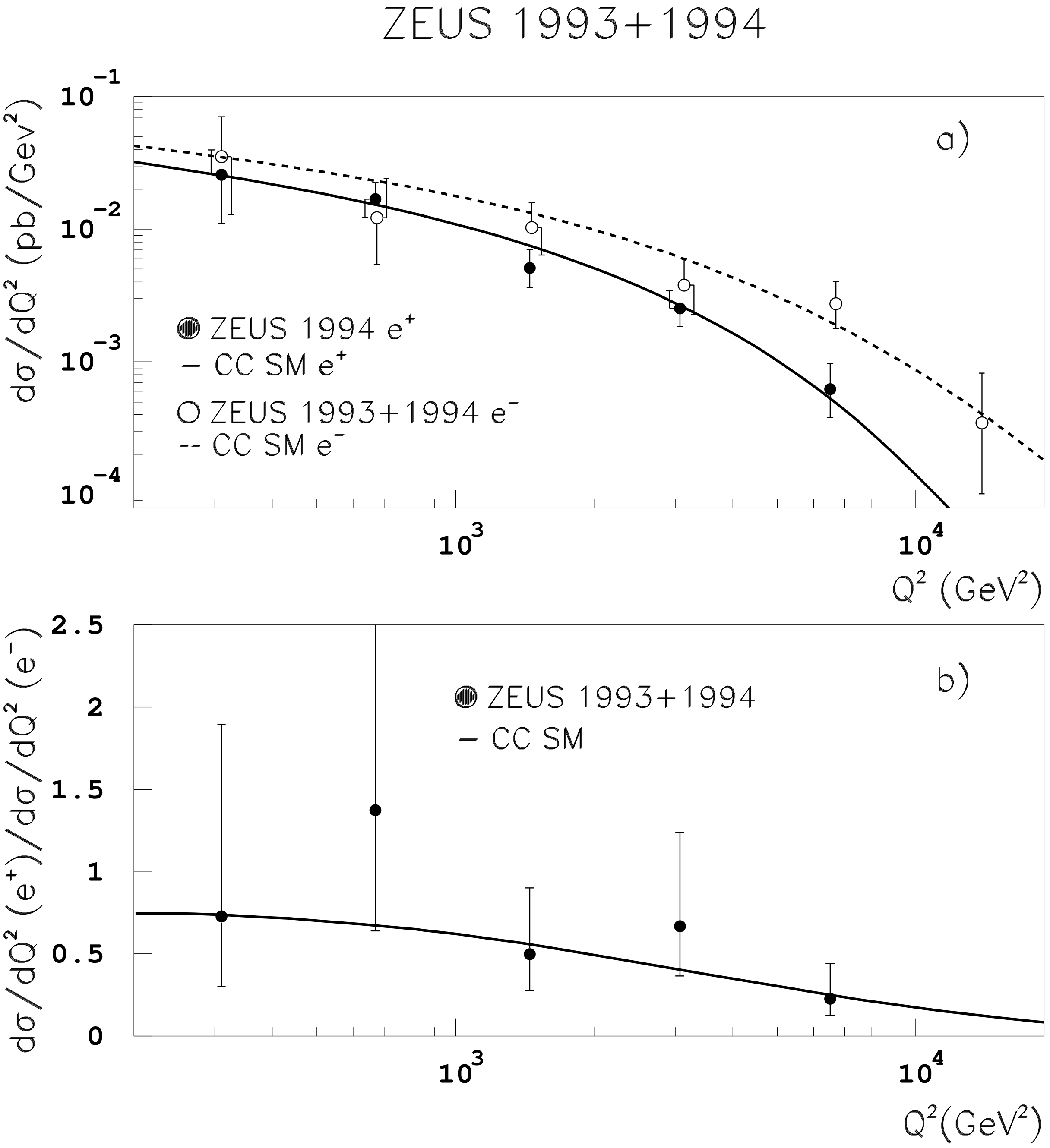

Figure 3.9: Differential CC cross section versus Q^2. In a), the filled (open) dots and the solid (dashed) curve represent the measured values and the Standard Model (SM) prediction of $d\sigma/dQ^2$ for e^+p (e^-p) collisions. Plot b) shows $(d\sigma_{e^+p\to\overline{\nu}X}/dQ^2)/(d\sigma_{e^-p\to\nu X}/dQ^2)$. The error bars indicate the statistical and systematic uncertainties combined in quadrature. The horizontal position of the points is given by the generator level Q^2 average of the MC events in each bin.

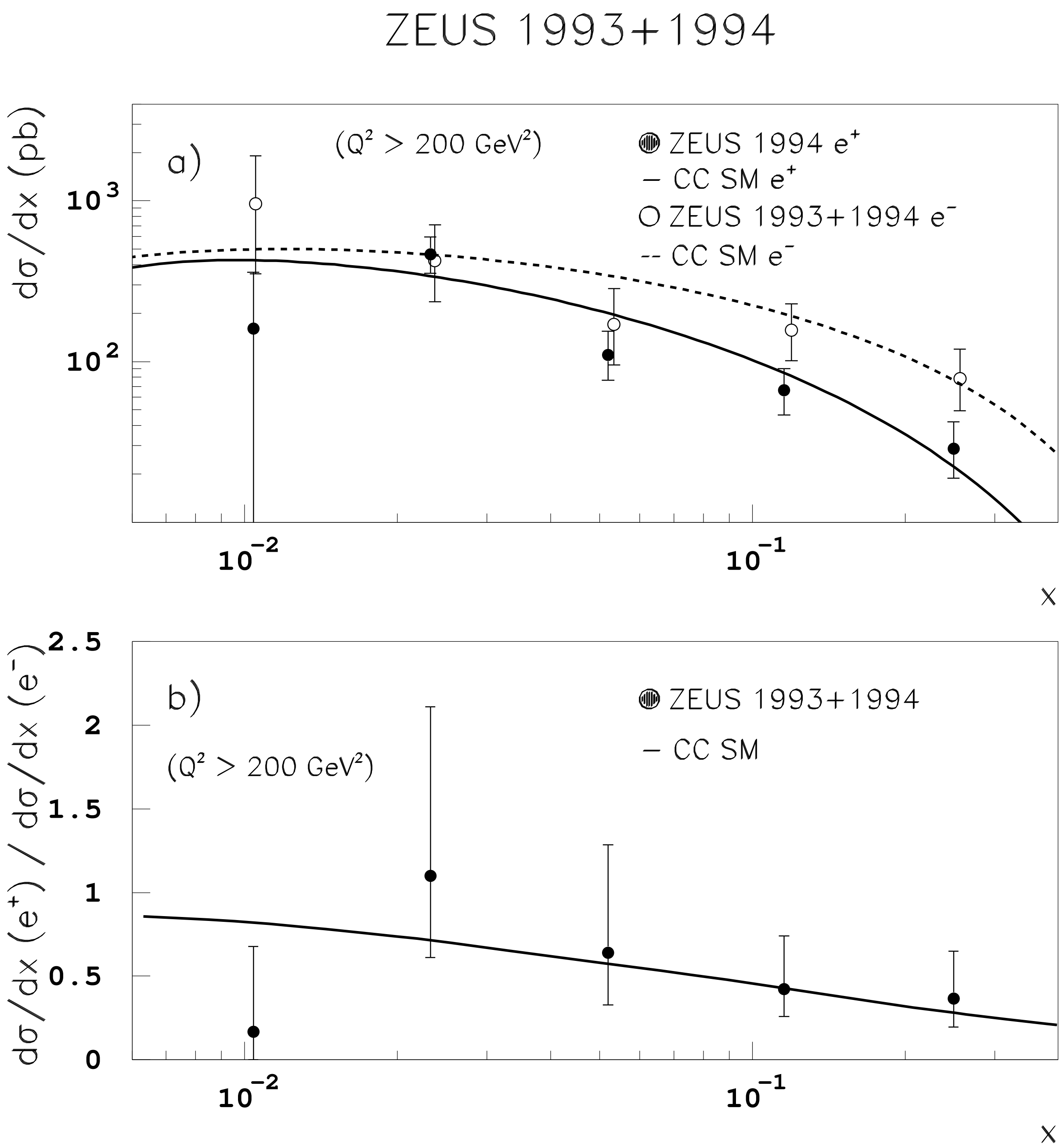

Figure 3.10: Differential CC cross section versus x for $Q^2 > 200\,\mathrm{GeV}^2$. In a), the filled (open) dots and the solid (dashed) curve represent the measured values and the Standard Model (SM) prediction of $d\sigma/dx$ for e^+p (e^-p) collisions. Plot b) shows $(d\sigma_{e^+p\to\overline{\nu}X}/dx)/(d\sigma_{e^-p\to\nu X}/dx)$. The error bars indicate the statistical and systematic uncertainties combined in quadrature. The horizontal position of the points is given by the generator level x average of the MC events in each bin.

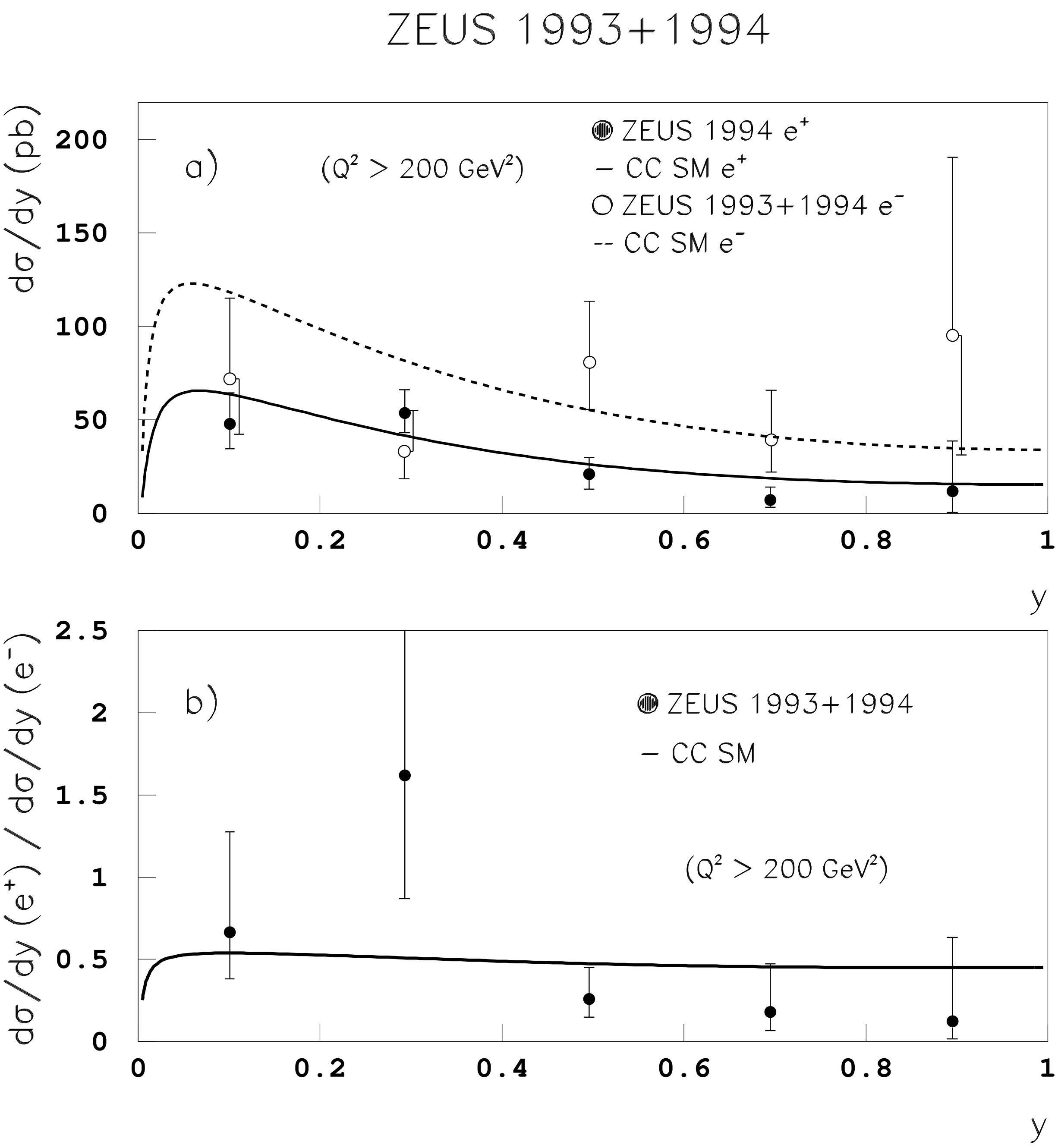

Figure 3.11: Differential CC cross section versus y for $Q^2 > 200\,\mathrm{GeV}^2$. In a), the filled (open) dots and the solid (dashed) curve represent the measured values and the Standard Model (SM) prediction of $d\sigma/dy$ for e^+p (e^-p) collisions. Plot b) shows $(d\sigma_{e^+p\to\overline{\nu}X}/dy)/(d\sigma_{e^-p\to\nu X}/dy)$. The error bars indicate the statistical and systematic uncertainties combined in quadrature. The horizontal position of the points is given by the generator level y average of the MC events in each bin.

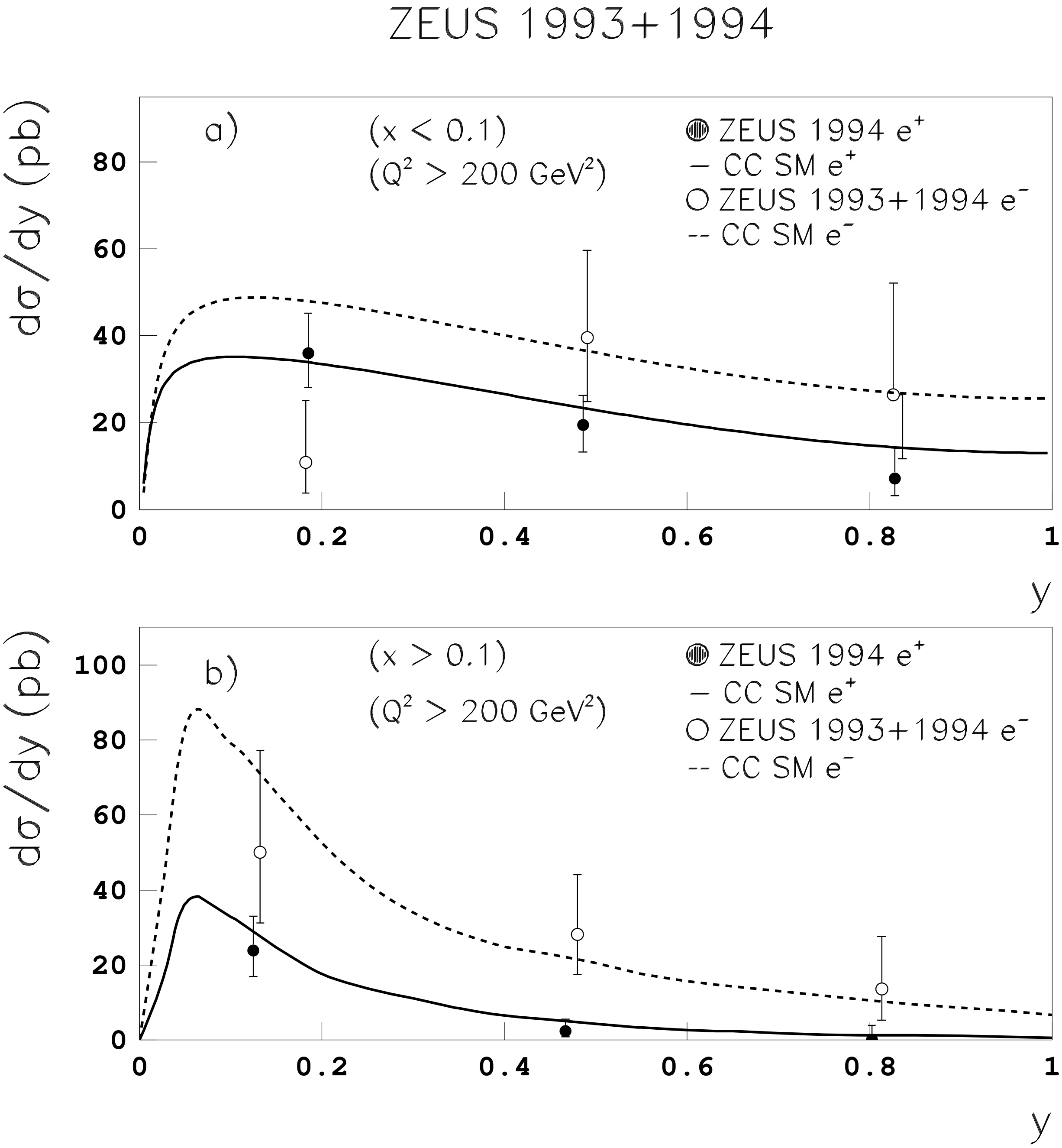

Figure 3.12: Differential CC cross section versus y for $Q^2 > 200\,\mathrm{GeV}^2$, a) for $x < 0.1$ and b) for $x > 0.1$. The filled (open) dots and the solid (dashed) curves represent the measured values and the Standard Model (SM) prediction of $d\sigma/d\,y$ for e^+p (e^-p) collisions. The error bars indicate the statistical and systematic uncertainties combined in quadrature. The horizontal position of the points is given by the generator level y average of the MC events in each bin.

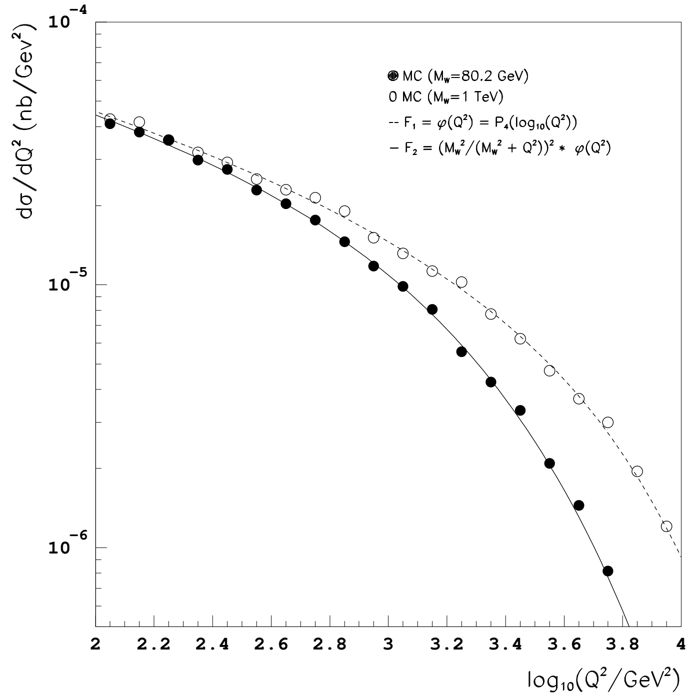

Figure 3.13: Description of the procedure used to determine the mass of the boson W from the shape of the Q^2 differential cross section in charged current interactions.

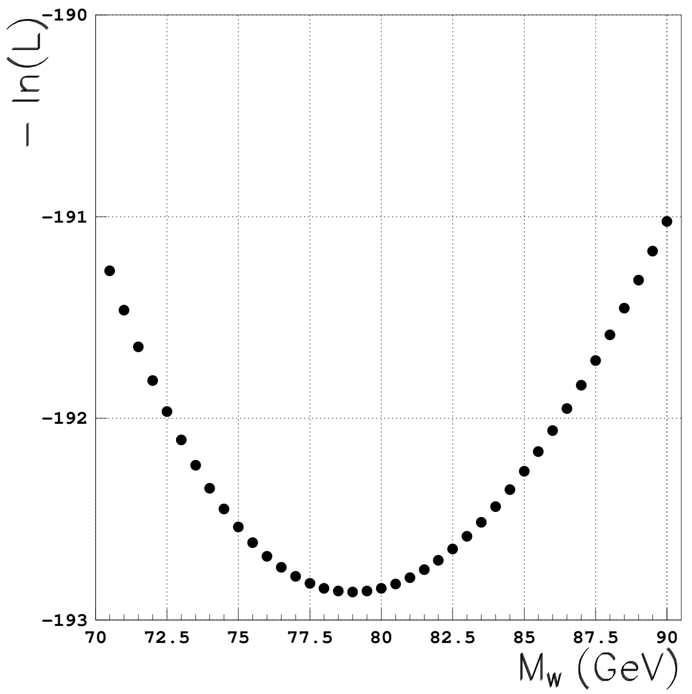

Figure 3.14: Combined maximum likelihood fit applied simultaneously to e^+p and e^-p charged current Q^2-differential cross sections in order to measure the W mass from the propagator term. Since (-L) was computed the x-coordinate of the observed minimum provides the M_W measurement.

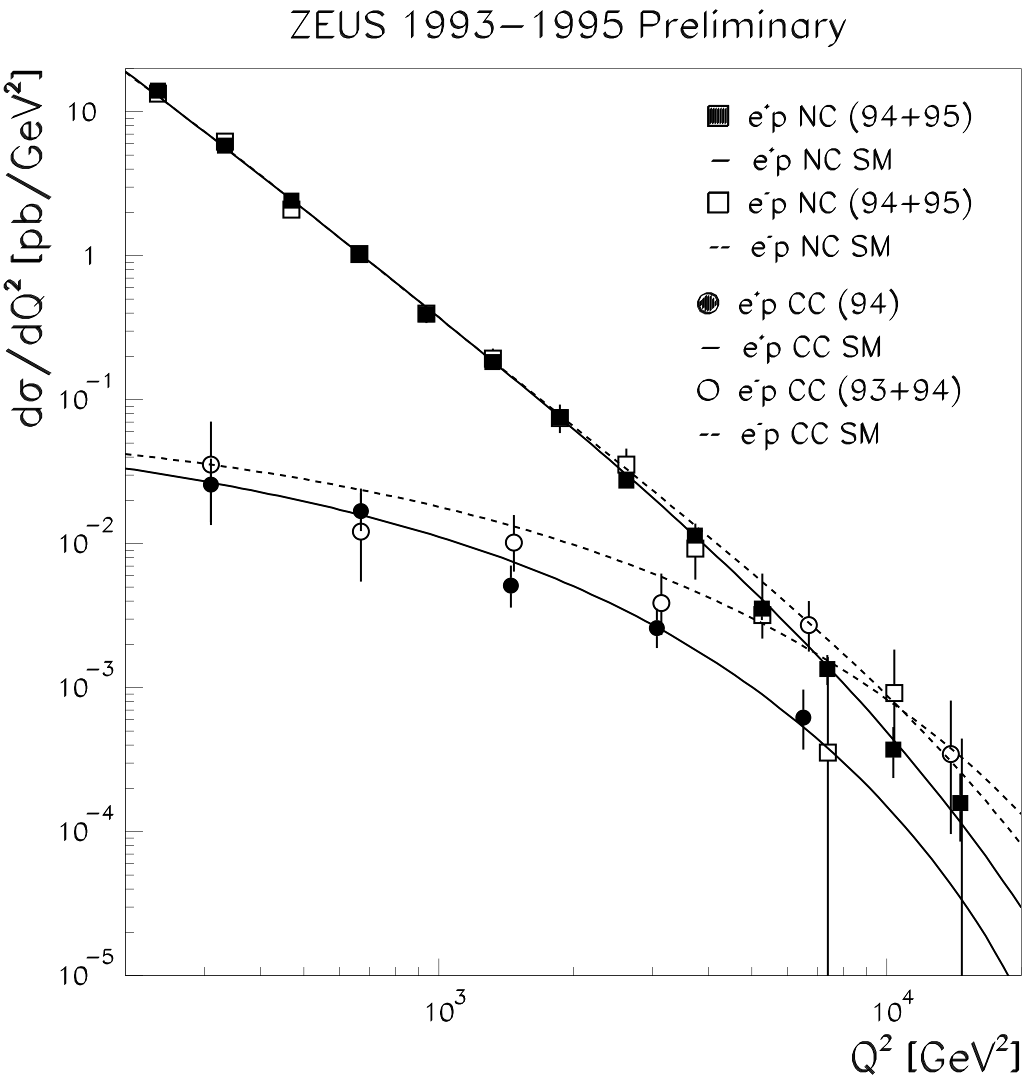

Figure 3.15: Comparison of the measured $d\sigma/dQ^2$ differential cross sections for e^+p and e^-p charged and neutral current interactions.

Bibliography

[1] CDHS Collaboration, H.Abramowicz et al., Z. Phys. **C25**(1984)29;
CHARM Collaboration, J.V.Allaby et al., Phys. Lett. **B197**(1987)281;
CDHSW Collaboration, J.P.Berge et al., Z. Phys. **C49**(1991)187;
CCFR Collaboration, E.Oltman et al., Z. Phys. **C53**(1992)51;
BEBC WA21 Collaboration, G.T.Jones et al., Z. Phys. **C62**(1994)575.

[2] H1 Collaboration, T.Ahmed et al., Phys. Lett. **B324**(1994)241.

[3] ZEUS Collaboration, M.Derrick et al., Phys. Rev. Lett. **75**(1995)1006.

[4] H1 Collaboration, S.Aid et al., Z. Phys. **C67**(1995)565.

[5] H1 Collaboration, S.Aid et al., DESY 96–046 (1996).

[6] CDF Collaboration, F.Abe et al., Phys. Rev. Lett. **75**(1995)11;
CDF Collaboration, F.Abe et al., Phys. Rev. **D52**(1995)4784;
D0 Collaboration, S.Abachi et al., Proc. Topical Workshop on Proton–Antiproton Collider Physics, Tsukuba, Japan (1993);
UA2 Collaboration, J.Alitti et al., Phys. Lett **B241**(1990)150.

[7] LEPTO 6.3: G.Ingelman, Proc. 1991 Workshop on Physics at HERA, ed. W.Buchmüller and G.Ingelman (DESY, Hamburg, 1992), Vol. 3, p.1366.

[8] HERACLES 4.4: A.Kwiatkowski, H.Spiesberger and H.J.Möhring, Proc. 1991 Workshop on Physics at HERA, ed. W.Buchmüller and G.Ingelman (DESY, Hamburg, 1992), Vol. 3, p.1294.

[9] DJANGO 6.1: G.Schuler and H.Spiesberger, Proc. 1991 Workshop on Physics at HERA, ed. W.Buchmüller and G.Ingelman (DESY, Hamburg, 1992), Vol. 3, p.1419.

[10] A.D.Martin, R.G.Roberts, W.J.Stirling, Phys. Rev. **D50**(1994)6734.

[11] ARIADNE 4.06: L.Lönnblad, LU TP–89–10;
L.Lönnblad, Comp. Phys. Comm. **71**(1992)15.

[12] PYTHIA 5.7 and JETSET 7.4: T.Sjöstrand, CERN–TH 7112–93 (1994);
T.Sjöstrand, LU–TP–95–20 (1995).

[13] HERWIG 5.8: B.R.Webber, Proc. 1991 Workshop on Physics at HERA, ed. W.Buchmüller and G.Ingelman (DESY, Hamburg, 1992), Vol. 3, p.1363.

[14] AROMA 2.1: G.Ingelman and G.Schuler, Proc. 1991 Workshop on Physics at HERA, ed. W.Buchmüller and G.Ingelman (DESY, Hamburg, 1992), Vol. 3, p.1346.

[15] R.Brun et al., CERN DD/EE–84–1 (1987).

[16] The ZEUS Detector, Status Report 1993, DESY (1993).

[17] F.Jacquet and A.Blondel, Proceedings of the study for an *ep* facility for Europe, DESY 79–48 (1979), p.391.

[18] H.Abramowicz, A.Caldwell, R.Sinkus, Nucl. Inst. Meth. **A365**(1995)508.

[19] S.Bentvelsen, J.Engelen, P.Kooijman, Proc. 1991 Workshop on Physics at HERA, ed. W.Buchmüller and G.Ingelman (DESY, Hamburg, 1992), Vol. 1, p.23.

[20] G.D'Agostini, DESY 94–099 (1994).

[21] A.D.Martin, R.G.Roberts, W.J.Stirling, Phys. Rev. **D47**(1993)867.

[22] A.D.Martin, R.G.Roberts, W.J.Stirling, Phys. Lett. **B306**(1993)147;
erratum in Phys. Lett. **B309**(1993)492.

[23] M.Glück, E.Reya, A.Vogt, Z. Phys. **C53**(1992)127.

[24] CTEQ Collaboration, J.Botts et al., Phys. Lett. **B304**(1993)159.

[25] BEBC WA21 Collaboration, G.T.Jones et al., Z. Phys. **C62**(1994)601.

[26] L.Montanet et al., Phys. Rev. **D50**(1994)1173.

[27] Zeus Collaboration. Results presented in La Thuile '96 and Moriond '96 Conferences.

Chapter 4

Measurement of Jet Shapes in High Q^2 DIS at HERA

4.1 Introduction

The internal structure of a jet is expected to depend mainly on the type of primary parton, quark or gluon, from which it originated and to a lesser extent on the particular hard scattering process. For jet cone algorithms [1, 2] a useful representation of the jet's internal structure is given by the jet shape [3]. For jets with sufficiently high-transverse energy (E_T^{jet}), the jet shape is expected to be driven mainly by gluon emission off the primary parton and, therefore, gluon jets should be broader than quark jets as a consequence of the larger gluon-gluon than quark-gluon coupling strength. This expectation can be tested by comparing measurements of the jet shape in different reactions.

Measurements of the jet shape have been made in $\bar{p}p$ collisions at $\sqrt{s} = 1.8$ TeV (TEVATRON) using only charged particles [4] and both neutral and charged particles [5], where a qualitative agreement with $O(\alpha_S^3)$ QCD calculations [3, 6] was found. Similar measurements have been made in e^+e^- interactions at LEP1 using both neutral and charged particles [7] and found to be well described by leading-logarithm parton-shower Monte Carlo calculations. It was observed [7] that the jets in e^+e^- are significantly narrower than those in $\bar{p}p$ and most of this difference was ascribed to the different mixtures of quark and gluon jets in these two environments.

Measurements of the jet shapes in quasi-real photon proton collisions at HERA have been presented [8] and found to be well described by leading-logarithm parton-shower Monte Carlo calculations except for the inclusive production of forward low-E_T jets. $O(\alpha_S^3)$ QCD calculations [9] are able to describe the measured jet shapes by adjusting the minimum distance in the pseudorapidity (η) - azimuth (φ) plane at which two partons are no longer merged into a single jet.

In this chapter, first measurements of the jet shapes in neutral and charged-current DIS at $Q^2 > 100$ GeV^2 are presented using the data collected by ZEUS during the 1995-1996 running period. Jets are searched for with an iterative cone algorithm [1, 2] in the $\eta - \varphi$ plane of the laboratory frame using a radius $R = 1$, and are selected with $E_T^{jet} > 14$ GeV and jet pseudorapidity in the range $-1 < \eta^{jet} < 2$. The jet shape is measured using the ZEUS calorimeter and corrected to the hadron level. The measurements are presented as a function of E_T^{jet} and η^{jet}. The measured jet shapes are compared to similar measurements in other reactions and to leading-logarithm parton-shower Monte Carlo calculations.

4.2 Jet Search and Definition of the Jet Shape

An iterative cone algorithm in the $\eta - \phi$ plane [1, 2] (PUCELL) is used to reconstruct jets from the energy measured in the UCAL cells for both data and simulated events, and also from the final state hadrons for simulated events.

The procedure is explained in detail for the jet reconstruction from the UCAL cell energies (*cal* jets). In a first step, each UCAL cell with a transverse energy in excess of 300 MeV is considered as a seed for the search. Their corresponding $\eta - \phi$ values are obtained from the unit vectors joining the vertex of the interaction and the geometric centres of the cells. The seeds are then combined into preclusters starting from that with highest transverse energy if their distance in the $\eta - \phi$ plane, $\sqrt{(\Delta\eta)^2 + (\Delta\phi)^2}$, is smaller than 1 unit. The axis of the precluster is defined according to the Snowmass convention [2], where $\eta^{precluster}$ ($\phi^{precluster}$) is the transverse-energy weighted mean pseudorapidity (azimuth) of all the seeds belonging to that precluster.

In a second step, a cone of radius $R = 1$ is drawn around each precluster and all the UCAL cells within that cone are combined to form a cluster. The axis of the cluster is defined according to the same prescription as for the preclusters but including all the UCAL cells belonging to that cluster. A new cone of $R = 1$ is then drawn around the axis of the resulting cluster. All cells with geometric centres inside the cone are used to recalculate a new cluster axis. The procedure is iterated until the content of the cluster remains unchanged. In a third step, the energy sharing of overlapping clusters is considered. Two clusters are merged if the overlapping energy exceeds 75% of the total energy of the cluster with the lower energy; otherwise two different clusters are formed and the common cells are assigned to the nearest cluster. Finally, a cluster is called a jet if the transverse energy as measured by the UCAL, $E_{T,cal}^{jet}$, exceeds 10 GeV. The angular variables associated with the *cal* jets are denoted by η_{cal}^{jet} and ϕ_{cal}^{jet}. In addition, in the present analysis only jets with η_{cal}^{jet} in the range $-1 < \eta_{cal}^{jet} < 2$ are selected.
In the case of jets reconstructed from the simulated hadronic final states, the same procedure is applied but considering all the particles with lifetime larger than 10^{-13} s and polar angles between 5^o and 175^o. The jets found are called *hadron* jets. Hadron jets with $E_{T,had}^{jet} > 14$ GeV and $-1 < \eta_{had}^{jet} < 2$ are selected.

The differential jet shape is defined as the average fraction of the transverse energy of the jet which lies inside an annulus of inner (outer) radius $r - \Delta r/2$ ($r + \Delta r/2$) concentric to the jet cone. The UCAL cells have been used to reconstruct the jet shape defined as:

$$\rho_{cal}(r) = \frac{1}{N_{jets}} \sum_{jets} \frac{E_{T,cal}^{jet}(r - \Delta r/2, r + \Delta r/2)}{E_{T,cal}^{jet}(0, R)}$$

where $E_{T,cal}^{jet}(r - \Delta r/2, r + \Delta r/2)$ denotes the sum of the transverse energy of the UCAL cells belonging to a given jet whose distance $r' = \sqrt{(\Delta\eta)^2 + (\Delta\phi)^2}$ to the jet axis is within the range $(r - \Delta r/2, r + \Delta r/2)$, and N_{jet} is the total number of jets in the sample.

The integrated jet shape is defined as the average fraction of the transverse energy of the jet which lies inside an inner cone of radius r concentric to the jet cone:

$$\psi_{cal}(r) = \frac{1}{N_{jets}} \sum_{jets} \frac{E_{T,cal}^{jet}(0, r)}{E_{T,cal}^{jet}(0, R)}$$

The sum runs over all the jets in the sample, N_{jet}. It must be noted that, due to the applied normalization, $\psi_{cal}(r = R) = 1$ by definition.

The same jet shape definitions as used above for the UCAL cells are applied to the final state particles in the case of simulated events and the resulting jet shapes are denoted by $\psi^{MC}_{had}(r)$ and $\rho^{MC}_{had}(r)$.

4.3 Event Selection

4.3.1 Trigger Configuration

Events were filtered online by a three-level trigger system [10].

- *Neutral Current DIS Events.*
  The first-level-trigger decision was based on the electromagnetic energy and the total transverse energy (E_T). The thresholds were significantly below the corresponding cuts applied in the subsequent selection. The second-level trigger rejected backgrounds (mostly p–gas interactions and cosmic rays) for which the UCAL timing was inconsistent with an ep interaction. In addition, the second-level trigger applied increased E_T thresholds and also required a minimum value of $E - p_Z$, where E and p_Z are the summed energy and the Z-component of the momentum measured in the UCAL. The third-level trigger applied more stringent timing cuts as well as increased energy and $E - p_z$ thresholds. In all cases, the requirements were less stringent than those imposed by the offline event selection.

- *Charged Current DIS Events.*
  The first–level-trigger conditions used in this analysis were based on electromagnetic energy, transverse energy, and missing transverse momentum in the UCAL. The thresholds were significantly below the corresponding cuts applied in the subsequent selection. The second-level trigger rejected backgrounds (mostly p–gas interactions and cosmic rays) for which the UCAL timing was inconsistent with an ep interaction. Events were accepted as CC candidates using the same trigger criteria explained in section 3.3.1 The third–level trigger applied also stringent timing cuts and pattern-recognition algorithms to reject cosmic rays.

4.3.2 Offline Selection

Events from NC DIS reactions have been selected from the 1995 ZEUS data, which corresponds to a total luminosity of 6.3 pb^{-1}, using similar criteria as reported previously [11].

- The event should have an identified scattered positron (identified using the pattern of energy deposits in the calorimeter [12]) with an uncorrected energy $E_e > 10$ GeV and $y_e < 0.95$. The energy and polar angle of the candidate have been determined from UCAL measurements. These cuts ensure high and well understood positron finding efficiency and reduce background from photoproduction reactions.

- In order to select a good candidate for the scattered positron, a cone of radius $R = 0.7$ (in the $\eta - \phi$ plane) is drawn around the positron candidate. If the total energy of the cells inside the cone, after removing those cells belonging to the candidate, is larger than 5 GeV the event is discarded. This condition removes photoproduction and DIS events where part of a jet has been falsely identified as the scattered positron.

- A track matching the scattered positron candidate is required. In order to accept also very high Q^2 events, where the positron track would be outside the CTD acceptance region, the matching track is not required for very forward positrons ($\eta^{e^+} > 2$), but they are required to have a transverse momentum $P_T^{e^+} > 20$ GeV/c.

- The event is required to fulfil 38< $E - p_Z < 65$ GeV, where E is the total energy measured by the UCAL and p_Z is the Z-component of the vector $\vec{p} = \sum_i E_i \vec{r}_i$ (E_i is the energy of cell i and $\vec{r}_i$ is the position of the center of the cell, with respect to the interaction vertex). This cut removes events with large initial-state radiation and further reduces the photoproduction background.

- The event is required to have $\frac{P_T}{\sqrt{E_T}} < 3$ GeV$^{1/2}$, where $P_T = \sqrt{p_X^2 + p_Y^2}$ and E_T is the total transverse energy measured by the UCAL. This cut removes events from cosmic rays and beam-related background.

- If a second positron candidate is identified (which has not an associated track in the CTD) and the energy of the UCAL, after subtracting both candidates, is lower than 10 GeV, then the event is considered as an elastic Compton interaction ($ep \rightarrow ep\gamma$) and it is removed from the sample.

- The event is required to have a vertex with a Z-component in the range -30 cm $< Z < 36$ cm.

- Algorithms to reject cosmic rays and sparks are applied.

- The event is required to fulfil $Q^2_{DA} > 100$ GeV^2, where Q^2 is reconstructed using the double angle method [13].

Events from CC DIS reactions have been selected from the 1995 and 1996 ZEUS data, which corresponds to a total luminosity of 14.8 pb^{-1}, using criteria similar to those of [14, 15] (see chapter 3). The following cuts have been applied:

- The event is required to have $P_T > 11$ GeV.

- The event is required to have $\frac{P_T}{E_T} > 0.5$.

- In order to remove background events from proton-gas interactions the condition $P_T^{out}/P_T > 0.8$ is applied.

- The event is required to have $\frac{N_{vtx}}{N_{tot}} \geq 0.2$, where N_{vtx} is the number of tracks fitted to the primary vertex and N_{tot} is the total number of tracks reconstructed in the event.

- The event is restricted to have a Z-component of the vertex within the range -30 cm $< Z < 36$ cm.

- The event is required to have at least one *good track* [1].
- The azimuthal direction of the hadronic final state as determined by the UCAL, ϕ_{cal}, is matched with the same quantity as determined using only *good tracks*, ϕ_{track} . The difference $\Delta\phi = |\phi_{cal} - \phi_{track}|$ must be smaller than 1 rad.
- The total transverse momentum as determined using only *good tracks* must be at least 10% of the transverse momentum computed using the UCAL. This condition is not applied if the event has a transverse momentum computed by UCAL larger than 25 GeV. This additional restriction is designed in order to keep high Q^2, x events, for which the hadronic final system is located in the very forward part of the UCAL, outside of the CTD acceptance region.
- A search for a scattered positron is performed as a veto for NC DIS candidates. The event is removed from the sample if:
  - There is a positron candidate with uncorrected energy E_e larger than 10 GeV.
  - This candidate has a track matching the electromagnetic cluster in the UCAL. The momentum of the track must be larger than 5 GeV, and the distance in the $\eta - \phi$ plane between the track and the cluster must be smaller than 0.07 units.
  - The positron candidate is isolated: the energy of the UCAL within a cone of radius $R = 0.7$ around the candidate (removing those cells belonging to the candidate) must be smaller than 5 GeV.
  - The number of vertex tracks within a cone of radius $R = 0.7$ around the candidate must be one. This condition is designed in order to avoid those cases where the positron-finder algorithm misidentifies part of a hadronic jet as a positron candidate.

  Only if all of these conditions are fulfilled by the candidate, the event is removed from the sample.
- If the cell with the maximal transverse energy in the UCAL has more than 70% of the total transverse energy in the UCAL, the event is removed from the sample. This criterium is used to avoid events where a cosmic muon or a spark produces large P_T values in the event.
- Algorithms to reject cosmic rays and sparks are applied.
- The events are required to have[2] $Q^2_{cor} > 100$ GeV^2.

A search fot jet structure using the UCAL cells (see previous section) is performed in both samples (NC and CC DIS) and events with at least one jet of corrected[3] transverse energy $E_T^{jet} > 14$ GeV and $\eta^{jet} \in (-1, 2)$ have been retained. The selected NC (CC) DIS sample consists of 6926 (231) events containing 7092 (233) jets. In both cases, the background from photoproduction has been estimated and found to be below 1%.

[1] A good track is defined as a track fitted to the primary vertex which has a polar angle between 15^o and 164^o and transverse momentum above 150 MeV.

[2] Q^2_{cor} denotes Q^2_{jb} corrected using a correction procedure similar to that explained in chapter 3.

[3] The jet-energy correction procedure is explained in appendix C.

4.4 Monte Carlo Simulation

Monte Carlo (MC) event simulation is used to correct for detector acceptance and smearing effects. The detector simulation is based on the GEANT program [16] and incorporates our current understanding of the detector, trigger and test beam results. Simulated NC and CC DIS events with electroweak radiative corrections were generated using LEPTO [17] interfaced to HERACLES [18] via DJANGO [19]. The CTEQ4 [20] set of proton parton densities was used. Higher QCD orders were simulated using the MEPS option of LEPTO. A second sample of NC DIS Monte Carlo events where the QCD cascade is simulated using the colour-dipole model (CDM) [21], as implemented in ARIADNE [22], was also studied. A third sample of DIS NC Monte Carlo events was considered based on the PYTHIA [23] program: a lowest-order electroweak calculation including initial and final state QCD radiation in the leading-logarithm parton-shower approximation. In the case of PYTHIA, the QCD matrix elements corresponding to $O(\alpha_s)$ subprocesses are not implemented. In all cases, the final state parton system is hadronized using the LUND string model [24] as implemented in JETSET [23].

4.5 Uncorrected Jet Shape.

A comparison of the differential and integrated jet shapes, as measured with the UCAL, between data and MC simulation has been performed for both NC and CC DIS events.

4.5.1 Neutral-Current DIS

- In figures 4.1 and 4.2 the integrated and differential jet shapes in the data for jets with $E_T^{jet} > 14$ GeV are compared with the expectations of ARIADNE and LEPTO-MEPS in different bins of η^{jet}. The measured jet shapes are well described by the ARIADNE MC in all the η^{jet} regions, while LEPTO-MEPS predicts jets slightly broader than in the data.

- In figures 4.3 and 4.4, the integrated and differential jet shapes in the data for jets with $-1 < \eta^{jet} < 2$ are compared with th expectations of ARIADNE and LEPTO-MEPS expectations in different bins of E_T^{jet}. The measured jet shapes are well described by the ARIADNE MC in all the E_T^{jet} regions. LEPTO-MEPS predicts jets slightly broader than in the data.

4.5.2 Charged-Current DIS

- In figures 4.5 and 4.6 the measured jet shapes in 1995+1996 data sample for jets with $E_T^{jet} > 14$ GeV are compared with the expectations of ARIADNE and LEPTO-MEPS in different bins of η^{jet}. The expectations for the integrated and differential jet shapes are in reasonable agreement with the data.

- In figures 4.7 and 4.8 the measured jet shapes in 1995+1996 data sample for jets with $-1 < \eta^{jet} < 2$ are compared with the expectations of ARIADNE and LEPTO-MEPS in different bins of E_T^{jet}. The Monte Carlo expectations are in reasonable agreement with the measurements.

4.6 Jet Shape Correction

The integrated and differential jet shapes as measured with the UCAL have been corrected back to the hadron level using Monte Carlo samples of events. The corrected integrated (differential) jet shapes, $\psi(r)$ ($\rho(r)$), refer to jets at the hadron level with a cone radius of one unit in the $\eta - \phi$ plane. The measurements are given for jets of corrected transverse energy $E_T^{jet} > 14$ GeV and $-1 < \eta^{jet} < 2$, and in the kinematic region determined by $Q^2 > 100$ GeV^2.
The reconstructed jet shapes are corrected for acceptance and smearing effects using the samples of Monte Carlo events. The correction factors also take into account the efficiency of the trigger, the selection criteria, the purity and efficiency of the jet reconstruction, and the effects of energy losses due to inactive material in front of the UCAL. The corrected integrated (differential) jet shapes are determined bin-by-bin as $\psi(r) = F_{cal}^{MC} * \psi_{cal}$ ($\rho(r) = G_{cal}^{MC} * \rho_{cal}$), where the correction factors, F_{cal}^{MC} (G_{cal}^{MC}) are defined as $F_{cal}^{MC} = \psi_{had}^{MC} / \psi_{cal}^{MC}$ ($G_{cal}^{MC} = \rho_{had}^{MC} / \rho_{cal}^{MC}$), and have been determined separately for each region of η^{jet} and E_T^{jet}.

- Figure 4.9 (4.10) shows the correction factors F_{CAL}^{MC} (G_{CAL}^{MC}) computed using ARIADNE to be applied to the NC DIS measured jet shapes, ψ_{cal} (ρ_{cal}).

- Figure 4.11 (4.12) shows the correction factors F_{CAL}^{MC} (G_{CAL}^{MC}) computed using ARIADNE to be applied to the CC DIS measured jet shapes, ψ_{cal} (ρ_{cal}).

The correction function F_{CAL}^{MC} decreases rapidly towards one as r increases from values typically around 1.2 (1.05) for $r = 0.2$ (r=0.4) and depends very little on η^{jet} and E_T^{jet}. The correction factor for the measurement at $r = 0.1$ is found to be large (between 1.4 and 1.7). The correction functions G_{CAL}^{MC} are flat in r for $r \geq 0.2$ (being ~ 0.8) and depend little on η^{jet} and E_T^{jet}. However, the correction factors for the lower bins of η^{jet} slightly increase as r increases (see figures 4.10 and 4.12). As for the integrated jet shape, the correction factor G_{CAL}^{MC} for $r = 0.1$ is large.

4.7 Systematic Uncertainties

A detailed study of the sources contributing to the systematic uncertainties of the measurements has been carried out for both integrated and differential jet shape measurements. In the case of the integrated jet shape the measurements at different points are strongly correlated and the largest change in the corrected value of $\psi(r)$ at a fixed value of r typically occurs ar $r = 0.1$ and the magnitude of the induced change decreases rapidly as r increases. In the differential measurements, since the points are not correlated (apart from their common normalization to the transverse energy of the jet), the systematic uncertainties are somewhat larger than for the integrated jet shape. The following sources of systematic uncertainties have been considered :

- To take into account the uncertainty on the energy scale of the UCAL, the transverse energy of a jet was varied by ($\pm 3\%$) in the MC.

- To take into account the uncertainty in the simulation of higher QCD orders in the MC calculations, the correction factors were computed using LEPTO-MEPS instead of ARIADNE-CDM.

- The uncertainty in the simulation of the UCAL response to low-energy particles.
- In NC DIS, the uncertainty on the positron energy scale has been considered ($\pm 3\%$).
- In the selection of NC DIS events, the uncertainty on $E - p_z$ ($\pm 3\%$).
- In CC DIS, the uncertainty on P_T (3%).

These studies have been performed for each bin of η^{jet} and E_T^{jet} considered. The final systematic error was computed adding in quadrature the differences (positive and negative separately) with respect to the central value obtained from each of the sources listed above. As an example, figure 4.13 (4.14) shows the systematic uncertainties for the NC DIS[4] integrated (differential) jet shapes in the lowest bins of η^{jet} and E_T^{jet}.

4.8 Jet shapes in neutral current DIS

4.8.1 η^{jet} Dependence of the Jet Shape

The jet shapes in the reaction $ep \rightarrow e + jet + X$ have been measured for jets in the E_T^{jet} range above 14 GeV integrated over four non-overlapping η^{jet} regions ($-1 < \eta^{jet} < 0$, $0 < \eta^{jet} < 1$, $1 < \eta^{jet} < 1.5$, $1.5 < \eta^{jet} < 2$).

In figures 4.15 (4.16) the measured integrated (differential) jet shapes have been compared to ARIADNE, LEPTO-MEPS and PYTHIA predictions The predictions from ARIADNE and LEPTO-MEPS describe the measured jet shapes well in all the η^{jet} regions considered. PYTHIA predicts jets slightly narrower than in the data.

4.8.2 E_T^{jet} Dependence of the Jet Shape

Measurements of the jet shapes have been performed for jets in the η^{jet} range between -1 and 2 integrated over four non-overlapping E_T^{jet} regions (14 GeV $< E_T^{jet} <$ 21 GeV, 21 GeV $< E_T^{jet} <$ 29 GeV, 29 GeV $< E_T^{jet} <$ 37 GeV, 37 GeV $< E_T^{jet} <$ 45 GeV). The results for $\psi(r)$ and $\rho(r)$ are shown in figures 4.17 and 4.18.

The predictions of ARIADNE are in good agreement with the measurements in all the E_T^{jet} regions. LEPTO-MEPS predicts jets slightly broader than the measured jet shapes in all the E_T^{jet} regions, but is able to describe the jet shapes in the region 14 GeV $< E_T^{jet} <$ 25 GeV. PYTHIA predictions are narrower than the measured jet shapes in the low-E_T^{jet} region (14 GeV $< E_T^{jet} <$ 21 GeV), but provide a good description of the measured jet shapes in the high-E_T^{jet} region.

4.8.3 Jet Shape at fixed r

The measured integrated jet shape at the fixed value of $r = 0.5$ ($\psi(r = 0.5)$) has been compared with model predictions as a function of η^{jet} and E_T^{jet} in figure 4.19. Since the integrated jet shape has been measured in ranges of E_T^{jet}, the measurements are located at the weighted mean in each E_T^{jet} range. The measured $\psi(r = 0.5)$ exhibits no significant dependence on η^{jet}. It is observed that the jet shape becomes narrower as E_T^{jet} increases.

[4] In CC DIS, similar results have been obtained.

4.9 Jet shapes in charged current DIS

The integrated and differential jet shapes in the reaction $ep \to \overline{\nu} + jet + X$ have been measured for jets in the E_T^{jet} range above 14 GeV integrated over the same four non-overlapping η^{jet} and E_T^{jet} regions as above.
Figure 4.20 (4.21) shows the comparison between the measured jet shapes $\psi(r)$ ($\rho(r)$) and the predictions of ARIADNE and LEPTO-MEPS. Figure 4.22 shows the dependence of the integrated jet shape, measured at a fixed value of r ($\psi(r = 0.5)$), with η^{jet} and E_T^{jet}. As in NC DIS, no significant η^{jet} dependence in the CC DIS measured jet shapes is observed. Both ARIADNE and LEPTO-MEPS are able to provide a reasonable description of the measured jet shapes.

Figure 4.23 (4.24) shows the comparison of the measured jet shapes $\psi(r)$ ($\rho(r)$) in NC and CC DIS for different regions of η^{jet}. The jet in CC are narrower than those in NC DIS in the region $-1 < \eta^{jet} < 1.5$. This can be ascribed to the different E_T^{jet} spectrum in the two processes: the E_T^{jet} distribution in CC DIS is harder than in NC DIS due to the W boson mass term in the propagator (see chapter 3). In the region $1.5 < \eta^{jet} < 2$ the measured jet shapes for NC and CC reactions are more similar. Figure 4.23 (4.24) also shows the comparison of the measured jet shapes $\psi(r)$ ($\rho(r)$) in NC and CC DIS for different regions of E_T^{jet}. They are found to be very similar in all the E_T^{jet} regions. The average Q^2 of the NC and CC DIS samples are comparable in each E_T^{jet} region.

4.10 Comparison to jet shapes in photoproduction

In photoproduction, two types of QCD processes contribute to jet production at LO [25, 26]: either the photon interacts directly with a parton in the proton (the direct process) or the photon acts as a source of partons which interact with those in the proton (the resolved process). In the case of dijet photoproduction the contributions of resolved and direct processes can be separated [27] by using the variable:

$$x_\gamma^{OBS} = \frac{\sum_{jets} E_T^{jet} e^{-\eta^{jet}}}{2E_\gamma},$$

where the sum runs over the two jets of highest E_T^{jet} and E_γ is the initial photon energy. This variable represents the fraction of the photon's momentum participating in the production of the two jets with highest E_T^{jet}. The LO direct and resolved processes largely populate different regions of x_γ^{OBS}, with the direct process concentrated at high values.

In Figure 4.25 the measured jet shapes in neutral current DIS are compared to those in dijet photoproduction [8] for two different regions in x_γ^{OBS}: $x_\gamma^{OBS} \geq 0.75$ and $x_\gamma^{OBS} \leq 0.75$.

The jets produced in NC DIS are narrower than those in dijet photoproduction and are closer to those in the region populated by the direct process ($x_\gamma^{OBS} \geq 0.75$).

These comparisons can be understood in terms of the fractions of final-state quark and gluon jets in the different processes. In lowest-order neutral-current DIS ($eq \to eq$), the final-state jets are predominantly quark initiated. In the case of direct processes in photoproduction, the dominant subprocess is photon-gluon fusion ($\gamma g \to q\bar{q}$), which gives rise only to quark jets. In the case of resolved processes, which populate the region $x_\gamma^{OBS} \leq 0.75$, the dominant subprocess in the kinematic regime studied [8] is $q_\gamma g_p \to qg$

and gives rise also to gluon jets. The differences between the jet shapes in NC DIS and resolved photoproduction may be attributed to the different fraction of quark and gluon jets in each reaction. The differences between the jet shapes in NC DIS and direct photoproduction processes may be understood in term of the contribution from resolved processes to dijet production with $x_\gamma^{OBS} \geq 0.75$. The similarity of the measured jet shapes in neutral current DIS and direct processes in photoproduction indicates that the pattern of final state QCD radiation around a primary quark is to a large extent independent of the hard scattering process.

4.11 Comparison to measurements in e^+e^- and $\bar{p}p$ collisions

The jet shapes for jets in CC and NC DIS at $Q^2 > 100$ GeV^2 with $37 < E_T^{jet} < 45$ GeV and $-1 < \eta^{jet} < 2$ have been compared to the measurements of jet shapes in $\bar{p}p$ collisions by CDF [4] and D0 [5], and in e^+e^- interactions by OPAL [7].

- The CDF data [4] have been obtained using an iterative cone algorithm similar to that is used here and correspond to a cone size $R = 1$. The measurements shown are for jets with transverse energy between 40 and 60 GeV, with a mean of 45 GeV, and pseudorapidity $0.1 < |\eta^{jet}| < 0.7$. The contribution to the jet shape due to the underlying event was found to be small.

- The D0 data [5] have been obtained using also an iterative cone algorithm similar to that used here and correspond to a cone size $R = 1$. The jet direction was redefined according to a convention different than that of Snowmass; however, it does not make a significant difference in the experimental measurements. The jet shapes have been measured for jets with transverse energy between 45 and 70 GeV, with a mean of 53 GeV, and pseudorapidity $|\eta^{jet}| < 0.2$. The jet shapes have been corrected to remove the contribution due to the underlying event.

- The OPAL data [7] have been obtained using a cone algorithm especially designed to emulate that of CDF measurements, i.e. defining the cone in the $\eta - \phi$ plane, using $R = 1$, demanding $|\eta^{jet}| < 0.7$ and measuring the energy flow in terms of transverse energy. The jet shapes have been measured for jets with energy greater than 35 GeV, with a mean of 40.4 GeV. The e^+e^- data as well as DIS data have no underlying event.

For the selected samples of jets, the jet shapes in e^+e^- interactions and DIS are expected to be similar due to the large fraction of final state quark jets in these two processes. However, some differences may appear since there are configurations of colour flow in DIS (as initial-state QCD radiation) which are not present in e^+e^-. The measured differential jet shapes in NC and CC DIS are compared to those by OPAL in figure 4.26 and found to be very similar. The striking similarity in the jet shapes indicates that the pattern of QCD radiation around a primary parton is to large extent independent of the hard scattering process. The measured integrated jet shapes in DIS are compared to those in e^+e^- interactions and $\overline{p}p$ collisions in figure 4.27. The measured jet shapes in DIS at HERA are found to be very similar to those in e^+e^- interactions and narrower than those in $\bar{p}p$ collisions. As observed in [7], the differences between the jet shapes in e^+e^- interactions and $\bar{p}p$ collisions can be ascribed to the large fraction of gluon jets in the latter reaction. The comparison between the measured jet shapes in DIS and $\bar{p}p$ collisions suggests that, also in this case, most of the difference can be attributed to differences between quark and gluon jet properties (see chapter 1).

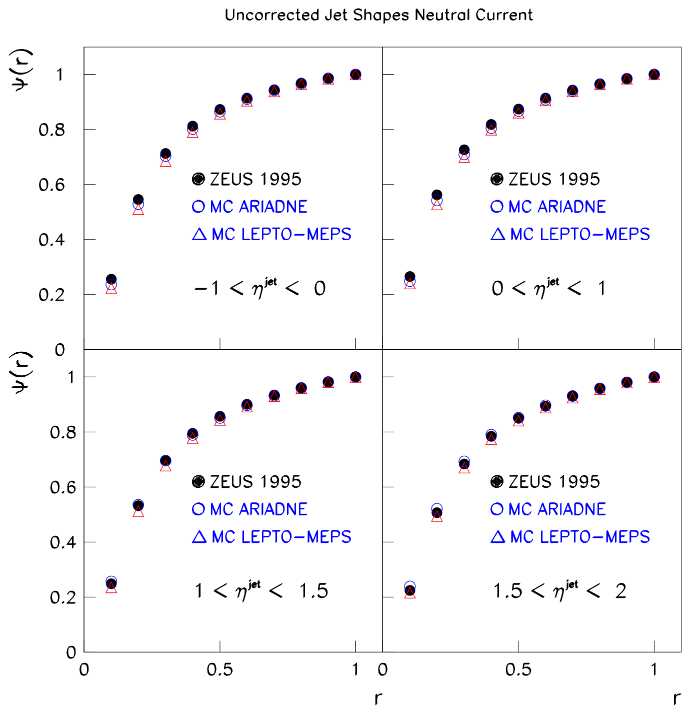

Figure 4.1: Measured uncorrected jet shapes $\psi_{cal}(r)$, for jets in neutral-current DIS at $Q^2_{da} > 100$ GeV^2 with E_T^{jet} above 14 GeV in different η^{jet} regions. The error bars show the statistical errors. For comparison, the expectations of ARIADNE (open circles) and LEPTO-MEPS (triangles) are shown.

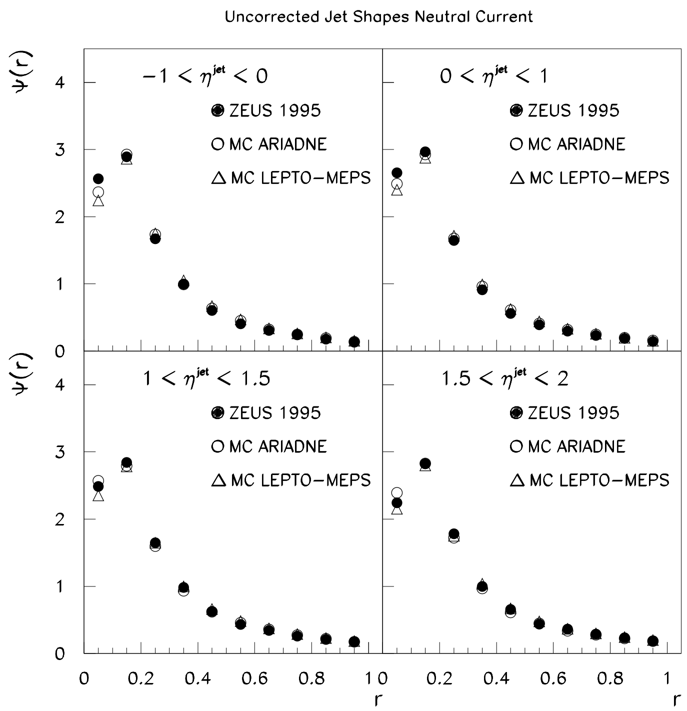

Figure 4.2: Measured uncorrected jet shapes $\rho_{cal}(r)$, for jets in neutral-current DIS at $Q^2_{da} > 100$ GeV^2 with E_T^{jet} above 14 GeV in different η^{jet} regions. The error bars show the statistical errors. For comparison, the expectations of ARIADNE (open circles) and LEPTO-MEPS (triangles) are shown.

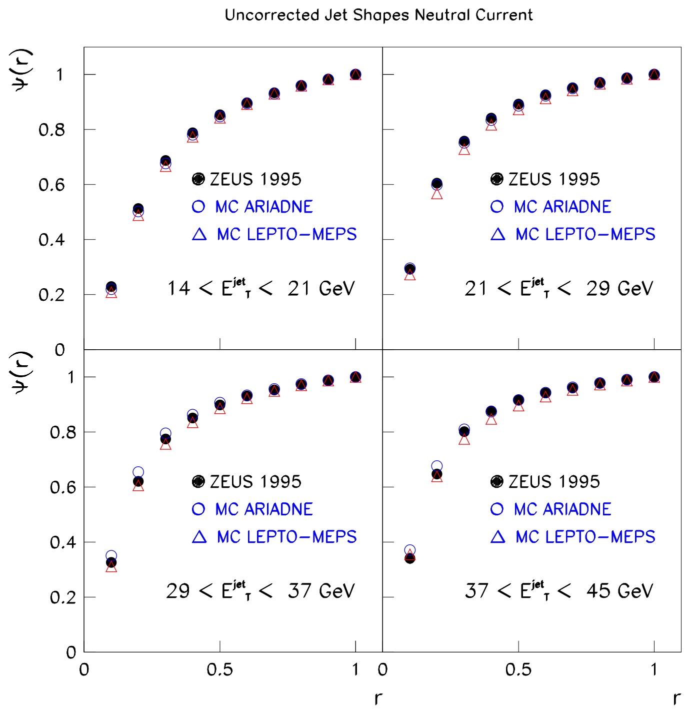

Figure 4.3: Measured uncorrected jet shapes $\psi_{cal}(r)$, for jets in neutral-current DIS at $Q^2_{da} > 100$ GeV^2 with $-1 < \eta^{jet} < 2$ in different E_T^{jet} regions. The error bars show the statistical errors. For comparison, the expectations of ARIADNE (open circles) and LEPTO-MEPS (triangles) are shown.

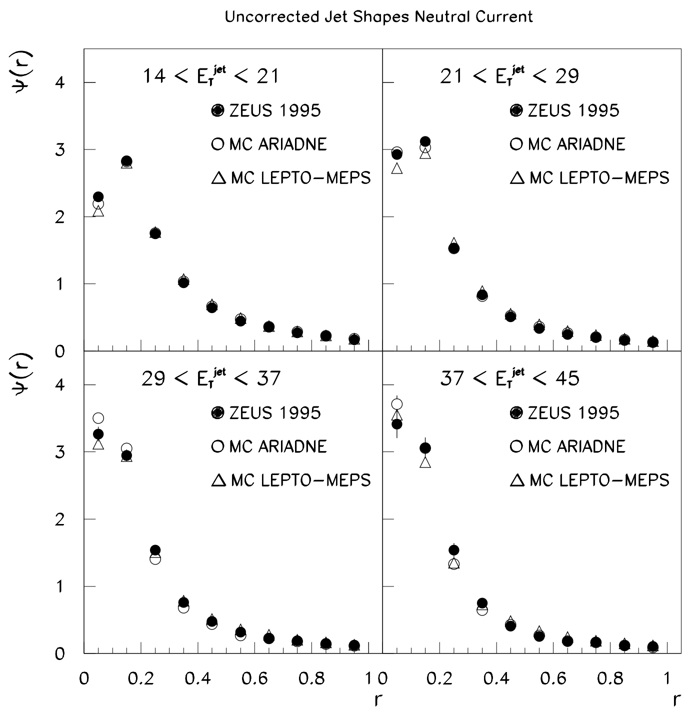

Figure 4.4: Measured uncorrected jet shapes $\rho_{cal}(r)$, for jets in neutral-current DIS at $Q^2_{da} > 100$ GeV^2 with $-1 < \eta^{jet} < 2$ in different E_T^{jet} regions. The error bars show the statistical errors. For comparison, the expectations of ARIADNE (open circles) and LEPTO-MEPS (triangles) are shown.

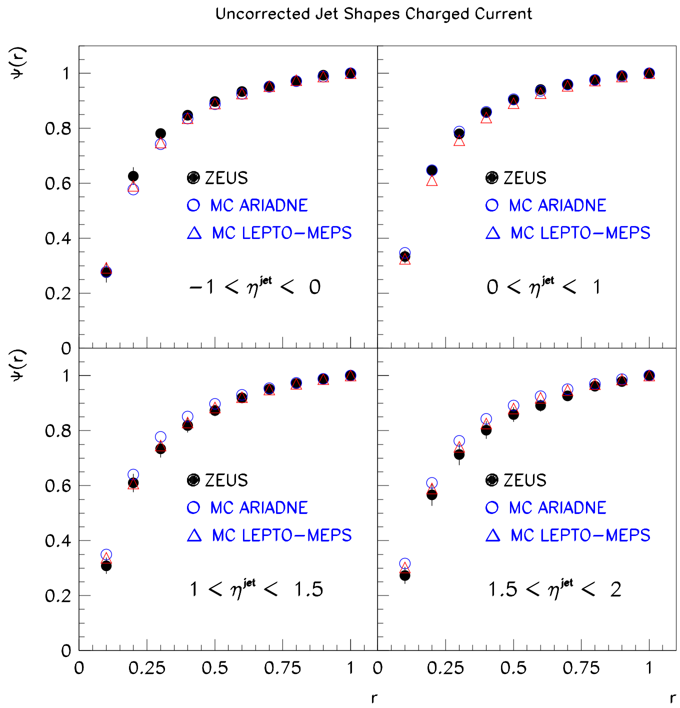

Figure 4.5: Measured uncorrected jet shapes $\psi_{cal}(r)$, for jets in charged-current DIS at $Q^2_{cor} > 100$ GeV^2 with E_T^{jet} above 14 GeV in different η^{jet} regions. The error bars show the statistical errors. For comparison, the expectations of ARIADNE and LEPTO-MEPS are shown.

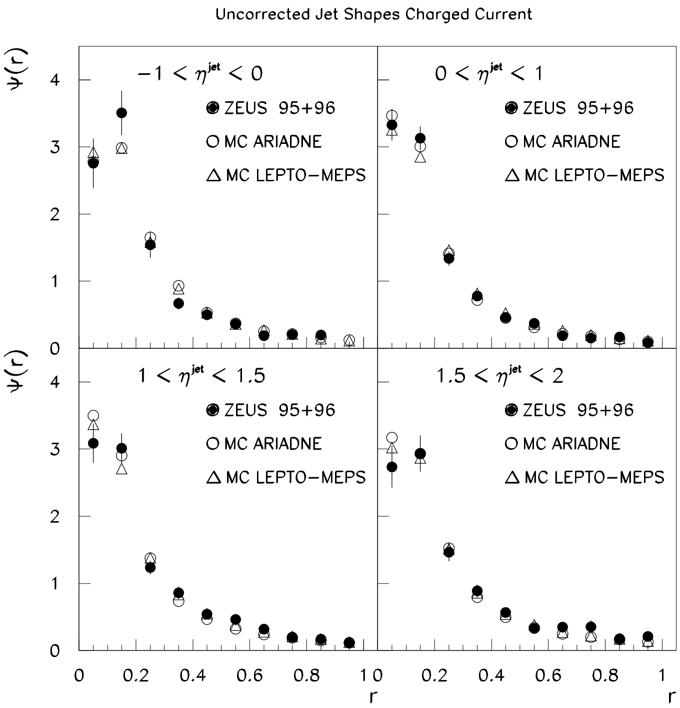

Figure 4.6: Measured uncorrected jet shapes $\rho_{cal}(r)$, for jets in charged-current DIS at $Q^2_{cor} > 100$ GeV^2 with E_T^{jet} above 14 GeV in different η^{jet} regions. The error bars show the statistical errors. For comparison, the expectations of ARIADNE and LEPTO-MEPS are shown.

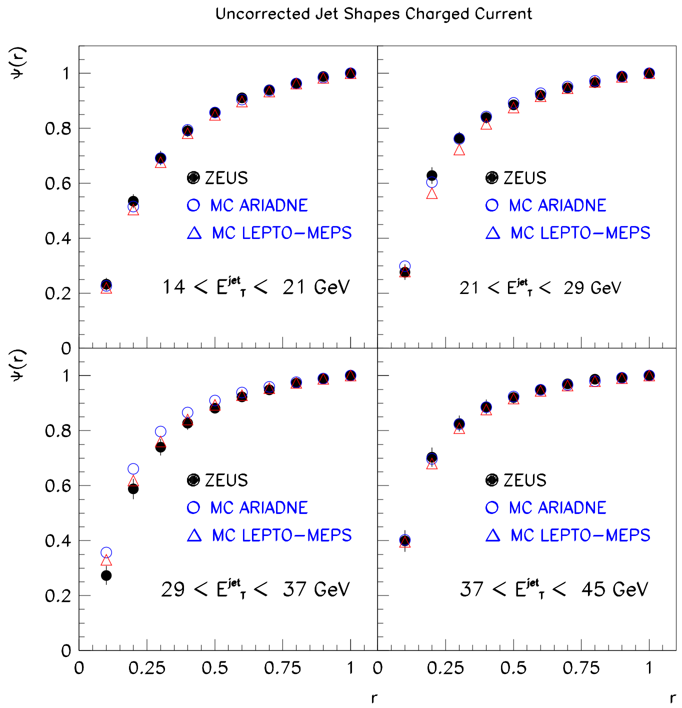

Figure 4.7: Measured uncorrected jet shapes $\psi_{cal}(r)$, for jets in charged-current DIS at $Q^2_{cor} > 100$ GeV^2 with $-1 < \eta^{jet} < 2$ in different E_T^{jet} regions. The error bars show the statistical errors. For comparison, the expectations of ARIADNE and LEPTO-MEPS are shown.

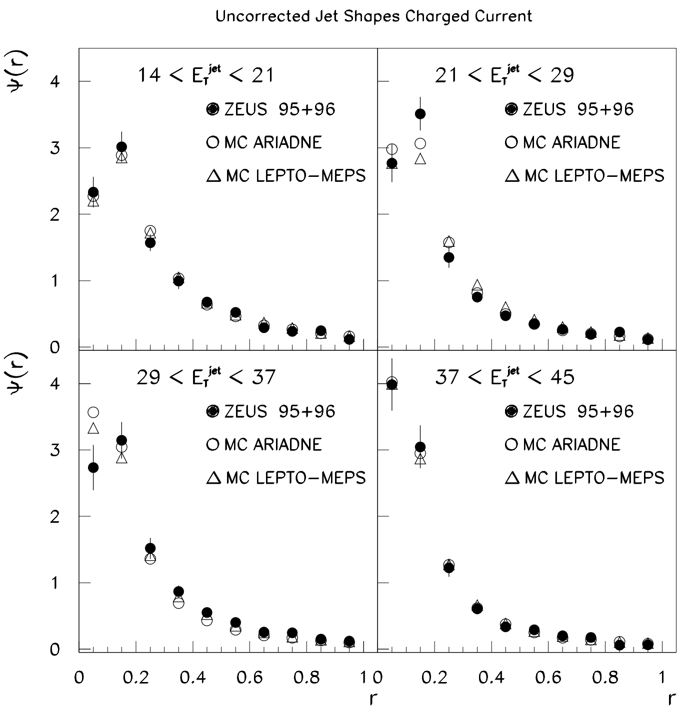

Figure 4.8: Measured uncorrected jet shapes $\rho_{cal}(r)$, for jets in charged-current DIS at $Q^2_{cor} > 100$ GeV^2 with $-1 < \eta^{jet} < 2$ in different E_T^{jet} regions. The error bars show the statistical errors. For comparison, the expectations of ARIADNE and LEPTO-MEPS are shown.

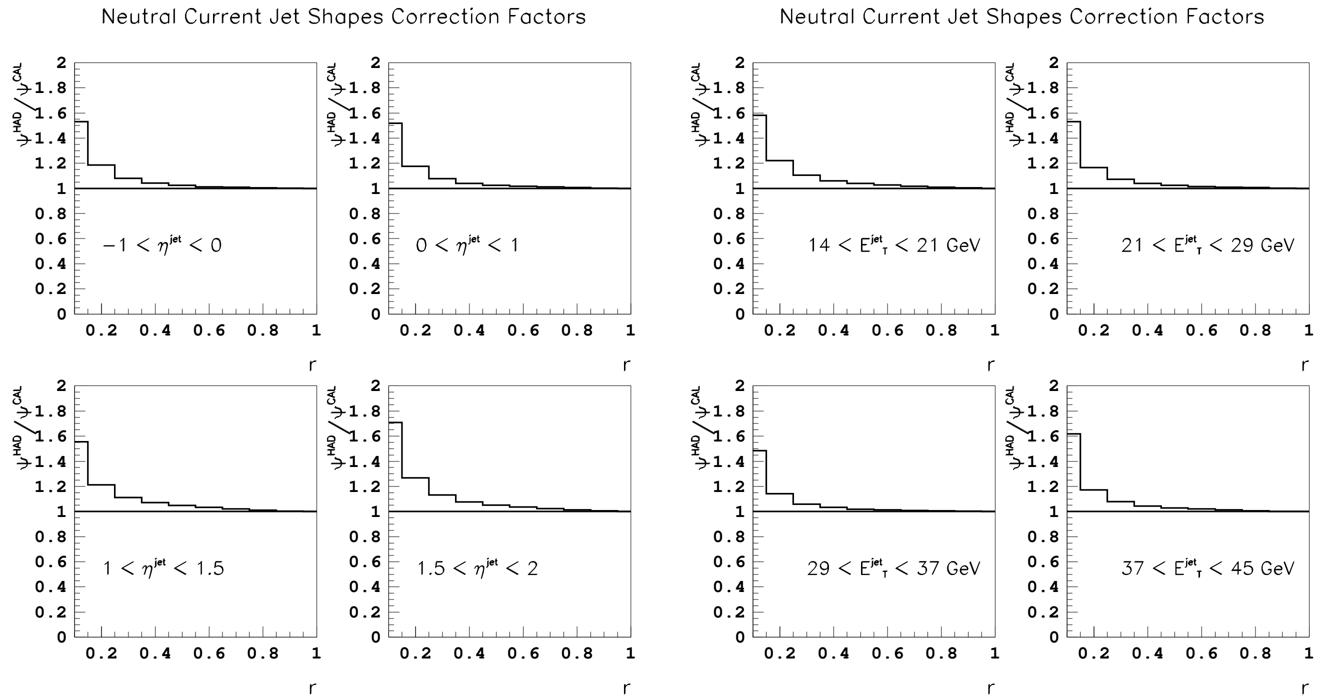

Figure 4.9: Correction factors ψ^{HAD}/ψ^{CAL} (as a function of r) in different η^{jet} and E_T^{jet} regions computed from the Monte Carlo sample of events of ARIADNE to be applied to the NC DIS measured jet shapes.

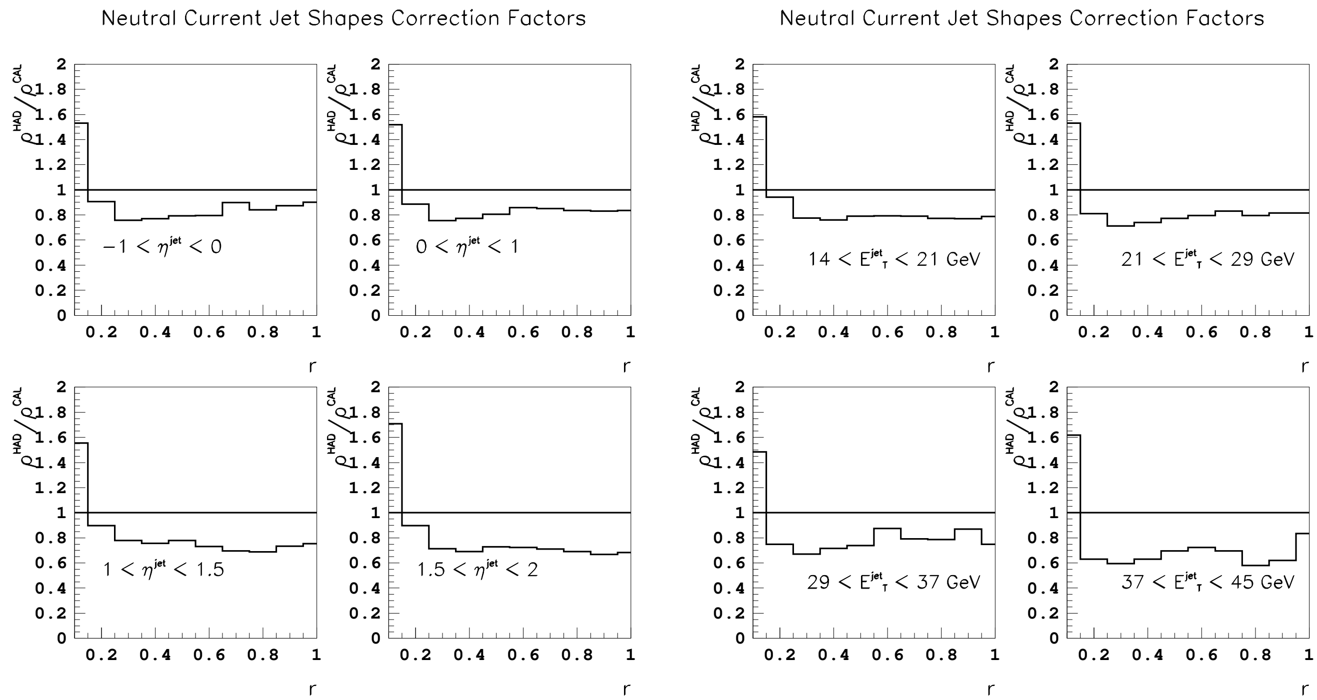

Figure 4.10: Correction factors ρ^{HAD}/ρ^{CAL} (as a function of r) in different η^{jet} and E_T^{jet} regions computed from the Monte Carlo sample of events of ARIADNE to be applied to the NC DIS measured jet shapes .

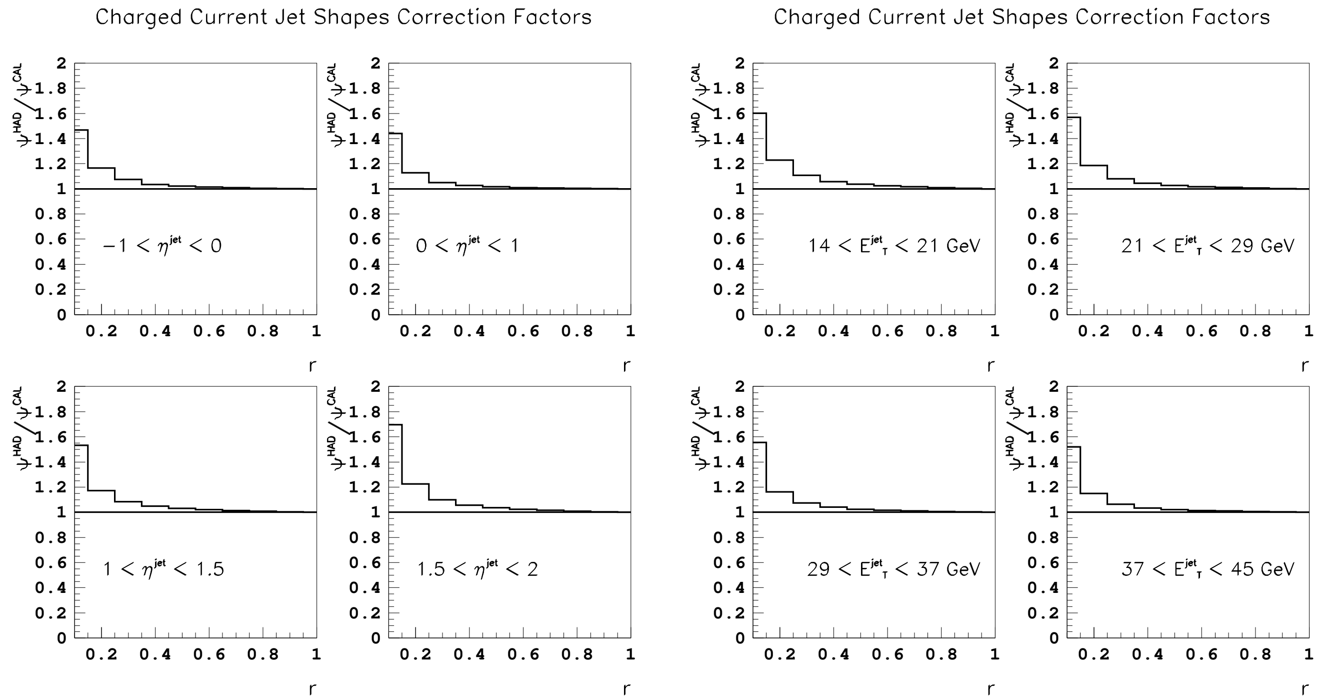

Figure 4.11: Correction factors ψ^{HAD}/ψ^{CAL} (as a function of r) in different η^{jet} and E_T^{jet} regions computed from the Monte Carlo sample of events of ARIADNE to be applied to the CC DIS measured jet shapes .

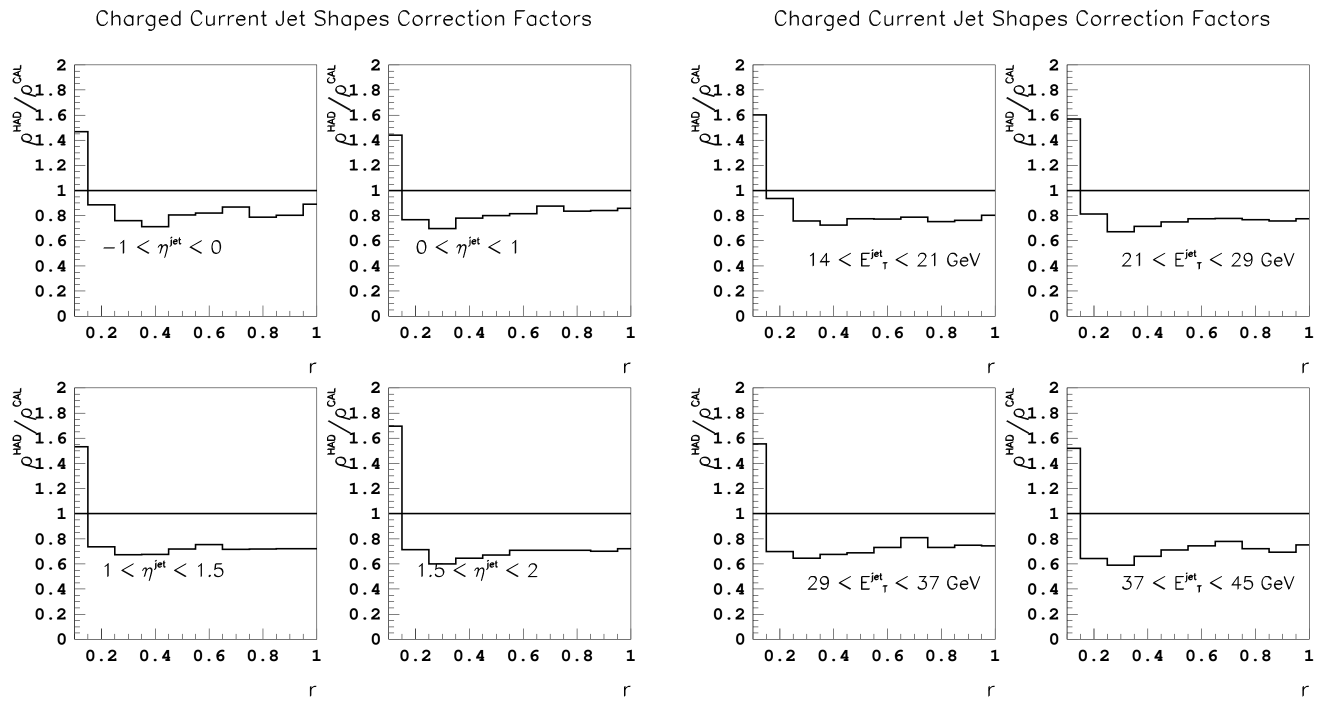

Figure 4.12: Correction factors ρ^{HAD}/ρ^{CAL} (as a function of r) in different η^{jet} and E_T^{jet} regions computed from the Monte Carlo sample of events of ARIADNE to be applied to the CC DIS measured jet shapes .

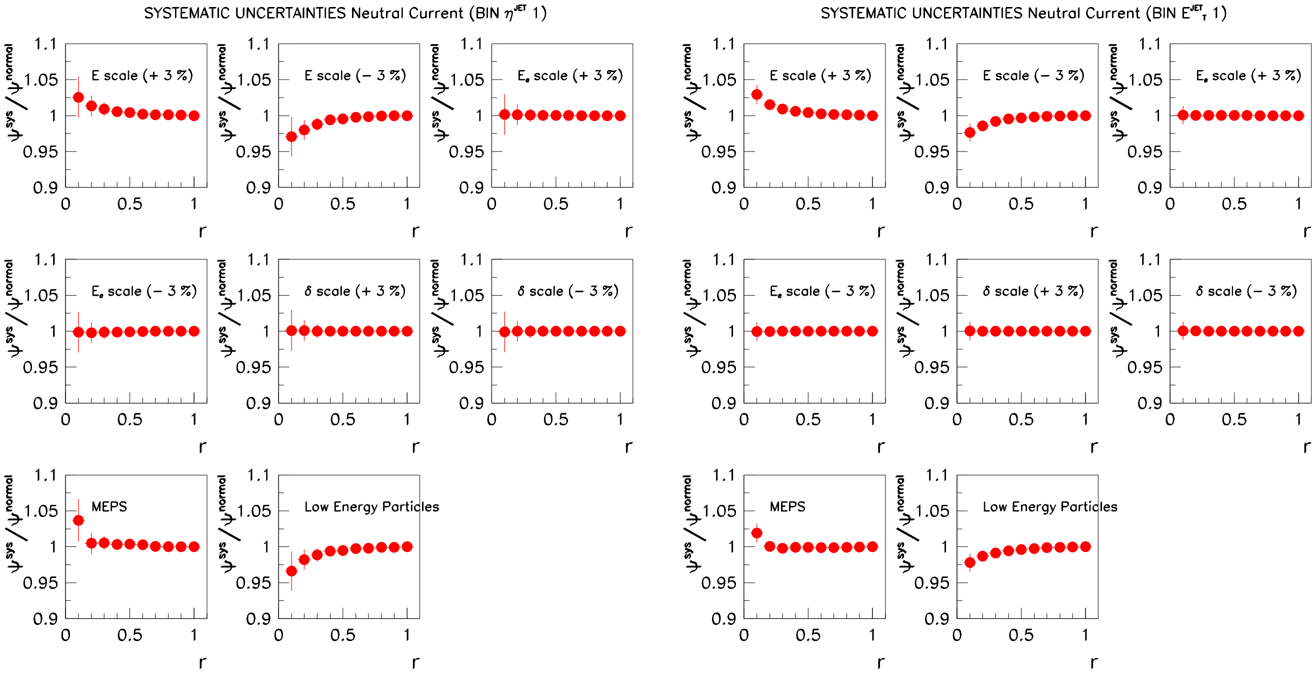

Figure 4.13: Systematic uncertainties in $\psi(r)$ for the NC DIS case computed for the lowest bins of η^{jet} and E_T^{jet} corresponding to $-1 < \eta^{jet} < 0$ and $14 < E_T^{jet} < 21$ GeV respectively.

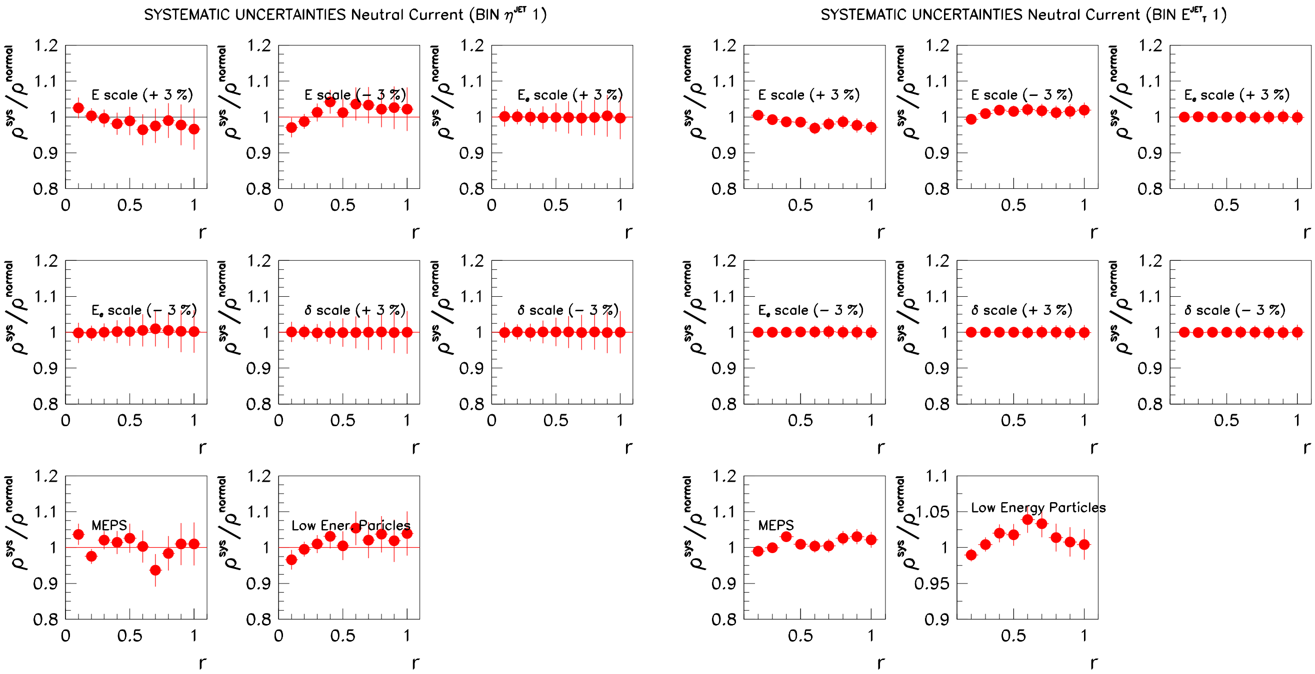

Figure 4.14: Systematic uncertainties in $\rho(r)$ for the NC DIS case computed for the lowest bins of η^{jet} and E_T^{jet} corresponding to $-1 < \eta^{jet} < 0$ and $14 < E_T^{jet} < 21$ GeV respectively.

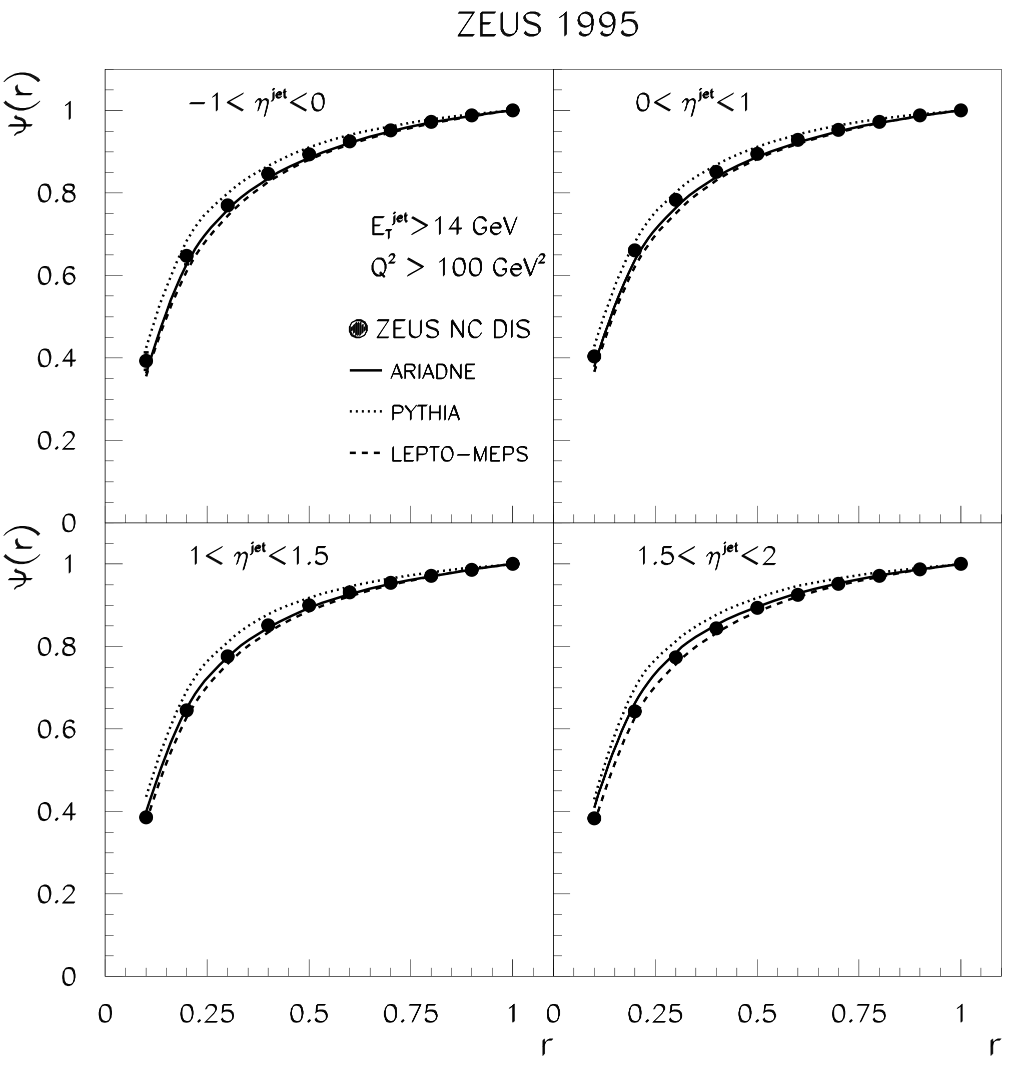

Figure 4.15: Measured integrated jet shapes corrected to the hadron level, $\psi(r)$, for jets in neutral-current DIS at $Q^2 > 100$ GeV^2 with E_T^{jet} above 14 GeV in different η^{jet} regions. The error bars show the statistical and systematic errors added in quadrature. For comparison, the expectations of PYTHIA (dotted line), ARIADNE-CDM (solid line), and LEPTO-MEPS (dashed line) are shown.

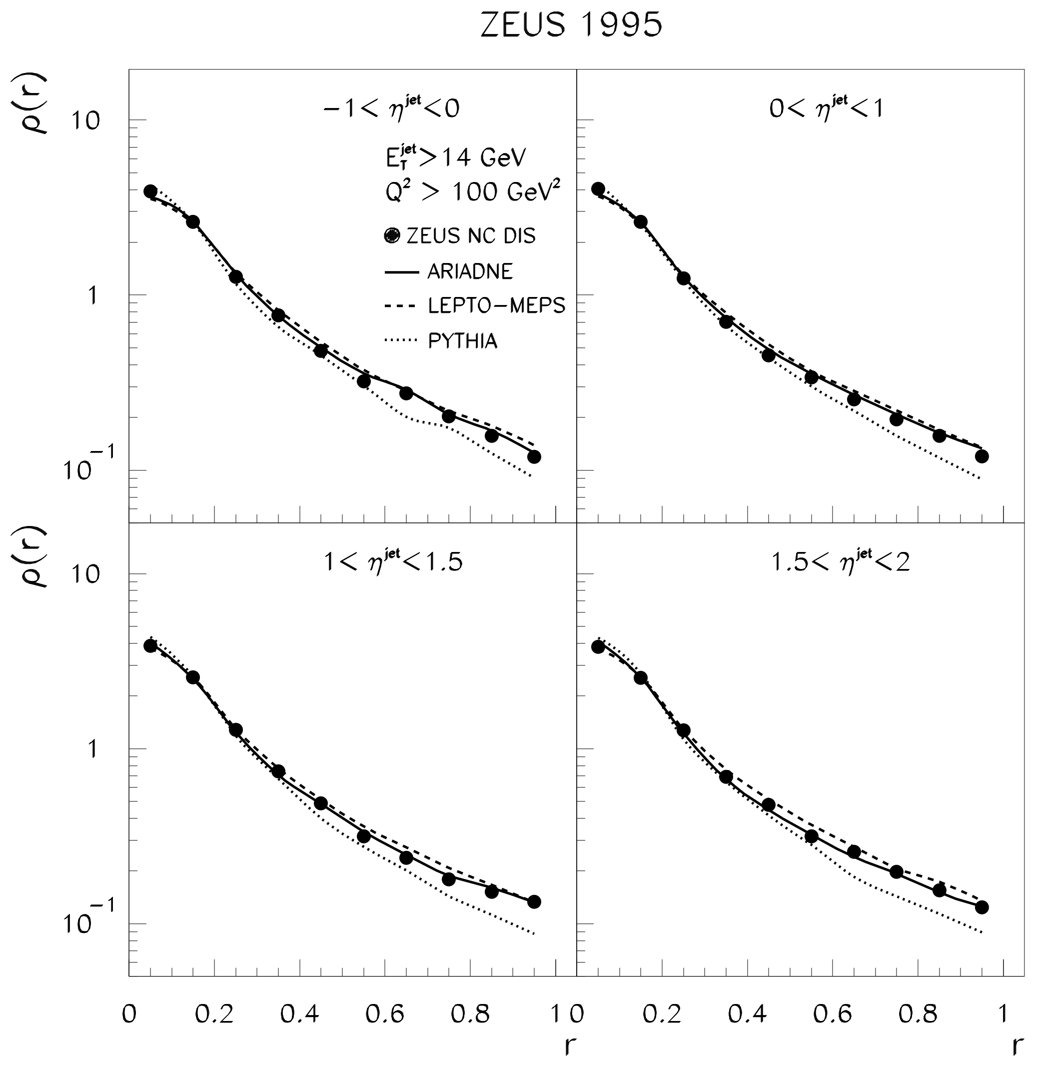

Figure 4.16: Measured differential jet shapes corrected to the hadron level, $\rho(r)$, for jets in neutral-current DIS at $Q^2 > 100$ GeV^2 with E_T^{jet} above 14 GeV in different η^{jet} regions. The error bars show the statistical and systematic errors added in quadrature. For comparison, the expectations of PYTHIA (dotted line), ARIADNE-CDM (solid line), and LEPTO-MEPS (dashed line) are shown.

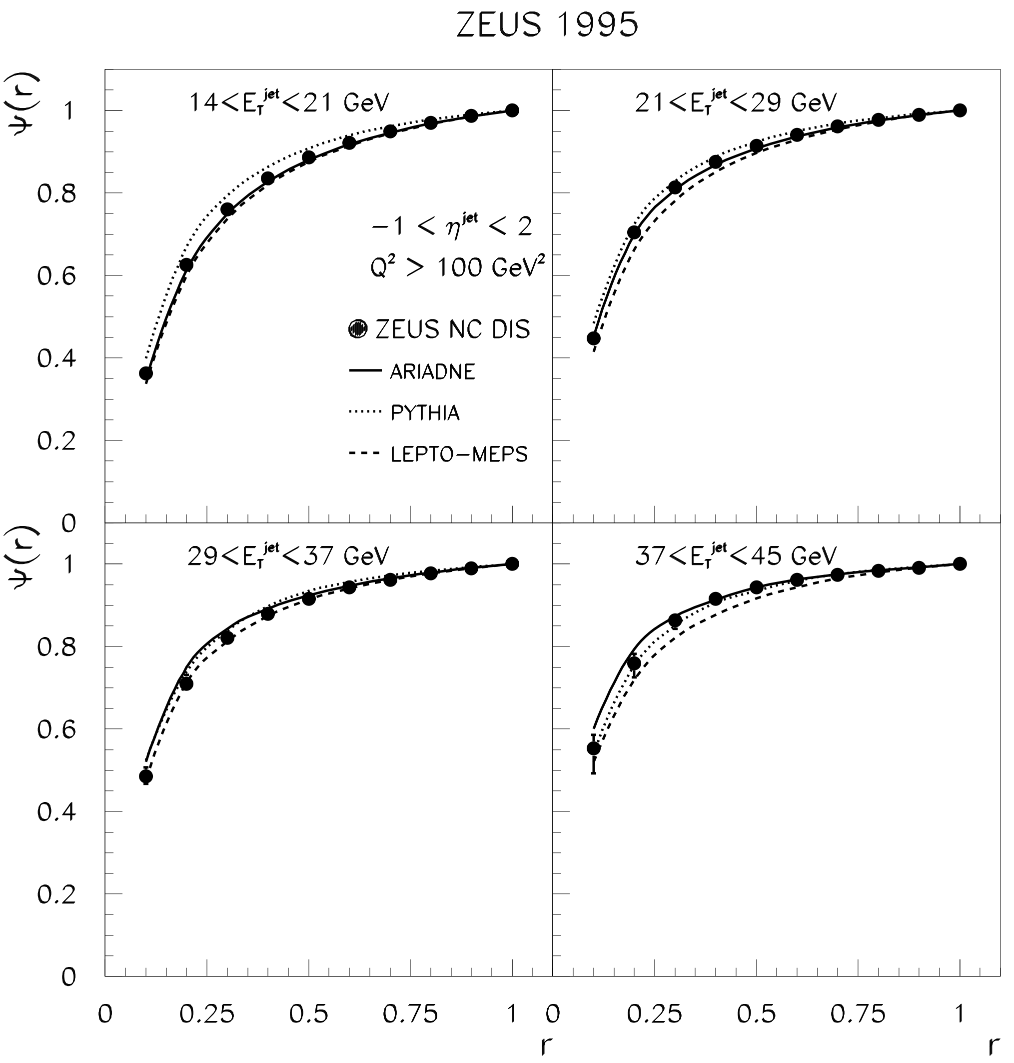

Figure 4.17: Measured integrated jet shapes corrected to the hadron level, $\psi(r)$, for jets in neutral-current DIS at $Q^2 > 100$ GeV^2 in the η^{jet} range between -1 and 2 in different E_T^{jet} regions. The error bars show the statistical and systematic errors added in quadrature. For comparison, the expectations of PYTHIA (dotted line), ARIADNE-CDM (solid line), and LEPTO-MEPS (dashed line) are shown.

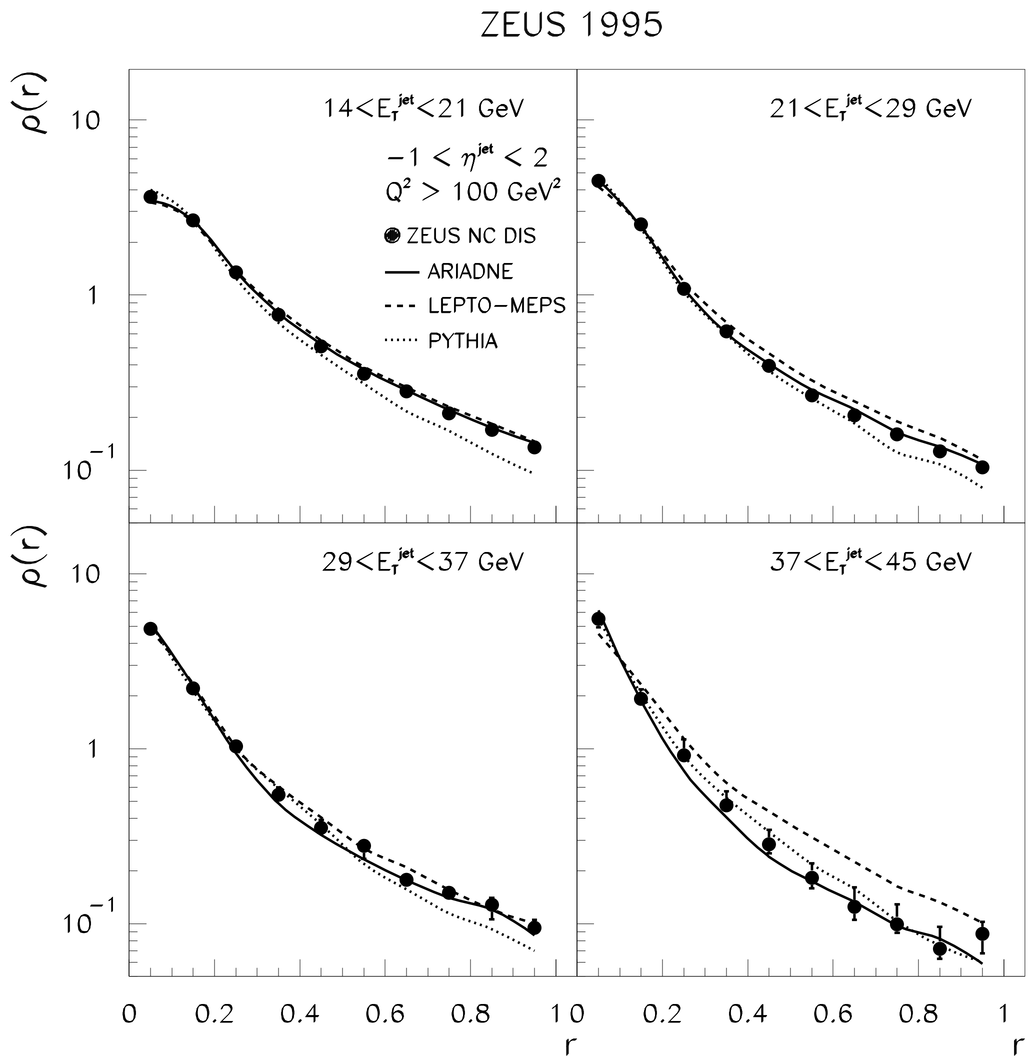

Figure 4.18: Measured differential jet shapes corrected to the hadron level, $\rho(r)$, for jets in neutral-current DIS at $Q^2 > 100$ GeV^2 in the η^{jet} range between -1 and 2 in different E_T^{jet} regions. The error bars show the statistical and systematic errors added in quadrature. For comparison, the expectations of PYTHIA (dotted line), ARIADNE-CDM (solid line), and LEPTO-MEPS (dashed line) are shown.

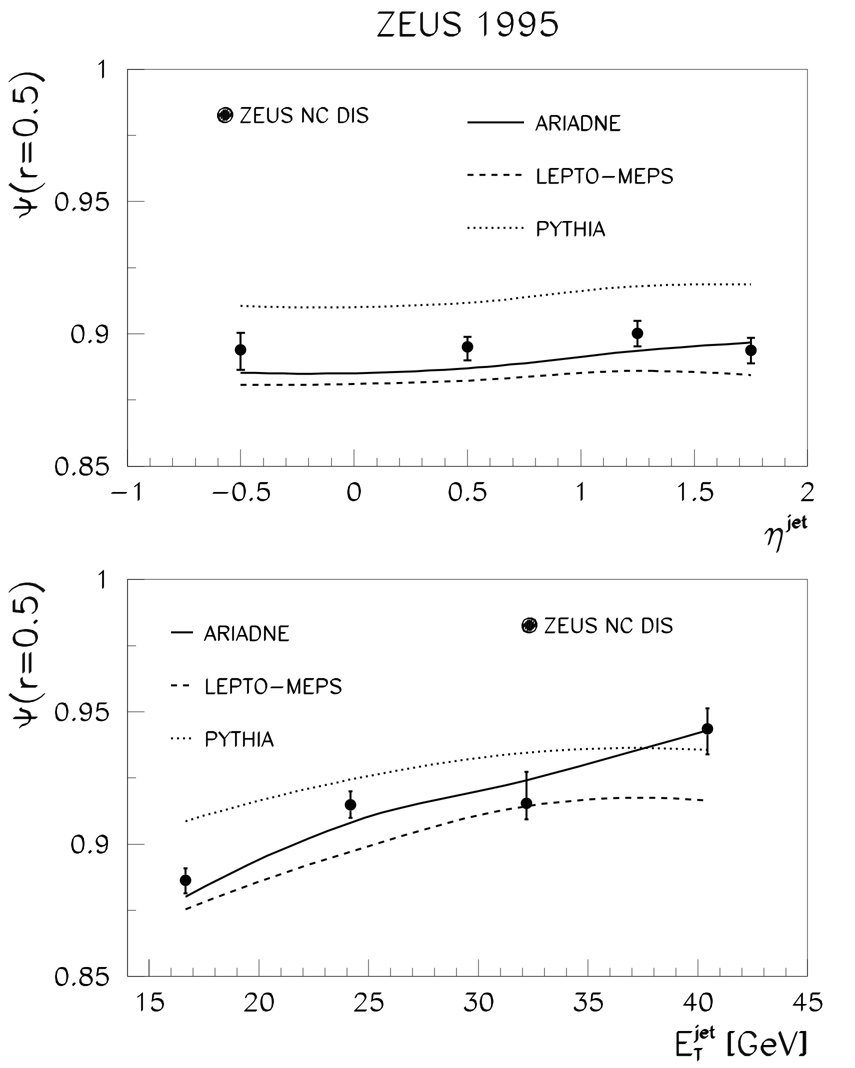

Figure 4.19: Measured integrated jet shape corrected to the hadron level at $r = 0.5$, $\psi(r = 0.5)$, for jets in neutral-current DIS at $Q^2 > 100$ GeV^2 as a function of η^{jet} and E_T^{jet}. The error bars show the statistical and systematic errors added in quadrature. For comparison, the expectations of PYTHIA (dotted line), ARIADNE-CDM (solid line), and LEPTO-MEPS (dashed line) are shown.

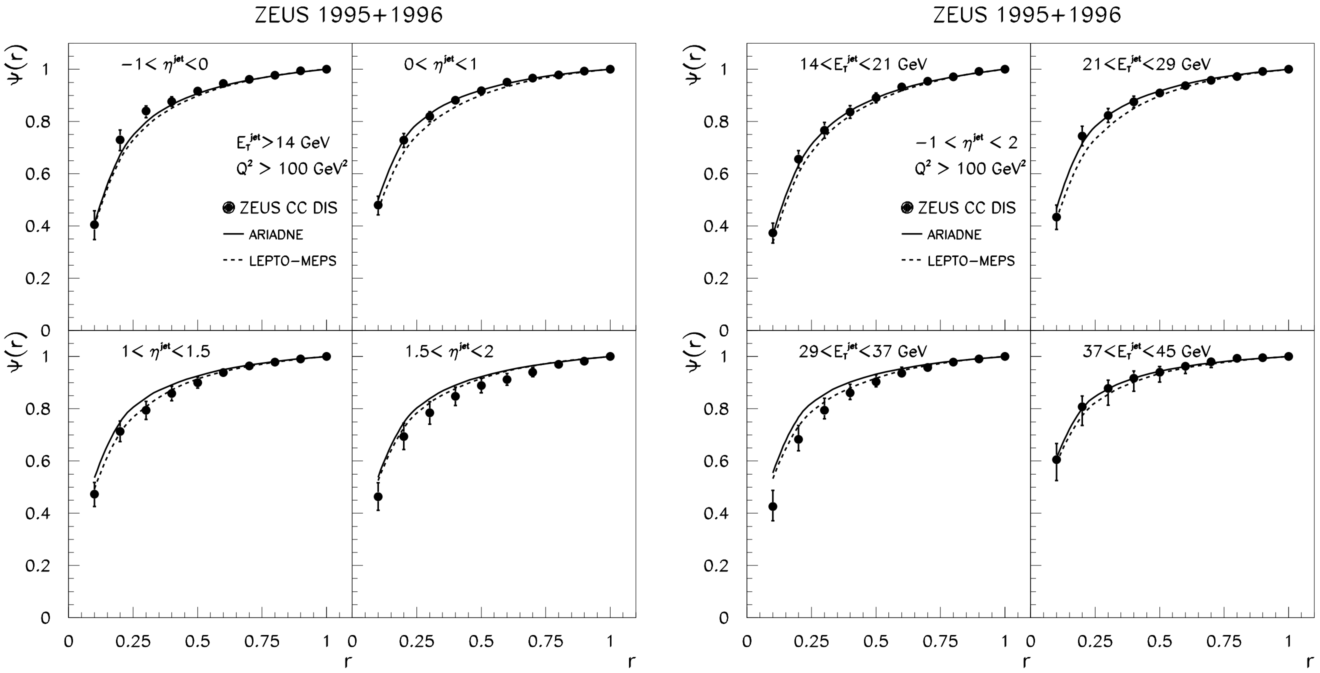

Figure 4.20: Measured integrated jet shapes corrected to the hadron level, $\psi(r)$, for jets in charged-current DIS at $Q^2 > 100$ GeV^2 in different η^{jet} and E_T^{jet} regions. The error bars show the statistical and systematic errors added in quadrature. For comparison, the expectations of ARIADNE-CDM (solid line) and LEPTO-MEPS (dashed line) are shown.

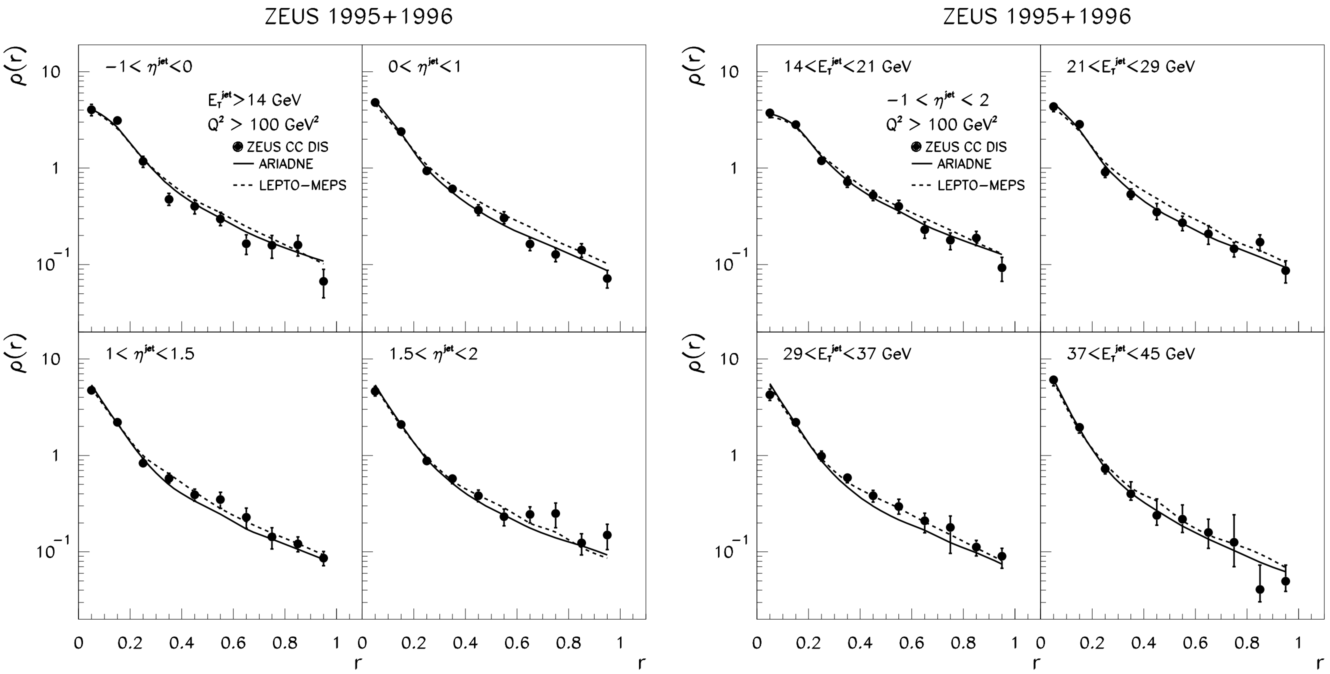

Figure 4.21: Measured differential jet shapes corrected to the hadron level, $\rho(r)$, for jets in charged-current DIS at $Q^2 > 100$ GeV^2 in different η^{jet} and E_T^{jet} regions. The error bars show the statistical and systematic errors added in quadrature. For comparison, the expectations of ARIADNE-CDM (solid line) and LEPTO-MEPS (dashed line) are shown.

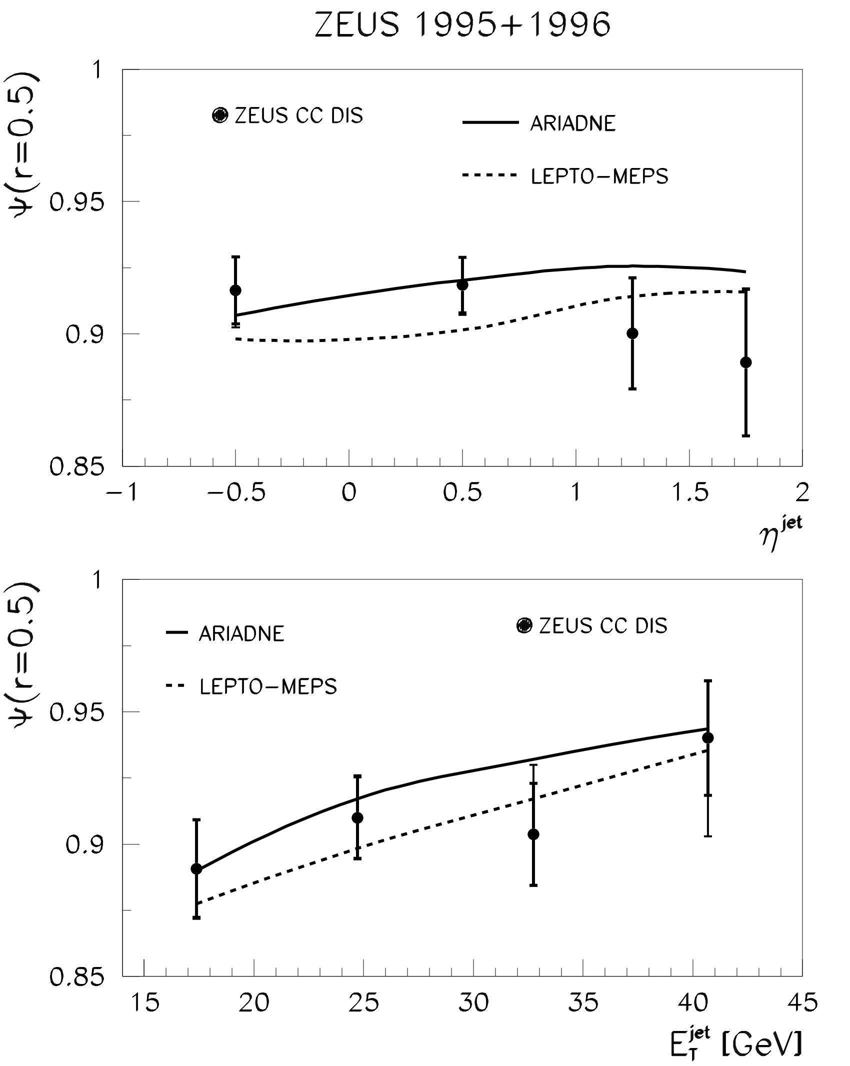

Figure 4.22: Measured integrated jet shapes corrected to the hadron level, $\psi(r = 0.5)$, for jets in charged-current DIS at $Q^2 > 100$ GeV^2 as a function of η^{jet} and E_T^{jet}. The thick error bars show the statistical errors. The thin error bars show the statistical and systematic errors added in quadrature. For comparison, the expectations of ARIADNE-CDM (solid line) and LEPTO-MEPS (dashed line) are shown.

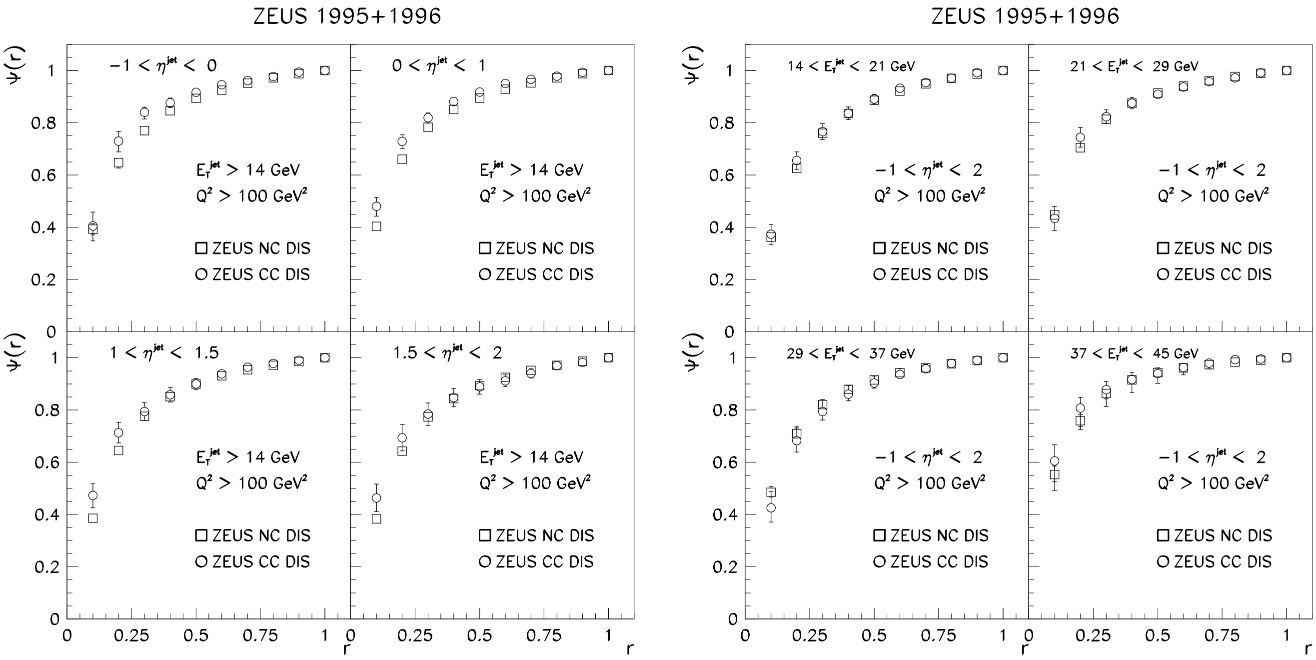

Figure 4.23: Measured integrated jet shapes corrected to the hadron level, $\psi(r)$, for jets in charged-current DIS at $Q^2 > 100$ GeV^2 in different η^{jet} and E_T^{jet} regions (open circles). For comparison, the measured jet shapes corrected to the hadron level for jets in neutral-current DIS at $Q^2 > 100$ GeV^2 in the same η^{jet} and E_T^{jet} regions as above are shown (open squares).

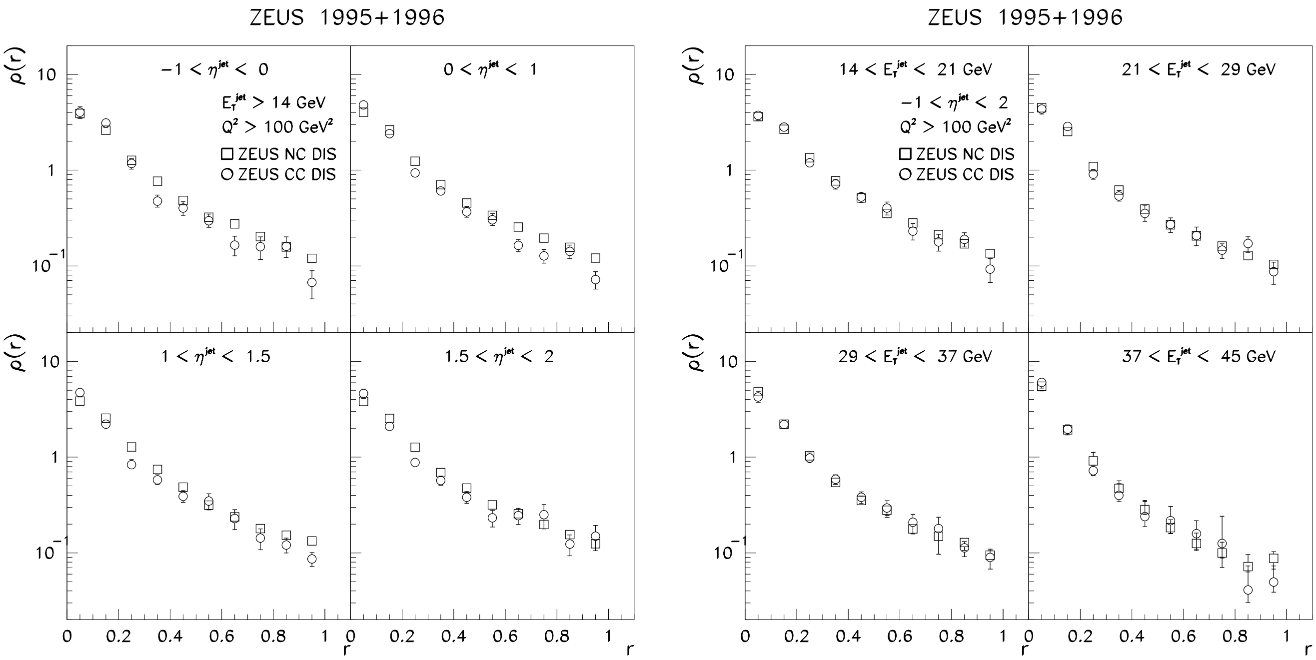

Figure 4.24: Measured differential jet shapes corrected to the hadron level, $\rho(r)$, for jets in charged-current DIS at $Q^2 > 100$ GeV^2 in different η^{jet} and E_T^{jet} regions (open circles). For comparison, the measured jet shapes corrected to the hadron level for jets in neutral-current DIS at $Q^2 > 100$ GeV^2 in the same η^{jet} and E_T^{jet} regions are shown (open squares).

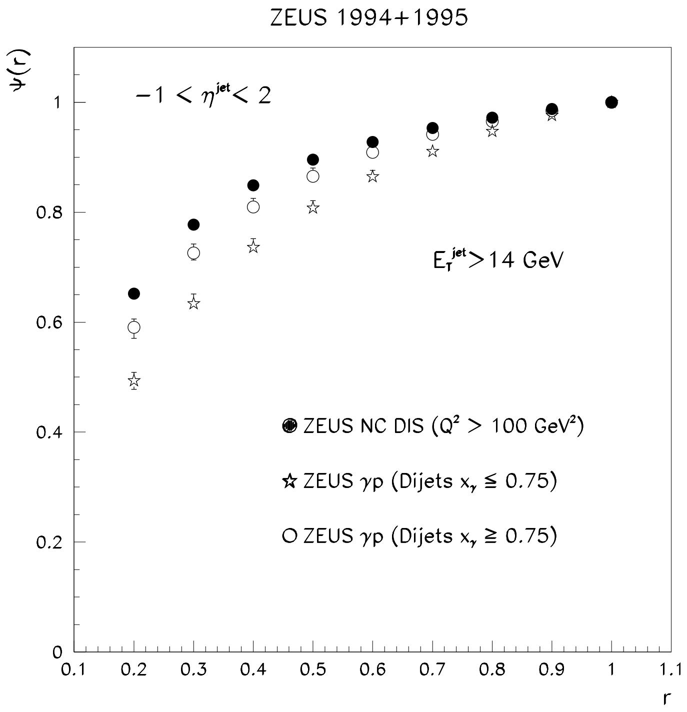

Figure 4.25: Measured integrated jet shapes corrected to the hadron level, $\psi(r)$, for jets in neutral-current DIS at $Q^2 > 100$ GeV^2 with E_T^{jet} above 14 GeV and $-1 < \eta^{jet} < 2$ (black dots). For comparison, the measured jet shapes corrected to the hadron level for jets in photoproduction with E_T^{jet} above 14 GeV and in the same η^{jet} region are shown: for dijet photoproduction $x_\gamma^{OBS} \leq 0.75$ (stars) and for dijet photoproduction with $x_\gamma^{OBS} \geq 0.75$ (open circles).

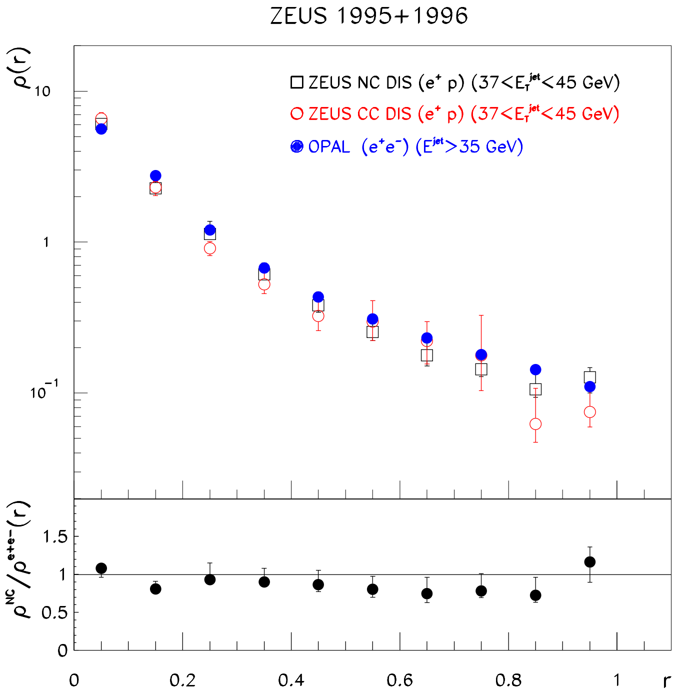

Figure 4.26: Measured differential jet shapes corrected to hadron level, $\rho(r)$, in neutral (charged) current DIS at $Q^2 > 100$ GeV^2 for jets with $-1 < \eta^{jet} < 2$ and $37 < E_T^{jet} < 45$ GeV are shown as squares (open circles). For comparison, the measurements of jet shapes in e^+e^- interactions by OPAL (black dots) are shown.

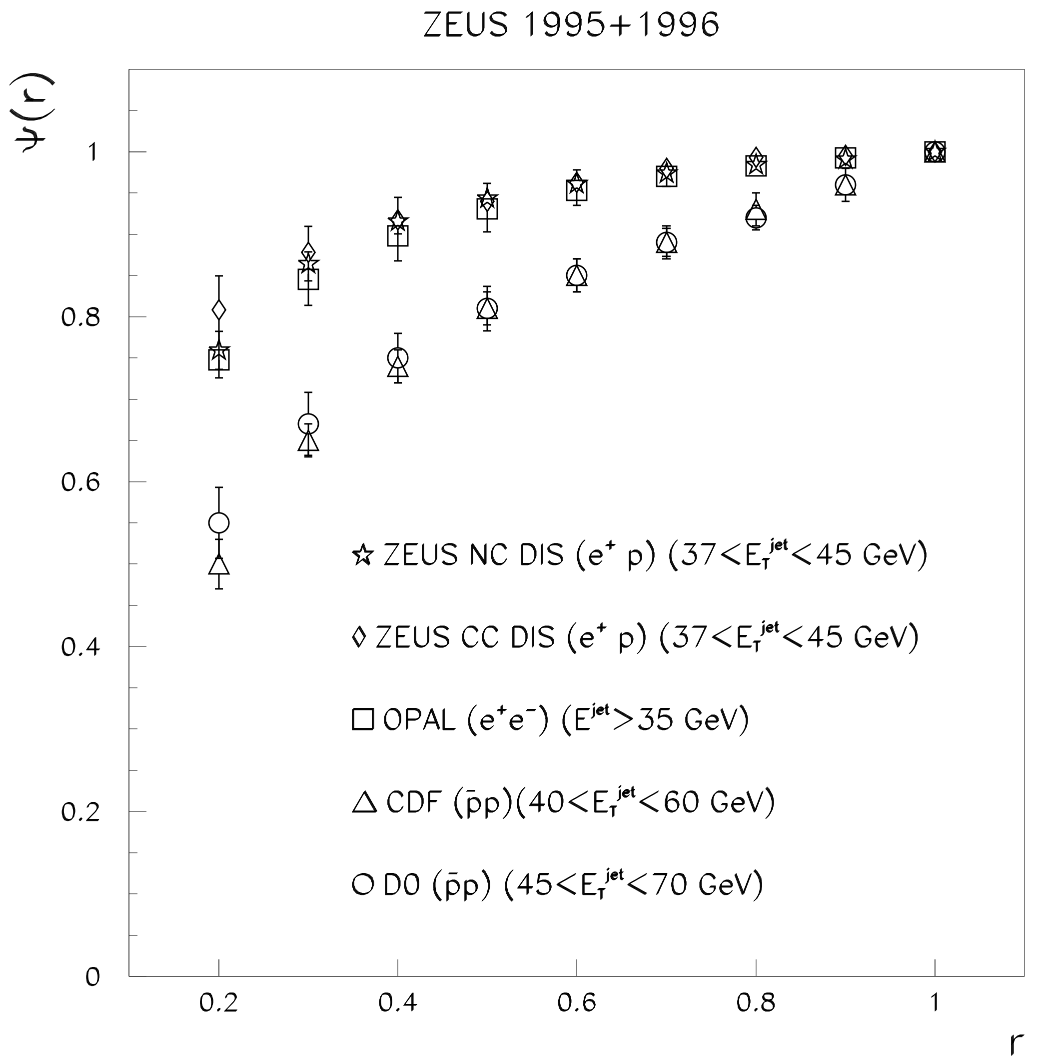

Figure 4.27: The measured jet shapes corrected to the hadron level, $\psi(r)$, for jets in neutral (charged) current DIS at $Q^2 > 100$ GeV^2 with η^{jet} in the range between -1 and 2 and $37 < E_T^{jet} < 45$ GeV are shown as stars (diamonds). For comparison, the measurements of jet shapes in $\bar{p}p$ collisions by CDF (triangles) and D0 (circles), and e^+e^- interactions by OPAL (squares) are shown.

Bibliography

[1] CDF Collab., F. Abe et al., Phys. Rev. D45 (1992) 1448.

[2] J. Huth et al., Proc. of the 1990 DPF Summer Study on High Energy Physics, Snowmass, Colorado, edited by E.L. Berger (World Scientific, Singapore,1992) p. 134.

[3] S.D. Ellis, Z. Kunszt and D.E. Soper, Phys. Rev. Lett. 69 (1992) 3615.

[4] CDF Collab., F. Abe et al., Phys. Rev. Lett. 70 (1993) 713.

[5] D0 Collab., S. Abachi et al., Phys. Lett. B357 (1995) 500.

[6] W.T. Giele, E.W.N. Glover and D.A. Kosower, Nucl. Phys. B403 (1993) 633.

[7] OPAL Collab., R. Akers et al., Z. Phys. C63 (1994) 197.

[8] ZEUS Collab., J. Breitweg et al, preprint DESY-97-191 (hep-ex/9710002).

[9] G. Kramer and S.G. Salesch, Phys. Lett. B317 (1993) 218, Phys. Lett. B333 (1994) 519; M. Klasen and G. Kramer, Phys. Rev. D56 (1997) 465.

[10] ZEUS Collab. The ZEUS Detector, Status Report 1993, DESY 1993.

[11] ZEUS Collab., M. Derrick et al., Z. Phys. C72 (1996) 399.

[12] H.Abramowicz, A.Caldwell, R.Sinkus, Nucl. Inst. Meth. **A365** (1995) 508.

[13] S.Bentvelsen, J.Engelen, P.Kooijman, Proc. 1991 Workshop on Physics at HERA, ed. W.Buchmüller and G.Ingelman (DESY, Hamburg, 1992), Vol. 1, p.23.

[14] *Study of charged current ep interactions at $Q^2 > 200$ GeV^2 with the ZEUS detector at HERA, A final report*, J. del Peso, U. Katz, M. Martínez ZEUS-Note 96-049.

[15] ZEUS Collab., M. Derrick et al., Z. Phys. C72 (1996) 47 47.

[16] R. Brun et al., CERN DD/EE-84-1 (1987).

[17] G. Ingelman, Proceedings of the Workshop on Physics at HERA, DESY (1992), 1366.

[18] K. Kwiatkowski, H. Spiesberger and H.-J. Möhring, Proceedings of the Workshop on Physics at HERA, DESY (1992), 1294.

[19] DJANGO 6.1: G.Schuler and H.Spiesberger, Proc. 1991 Workshop on Physics at HERA, ed. W.Buchmüller and G.Ingelman (DESY, Hamburg, 1992), Vol. 3, p.1419.

[20] H.L. Lai et al., Phys. Rev. D55 (1997) 1280.

[21] Y. Azimov, Y. Dokshitzer, V. Khoze and S. Troyan, Phys. Lett. B165 (1985) 147; G. Gustafson, Phys. Lett. B175 (1986) 453; G. Gustafson and U. Petersson, Nucl. Phys. B306 (1988) 746; B. Andersson, G. Gustafson and L. Lönnblad, Z. Phys. C43 (1989) 625.

[22] L. Lönnblad, Comp. Phys. Comm. 71 (1992) 15; L. Lönnblad, Z. Phys. C65 (1995) 285.

[23] H.-U. Bengtsson and T. Sjöstrand, Comp. Phys. Comm. 46 (1987) 43; T. Sjöstrand, Comp. Phys. Comm. 82 (1994) 74.

[24] B. Andersson et al., Phys. Rep. 97 (1983) 31.

[25] J.F. Owens, Phys. Rev. D21 (1980) 54.

[26] W.J. Stirling and Z. Kunszt, Proceedings of the HERA Workshop (1987) 331; M. Drees and F. Halzen, Phys. Rev. Lett. 61 (1988) 275; M. Drees and R.M. Godbole, Phys. Rev. D39 (1989) 169.

[27] ZEUS Collab., M. Derrick et al., Phys. Lett. B322 (1994) 287; Phys. Lett. B348 (1995) 665.

[28] ZEUS Collab., M. Derrick et al., Z. Phys. C72 (1996) 47.

Chapter 5

Measurement of the Inclusive Jet Cross Section in High-Q^2

5.1 Introduction

At HERA, multijet events have been observed in neutral and charged-current deep-inelastic ep scattering at large Q^2 [1, 2]. Measurements of jet cross sections as a function of jet transverse energy (E_T^{jet}) and jet pseudorapidity (η^{jet}) for jets with high E_T^{jet} in neutral and charged-current DIS at high Q^2 constitute a stringent test of perturbative QCD calculations. These jet cross sections are also sensitive to the production of new particles and new interactions.

In this chapter, measurements of the differential inclusive jet cross sections $d\sigma/d\eta^{jet}$ and $d\sigma/dE_T^{jet}$ in neutral current DIS at $Q^2 > 125$ GeV^2 and $\sqrt{s} = 300$ GeV are presented. Jets are searched for with the same iterative cone algorithm used in the jet shape study [3] (see previous chapter) in the $\eta - \varphi$ plane of the laboratory frame with a cone radius $R = 1$, and are selected with $E_T^{jet} > 14$ GeV and $-1 < \eta^{jet} < 2$. The measurement of $d\sigma/dE_T^{jet}$ extends up to E_T^{jet} values of 79 GeV. The measurements are compared to Monte Carlo calculations based on next-to-leading-order electroweak and leading-order QCD matrix elements plus parton showers. The data sample used in this analysis corresponds to an integrated luminosity of 6.3 pb^{-1} .

5.2 Jet search and data selection

Jets are reconstructed from the energy measured in the UCAL cells. A detailed description of the algorithm can be found in the previous chapter. The axis of the jet is defined according to the Snowmass convention [4], where η^{jet} (φ^{jet}) is the transverse-energy weighted mean pseudorapidity (azimuth) of all the UCAL cells belonging to that jet. The UCAL cells assigned to the positron candidate are excluded from the jet search. The cone radius used in the jet search has been set equal to 1 and events with at least one jet of $E_T^{jet} > 14$ GeV and $-1 < \eta^{jet} < 2$ are retained.

Events from neutral-current DIS interactions are selected offline using the same criteria as reported in the previous chapter, and the sample is restricted to the kinematic range $Q^2 > 125$ GeV^2, where the Q^2 variable is determined using the double-angle method [5]. Figure 5.1 shows an event picture correspondig to one of the selected events. The distributions of the kinematic and jet variables from the selected data sample have been compared with the Monte Carlo expectations from ARIADNE [6] and LEPTO-MEPS [7]:

- In figure 5.2 the distributions of kinematic variables are compared between the selected data sample and the Monte Carlo simulations. Good agreement is observed in the shapes of all the distributions. It must be noted that the Q^2_{DA} distribution peaks at a value larger than the applied threshold ($Q^2 > 125\ GeV^2$) as a consequence of the E_T^{jet} requirement. The Monte Carlo predictions are able to describe the measured y distribution, even in the lowest y region. This is due to the jet requirement, which ensures some minimum transverse energy in the calorimeter.

- In figure 5.3 the distributions of scattered positron variables are compared with Monte Carlo expectations. The polar angle of the scattered positron is always smaller than 160^o due to the Q^2_{DA} requirement. The Monte Carlo predictions are able to describe these distributions.

- In figure 5.4 the distribution of the uncorrected transverse energy of the jet (E_T^{jet}) and the jet pseudorapidity distribution (η^{jet}) are compared with Monte Carlo expectations. Good agreement is observed.

5.3 Unfolding and Study of Systematic Uncertainties

The transverse energy of a jet is corrected using a procedure similar to that in the previous chapter (see appendix C). The measured distributions of the transverse energy and pseudorapidity of the jets were corrected back to the hadron level using a bin-by-bin correction which accounts for the acceptance of the selection criteria and detector effects. A preliminary systematic study, analogous to the study performed in the analysis of the jet shapes, was carried out (see figures 5.5 and 5.6). The systematic uncertainties not associated with the absolute energy scale of the UCAL have been added in quadrature to the statistical errors and are shown as thin error bars. The dominant source of systematic error ($\sim 15\%$) is due to the uncertainty on the absolute energy scale of the UCAL ($\pm 3\%$) and is shown as a shaded band in each figure. We note that this systematic uncertainty has a large degree of correlation from bin to bin. In addition, there is an overall normalisation uncertainty of 1.5% from the luminosity determination, which is not included.

5.4 Results

Using the selected data sample of jets, the differential inclusive jet cross sections for the reaction $ep \to e$ + jet + X in the kinematic region defined by $Q^2 > 125$ GeV^2 have been measured. These cross sections refer to jets at the hadron level with a cone radius of 1 unit in the $\eta - \varphi$ plane. The cross section $d\sigma/d\eta^{jet}$ has been measured in the η^{jet} range between -1 and 2 integrated over E_T^{jet} above 14 GeV. The cross section $d\sigma/dE_T^{jet}$ has been measured in the E_T^{jet} range between 14 GeV and 79 GeV integrated over $-1 < \eta^{jet} < 2$. The results are presented in Figures 5.7 and 5.8. In both figures, the statistical errors are indicated as thick error bars. The measured $d\sigma/d\eta^{jet}$ increases as η^{jet} increases and reaches a plateau at $\eta^{jet} \sim 1$. The measured $d\sigma/dE_T^{jet}$ exhibits a steep fall-off of 3 orders of magnitude in the E_T^{jet} range considered.

Monte Carlo calculations based on next-to-leading-order electroweak [8] and leading-order QCD matrix elements ($eq \rightarrow eqg$ and $eg \rightarrow eq\bar{q}$) as implemented in the LEPTO program [7] are compared to the measurements. Both photon and Z° exchanges are included, and the CTEQ4 [9] proton parton distributions have been used. Additional QCD parton radiation is simulated using a leading-logarithm parton-shower approximation. The final-state parton system is hadronised using the LUND string model [10] as implemented in JETSET [11]. The predictions for the jet cross sections, shown in Figures 5.7 and 5.8, have been obtained by selecting jets of hadrons using the same jet algorithm as for the data. The shape and magnitude of the measured $d\sigma/dE_T^{jet}$ and $d\sigma/d\eta^{jet}$ are described by the predictions in the entire kinematic region studied. These measurements provide a testing ground for perturbative QCD calculations.

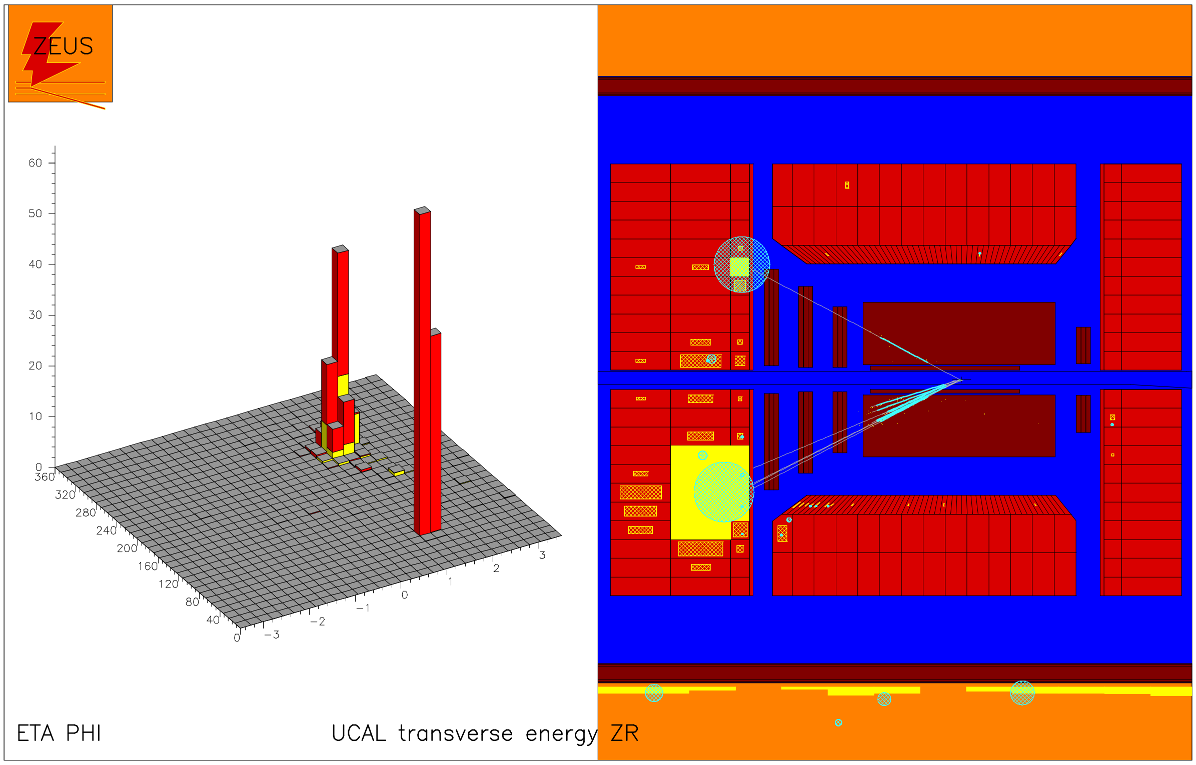

Figure 5.1: Event picture corresponding to one of the selected neutral-current events.

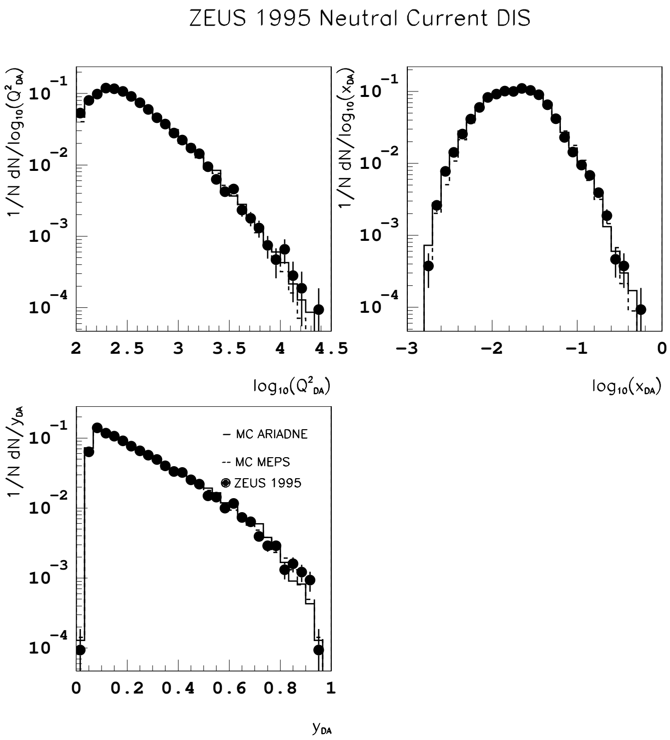

Figure 5.2: Comparison of some kinematic distributions between the selected NC DIS data sample and the Monte Carlo expectations from ARIADNE (solid line) and LEPTO-MEPS (dashed line) programs.

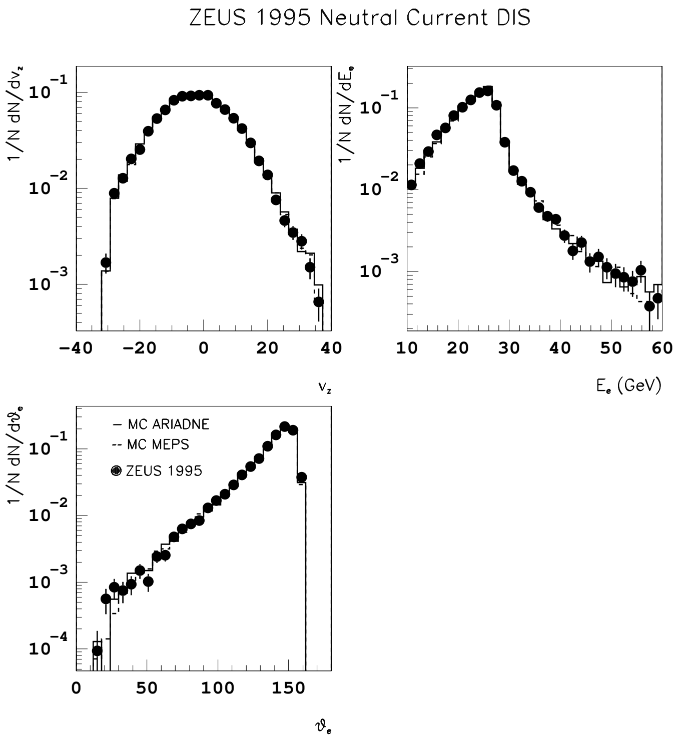

Figure 5.3: Comparison of some kinematic distributions between the selected NC DIS data sample and the Monte Carlo expectations from ARIADNE (solid line) and LEPTO-MEPS (dashed line) programs.

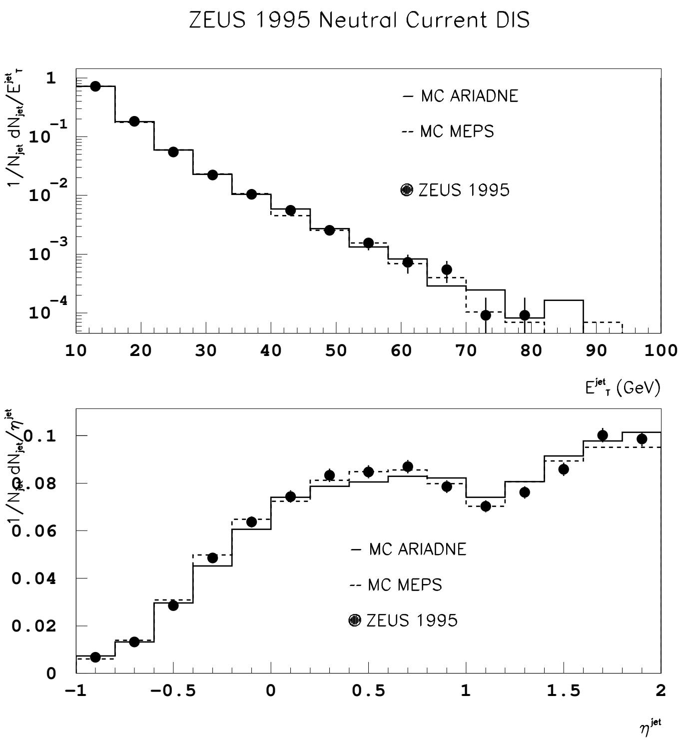

Figure 5.4: Comparison of the jet distributions between the selected NC DIS data sample and the Monte Carlo expectations from ARIADNE (solid line) and LEPTO-MEPS (dashed line) programs.

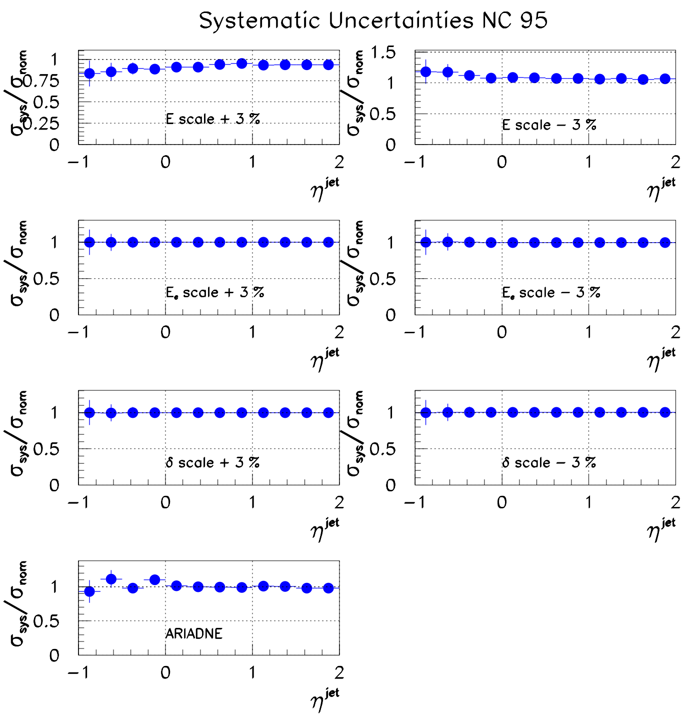

Figure 5.5: Study of systematic uncertainties performed in the measurement of $d\sigma/d\eta^{jet}$. The central value was computed using the correction factors from LEPTO-MEPS to unfold the data.

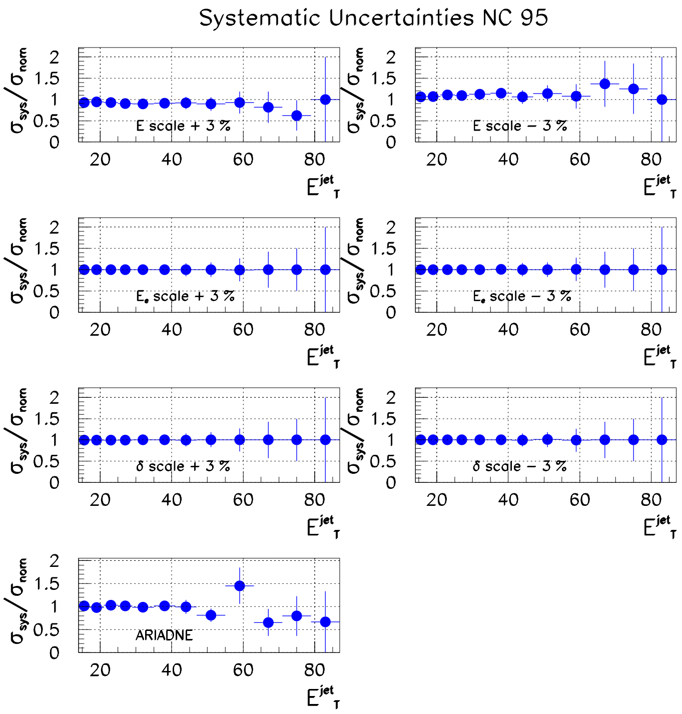

Figure 5.6: Study of systematic uncertainties performed in the measurement of $d\sigma/dE_T^{jet}$. The central value was computed using the correction factors from LEPTO-MEPS to unfold the data.

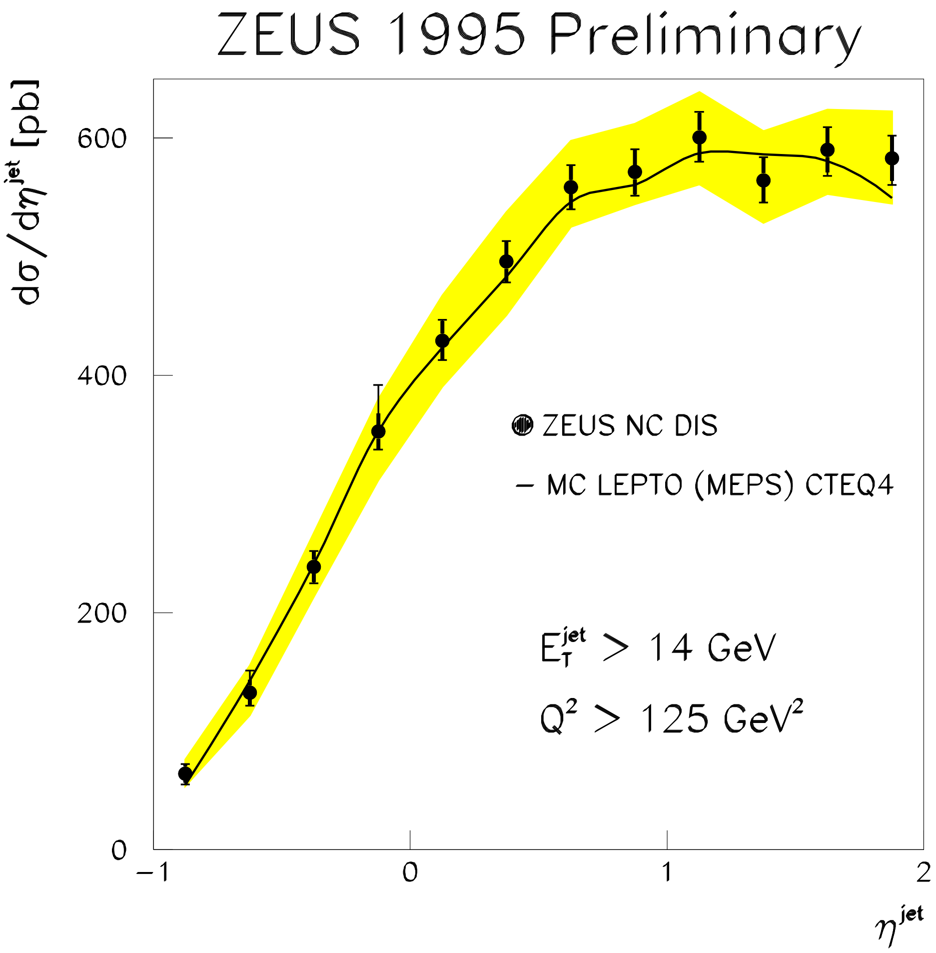

Figure 5.7: Measured differential cross section $d\sigma/d\eta^{jet}$ for inclusive jet production in neutral-current DIS with $Q^2 > 125$ GeV^2 integrated over $E_T^{jet} > 14$ GeV (black dots). The thick error bars represent the statistical errors of the data, and the thin error bars show the statistical errors and systematic uncertainties not associated with the absolute energy scale of the UCAL added in quadrature. The shaded band displays the uncertainty due to the absolute energy scale of the UCAL. For comparison, the prediction of LEPTO based on next-to-leading-order electroweak and leading-order QCD matrix elements plus parton showers (MEPS) and using the CTEQ4 proton parton distributions (solid line) is shown.

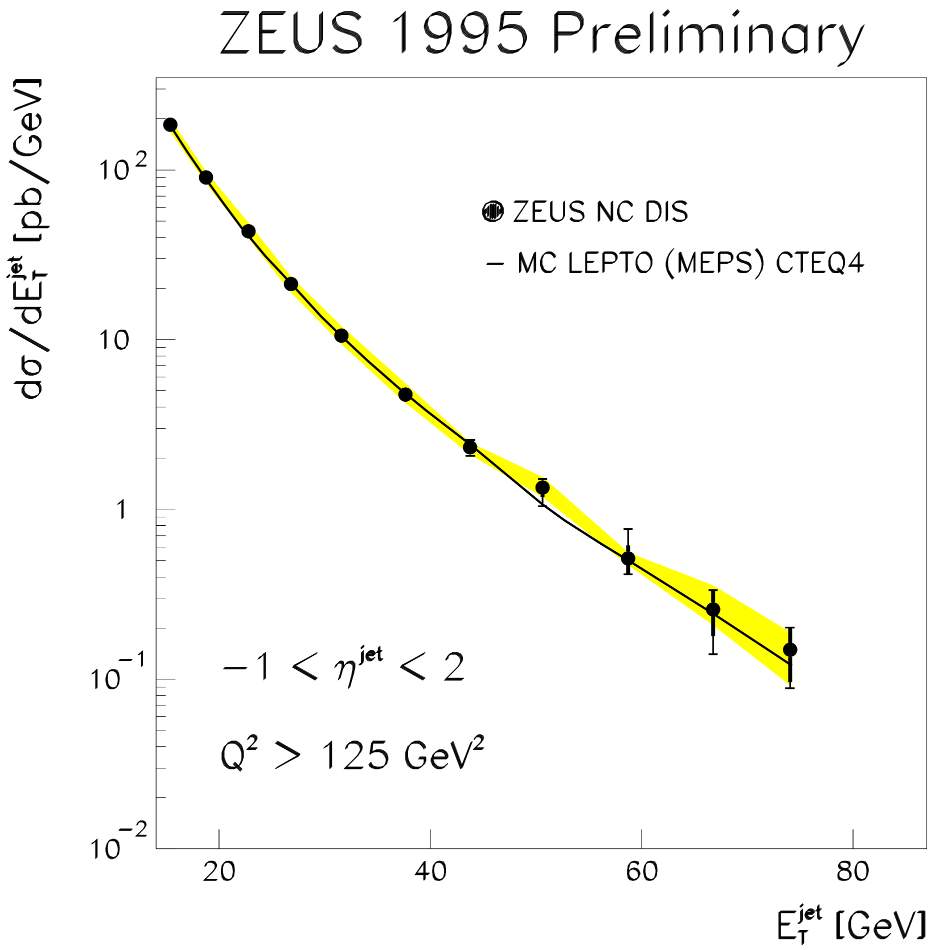

Figure 5.8: Measured differential cross section $d\sigma/dE_T^{jet}$ for inclusive jet production in neutral current DIS with $Q^2 > 125$ GeV^2 integrated over $-1 < \eta^{jet} < 2$ (black dots). The thick error bars represent the statistical errors of the data, and the thin error bars show the statistical errors and systematic uncertainties not associated with the absolute energy scale of the UCAL added in quadrature. The shaded band displays the uncertainty due to the absolute energy scale of the UCAL. For comparison, the prediction of LEPTO based on next-to-leading-order electroweak and leading-order QCD matrix elements plus parton showers (MEPS) and using the CTEQ4 proton parton distributions (solid line) is shown.

Bibliography

[1] ZEUS Collab., M. Derrick et al., Phys. Lett. B306 (1993) 158, Zeit. f. Phys. C67 (1995) 81 and Phys. Lett. B363 (1995) 201.

[2] H1 Collab., I. Abt et al., Zeit. f. Phys. C61 (1994) 59 and Phys. Lett. B346 (1995) 415.

[3] CDF Collab., F. Abe et al., Phys. Rev. D45 (1992) 1448.

[4] J. Huth et al., Proc. of the 1990 DPF Summer Study on High Energy Physics, Snowmass, Colorado, edited by E.L. Berger (World Scientific, Singapore,1992) p. 134.

[5] S. Bentvelsen, J. Engelen and P. Kooijman, Proceedings of the Workshop on Physics at HERA, DESY (1992), 23.

[6] L.Lönnblad, LU TP–89–10;
L.Lönnblad, Comp. Phys. Comm. **71**(1992)15.

[7] G. Ingelman, Proceedings of the Workshop on Physics at HERA, DESY (1992), 1366.

[8] K. Kwiatkowski, H. Spiesberger and H.-J. Möhring, Proceedings of the Workshop on Physics at HERA, DESY (1992), 1294.

[9] H.L. Lai et al., Phys. Rev. D55 (1997) 1280.

[10] B. Andersson et al., Phys. Rep. 97 (1983) 31.

[11] H.-U. Bengtsson and T. Sjöstrand, Comp. Phys. Comm. 46 (1987) 43; T. Sjöstrand, Comp. Phys. Comm. 82 (1994) 74.

Chapter 6

Summary and Conclusions

In this thesis, measurements have been presented of cross sections and jet structure in neutral and charged-current deep inelastic scattering at high-Q^2, using the ZEUS detector at HERA.

The cross sections for charged–current deep inelastic scattering $e^+p \to \overline{\nu}X$ and $e^-p \to \nu X$ have been measured in the kinematic region $x > 0.006$ and $Q^2 > 200\,\mathrm{GeV}^2$, using the e^+p and e^-p data collected with the ZEUS detector during 1993 and 1994. The integrated cross sections are measured to be

$$\begin{aligned}
\sigma_{e^+p\to\overline{\nu}X}(Q^2{>}200\,\mathrm{GeV}^2) &= 30.3\,^{+\ 5.5}_{-\ 4.2}\,[\mathrm{stat}]\,^{+1.6}_{-2.6}\,[\mathrm{syst}]\,\mathrm{pb} \\
\sigma_{e^-p\to\nu X}(Q^2{>}200\,\mathrm{GeV}^2) &= 54.7\,^{+15.9}_{-\ 9.8}\,[\mathrm{stat}]\,^{+2.8}_{-3.4}\,[\mathrm{syst}]\,\mathrm{pb}
\end{aligned}$$

and found to be in good agreement with the Standard Model expectations of 32.3 pb and 65.8 pb, respectively. The differential cross sections have been measured as functions of Q^2, x and y. The differences between e^+p and e^-p scattering, which are expected from the $V - A$ helicity structure of the weak interaction and from the quark content of the proton, are clearly observed. No significant deviation from the Standard Model predictions is found. The measured Q^2 dependence of the differential cross sections for e^+ and e^--induced CC DIS reactions is used to determine the W mass. The measured value of M_W is

$$M_W = 79\,^{+8}_{-7}\,^{+4}_{-4}\,\mathrm{GeV},$$

and found to be in good agreement with direct measurements. The measured cross sections $d\sigma/dQ^2$ for neutral and charged-current interactions are observed to be comparable in the region $Q^2 > 5000$ GeV^2, demonstrating the equal strengths of the weak and electromagnetic forces at high Q^2 as a consequence of the unification of electromagnetic and weak interactions at the (W,Z) mass scale.

The shape of the jets produced in high-Q^2 interactions has been measured. Measurements of integrated and differential jet shapes in neutral and charged-current deep inelastic ep scattering at $\sqrt{s} = 300$ GeV using data collected by ZEUS in 1995 and 1996 have been presented. The jet shapes refer to jets at the hadron level with a cone radius of one unit in the $\eta - \phi$ plane and are given for $Q^2 > 100$ GeV^2 . Jets with $E_T^{jet} > 14$ GeV and $-1 < \eta^{jet} < 2$ have been considered. In neutral-current DIS, the jet narrows as E_T^{jet} increases, but no significant η^{jet} dependence of the jet shape has been observed. The measured jet shapes have been compared to the predictions of Monte Carlo generators using different approximations for the QCD radiation. It is concluded that only those models which incorporate $O(\alpha_s)$ QCD matrix elements provide a reasonable description of the measured jet shapes in all the η^{jet} and E_T^{jet} regions studied. The measured jet shapes in neutral and charged-current DIS are found to be very similar to each other. The jet shapes in neutral-current DIS are measured to be narrower than those in dijet photoproduction and closer to those in direct processes for the same ranges in jet transverse energy and pseudorapidity. The jets in DIS are found to be narrower than those in $\bar{p}p$ collisions. This difference can be attributed to a larger contribution of gluon jets in $\bar{p}p$ collisions. The measured jet shapes in neutral and charged-current DIS are very similar to those in e^+e^- interactions for comparable ranges of jet transverse energy. Since the jets in e^+e^- interactions and deep inelastic e^+p scattering are predominantly quark initiated, the similarity in the jet shapes indicates that the pattern of final state QCD radiation around a primary quark is to a large extent independent of the hard scattering process.

Finally, measurements of inclusive jet differential cross sections in neutral-current deep inelastic ep scattering at $\sqrt{s} = 300$ GeV using data collected by ZEUS in 1995 have been performed. The jet cross sections, $d\sigma/d\eta^{jet}$ and $d\sigma/dE_T^{jet}$, refer to jets at the hadron level with a cone radius of one unit in the $\eta - \varphi$ plane and are given for $Q^2 > 125$ GeV^2 . The cross section $d\sigma/d\eta^{jet}$ has been measured in the η^{jet} range between -1 and 2 integrated over $E_T^{jet} > 14$ GeV. The cross section $d\sigma/dE_T^{jet}$ has been measured in the E_T^{jet} range between 14 GeV and 79 GeV integrated over $-1 < \eta^{jet} < 2$. Monte Carlo calculations based on next-to-leading-order electroweak and leading-order QCD matrix elements plus parton showers describe the shape and magnitude of the measured cross sections. These measurements provide a testing ground for perturbative QCD calculations.

Appendix A

Neutral Current Control Sample

A.1 Global correction

The first global correction procedure and its description by the charged current Monte Carlo is cross checked using the neutral current reweighted sample. In figures (A.1 - A.3) the resolution of the kinematic variables after the correction is shown. The correction method is checked for the different bins of Q^2 and x using the NC sample, considering the double angle variables as the true variables (see figures A.4 - A.6).

A.2 Efficiencies

The efficiencies computed from the Monte Carlo have been also cross checked using this NC sample. The comparison with the Monte Carlo predictions is presented in figure A.7 for e^+p in bins of Q^2,x and y. The global selection efficiency for e^+p and e^-p is also compared with the value obtained from the CC MC (see table A.1). Considering a NC selection efficiency around 90%, the final value, after all cuts were applied, is quite similar to the value obtained from the CC MC.

A.3 Unfolding

The smearing matrices used for the Bayes unfolding procedure as extracted from the NC sample were found compatible with those obtained from MC CC (within the present limitations of the NC study).

$$\begin{pmatrix} 32.3 & 12.3 & 0.2 & 0.0 & 0.0 \\ 4.3 & 45.2 & 14.2 & 2.8 & 0.0 \\ 0.0 & 4.7 & 57.3 & 28.2 & 7.1 \\ 0.0 & 0.0 & 3.2 & 50.7 & 26.3 \\ 0.0 & 0.0 & 0.0 & 0.0 & 48.1 \end{pmatrix}$$

$$A_{ij}(NC\ reweighted) = Q^2_{i,cor,cuts}/Q^2_{j,da}(\%)$$

$$\begin{pmatrix} 55.9 & 14.4 & 0.0 & 0.0 & 0.0 \\ 7.5 & 52.8 & 14.3 & 2.0 & 0.0 \\ 0.0 & 5.5 & 58.7 & 19.7 & 0.0 \\ 0.0 & 0.0 & 3.2 & 35.8 & 1.6 \\ 0.0 & 0.0 & 0.0 & 0.3 & 35.5 \end{pmatrix}$$

$$B_{ij}(NC\ reweighted) = x_{i,cor,cuts}/x_{j,da}(\%)$$

$$\begin{pmatrix} 43.8 & 7.8 & 0.0 & 0.0 & 0.0 \\ 1.3 & 76.9 & 18.8 & 0.0 & 0.0 \\ 0.0 & 2.7 & 59.8 & 27.6 & 0.0 \\ 0.0 & 0.0 & 0.8 & 39.5 & 49.3 \\ 0.0 & 0.0 & 0.0 & 0.9 & 15.0 \end{pmatrix}$$

$$C_{ij}(NC\ reweighted) = y_{i,cor,cuts}/y_{j,gen}(\%)$$

A.4 Systematic checks.

Systematic checks were redone using the “modified” NC sample. The results obtained for the e^+p case are shown in tables (A.2,A.3,A.4). Due to the observed differences in the kinematic distributions between the CC Monte Carlo and the NC reweighted sample (see figures A.8,A.9), the comparison of the systematics only allowed to check that the order of magnitude and the variation with systematic check is similar to the obtained from the CC MC.

CUTS NC reweighted DATA ($Q^2_{cor} > 200GeV^2$)	$\sum_i w_i$ (e^+)	$\sum_i w_i$ (e^-)
($Q^2_{cor} > 200GeV^2$)	70.26 (100 %)	7.90 (100 %)
Trigger	65.35 (93.0 %)	7.37 (93.3 %)
$\not{P}_t > 11\ GeV$	62.62 (89.1 %)	7.26 (91.9 %)
$\lvert V_z \rvert < 45\ cm$	60.12 (85.6 %)	6.93 (87.8 %)
$\not{P}_t^{out} / \not{P}_t > 0.6$	58.15 (82.7 %)	6.75 (85.5 %)
Good Tracks	56.05 (79.7 %)	6.64 (84.2 %)
$\lvert \Delta\phi \rvert < 1$	54.03 (76.9 %)	6.62 (83.8 %)
$y_{jb} < 0.8$	53.91 (76.7 %)	6.43 (81.4 %)
$\not{P}_t / E_t > 0.4$	52.77 (75.1 %)	6.26 (79.4 %)
$\not{P}_t^{tracks} / \not{P}_t > 0.1$	50.94 (72.5 %)	6.22 (78.8 %)
Muon,Timing,Sparks	50.79 (72.3 %)	6.20 (78.5 %)

Table A.1: Global CC efficiency from the NC reweighted sample. Taking into account the NC selection global efficiency (around 90%,) the value for the final efficiency is in reasonable agreement with the prediction obtained from CC MC.

CUT	Q^2_1 (%)	Q^2_2 (%)	Q^2_3 (%)	Q^2_4 (%)	Q^2_5 (%)
Energy +3%	8.0	5.6	1.1	-2.2	-9.1
Energy −3%	-9.4	-1.2	-2.3	2.0	11.9
$\not{P}_t > 12\ GeV$	-8.1	-1.6	0.4	0.0	0.0
$\not{P}_t > 10\ GeV$	4.5	0.06	0.01	0.0	0.0
$\not{P}_t^{tracks} / \not{P}_t > 0.12$	-1.2	-1.8	-2.6	-0.9	0.0
$\not{P}_t^{tracks} / \not{P}_t > 0.08$	0.4	1.0	-0.04	-0.08	-0.1
$\lvert \Delta\phi \rvert < 0.8$	-0.4	0.7	-0.5	-0.5	0.4
$\lvert \Delta\phi \rvert < 1.2$	0.3	-0.3	-0.3	1.4	-0.1
$\not{P}_t / E_t > 0.45$	0.2	-0.3	-0.3	0.3	0.0
$\not{P}_t / E_t > 0.35$	0.1	-0.4	-0.7	-0.2	0.0
$y < 0.75$	0.0	0.0	0.2	0.6	1.2
$y < 0.85$	0.0	0.0	-0.01	-0.6	-1.9
Good Tracks	4.9	2.3	3.9	1.0	8.5

Table A.2: Systematics from reweighted NC DIS DATA sample e^+p

CUT	x_1 (%)	x_2 (%)	x_3 (%)	x_4 (%)	x_5 (%)
Energy $+3\%$	5.6	4.1	0.7	-1.9	-8.2
Energy -3%	-3.4	-3.3	-0.7	0.8	10.1
$\not{P}_t > 12\ GeV$	-8.4	-0.1	-0.3	0.0	0.0
$\not{P}_t > 10\ GeV$	3.6	1.1	0.3	0.0	0.0
$\not{P}_t^{tracks}/\not{P}_t > 0.12$	-2.0	-0.4	-3.7	-1.5	0.0
$\not{P}_t^{tracks}/\not{P}_t > 0.08$	-1.0	-0.6	0.7	1.3	0.0
$\|\Delta\phi\| < 0.8$	0.1	-0.6	0.5	-0.3	0.6
$\|\Delta\phi\| < 1.2$	0.3	-0.3	-0.4	0.7	3.0
$\not{P}_t/E_t > 0.45$	2.0	-0.5	0.7	0.0	0.0
$\not{P}_t/E_t > 0.35$	-3.0	-0.7	-0.4	0.0	0.0
$y < 0.75$	0.0	0.2	1.3	0.1	0.0
$y < 0.85$	0.0	-0.2	-0.9	-0.6	0.0
Good Tracks	0.2	0.4	0.4	2.5	-0.5

Table A.3: Systematics from reweighted NC DIS DATA sample e^+p

CUT	y_1 (%)	y_2 (%)	y_3 (%)	y_4 (%)	y_5 (%)
Energy $+3\%$	3.1	-0.4	-0.5	-4.5	-25.0
Energy -3%	-4.3	0.6	1.9	7.5	24.7
$\not{P}_t > 12\ GeV$	-2.3	-1.4	-2.3	-3.2	1.8
$\not{P}_t > 10\ GeV$	3.3	0.9	1.7	-0.4	26.0
$\not{P}_t^{tracks}/\not{P}_t > 0.12$	-2.2	-2.1	-1.0	-2.0	0.0
$\not{P}_t^{tracks}/\not{P}_t > 0.08$	2.1	-0.04	-0.5	-0.6	0.0
$\|\Delta\phi\| < 0.8$	-0.07	0.2	0.1	-1.2	-9.2
$\|\Delta\phi\| < 1.2$	1.4	-0.3	-0.3	-0.2	0.0
$\not{P}_t/E_t > 0.45$	-0.09	0.4	-1.0	-2.3	-9.2
$\not{P}_t/E_t > 0.35$	0.3	0.2	0.3	-2.2	-1.8
$y < 0.75$	0.0	0.0	0.0	0.0	5.0
$y < 0.85$	0.0	0.0	0.0	0.0	-15.2
Good Tracks	12.0	2.5	0.5	-0.4	-16.4

Table A.4: Systematics from reweighted NC DIS DATA sample e^+p

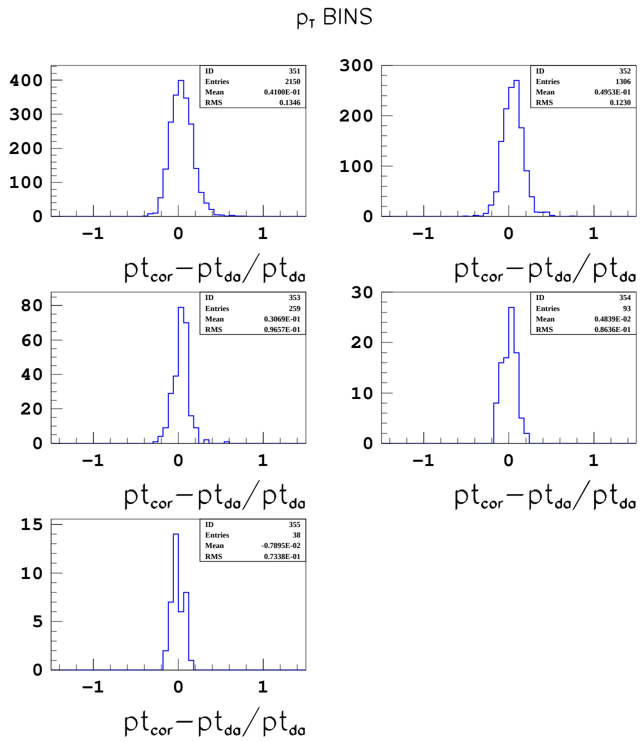

Figure A.1: Comparison of $P_{T,cor}$ and $P_{T,DA}$ using the reweighted neutral current sample in bins of P_T.

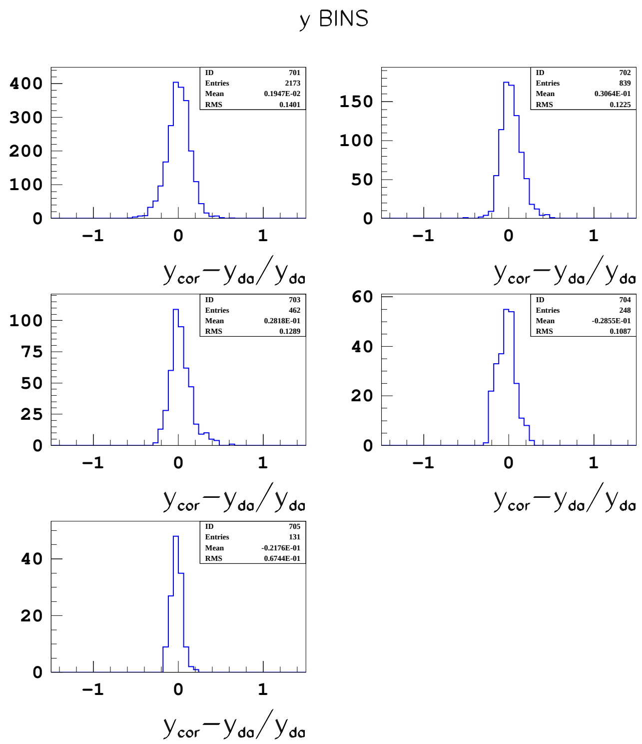

Figure A.2: Comparison of y_{cor} and y_{DA} using the reweighted neutral current sample in bins of y.

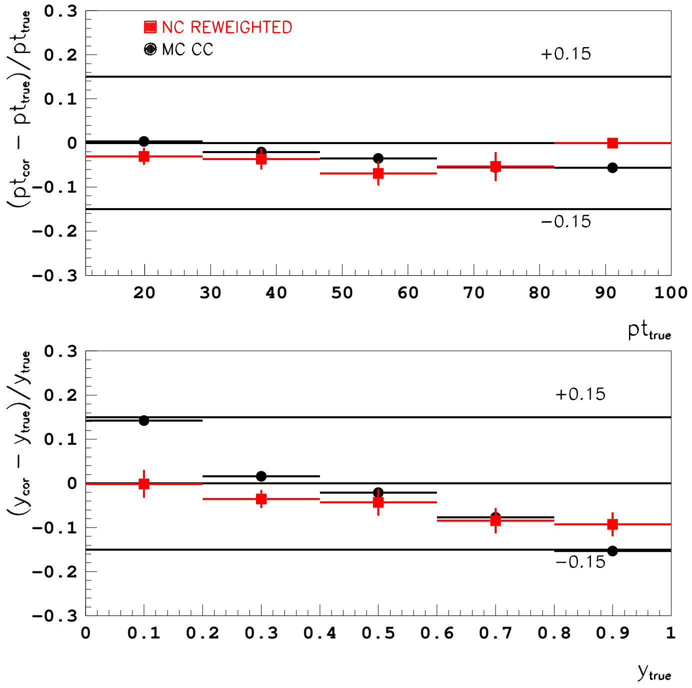

Figure A.3: Relative difference of $P_{T,cor}$ and y_{cor} respect to the true variables (double angle variables) as computed from MC CC (NC reweighted sample)

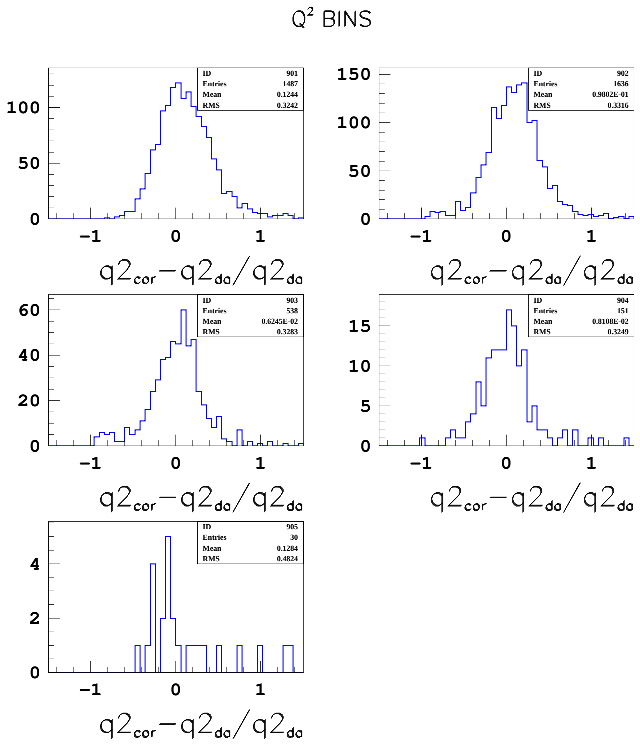

Figure A.4: Comparison of Q^2_{cor} and Q^2_{DA} using the reweighted neutral current sample in bins of Q^2.

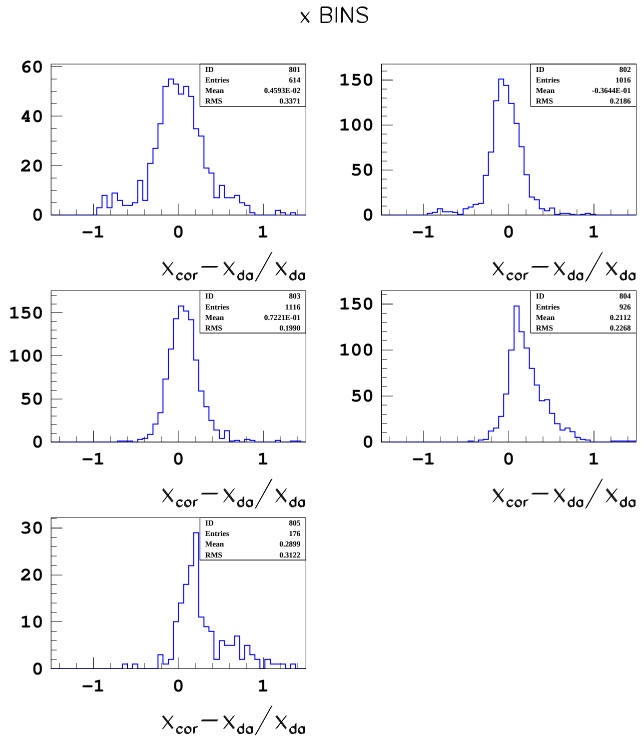

Figure A.5: Comparison of x_{cor} and x_{DA} using the reweighted neutral current sample in bins of x.

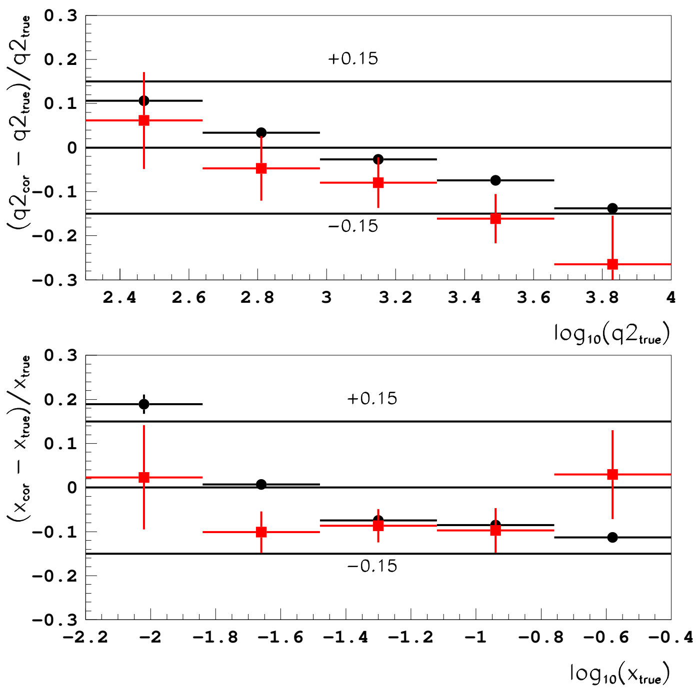

Figure A.6: Relative difference of Q^2_{cor} and x_{cor} respect to the true variables (double angle variables) as computed from MC CC (NC reweighted sample)

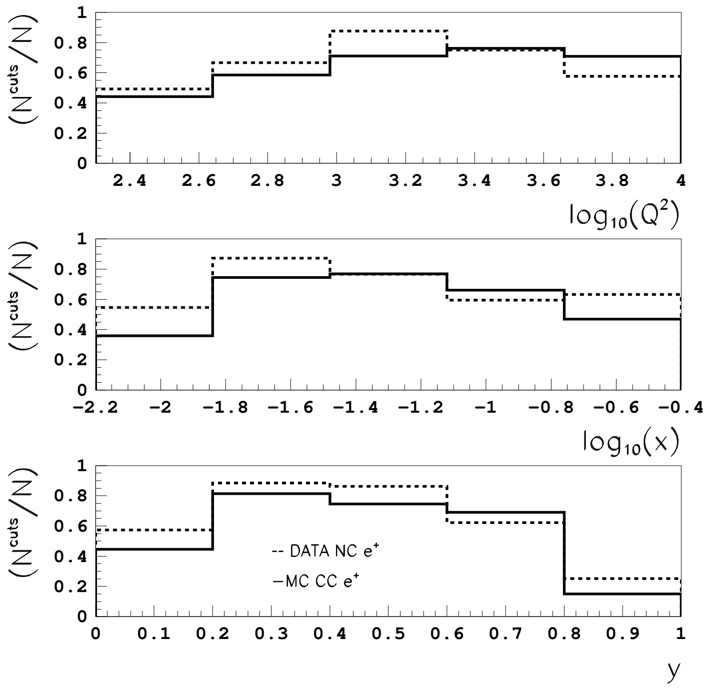

Figure A.7: Comparison of the selection cut efficiencies from the CC MC and the NC reweighted sample. It must be noted that the neutral current sample was not corrected by the neutral current selection efficiency.

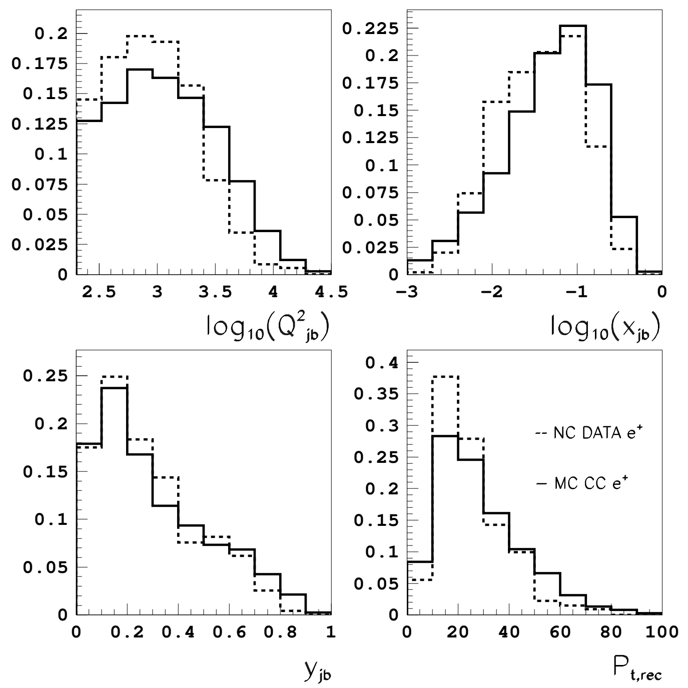

Figure A.8: Comparison of the reconstructed kinematic variables from charged current MC and NC data reweighted. The results only allow to make cross checks of the CC Monte Carlo predictions.

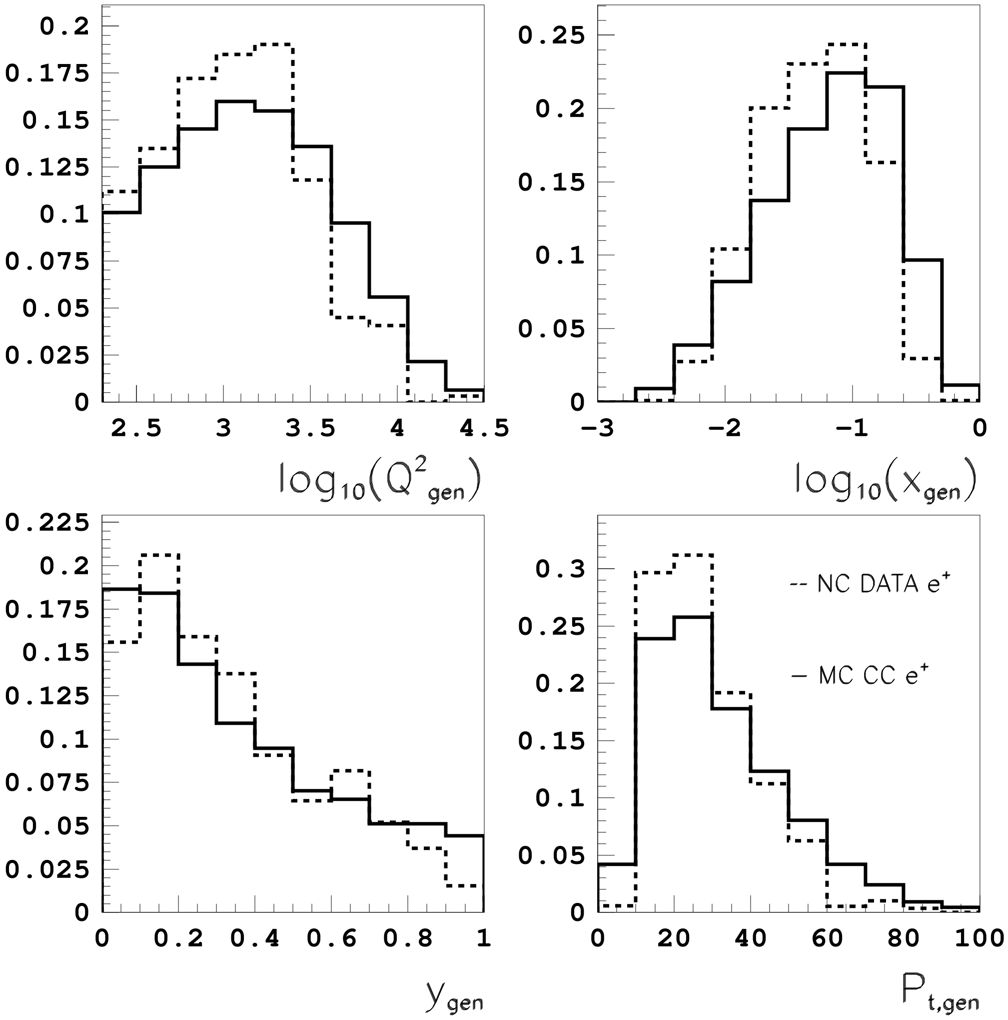

Figure A.9: Comparison of the generated (double angle) kinematic variables from charged current MC and NC data reweighted. The results only allow to make cross checks of the CC Monte Carlo predictions.

Appendix B

Comparison between Neutral and Charged Current Interactions

B.1 Event Selection

The NC DIS events are characterized by their deflected electron, which, for $Q^2 = 200$ GeV^2, has an average energy of approximately 22 GeV and is restricted to $\theta_e < 150^0$. As Q^2 increases, the electrons are produced with higher momentum and smaller angles. For NC DIS, the event variable δ is equal to twice the electron beam energy if no energy leaks through the rear beam hole of the calorimeter. In addition high Q^2 events in which the electron strikes the FCAL ($Q^2 > 1000 GeV^2$) are characterized by large transverse energy E_t.

The events are preselected using the ZEUS three level trigger. The first level trigger required a total electromagnetic energy of 3.4 GeV in the RCAL or 4.8 GeV in the BCAL, or $E_t^{cone} > 15$ GeV, where E_t^{cone} was calculated excluding the two rings of towers nearest the forward beampipe. The E_t^{cone} requirement is designed to tag high Q^2 events by their large E_t hadronic energy while rejecting beam-gas background associated with large energy deposits at low θ angles. Background rates were reduced at the second level trigger by removing events with calorimeter timing inconsistent with an ep interaction. For the third level trigger, events were reconstructed and the requirements were similar to the offline cuts described below.

Offline, electrons are identified in the calorimeter using a neutral-network algorithm. To ensure high purity, the electron is required to have at least 10 GeV of energy, where the Monte Carlo studies show that the identification efficiency is also better than 96 %. To reduce background produced by electromagnetic showers in hadronic jets from photoproduction, y calculated from the electron candidate (y_e) is required to be less than 0.95. In addition, each electron must be matched to a charged track of at least 5 GeV of momentum, except in the forward direction $\theta < 15^0$ where the electron must have at least 20 GeV transverse energy as measured by the calorimeter. To further reduce background, isolated electrons are selected by requiring no more than 5 GeV of energy in calorimeter cells not associated with the electron in an $\eta - \phi$ cone of radius 0.8 centered on the electron. If more than one electron candidate that passes these cuts is found in an event, the one with the highest transverse momentum is assumed to be the DIS electron. To remove background, additional checks are performed on events with multiple electron candidates. If a second electron candidate of any energy and with or without a matching track is discovered with an angle $\theta > 165^0$ (beyond fully efficient tracking) then the event is discarted to remove

low Q^2 background. In addition, if there is no more than 10 GeV energy left in the calorimeter after subtracting the two electrons, it is assumed that the event is an elastic Compton event and is also discarded. To ensure that event quantities can be accurately determined, a reconstructed vertex with $-50 < v_z < 100$ cm is required, as consistent with an ep interaction. To suppress photoproduction events where the deflected electron escapes through the beam hole in the RCAL, δ is required to be greater than 35 GeV.
To remove cosmic rays and beam related background, the total transverse momentum P_t is required to be less than $3\sqrt{E_t}$GeV, where E_t is the total transverse energy.
The efficiency of these cuts is approximately 80%, roughly independent of Q^2. The main loss of events (10%) is from the requirement of an electron of at least 10 GeV, but this loss is restricted to $Q^2 < 1000$ GeV^2 and high y. In addition, 7% of events fail the tracking requirement, primarily due to final-state radiation and Bremsstrahlung, except at high Q^2 where there were additional losses due to falling tracking efficiency and momentum resolution at small angles.

B.2 Reconstruction and Unfolding

Q^2 and x are measured using the double angle method

$$Q^2_{DA} = 4A^2 \frac{sin\gamma_h(1 + cos\theta_e)}{sin\gamma_h + sin\theta_e - sin(\gamma_h + \theta_e)}$$

$$x_{DA} = \frac{4A^2}{s} \frac{sin\gamma_h + sin\theta_e + sin(\theta_e + \gamma_h)}{sin\gamma_h + sin\theta_e - sin(\gamma_h + \theta_e)}$$

where A is the energy of the electron beam, θ_e is the angle of the scattered electron, and γ_h, in the naive quark parton model picture of DIS, is the polar angle of the struck quark. The angle θ_e is measured with the tracking chambers when the electron is inside the tracking acceptance and otherwise from the center of the electron shower in combination with the electron vertex. The angle γ_h is calculated from the event quantities $P_{t,h}$ and δ_h, which are calculated from all calorimeter cells except those assigned to the electron.

$$cos\gamma_h = \frac{P^2 t, h - \delta_h^2}{P^2 t, h + \delta_h^2}$$

A plot of Q^2_{DA} versus x_{DA} for the e^+p data is shown in figure B.1. The comparison of some relevant variables between data and Monte Carlo are presented in figure B.2. Reasonable agreement is seen.

To measured the differential cross section, the efficiency and migration estimated from a Monte Carlo DJANGO event sample are used to unfold the data binned in Q^2_{DA} and produce a cross section binned in corrected Q^2.

B.3 Systematic Uncertainties

A complete study of the systematic uncertainties is performed:

- The systematic error associated with the determination of γ_h was investigating by varying the energy scale of each part (RCAL,FCAL,BCAL) of the detector independently by $\pm 2\%$, reducing the energy in regions of θ to reflect uncertainties in inactive material in front of the calorimeter, changing the energies of the calorimeter cells adjacent to the forward beam-pipe by $\pm 20\%$, and exploring the difference between predictions from the MEPS and ARIADNE models of fragmentation. The net result is an estimated error of less than 1% in the differential cross section in the entire kinematic range.

- A comparison of electron energies predicted by Q^2_{DA} and measured in the calorimeter shows an agreement of energy scale within 2% and energy resolution to within 5% of Monte Carlo predictions. Such uncertainties result in a $< 1\%$ systematic error in the cross section.

- Doubling the electron identification inefficiency predicted by the Monte Carlo produced errors of $2 - 3\%$.

- Uncertainties in the tracking resolution and selection for low-angle tracks produced a much as a 20% systematic error, but limited to the bins in the range $10000 < Q^2 < 20000$ GeV^2.

- Uncertainties associated with calorimeter-tracking alignment and calorimeter P_t resolution were all found to be below 2%.

- Biases in unfolding were investigated. The results change by no more than 1.5%.

B.4 Results

The cross section results are tabulated in table B.1 and illustrated in figures B.3 B.4. Also plotted are Standard Model predictions using the GRV94 H0, CTEQ 3 or MRSG parton distributions. Agreement with the data is observed within errors. The predictions from the three parton distributions differ by no more than 15% over the entire Q^2 range.

Q^2 (GeV^2)	N_i e^-p	$\sigma(e^-p)$ (pb)	N_i e^+p	$\sigma(e^+p)$ (pb)
$200 - 282$	542	1060 ± 60 $^{+40}_{-20}$	6737	1100 ± 20 $^{+40}_{-20}$
$282 - 399$	367	719 ± 45 $^{+21}_{-7}$	4257	674 ± 12 $^{+20}_{-6}$
$399 - 563$	199	326 ± 29 $^{+9}_{-3}$	2706	377 ± 9 $^{+10}_{-3}$
$563 - 795$	139	229 ± 23 $^{+7}_{-2}$	1708	230 ± 7 $^{+7}_{-2}$
$795 - 1120$	84	128 ± 18 $^{+3}_{-1}$	1010	126 ± 5 $^{+3}_{-1}$
$1120 - 1590$	56	88.8 ± 14.3 $^{+2.2}_{-0.5}$	647	83.7 ± 4.0 $^{+2.0}_{-0.5}$
$1590 - 2240$	31	48 ± 11 $^{+1}_{-0}$	373	48.3 ± 3.0 $^{+1.4}_{-0.3}$
$2240 - 3160$	20	33 $^{+9}_{-8}$ $^{+1}_{-0}$	198	25.2 ± 2.2 $^{+0.8}_{-0.3}$
$3160 - 4470$	8	12 $^{+6}_{-5}$ $^{+0}_{-0}$	115	15.0 ± 1.6 $^{+0.5}_{-0.3}$
$4470 - 6310$	4	5.8 $^{+5.5}_{-1.8}$ $^{+0.3}_{-0.2}$	55	6.4 ± 1.1 $^{+0.3}_{-0.2}$
$6310 - 8900$	1	0.94 $^{+3.33}_{-0.94}$ $^{+0.08}_{-0.08}$	29	3.5 ± 0.8 $^{+0.3}_{-0.2}$
$8900 - 12600$	2	3.4 $^{+3.3}_{-2.0}$ $^{+0.4}_{-0.4}$	12	1.3 $^{+0.6}_{-0.5}$ $^{+0.2}_{-0.2}$
$12600 - 17800$	0	< 2.3	6	0.83 $^{+0.47}_{-0.35}$ $^{+0.12}_{-0.12}$
$17800 - 25100$	2	3.4 $^{+3.2}_{-1.9}$ $^{+0.6}_{-0.6}$	2	0.26 $^{+0.34}_{-0.14}$ $^{+0.06}_{-0.05}$
$25100 - 35400$	0	< 2.6	0	< 0.24
$35400 - 50000$	0	< 2.7	1	0.18 $^{+0.19}_{-0.18}$ $^{+0.04}_{-0.01}$
$200 - 50000$	1455	2730 ± 72 $^{+75}_{-30}$	17978	2780 ± 21 $^{+76}_{-30}$

Table B.1: The number of e^+p and e^-p NC DIS events in each Q^2_{DA} bin before unfolding and the resulting unfolded cross sections in each Q^2 bin. Also shown are the values for the entire Q^2 range. The first error for the cross sections is statistical, the second systematic.

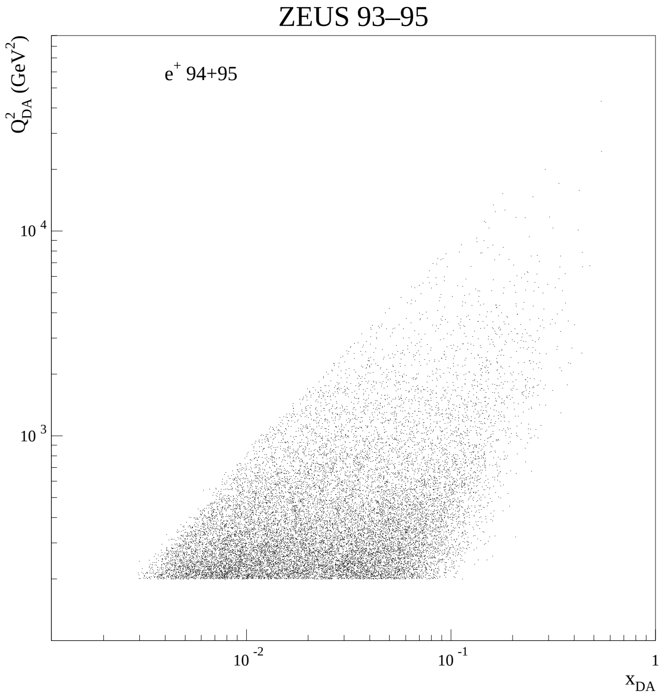

Figure B.1: Region of the Q^2_{DA}-x_{DA} plane covered by the e^+p data sample used in the analysis.

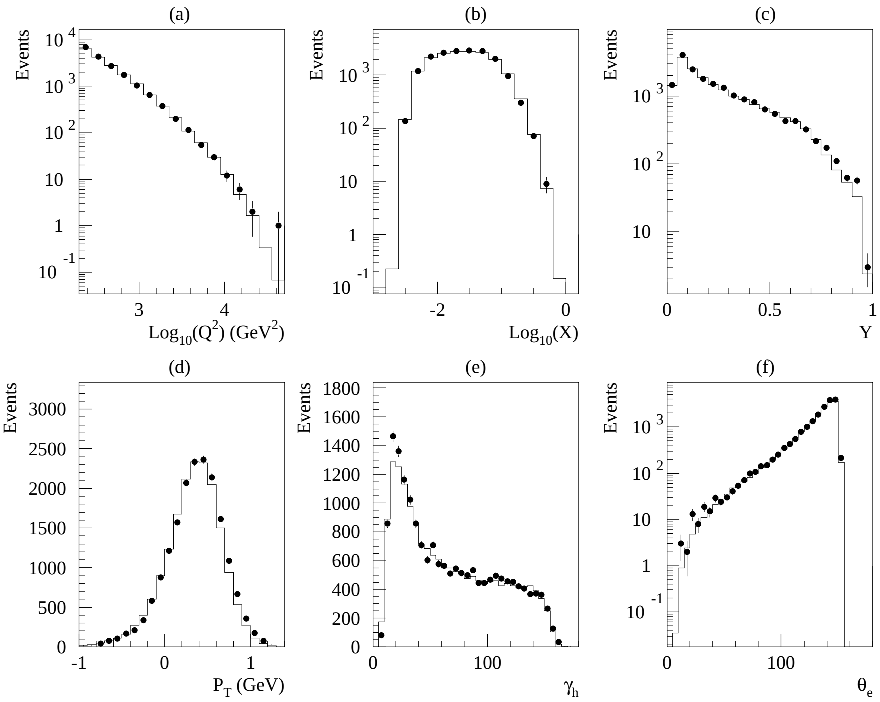

Figure B.2: Comparison between data (points) and Monte Carlo (histogram) of some relevant variables: (a) $log_{10}(Q^2_{DA})$, (b) $log_{10}(x_{DA})$, (c) y_{DA}, (d) total calorimeter P_t, (e) hadronic angle γ_h and (f) electron angle θ_e.

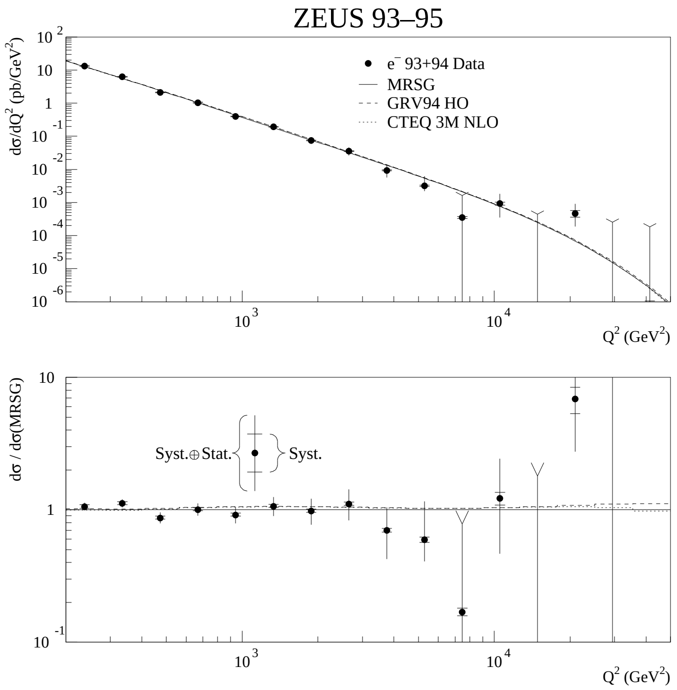

Figure B.3: Differential cross section $d\sigma/dQ^2$ for e^-p NC DIS events (points) compared with Standard Model predictions with different structure functions parameterizations (curves) [top], and the ratio of data and GRV94 and CTEQ3M predictions over the prediction using MRSG [bottom].

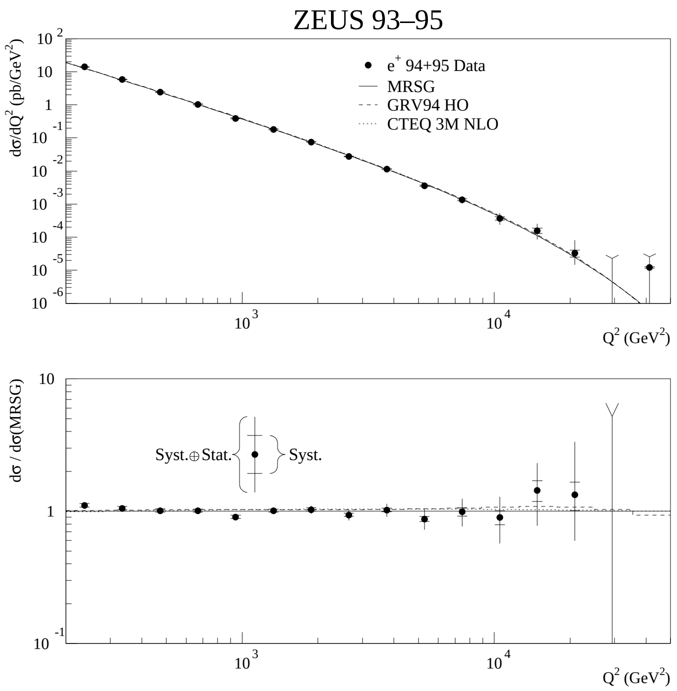

Figure B.4: Differential cross section $d\sigma/dQ^2$ for e^+p NC DIS events (points) compared with Standard Model predictions with different structure functions parameterizations (curves) [top], and the ratio of data and GRV94 and CTEQ3M predictions over the prediction using MRSG [bottom].

Appendix C

Jet Energy Correction Procedure

C.1 Reconstruction of jet variables

In order to compare HAD and CAL jets, definite ranges in η^{jet} and thresholds in E_T^{jet} have to be considered.

The following ranges were used:

- **CAL jets**: $E_T^{CAL}(jet) > 6$ GeV and $-1 < \eta_{CAL}(jet) < 2$
- **HAD jets**: $E_T^{HAD}(jet) > 8$ GeV and $-1 < \eta_{HAD}(jet) < 2$

In a given event several jets of each type can be found and a definite rule for associating CAL jets to HAD jets has to be setup: for each HAD jet the distance in the $\eta - \phi$ plane between that jet and each of the CAL jets is computed as:

$$d(HAD - CAL) = \sqrt{(\phi^{HAD}(jet) - \phi^{CAL}(jet))^2 + (\eta^{HAD}(jet) - \eta^{CAL}(jet))^2}$$

and the pair with minimum $d(HAD - CAL)$ is taken if that distance is smaller than 1 unit. Then, the variables characterizing the pair of matched jets are compared.

In figures C.1 and C.2 (C.3 and C.4) the comparison of jet variables for each pair of matched jets in NC DIS (CC DIS) are presented. These distributions show that the variables of the CAL are well correlated with the hadronic variables. The distributions for:

- $\Delta\eta \equiv \eta_{CAL}(jet) - \eta_{HAD}(jet)$
- $\Delta\phi \equiv \phi_{CAL}(jet) - \phi_{HAD}(jet)$
- $\Delta E_T/E_T \equiv (E_T^{CAL}(jet) - E_T^{HAD}(jet))/E^{HAD}(jet)$

have been fitted to gaussian functions. In the case of the angular variables, there is no significant systematic bias and the resolution is around 0.06 (0.05) for ϕ^{jet} and 0.05 (0.03) units for η^{jet}. For the reconstruction of the transverse energy of the jet, $E_T(jet)$, a systematic shift of 16 % (12 %) is observed and the resolution is 11 % (9 %). From this study we conclude that the *angular* jet variables do not need to be corrected and that the jets transverse energy needs correction. The procedure to obtain the corrected E_T^{jet} is explained in the next section.

C.2 Jet Energy Correction

In the previous section the $(E_T^{CAL} - E_T^{HAD})/(E_T^{HAD})$ distribution was shown for NC and CC Monte Carlo events. A systematic shift was observed which indicates that there are energy losses affecting the E_T^{jet} measured by the CAL. The energy corrections are computed using Monte Carlo samples of events that were processed through a simulation of the ZEUS detector which takes into account all the known effects that produce energy loss. The correction for E_T^{jet} is constructed as a multiplicative factor which depends on both η^{jet} and E_T^{jet}:

$$E_T^{COR}(jet) = K(E_T^{CAL}(jet), \eta_{CAL}(jet)) * E_T^{CAL}(jet)$$

The evaluation of the function K depends on the threshold applied to $E_T^{CAL}(jet)$. As a first step this threshold is determined as a function of η^{jet}. One expects that the threshold function will depend on η^{jet} due to the different amount of dead material as a function of the polar angle. In order to compute the threshold, HAD jets are compared with the matched CAL jets. The mean value of the distribution for E_T^{HAD}/E_T^{CAL} in each bin of η^{CAL} $(-1 < \eta^{CAL}(jet) < 2)$ is computed,

$$T_i =< E_T^{HAD}(jet)/E_T^{CAL}(jet) > (\eta^{CAL}(jet) \in bin \;\; i)$$

The T-function has been calculated using the Monte Carlo samples of events for NC and CC interactions separately. The results are shown in figure C.5. It must be noted the two peaks in the regions $\eta^{jet} \sim 1$ and $\eta^{jet} \sim -1$. These are understood in terms of the increase of inactive material in front of the CAL in those regions. The observed differences in the T-function for NC and CC reactions results from the different E_T^{jet} spectrum. After computing the T-functions, CAL jets will be selected according to an η^{jet} dependent threshold in $E_T^{CAL}(jet)$.

$$E_T^{CAL}(jet)(\eta_{CAL}(jet) \in bin \;\; i) \geq \frac{8 \;\; GeV}{T_i}$$

In order to estimate the CAL response to HAD jets, the distribution of $E_T^{HAD}(jet)/E_T^{CAL}(jet)$ in bins of $(E_T^{CAL}(jet), \eta_{CAL}(jet))$ is determined. The mean value of these distributions are displayed in figures C.6 (C.7) for NC (CC) interactions, as a function of $E_T^{CAL}(jet)$ for each bin of $\eta_{CAL}(jet)$. These function have been fitted to the form

$$C_i(E_T^{CAL}(jet)) = A_i^1 + A_i^2 * e^{A_i^3 * E_T^{CAL}(jet)}$$

The resulting parameterisations are displayed as solid lines. The complete set of 10 functions, $C_i(E_T^{CAL}(jet)) \;\; i = 1, ..., 10$, for a given Monte Carlo sample of events, constitutes the correction factor for the transverse energy of the jets. Figures C.8 and C.9 shown the comparison of the hadronic and corrected jet transverse energy as a function of the corrected transverse energy in different regions of $\eta_{CAL}(jet)$. It is noted that the transverse energy of the jets has been properly corrected in all the regions. Finally, figures C.10 and C.11 show the comparison of the corrected and hadronic $E_T(jet)$ in the different $E_T(jet)$ regions used in the jet shape analyses for neutral and charged current DIS respectively. It is observed that the mean value of the gaussian distributions are well corrected.

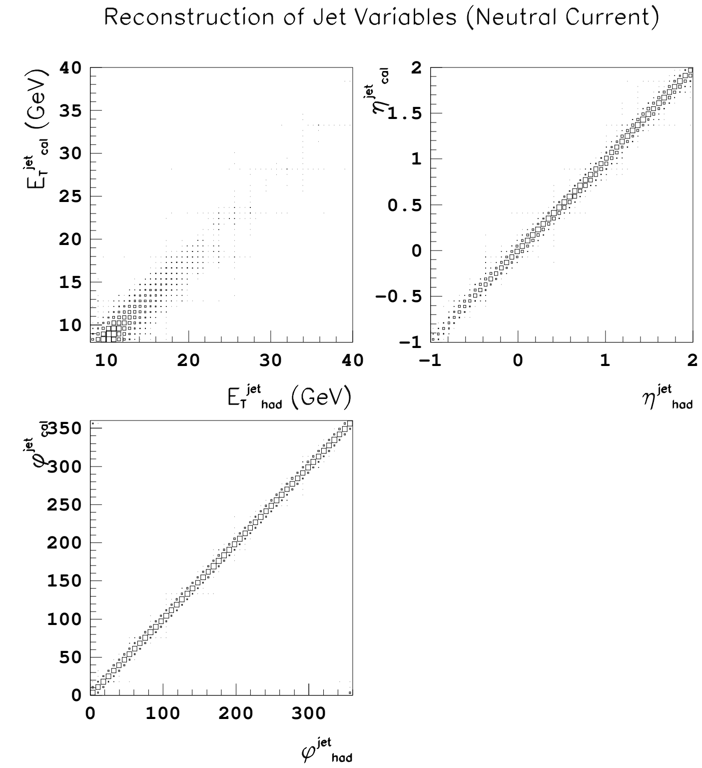

Figure C.1: Comparison of the hadronic and measured in the CAL jet variables as determined from neutral current Monte Carlo events.

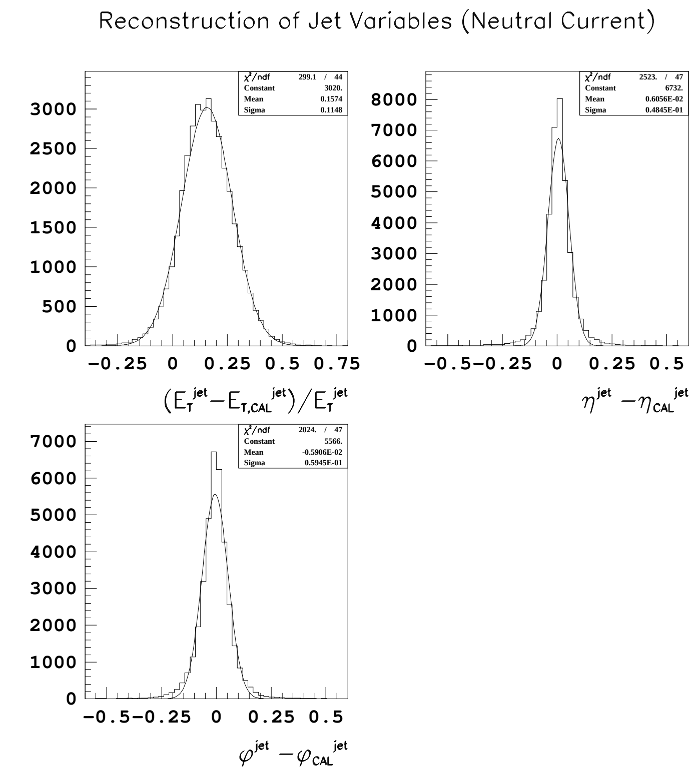

Figure C.2: Comparison of hadronic and CAL jet variables for neutral current interactions.

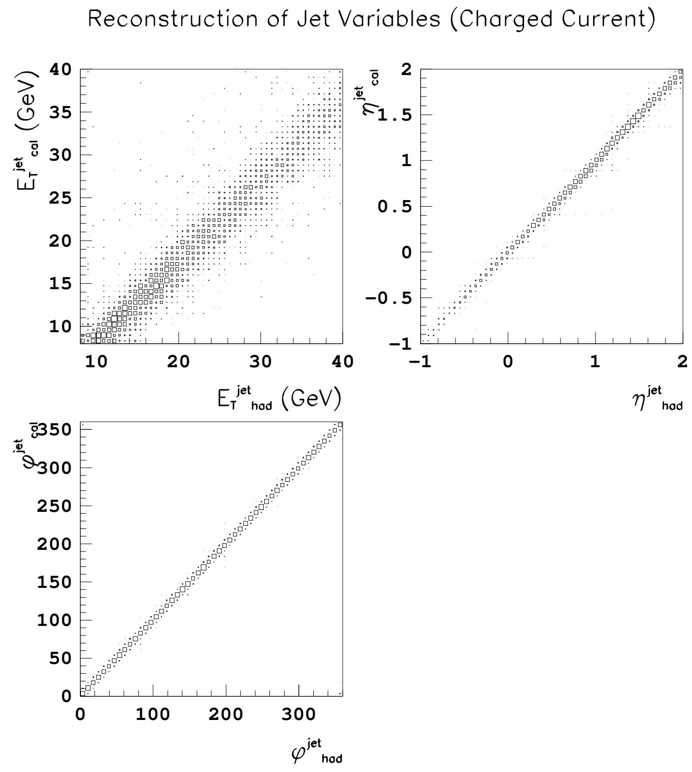

Figure C.3: Comparison of the hadronic and measured in the CAL jet variables as determined from charged current Monte Carlo events.

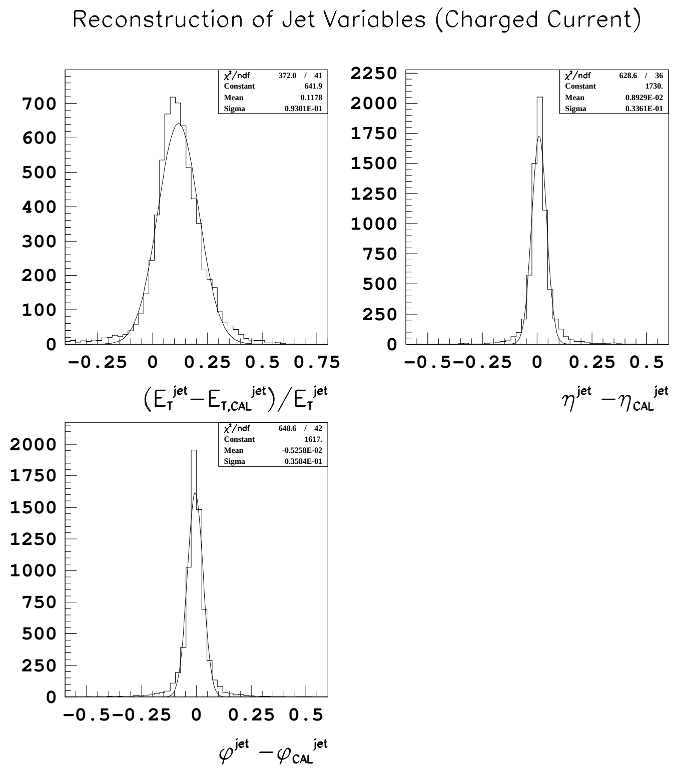

Figure C.4: Comparison of hadronic and CAL jet variables for charged current interactions.

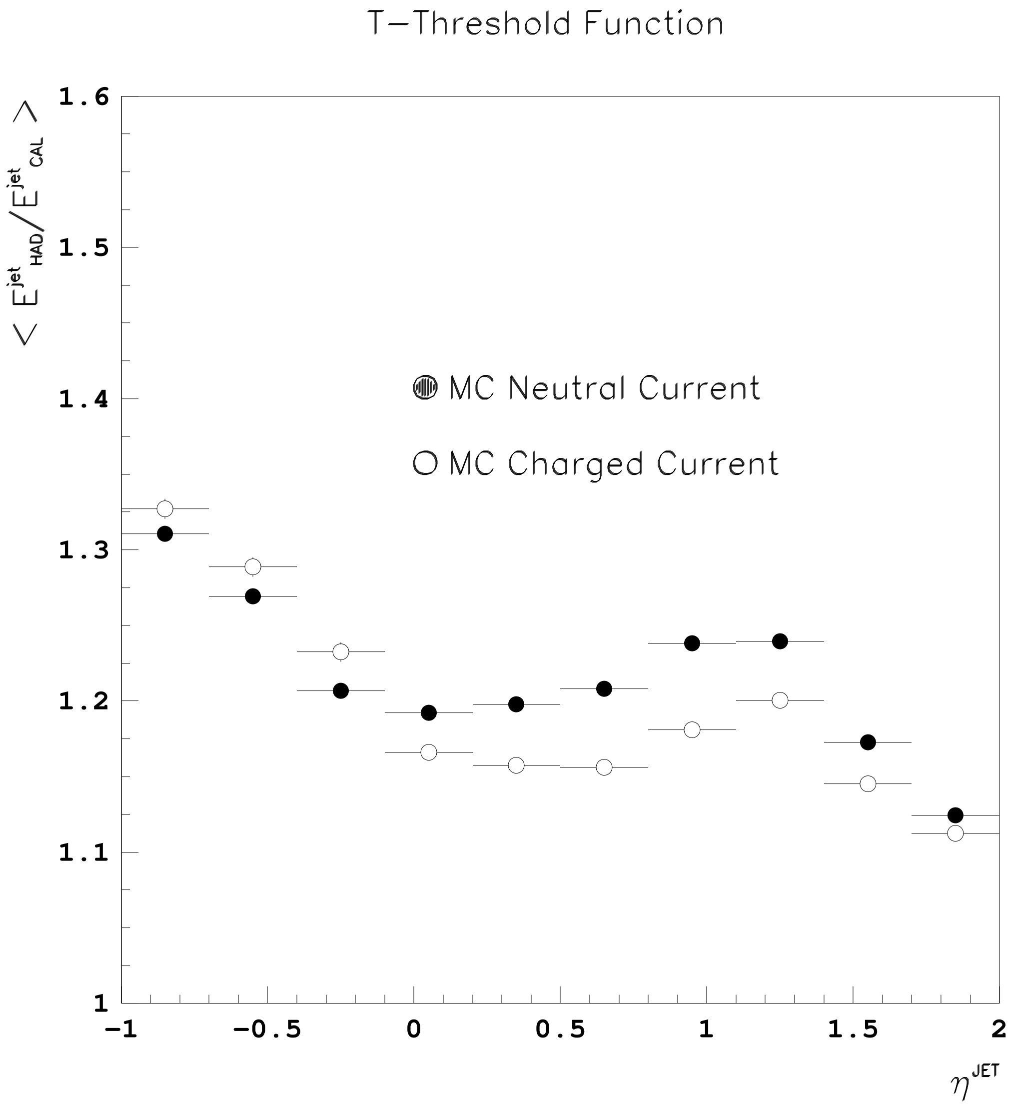

Figure C.5: Threshold functions determined for neutral and charged current interactions from Monte Carlo events.

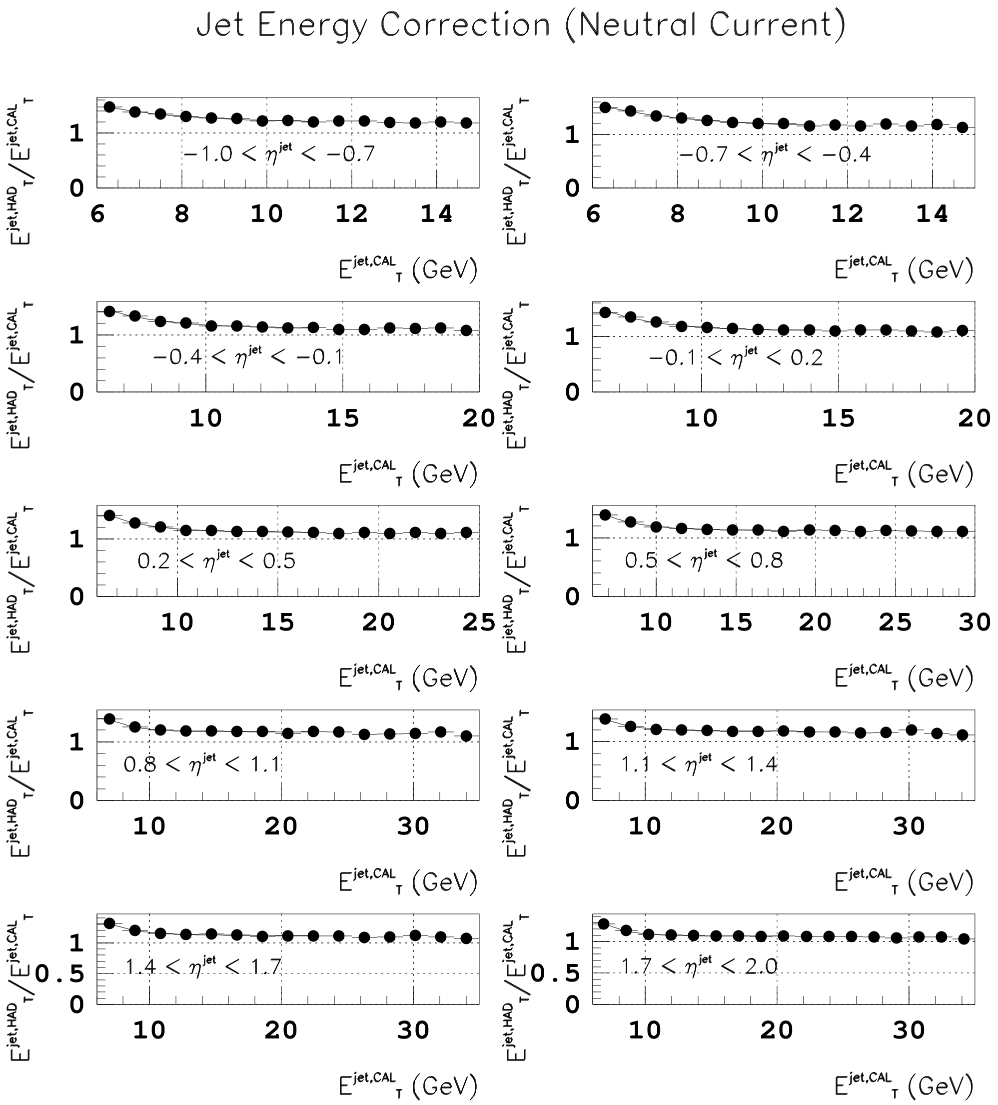

Figure C.6: Correction of the transverse energy of the jet in neutral current interactions as a function of $E_T^{CAL}(jet)$ in different regions of $\eta^{CAL}(jet)$.

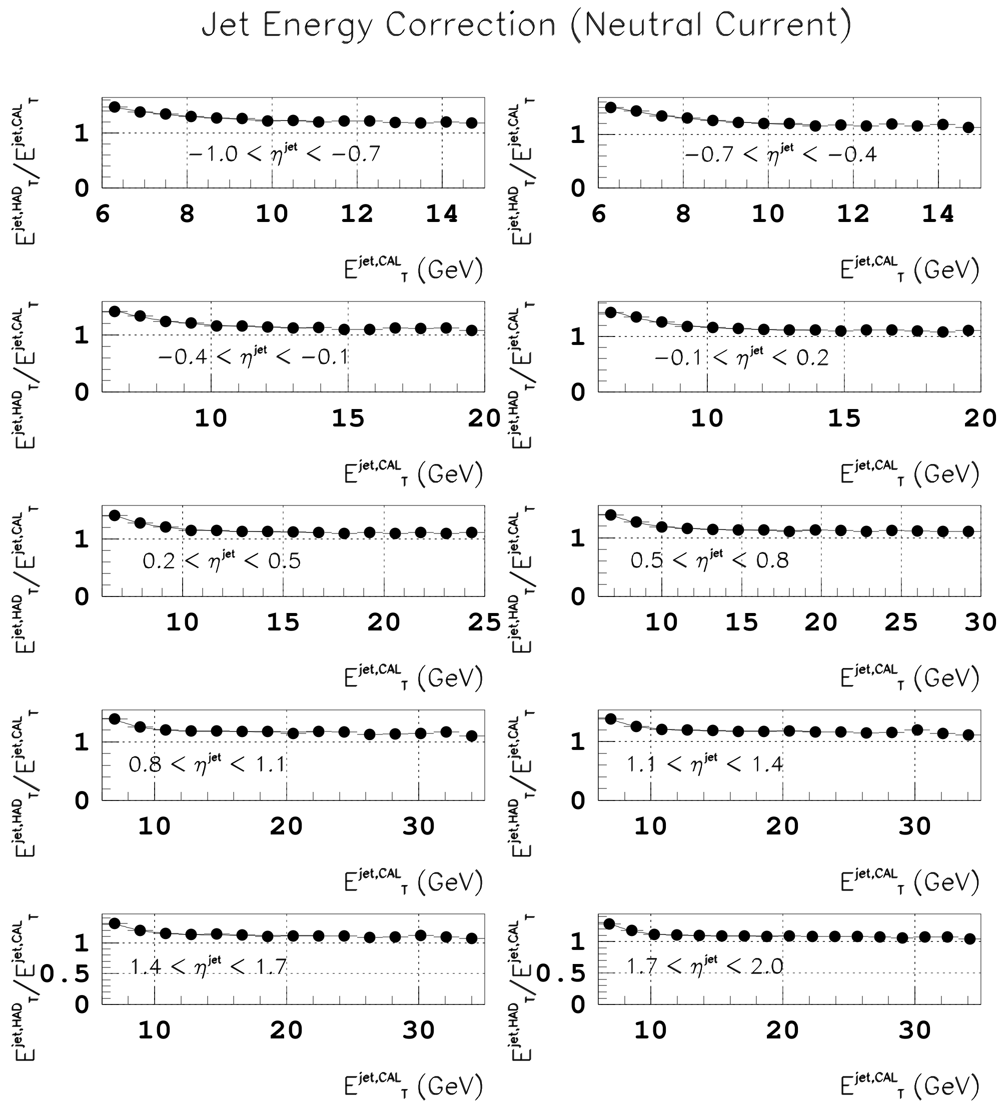

Figure C.7: Correction of the transverse energy of the jet in charged current interactions as a function of $E_T^{CAL}(jet)$ in different regions of $\eta^{CAL}(jet)$.

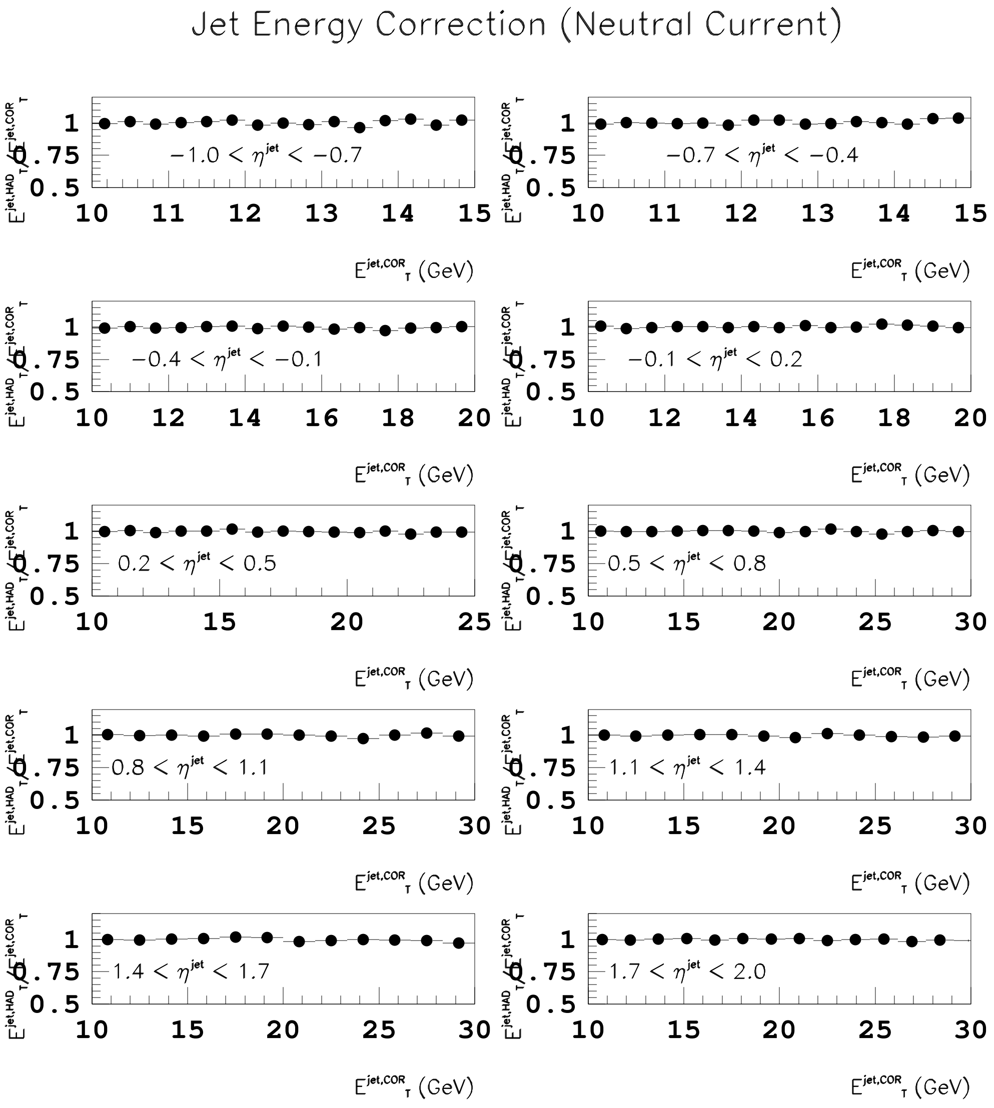

Figure C.8: Comparison of the hadronic and corrected jet transverse energy as a function of the corrected jet transverse energy in different regions of $\eta_{CAL}(jet)$ for jets in neutral current DIS.

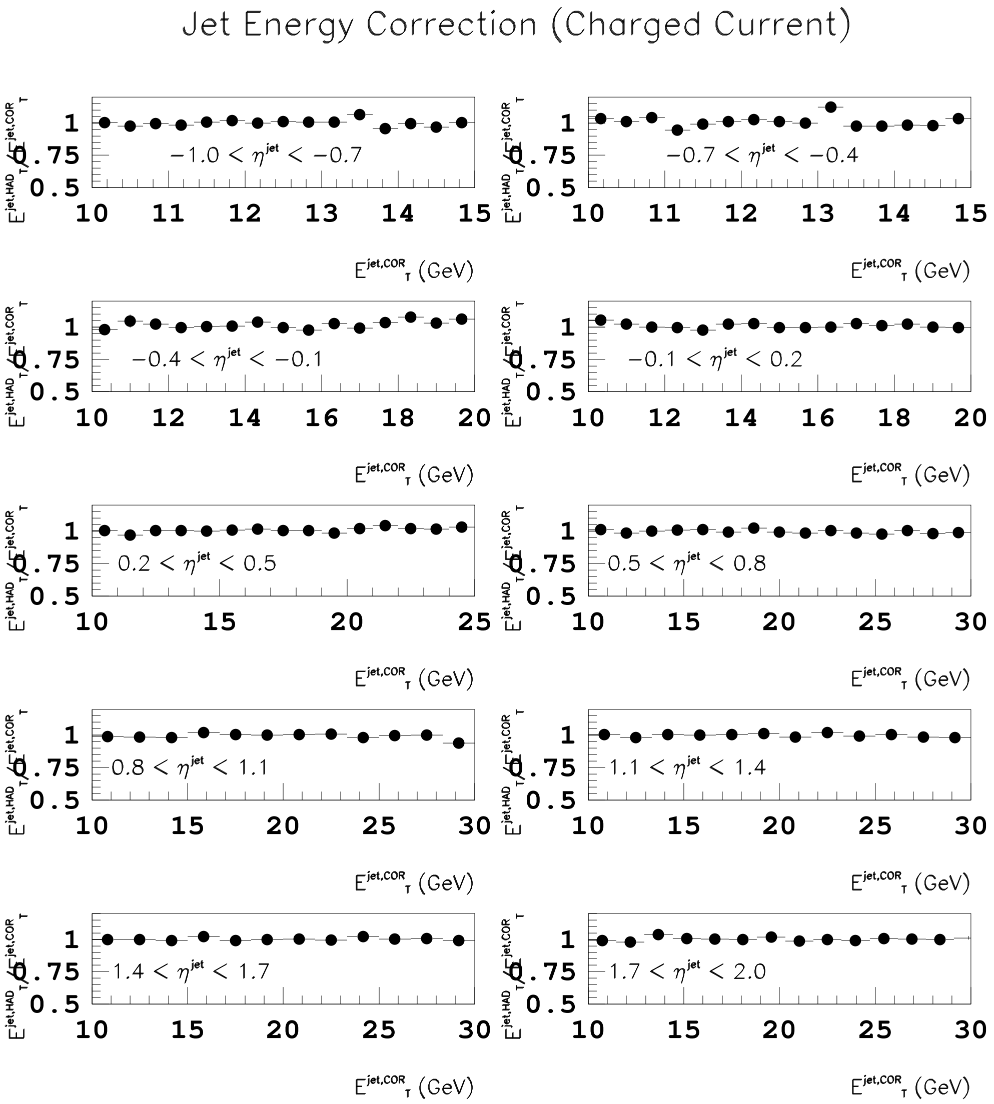

Figure C.9: Comparison of the hadronic and corrected jet transverse energy as a function of the corrected jet transverse energy in different regions of $\eta_{CAL}(jet)$ for jets in charged current DIS.

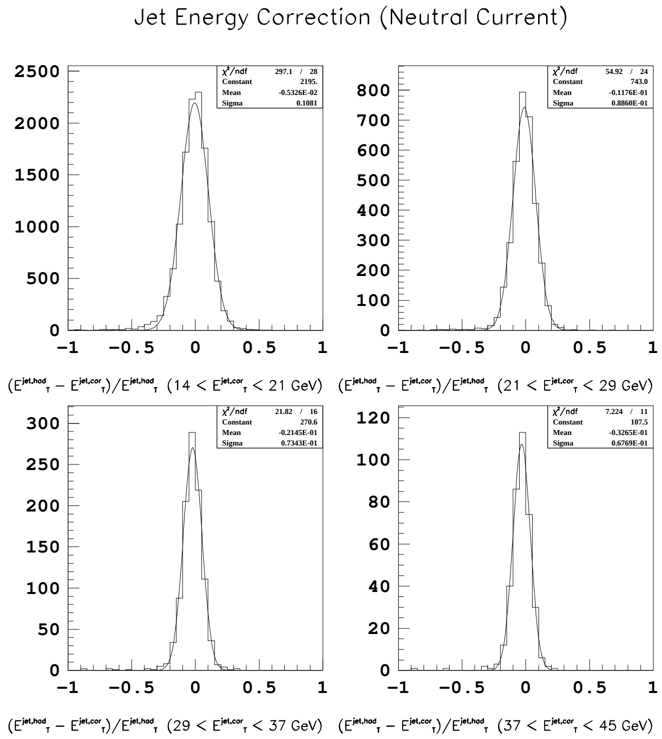

Figure C.10: Comparison of the hadronic and corrected transverse energy of the jet in the different regions considered in the jet shape measurements for neutral current DIS.

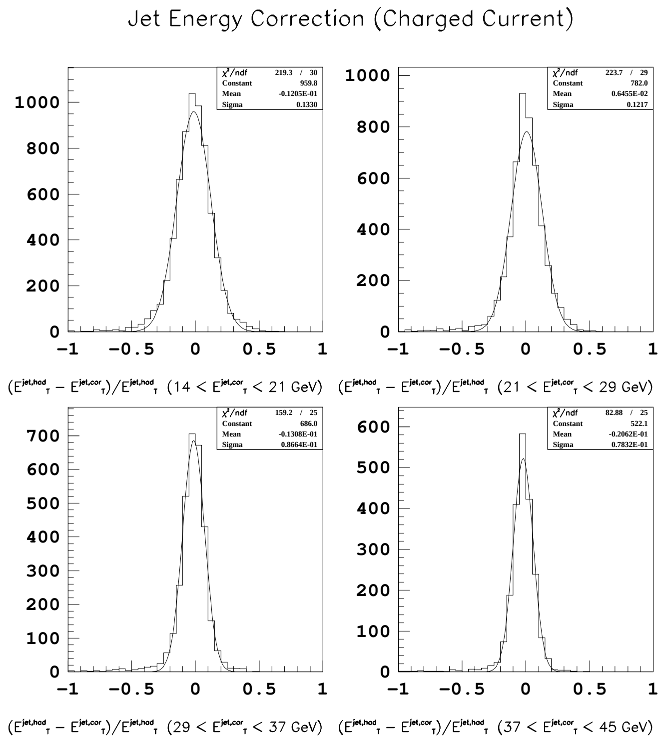

Figure C.11: Comparison of the hadronic and corrected transverse energy of the jet in the different regions considered in the jet shape measurements for charged current DIS.

Appendix D

Jet Shapes Studies using Tracks

The tracking component of the ZEUS detector provides an independent method to reconstruct the shape of a jet. The procedure is as follows: for each jet, the sum of the transverse momenta of those tracks assigned to the given jet whose distance $r' = \sqrt{(\Delta\eta)^2 + (\Delta\phi)^2}$ to the jet axis is smaller than r is computed, $E^{jet}_{T,tracks}$, and divided by $E^{jet}_{T,tracks}(r = R)$. Hence, the jet shape measured with the tracks, $\psi_{track}(r)$, is defined as

$$\psi_{track}(r) = \frac{1}{N_{jets}} \sum_{jets} \frac{E^{jet}_{T,track}}{E^{jet}_{T,track}(r = R)}$$

where the sum runs over all the jets in the selected sample that satisfy $E^{jet}_{T,track} > 0$ and N_{jet} is the total number of jets satisfying $E^{jet}_{T,tracks}(r = R) > 0$. The assignment of a track to a given jet is based on the following procedure:

- Only the tracks from the primary vertex with a polar angle $15^o < \theta_{track} < 164^o$, a transverse momentum $0.15 < p_T^{track} < 150$ GeV and $N_{dof} \geq 10$ are considered.
- The distance between the track and the jet axis, in the $\eta - \phi$ plane, is computed

  $$r' = \sqrt{(\eta^{track} - \eta^{jet})^2 + (\phi^{track} - \phi^{jet})^2}$$

  If $r' < 1$ the track is associated to the given jet.
- If one track belongs to several jets, the track is associated to the nearest one.

The use of tracks instead of CAL cells in the reconstruction of the jet shapes provides a better resolution in angular position and transverse momentum at relatively low P_T. Nevertheless, this method is obviously only sensitive to charged particles and suffers from the limited acceptance of the CTD in the backward and forward regions. Hence, the results of this study are only used as an independent check to those obtained using the CAL. Figures D.1,D.2 show the comparison of the uncorrected jet shapes as a function of η^{jet} and E_T^{jet} for jets in neutral current interactions.

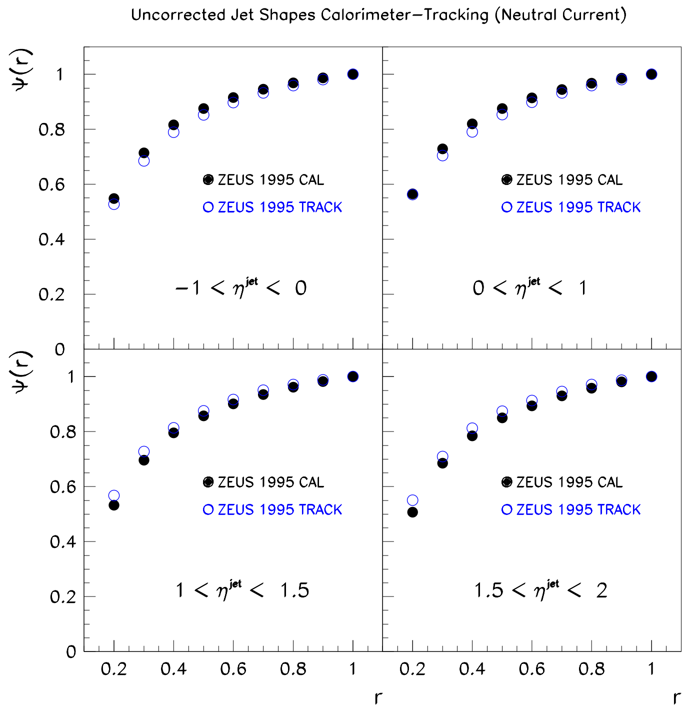

Figure D.1: Comparison of the uncorrected jet shapes in neutral current interactions measured using the calorimeter and the central tracking detector in different regions of η^{jet}.

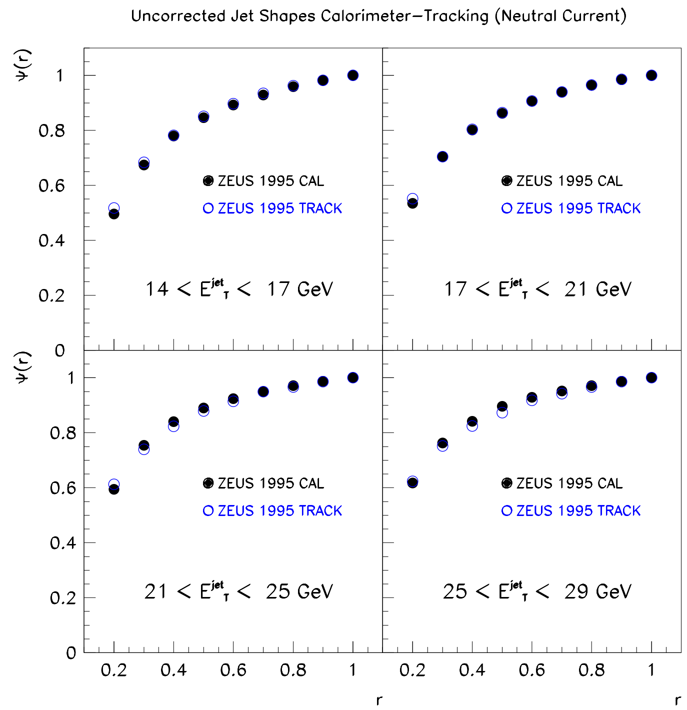

Figure D.2: Comparison of the uncorrected jet shapes jet shapes in neutral current interactions measured using the calorimeter and the central tracking detector in different regions of E_T^{jet}.